COLLOIDAL SUSPENSION HYDRODYNAMICS AND TRANSPORT PROCESSES IN MICROCAPILLARY AND POROUS MEDIA FLOWS STUDIED USING DYNAMIC NUCLEAR MAGNETIC RESONANCE

by

Einar Orn Fridjonsson

A dissertation submitted in partial fulfillment
of the requirements for the degree

of

Doctor of Philosophy

in

Engineering

MONTANA STATE UNIVERSITY
Bozeman, Montana

July 2010

APPROVAL

of a dissertation submitted by

Einar Orn Fridjonsson

This dissertation has been read by each member of the dissertation committee and has been found to be satisfactory regarding content, English usage, format, citation, bibliographic style, and consistency, and is ready for submission to the Division of Graduate Education.

Dr. Joseph D. Seymour

Approved for the Department of Chemical and Biological Engineering

Dr. Ron Larsen

Approved for the Division of Graduate Education

Dr. Carl A. Fox

STATEMENT OF PERMISSION TO USE

In presenting this dissertation in partial fulfillment of the requirements for a doctoral degree at Montana State University, I agree that the Library shall make it available to borrowers under rules of the Library. I further agree that copying of this dissertation is allowable only for scholarly purposes, consistent with “fair use” as prescribed in the U.S. Copyright Law. Requests for extensive copying or reproduction of this dissertation should be referred to ProQuest Information and Learning, 300 North Zeeb Road, Ann Arbor, Michigan 48106, to whom I have granted “the exclusive right to reproduce and distribute my dissertation in and from microform along with the non-exclusive right to reproduce and distribute my abstract in any format in whole or in part.”

Einar Orn Fridjonsson

July 2010

TABLE OF CONTENTS

TABLE OF CONTENTS-CONTINUED

TABLE OF CONTENTS-CONTINUED

LIST OF TABLES

LIST OF FIGURES

Figure Page

LIST OF FIGURES - CONTINUED

Figure Page

LIST OF FIGURES - CONTINUED

Figure Page

LIST OF FIGURES - CONTINUED

LIST OF FIGURES - CONTINUED

ABSTRACT

The research presented in this dissertation uses Magnetic Resonance Microscopy (MRM) to investigate complex fluid dynamics systems. The systems investigated are colloidal transport in a microcapillary, bifurcation and porous medium, reactive transport in porous medium, transport through β-lactoglobulin gels and the effect of peptide surfactants on droplet deformation in a Taylor-Couette device. Complex transport phenomena underlies many applications in engineering and thorough understanding of convective and diffusive motion in multiphase systems is important. MRM allows for the investigation of multi-phase transport phenomena noninvasively and can be used to investigate different moments of motion by sequence of the application of magnetic field gradients. The measurement of coherent and incoherent motion separately and the simultaneous measurement of multiple phases (colloids or suspending fluid) is possible.

The colloidal flow studies show the effects shear induced migration, deposition, incoherent and coherent motion have on the macro- and microscopic structure of the fluids. Results show the direct effect increased shear has on the onset of secondary and chaotic fluid motion due to microscopic particle-particle and macroscopic fluid-structure interactions indicating the presence of shear thresholds.

Reactive transport in porous media is important for understanding the spread of contaminants in the Earth's subsurface. The effect of calcium carbonate precipitation in a model porous medium due to *Sporosarcina pasturii* growth on the hydrodynamics was measured using MRM. These measurements show an increase in mechanical mixing causing a more rapid asymptote to Gaussian dynamics than for the same system without precipitation.

The transport measurements of water with and without NaCl flowing through a homogeneous (pH 7.0) and heterogeneous (pH 5.2) β-lactoglobulin gels quantifies the hydrodynamic dispersion in the gels and provided direct information on the gel structure noninvasively.

Droplet deformation of (36/64)%wt toluene/chloroform droplets in a continuous phase of glycerol inside a Taylor-Couette device with and without surfactants (2%wt Tween60, AM1 and AFD4 peptide surfactants) is measured using a rapid MRM sequence (ROTACOR) which compensates for system rotation. MRM measurements show a restriction to droplet deformation due to the presence of the peptide surfactants.

INTRODUCTION

The research presented in this thesis can be described as the application of Magnetic Resonance Microscopy (MRM) [1] to investigate complex fluid dynamics systems. The systems that will be investigated using MRM are colloidal transport in a microcapillary (chapter 4), bifurcation (chapter 5) and porous medium (chapter 6), reactive transport in porous medium (chapter 7), transport through β-lactoglobulin gels (chapter 8) and the effect of peptide surfactants on droplet deformation in a Taylor-Couette device (chapter 9). Before investigating each individual research project the fundamentals of Nuclear Magnetic Resonance (NMR) will be presented (chapter 2), with an emphasis on explaining the fundamentals necessary to understand the NMR experiments being conducted. Since colloidal suspensions figure heavily in this work and represent a complex system whose transport is not yet completely understood, a detailed section on colloidal transport theory will also be presented (chapter 3) as this is necessary to appreciate many of the phenomena that occur in the geometries being investigated.

The motivation for this research is to investigate the potential of MRM to investigate complex fluid problems with the goal of bringing new experimental information to the scientific discussion. MRM is well suited to investigate multi-phase transport phenomena noninvasively and can be used to investigate different moments of motion by varying the application of gradients. This allows for example for the measurement of coherent and incoherent motion separately as well as the simultaneous measurement of multiple phases (colloids or suspending fluid). Many of the projects

presented in this thesis represent the first time MRM has been used in their study and contains novel information. This sometimes leads to the challenge of how to analyze the information using the proper analytical tools. The approaches used in the following thesis work borrow heavily both from traditional fluid mechanics as well from statistical mechanics and as such can pose a challenge to a reader unfamiliar with those fields. Additionally, the transport information obtained by the use of MRM is in a Lagrangian reference frame which can be a challenging proposition to those mostly familiar with a Eulerian reference frame, as such it can be illuminating to ask oneself how does the information about the transport in each reference frame relate to the other before assuming a figure shows something it does not, a common mistake.

The MRM data presented always represents an ensemble average of the dynamics during a given observation time and therefore using single particle models in thought experiments can be highly erroneous unless one is comfortable with adding up particles or putting a weighting factor on each representative particle to achieve a probabilistic description. A more fruitful approach is to familiarize oneself with the time evolution of probability distribution functions and then impose correlation times. This introduces a fundamental challenge in the use of MRM. Another challenge with MRM is that it is based on a quantum mechanical phenomena, although with many aspects describable in terms of classical mechanics, which necessitates significant mathematical and quantum mechanical understanding to fully appreciate.

The author has attempted to organize this thesis work so that the chapters are fairly independent of each other with only minimal reference across chapters. This is to

make the thesis an easier read, although reading chapters 2 & 3 first is recommended.

Enjoy!

BASICS OF NUCLEAR MAGNETIC RESONANCE

Introduction

In this chapter, the basic theory of nuclear magnetic resonance (NMR) relevant to this thesis work is described; for a more in-depth understanding of individual topics the reader is encouraged to investigate the many excellent textbooks available on NMR [1-6]. NMR was first described and observed in the late 1930s in molecular beam experiments by I. Rabi [7] and later refined to the study of liquid (water) and solid (paraffin wax) samples by E.M. Purcell and F. Bloch [8, 9]. For these discoveries all three obtained Nobel prizes in physics, I. Rabi in 1944 and F. Bloch and E.M. Purcell in 1952. Since these early days the use of NMR has expanded to becoming a mainstay in medical and chemical research [10, 11] as well as being used to study a plethora of interesting physical phenomena [5]. However, the relevance of NMR to engineering and industrial practices has only been illustrated relatively recently [12, 13].

Fundamentals of NMR

Nuclear Magnetic Resonance is caused by the interaction of the nuclear spin, or quantized angular momentum, with an external magnetic field, causing the spin to resonate at a specific frequency. The simplest, incorrect though useful, analogy is to think of each spin as a tiny spinning bar magnet. These sorts of physical analogies are prevalent in fields where quantum phenomena are relevant, because of the want to describe quantized phenomena in terms of a macroscopic picture, but a purely

mathematical description with an ambiguous or non-existent macroscopic description is usually the proper form of describing these phenomena. Using this latter approach, P.A.M. Dirac showed that the spin is a relativistic phenomena emerging naturally from the relativistic extension of quantum mechanics [14]. This need to connect classical physics and quantum physics dates back to the foundation of the theory of quantum mechanics, when E. Schrödinger developed wave mechanics using descriptions from classical physics to define the quantum realm. This was in response to the development of matrix mechanics by W. Heisenberg whose theory lacked physical pictures. Dirac then developed quantum algebra and showed that matrix mechanics and wave mechanics were special cases of his more general description [14] which defined the quantum realm using a purely mathematical approach [15]. This approach allowed Dirac, for example, to predict the existence of anti-matter. An example of the weirdness or non-macroscopic equivalence is that at absolute zero temperature where all motion should cease, the spin is still active. Of course the weirdness is due to the reference frame imposed, because there is no requirement that what happens on the atomic scale has any equivalence on the macroscopic scale, *i.e.* there is no macroscopic object that behaves like a spin. The spin ($\boldsymbol{P}$) is a form of quantized angular momentum with a magnitude P [7]

$$P = \hbar[I(I+1)]^{1/2} \qquad (2.1)$$

where $\hbar$ is the reduced Planck constant and I is the spin quantum number. I relates to the atomic nuclei structure in such a way that if the nuclei have an even number of neutrons and protons they have no "spin", while if the nuclei have odd mass numbers such as ^{1}H or ^{13}C they have a half-integer spin quantum number, for example ^{1}H, or proton, has I = ½

and is known as a spin-½ nuclei. If nuclei have an odd atomic number and even mass number, for example ^{2}H or ^{14}N, they have a integer spin quantum number. The quantized angular momentum $\boldsymbol{P}$ relates to the quantized magnetic dipole moment $\boldsymbol{\mu}$ through [7]

$$\boldsymbol{\mu} = \gamma \boldsymbol{P} \quad (2.2)$$

where γ is the gyromagnetic ratio, (or ratio between the quantized angular and magnetic moments, and is nuclei specific). NMR is concerned with the detection of changes in these quantized magnetic dipole moments ($\boldsymbol{\mu}$) of the nuclei due to, for example, the manipulation of external magnetic fields and the motion of spin carrying particles across these fields. In this thesis work only ^{1}H or protons are excited and therefore this theory section is only concerned with the NMR properties of spin-½ nuclei.

The projection of $\boldsymbol{P}$ onto any axis; (x, y, z) for a Cartesian coordinate system, will yield magnetic quantum numbers m, with $(2I+1)$ values ranging from $-I$ to $+I$. So for a spin-½ nuclei (I = 1/2) there are only two possible states for the quantized angular momentum P_z: $P_z = \hbar/2$ and $P_z = -\hbar/2$. In the absence of a magnetic field, P will have no preferred direction. However, in the presence of an external static magnetic field $\boldsymbol{B_0}$ spin-½ nuclei will align either parallel or anti-parallel to this field. The interaction energy E between the quantized magnetic dipole moment $\boldsymbol{\mu}$ and the static magnetic field $\boldsymbol{B_0}$ is [7]

$$E = -\boldsymbol{\mu} \cdot \boldsymbol{B}_0 = -m\hbar\gamma B_0 \quad (2.3)$$

known as the Zeeman interaction. Nuclei move between these energy states in quantized jumps of $\Delta m = \pm 1$, (see figure 2.1. for the effect of a magnetic field $\boldsymbol{B}_0$ on ΔE for a spin-

½ system). The energy required for these jumps is provided by electromagnetic radiation

$$\Delta E = h\nu = \hbar\gamma B_0 \quad (2.4)$$

with a frequency (ν) given by

$$\nu = \frac{\gamma B_0}{2\pi} \quad (2.5)$$

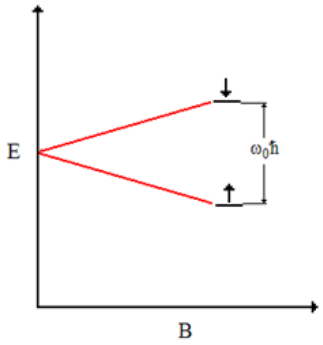

Figure 2.1 Energy diagram for the splitting of a spin-1/2 system into spin-up and spin-down energy states, where the energy separation is $\Delta \boldsymbol{E} = \hbar\boldsymbol{\gamma B_0} = \boldsymbol{\omega_0 B_0}$, with a slightly larger number of spins in the spin-up or parallel energy state due to its smaller energy requirement with this distribution being described by the Boltzmann distribution at thermal equilibrium.

For ^{1}H nuclei, with γ = 2.675x10^8 rad s^{-1} T^{-1}, in a magnetic field of 7 Tesla (T), the frequency required to induce these energy jumps is 300MHz. This frequency is known as the Larmor frequency ω_0 and is given by [1]

$$\omega_0 = \gamma B_0 \quad (2.6).$$

At thermal equilibrium, the distribution of spin-½ nuclei between the two energy states (spin-up and spin-down) is given by the Boltzmann distribution [1]

$$\frac{N_{-1/2}}{N_{+1/2}} = exp\left[\frac{-\hbar\gamma B_0}{k_B\varphi}\right] \quad (2.7)$$

where N_i are the populations of the discrete spin states, k_B is the Boltzmann constant and φ is the absolute temperature. For ^{1}H nuclei in a 7.0 T field at room temperature, the ratio between the nuclei populations in the upper and lower states is such that only 1 in 100,000 spins have magnetic moments that are not cancelled. These spins form the net magnetic moment and this small contribution of spins is why NMR is considered as a low signal-to-noise experimental technique. Due to the large number of spins in any volume investigated this small net magnetic moment can be viewed as a vector ($\boldsymbol{M}$) with magnitude M_0 aligned with the external magnetic field $\boldsymbol{B}_0$, and this classical mechanics description will be used for most of the NMR theory that follows.

Spin Excitation and the Rotating Reference Frame

By using the description of $\boldsymbol{M}$ as a vector to describe the ensemble motion of the nuclei, it is possible to formulate a description of the torque between $\boldsymbol{M}$ and $\boldsymbol{B}_0$

$$\frac{d\boldsymbol{M}}{dt} = \gamma \boldsymbol{M} \times \boldsymbol{B}_0 \quad (2.8)$$

which describes the precession of $\boldsymbol{M}$ around $\boldsymbol{B}_0$ at a rate of $\omega_0 = \gamma B_0$. If an oscillating magnetic field $\boldsymbol{B}_1$ is introduced in the transverse (X-Y) plane this will cause $\boldsymbol{M}$ to precess around $\boldsymbol{B}_0$ and $\boldsymbol{B}_1$ simultaneously at ω_0 and ω_1. The precession in the transverse plane by $\boldsymbol{M}$ induces a sinusoidal current in the radiofrequency (rf) coil, explained by the Maxwell-Faraday equation [16]

$$\nabla \times \boldsymbol{E}(\boldsymbol{r}, t) = -\frac{\partial \boldsymbol{B}(\boldsymbol{r}, t)}{\partial t} \quad (2.9)$$

where $\boldsymbol{E}$ is the electric field and $\boldsymbol{B}$ is the magnetic field, which can be written on a more physically relevant form to the present discussion as

$$\varepsilon = -\frac{d\Phi_B}{dt} \quad (2.10)$$

where Φ_B is the magnetic flux and ε is the electromotive force (emf) on the wire. The important point to notice is that a change in the magnetic field induces a change in the electric field and vice versa. When following the motion of the vector ***M*** called "nutation" through the induction process it is convenient to use a rotating reference frame (x_{rot},y_{rot},z_{rot}) instead of the stationary laboratory frame (x,y,z), see figure 2.2, where the rotating reference frame rotates at the Larmor frequency.

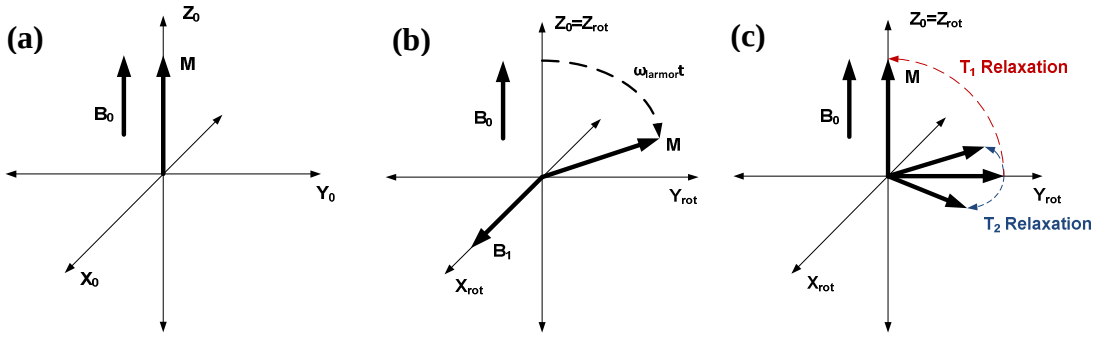

Figure 2.2 The evolution of the net magnetization vector ***M***. Initially the $\boldsymbol{B}_0$ field due to Zeeman interaction characterizes the magnitude of the net magnetization (a), then a $\boldsymbol{B}_1$ field is applied transverse to the $\boldsymbol{B}_0$ field causing ***M*** to flip into the transverse (X-Y) plane (b), after the application of $\boldsymbol{B}_1$ceases ***M*** relaxes by two mechanisms, T_1 relaxation by which M returns to thermal equilibrium and T_2 relaxation where spin-spin interactions cause a dephasing or spreading of ***M***. X_0, Y_0, Z_0 is the laboratory reference frame while X_{rot}, Y_{rot}, Z_{rot} is the rotating reference frame.

If the transverse rf field oscillates at ω_0 then the longitudinal (Z) component of ***M*** will disappear when ***M*** has experienced an angular displacement corresponding to 90^o + $180^o \cdot n$, where $n = 0,1,2$ .... A rf pulse which causes a 90^o angular displacement of ***M*** into the transverse plane is known as a 90^o or $\pi/2$ pulse. A pulse which causes a 180^o angular displacement of ***M*** is known as a 180^o or π pulse. If the applied rf pulse is off-resonance, $\omega_1 \neq \omega_0$, then a residual magnetization along the longitudinal axis causes ***M***

to precession about a net effective field $\boldsymbol{B}_{eff}$ at a frequency ω_{eff}. After a rf pulse has flipped a component of $\boldsymbol{M}$ into the transverse plane, the magnetization will experience two relaxation processes known as T_1 and T_2 relaxation, the former causing the relaxation back to thermal equilibrium while the latter causes the dephasing of $\boldsymbol{M}$, *i.e.* spreading of subpopulation precession frequencies over time. The effect on $\boldsymbol{M}$ due to these individual processes is demonstrated in figure 2.2c.

T_1 Relaxation

The process of T_1 or spin-lattice relaxation involves the transfer of energy from the spins to the surroundings (the "lattice") as the spins return to their longitudinal alignment (parallel to $\boldsymbol{B}_0$), or thermal equilibrium. The phenomenological description of this relaxation is [1]

$$\frac{dM_z}{dt} = -\left(\frac{M_z - M_0}{T_1}\right) \quad (2.11)$$

where $M_z = M_z(t)$ is the longitudinal (Z) component of $\boldsymbol{M}$, M_0 is the magnitude of $\boldsymbol{M}$ at thermal equilibrium and T_1 is a time constant known as the spin-lattice relaxation time. T_1 varies depending on the state of the matter being investigated; for example, diamonds have been measured having $T_1 \sim$ 36hrs [17], while typical values for pure liquids freely diffusing or confined in a porous medium range from 0.1 to 10 seconds. These times can be shortened by the addition of paramagnetic species such as Gd^{3+} which have unpaired electrons, which induce alternating magnetic field gradients affecting the hydrogen nuclei causing faster relaxation. This is very useful when NMR experimental times need to be shortened. To measure the T_1 of a sample, an inversion-recovery [1] pulse sequence can

be used, see figure 2.3, where a 180° rf pulse inverts ***M*** from aligning along the +Z to aligning along the –Z axis. The relaxation of ***M*** is characterized by

$$M(\tau) = M_0\left[1 - 2exp\left(\frac{-\tau}{T_1}\right)\right] \quad (2.12)$$

where τ is the time at which the longitudinal magnetization is flipped by a 90° rf pulse into the transverse plane where its magnitude can be measured. This is repeated for different τ times and the results are fit by Eqn. 2.12 to obtain T_1. If $\tau = \text{Ln}(2) \cdot T_1$, then no magnetization is flipped into the transverse plane. This is an important signal selection mechanism; if a sample has multiple populations with different T_1 this allows for selective excitation of different populations. To ensure the full recovery of ***M*** to thermal equilibrium it is advisable to use a relaxation time (T_R), the time between successive experiments, of at least $5 \cdot T_1$.

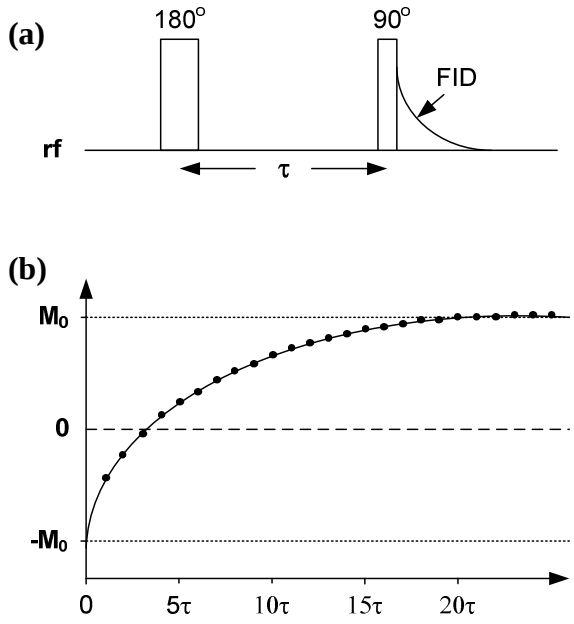

Figure 2.3 Inversion recovery pulse sequence (a), where $\boldsymbol{\tau}$ is varied and a $T_R > 5T_1$ is used between experimental runs. The resulting data fit with Eqn. (2.12), solid line, to obtain T_1 (b), the "nulling" point can be seen. As can be inferred from this figure and Eqn. (2.12) the sampling of $\boldsymbol{\tau}$ should be done on a log-scale.

An alternative to inversion-recovery is the use of a saturation recovery sequence, where a train of 90^o pulses saturates $\boldsymbol{M}$ such that there is no magnetization at time t = 0. Then the sample relaxes and the growth of magnetization is observed by a 90^o pulse after a delay τ. This sequence does not require full relaxation between successive excitations, decreasing the required overall experimental time.

T_2 Relaxation

The process of T_2 or spin-spin relaxation involves the irreversible thermal relaxation between nuclear "spins", which occurs in the transverse plane. There is no loss of energy from the system to the surroundings due to this type of relaxation unlike T_1 relaxation, but there is an increase in entropy which causes dephasing of the spins, causing the dephasing of $\boldsymbol{M}$ with time. Any inhomogeneity in the magnetic field causes different spins to experience different precession frequencies, which are perturbed from ω_0. These spins interact with their neighbors causing a loss of spin coherence with time. This dephasing can be reversed by the application of a 180^o rf pulse which causes a flip in the sense of precession of spins, and this reversible relaxation is described by the time constant T_2' allowing us to write

$$\frac{1}{T_2^*} = \frac{1}{T_2} + \frac{1}{T_2'} \quad (2.14)$$

where T_2^* is the relaxation due to spin-spin relaxation (T_2) which is irreversible and T_2' due to magnetic field inhomogeneity which is reversible. It is T_2^* which is directly measured in the Free Induction Decay (FID) in the time domain of a pulse and collect experiment and the Full Width at Half Maximum (FWHM) of the Fourier transformed data in the frequency domain. The FID of a single-resonant liquid (water), results in a

Lorentzian line shape in the frequency domain with the width ($\Delta\nu$) measured as the FWHM, where the following relationship exists

$$T_2^* = \frac{1}{\pi\Delta\nu} \quad (2.15).$$

If the sample is sufficiently shimmed, where magnetic field homogeneity is adjusted by gradient coils, and there are not phase boundaries causing magnetic susceptibilities, then $T_2^* \sim T_2$. Alternatively, T_2 can be directly measured using the Carr-Purcell-Meiboom-Gill [18, 19] (CPMG) pulse sequence, see figure 2.4, which is a spin-echo based technique with a train of 180^o rf pulses, where the 180^o rf pulse refocus the reversible dephasing due to magnetic field inhomogeneities.

The Spin, or Hahn, echo involves the addition of an 180^o rf pulse at time τ after a 90^o rf pulse. This 180^o pulse acts to change the sense of precession of the spins, with the famous analogy of Hahn [20] of racers on a race track being a nice way of explaining this phenomena, see figure 2.4a. An alternative method to produce an echo is to use an inverse pair of magnetic field gradients, which refocus the spins in the sample, known as a gradient echo, see figure 2.4b. The latter method will not refocus T_2' and is therefore useful when magnetic susceptibility effects are of interest. It has been shown that $T_2 \leq T_1$ [1], where the phenomenological description of T_2 relaxation is [1]

$$\frac{dM_{x,y}}{dt} = \frac{-M_{x,y}}{T_2} \quad (2.16)$$

which has the solution

$$M_{x,y}(t) = M_{x,y}(0)exp\left(-\frac{t}{T_2}\right) \quad (2.17)$$

where $M_{x,y}(t)$ is the magnitude of *M* in the transverse (X-Y) plane.

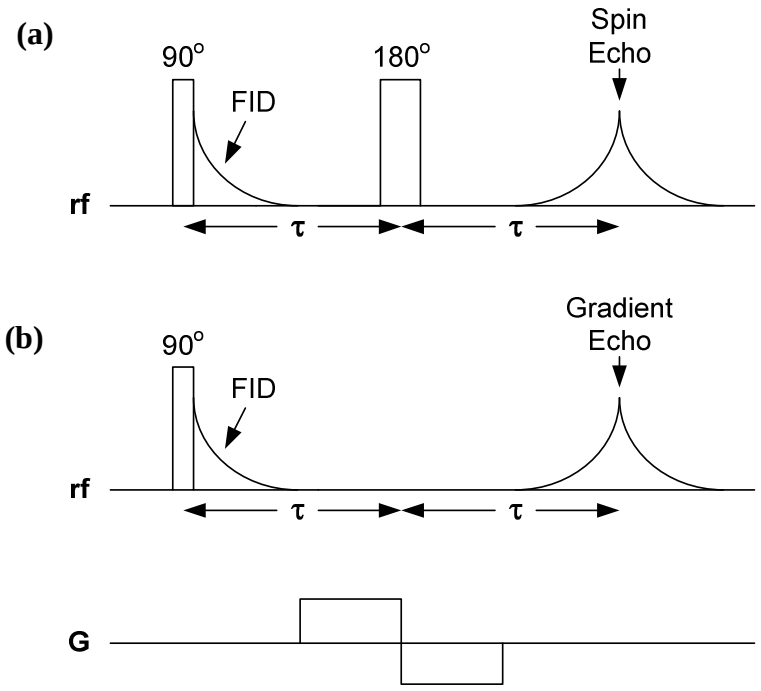

Figure 2.4 Spin echo or Hahn echo pulse sequence (a) and gradient echo pulse sequence (b). Both sequences involve the excitation of $\boldsymbol{M}$ by a 90° rf pulse and the recovery of an echo after $2\boldsymbol{\tau}$, they differ in the method by which the magnetization of the spins is refocused. For the spin echo a 180° rf pulse is used, while for the gradient echo a gradient pair is used. By using a gradient pair the latter is more susceptible to magnetic inhomogeneities in the sample**.**

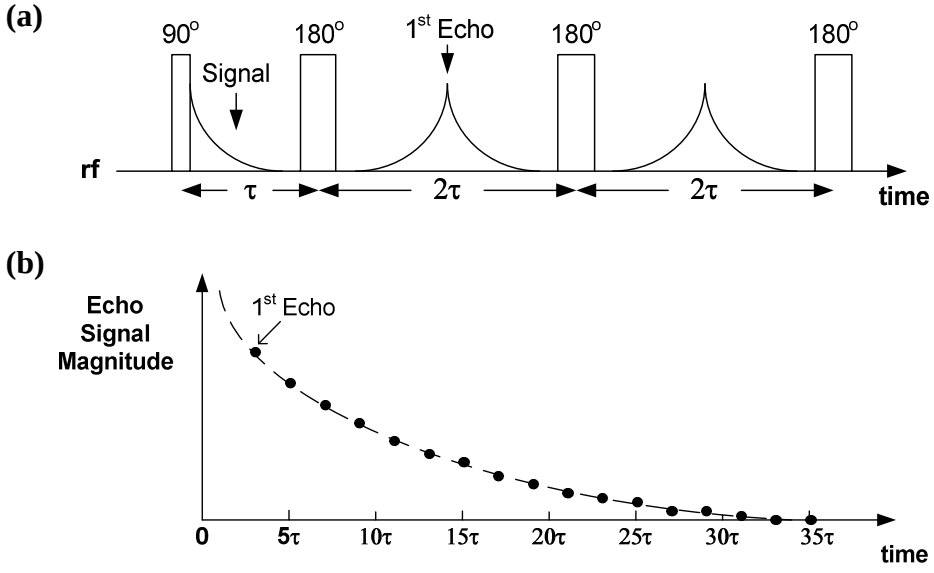

Figure 2.5 Carr-Purcell-Meiboom-Gill (CPMG) pulse sequence (a). The amplitude of each successive echo is $\boldsymbol{T_2}$ modulated with the train of 180° rf pulses being repeated until the signal attenuation due to relaxation becomes too severe, (b) shows an example of the attenuation of the echo signal magnitude, with the dashed line as a guideline.

Bloch Equations

With Eqn. 2.11 and 2.16 describing the longitudinal and transverse relaxation of ***M*** it is possible to combine these with Eqn. 2.8 to obtain the now famous Bloch equations [21]

$$\frac{dM_x}{dt} = \gamma M_y(B_0 - \omega/\gamma) - \frac{M_x}{T_2} \quad (2.17a)$$

$$\frac{dM_y}{dt} = \gamma M_z B_1 \gamma M_x(B_0 - \omega/\gamma) - \frac{M_y}{T_2} \quad (2.17b)$$

$$\frac{dM_z}{dt} = \gamma M_y B_1 - \frac{(M_z - M_0)}{T_1} \quad (2.17c)$$

which describe the evolution of ***M*** with time and serve as an important reference when describing NMR phenomena. With this description and the understanding of what each term represents it is possible to discuss spin manipulation techniques and other details.

Signal Detection

To understand the data being acquired in an NMR experiment it is important to have a grounding in what the signal detection process encompasses. Following the application of a 90^o rf pulse in a pulse-acquire experiment, where the signal is acquired after the rf pulse ceases, the spins in the sample will relax by the mechanisms discussed in the previous sections, with the precession of the spins after the 90^o rf pulse being known as a Free Induction Decay (FID). This precession induces a voltage in the rf coil due to Faraday's law, *i.e.* a moving magnetic field induces motion in an electric charge. The amplitude of this voltage is on the order of μV. The frequency response A(ν) is related to the FID signal intensity S(t) in the time domain by

$$A(\nu) = \int_{-\infty}^{+\infty} S(t) \exp(i2\pi\nu t)\, dt \quad (2.18).$$

In practice the NMR signal is digitally sampled, where the time between successive samples is known as the dwell time (t_d) and is related to the sweep width (f_{sw}) in the frequency domain by the inverse relation $f_{sw} = 1/t_d$. Inverse relationships are ever present when discussing the time and frequency domains and an understanding of the relationships is fundamental to NMR, with Fast Fourier Transforms (FFT) [22] being the mathematical tool for transforming between the domains. The importance of t_d and f_{sw} is that if they are respectively too long and too narrow, it can lead to signal truncation and emergence of artifacts. Alternatively, using too short or too wide a t_d and f_{sw} leads to unnecessary noise being sampled. These phenomena are described by the Nyquist sampling theorem [23], *i.e.* a function f(t) which has no frequencies higher than T hertz is completely determined by sampling its ordinates at a series of points spaced 1/(2*T*) seconds apart. In addition to sampling the FID digitally, the rf receiver mixes the output with outputs from reference rf oscillators which are 90^o out-of-phase from each other and operate at the Larmor frequency, in a process called heterodyne mixing. This process is what makes it possible to separate the in-phase (M_x) and quadrature (M_y) phase signals. These separated phase signals are used in the process of "phase cycling" which allows for the elimination of both incoherent magnetization and artifacts arising due to hardware imperfections [24]. Typically, phase cycling involves running the same pulse sequence repeatedly but varying the phase (x, -x, y, -y) of applied rf pulses and receiver such that when these experiments are added together undesired spin states are eliminated and only the desired spin states form the acquired signal. Generally this phase cycling procedure is done via the data acquisition software [1].

Spin Excitation and RF Pulses

In the above discussion of excitation the rf pulses were chosen to be 90^o and 180^o based on the energy required to cause ***M*** to flip by these angular displacements. These energy requirements are independent of the shape of the rf pulse in the time domain, which means that different shaped pulses will still cause ***M*** to flip into the transverse plane. There are two categories of pulses known as "hard" and "soft" pulses. A "hard" pulse is applied for a short duration such as to excite a bandwidth that covers all possible frequencies of spins in a sample and are therefore characterized as intense, non-selective, and broadband. The opposite of "hard" pulses are "soft" pulses which are less intense and therefore are long duration, selective and narrow band. These are used to selectively excite specific frequencies in a sample and are therefore used for slice selection, where a linear gradient applied across a sample causes a spatially linear variation in spin precession frequencies and only a small bandwidth is excited. To understand the shapes of pulse that are amenable to each task it is important to understand the Fourier relationships between different functions. A Heaviside hat function in the time domain will produce a sinc function in the frequency domain. Additionally a short duration large magnitude 90^orf pulse in the time domain will excite a large bandwidth, while a long duration small magnitude 90^orf pulse will excite a narrow bandwidth. By combining these facts it is evident that a "hard" pulse would ideally have the shape of a hat-function, with large magnitude and short duration such as to produce a sinc shaped response in the frequency domain, where the frequency of the sample is all very close to the origin and not affected by the shape. Likewise the "soft" pulse can be chosen to be a sinc function,

with small magnitude and long duration such as to excite the desired hat function in the frequency domain, where narrowing of the bandwidth is accomplished by lengthening the duration of the pulse. A possible problem in practice is that it is only possible to have a finite lobe sinc shaped rf pulse and an approximate hat function. The former is more of a problem than the latter since slice selection leaves the possibilities of spins with frequencies close to those of the desired spins present inside the rf coil. A finite sinc shaped rf pulse will excite some spins outside the desired slice, but generally only to a small extent. An alternative pulse shape is that of a Gaussian in the time domain which Fourier transforms to a Gaussian in the frequency domain. All these pulse shapes and their Fourier transforms are presented in figure 2.6.

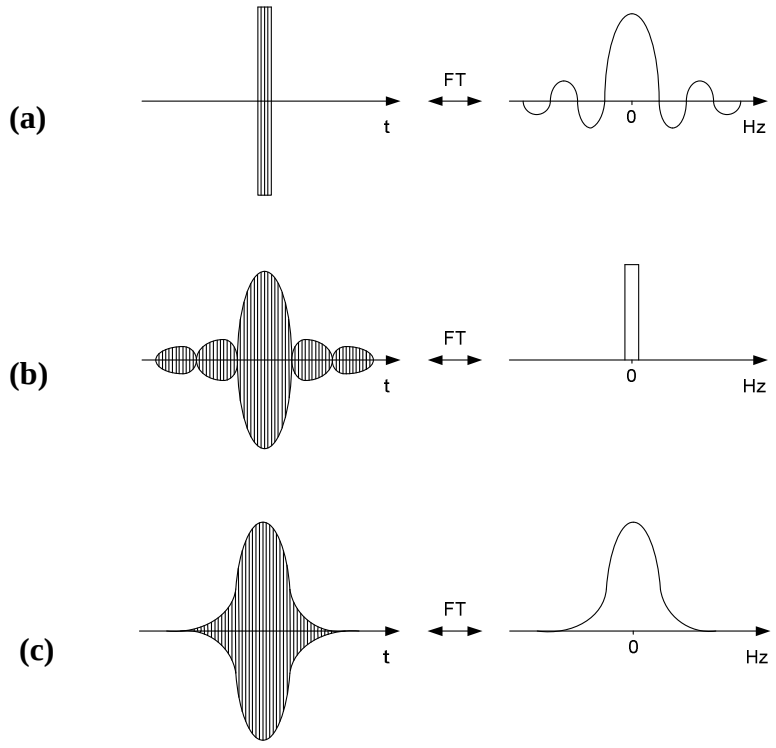

Figure 2.6 The Fourier relationships for the applications of a hat function (a), sinc function (b) and Gaussian function (c) in the time domain to the resulting excited frequency in the frequency domain.

Chemical Shift and J-Coupling

Given the above discussions of magnetic field inhomogeneities and slice selection which are due to the spins experiencing different local magnetic fields, it is important to discuss the chemical shift due to the magnetic shielding caused by electrons orbiting the nucleus of an atom. This causes the Larmor frequency of the spins to be displaced in a characteristic manner associated with the local chemical environment. The electronic environment around a nuclei can be very different depending on the bonding and nature of neighboring nuclei causing specific frequency shifts for nuclei on the same molecule but with different neighbors. This shielding reduces the local magnetic field by a factor σ causing the nucleus to experience an effective (B_{eff}) field

$$B_{eff} = B_0(1 - \sigma) \quad (2.19).$$

Because the chemical shift will vary depending on B_0 it is more convenient to express the chemical shift in terms of δ_{ppm} or the resonance frequency of the nuclei (ν) relative to a reference nuclei (ν_{ref}). The reference molecule is usually tetramethylsilane (TMS), and the chemical shift is calculated by using

$$\delta_{ppm} = \frac{10^6(\upsilon - \upsilon_{ref})}{\upsilon_{ref}} \quad (2.20)$$

This allows for the comparison of data between magnets with different field strengths. For the work in this thesis this chemical shift effect is used to track both a particulate phase (colloids filled with hexadecane) and a suspending fluid phase (water) of a colloidal suspension, see figure 2.7. The finest structural details available using NMR are due to spin-spin or J-coupling, which is an indirect interaction between nuclei via the

mediation of their electron environments. This causes a further splitting of high resolution spectra and is what causes a methyl-signal peak to split into a triplet due to each of the hydrogens in the methyl group. By measuring the chemical shift and J-coupling using high resolution NMR it is possible to produce a chemical fingerprint, or detailed map of the chemical structure. In the colloidal research presented in this thesis the chemical shift between water and hexadecane allows for the simultaneous detection of both phases. Hexadecane splits into two peaks due to the methyl groups at the ends of the linear molecule, which could be used to investigate molecular orientation.

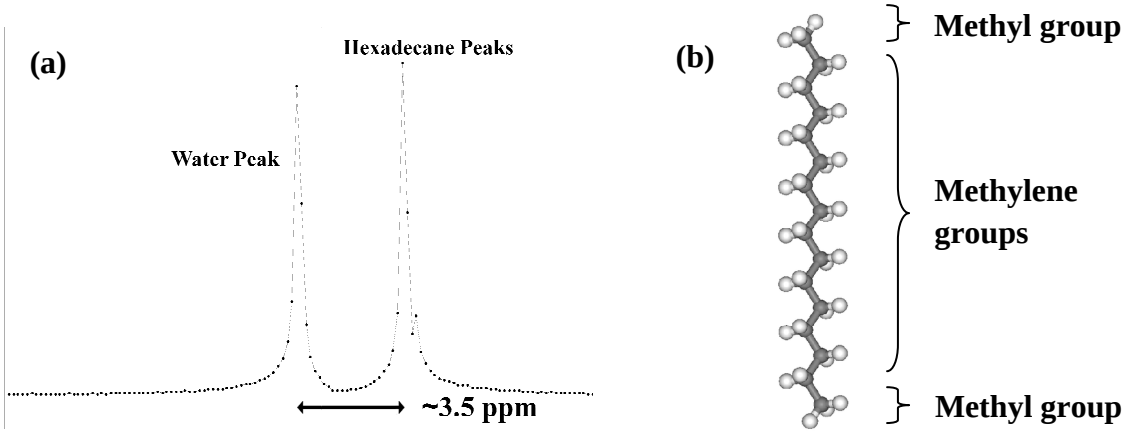

Figure 2.7 The frequency spectrum from a doped sample of 22%wt colloidal dispersion (a) where a water peak and hexadecane peaks are visible due the chemical shift effect, the hexadecane splits into two peaks, due to the methylene group and the methyl group. For clarity the hexadecane molecule is shown in (b).

The Stimulated Echo

A problem inherent with using spin or gradient echoes for NMR experiments where long time dynamics are of interest is that they are dependent on phase coherence and therefore the T_2 time. As was noted above, $T_2 \leq T_1$ which means that if magnetization ($\boldsymbol{M}$) can be flipped into the longitudinal direction, where only T_1 relaxation

affects it, it is possible to "store" magnetization for a longer time. This process of "storing" is done by applying a 90° rf pulse to $\boldsymbol{M}$ when it is in the transverse plane rotating it into the longitudinal direction for "storage", then after time T_s the magnetization can be rotated back into the transverse plane. Any magnetization which isn't rotated into the longitudinal direction can be dephased or "crushed" using a homospoil or "crusher" gradient applied between the two 90° rf pulses, see figure 2.8. For samples where $T_1 \gg T_2$ this technique allows for much longer experimental delays and therefore allows the observation of longer-time displacements. The echo which is observed using this technique is known as a "stimulated echo".

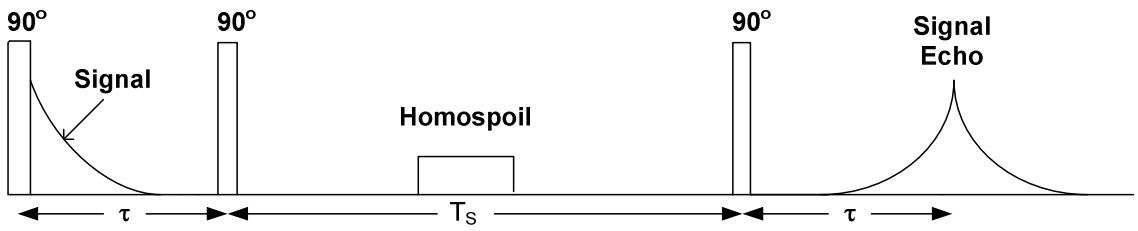

Figure 2.8 Stimulated echo pulse sequence. $\boldsymbol{M}$ is excited into the transverse plane by a 90° rf pulse, then a 90° rf pulse flips $\boldsymbol{M}$ into the longitudinal direction, where only T_1 relaxation affects it, a homospoil gradient is applied to dephase any component of M left in the transverse plane, then at $T_s + \tau$ the magnetization in the longitudinal direction is excited into the transverse plane and the Stimulated Echo peak occurs at $T_s + 2\tau$. This method is based on $T_1 > T_2$ allowing for longer times to be probed.

Nuclear Magnetic Resonance Imaging (NMRI or MRI)

Magnetic Resonance Imaging (MRI) is based on the fact that the Larmor frequency at which isochromats, *i.e.* spins which experience the same magnetic field, precess is dependent on the magnetic field strength ($\boldsymbol{B}_0$) at that location. By applying a linear gradient $\boldsymbol{G} = \frac{d\boldsymbol{B}}{d\boldsymbol{r}}$ across a sample the resonance frequency experienced by the isochromats is written

$$\omega(\mathbf{r}) = \gamma(\boldsymbol{B}_0 + \boldsymbol{G} \cdot \boldsymbol{r}) \quad (2.21).$$

For a volume element (dV) at position $\boldsymbol{r}$ with a spin density $\rho(\boldsymbol{r})$, the observed signal *dS* is given by

$$dS(\boldsymbol{G}, t) = \rho(\boldsymbol{r}) dV exp[i\gamma(\boldsymbol{B}_0 + \boldsymbol{G} \cdot \boldsymbol{r})] \quad (2.22).$$

This NMR signal is "heterodyned" with a reference frequency of $\gamma \boldsymbol{B}_0$, leading to a signal that oscillates at $\gamma \boldsymbol{G} \cdot \boldsymbol{r}$. If this signal is integrated over the sample volume we obtain [1]:

$$S(t) = \iiint \rho(\boldsymbol{r}) exp[i\gamma \boldsymbol{G} \cdot \boldsymbol{r} t] d\boldsymbol{r} \quad (2.23).$$

Using the reciprocal space vector, $\boldsymbol{k}$

$$\boldsymbol{k} = \frac{\gamma \boldsymbol{G} \mathrm{t}}{2\pi} \quad (2.24)$$

it is possible to rewrite Eqn. 2.23

$$S(\boldsymbol{k}) = \iiint \rho(\boldsymbol{r}) exp[i2\pi \boldsymbol{k} \cdot \boldsymbol{r}] d\boldsymbol{r} \quad (2.25)$$

which has the Fourier conjugate

$$\rho(\boldsymbol{r}) = \iiint S(\boldsymbol{k}) exp[-i2\pi \boldsymbol{k} \cdot \boldsymbol{r}] d\boldsymbol{k} \quad (2.26).$$

This Fourier relationship is at the heart of MRI, where the information of interest is $\rho(\boldsymbol{r})$ or the spatial spin density. This information is obtained in practice by traversing $\boldsymbol{k}$-space and obtaining signal such that all of the necessary $S(\boldsymbol{k})$ is sampled and then Fourier transformed to obtain the $\rho(\boldsymbol{r})$. To illustrate this process a sampling process known as spin-warp imaging [25] is demonstrated in figure 2.9. This process samples $\boldsymbol{k}$ -space by acquiring a single line of $\boldsymbol{k}$ -space by acquiring the signal during the application of a constant "read" gradient $\boldsymbol{G}_{read}$. This single line imaging is called frequency encoding, and allows for rapid 1D imaging.

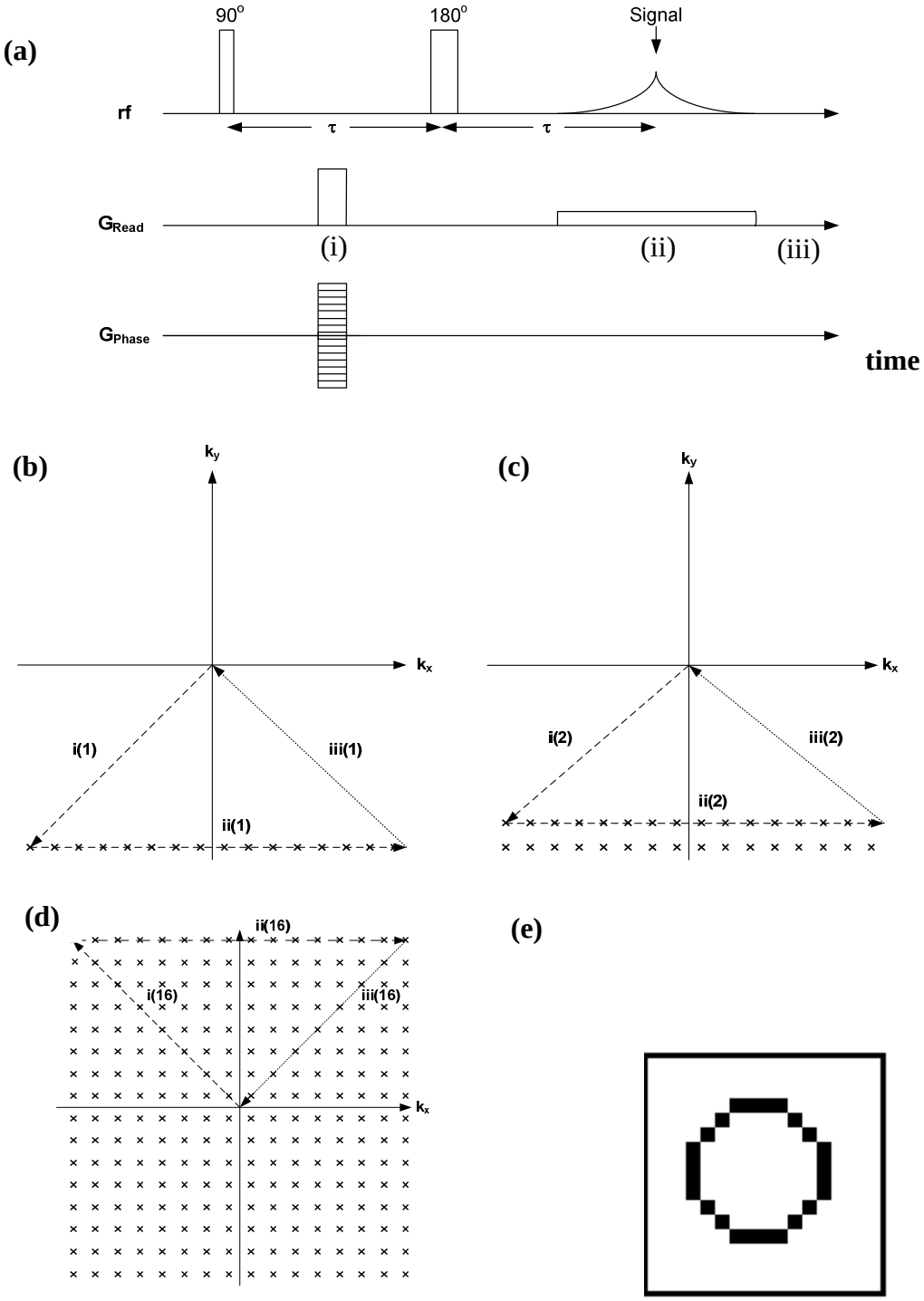

Figure 2.9 The timing diagram for a 2D imaging experiment (a) where the evolution in k-space is indicated by images (b), (c) and (d). Image (e) shows a hypothetical 16x16 pixel image resulting from a FT of the data obtained in (d).

To acquire data in a second or third direction in $\boldsymbol{k}$ -space an additional orthogonal "phase encoding" gradient $\boldsymbol{G}_{phase}$ is applied after each frequency encoding step shifting the starting point of the "frequency encoding".

By defining the Cartesian raster in this manner, we can write

$$S(k_x, k_y) = \iint \rho(x,y) exp\left[i2\pi\left(k_x x + k_y y\right)\right] dxdy \quad (2.27)$$

where the orthogonal directions *x* and *y* are analogous to the read and phase directions. Fourier transforming this signal obtains $\rho(x,y)$.Using the Cartesian raster the Field Of View (FOV) relates to the inverse of the increment traversed in $\boldsymbol{k}$-space ($\Delta\boldsymbol{k}$)

$$FOV = \frac{1}{\Delta \boldsymbol{k}} = \frac{2\pi}{\gamma G t} \quad (2.28).$$

Selective Excitation

When it is desired to acquire spectral information from a section of a sample inside a rf coil it is necessary to combine the use of magnetic field gradients and a "soft" pulse such that only the desired "slice", Δz, of frequencies inside the rf coil is excited, written as

$$\Delta z = \frac{2\pi \Delta f_s}{\gamma \boldsymbol{G}_{slice}} \quad (2.29)$$

where G_{slice} is the applied slice gradient strength and Δf_s is the excited bandwidth. The shape of the rf pulse determines the shape of the frequencies excited in the frequency domain, see figure 2.10. Therefore a sinc function excites a hat function in the frequency domain, *i.e*. a slice in the Z-direction. There are multiple possible combinations of gradients and rf pulses that can excite a "slice" in the frequency domain, but the method used in this thesis research is shown in figure 2.10. This sequence can be combined with other rf pulse sequences presented to produce a slice selective rf pulse sequence.

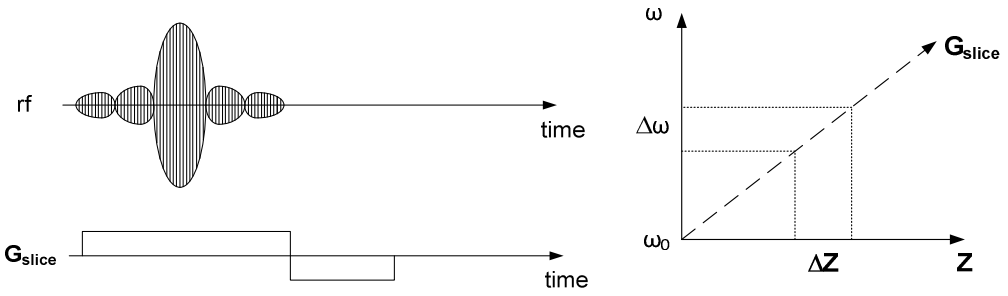

Figure 2.10 Slice selection pulse sequence timing diagram (left) while (right) shows the excited bandwidth (**Δ*ω***) and corresponding slice thickness (**ΔZ**) relative to the slice gradient (G_{slice}).

While a specific set of methods to sample ***k***-space, slice select and excite the signal has been presented, there is an open template to create alternative methods to produce the same physical results but by, for example, sampling ***k***-space with a radial raster or by spiral sampling, excite a slice with different timing sequences or pulse shapes [1]. For example much of the basis for rapid sampling techniques, *i.e.* experiments where the time of total acquisition is on the order of milliseconds, is the elimination of T_R or relaxation time between pulse sequence steps. This is done either only exciting a fraction of the magnetization (***M***) by a rf pulse << 90^o or by refocusing the magnetization between each line sampling. Examples of these kinds of rapid imaging sequences are Fast Low-Angle SHot imaging (FLASH) [26] and the gradient echo based Echo Planar Imaging (EPI) such as Blipped Echo planar Single-pulse Technique (BEST) [27] and Modulus BEST (MBEST) [28], and the spin echo based rapid acquisition with Relaxation Enhancement (RARE) [29]. These techniques are high signal-to-noise methods, requiring large voxel sizes, and do not generally fall into being magnetic resonance microscopy techniques, *i.e.* with voxel sizes 100x100x100 μm^3 or smaller [1]. However

they allow for imaging of a sample in a time as fast as tens of milliseconds and are therefore important techniques to understand.

Dynamic NMR Transport Measurements

NMR can be used to obtain information about the molecular motion of particular chemical species within a sample non-destructively. The most common and useful method is Pulsed Field Gradient (PFG) NMR. If the translational motion of a nucleus has a time dependent displacement of $\boldsymbol{r}(t)$ then the self-motion of a nuclear spin is described by the conditional probability $P(\boldsymbol{r}|\boldsymbol{r'},t)$ that a nuclear spin originally at $\boldsymbol{r}$ will move to $\boldsymbol{r}'$ over time t. A basic PFG experiment is the Pulsed Gradient Spin Echo (PGSE) sequence shown in figure 2.11. In this sequence a magnetic field gradient pulse $\boldsymbol{g}$ of duration δ, initially imparts a spatially dependent phase shift $\phi(\boldsymbol{r})$ on the spins

$$\phi(\boldsymbol{r}) = \gamma\delta\boldsymbol{g}\cdot\boldsymbol{r} \quad (2.30).$$

After a delay, also known in this thesis as the experimental time Δ, the spins will have migrated to $\boldsymbol{r}'$, and a second equal but oppositely-orientated gradient pulse is applied to the system. The net phase shift imposed on the spins by the pair of gradient pulses is

$$\phi(\boldsymbol{r}) = \gamma\delta\boldsymbol{g}\cdot(\boldsymbol{r'}-\boldsymbol{r}) \quad (2.31).$$

For the case of stationary spins, a perfectly refocused echo occurs. In the case of motion, there is a net phase shift in the echo, which is a product of the dynamic displacement $(\boldsymbol{r'}-\boldsymbol{r})$ and the wave vector $\gamma\delta\boldsymbol{g}$. The normalized echo signal that is acquired following this second gradient pulse has the form

$$S(\boldsymbol{g},\delta,\Delta) = \int\rho(\boldsymbol{r})\int P_i(\boldsymbol{r}|\boldsymbol{r'},\Delta)\,exp[i\gamma\delta\boldsymbol{g}\cdot(\boldsymbol{r'}-\boldsymbol{r})]d\boldsymbol{r'}d\boldsymbol{r} \quad (2.32).$$

Where $\rho(\boldsymbol{r})$ is the initial spin density of the sample. As negligible motion is assumed to occur during gradient phasing the so-called "narrow pulse approximation" ($\delta \ll \Delta$) is normally used. The total signal is a superposition of transverse magnetization, in which each phase term $exp[i\gamma\delta\boldsymbol{g}\cdot(\boldsymbol{r'}-\boldsymbol{r})]$ is weighted by the probability of a spin, originally located at $\boldsymbol{r}$, moving to $\boldsymbol{r'}$ in the time Δ, *i.e.* $\rho(\boldsymbol{r})P_i(\boldsymbol{r}|\boldsymbol{r'},\Delta)$. Introducing a dynamic displacement $\boldsymbol{R} = \boldsymbol{r'}-\boldsymbol{r}$ and taking the ensemble average over all spins, $\int \rho(\boldsymbol{r})\,P_i(\boldsymbol{r}|\boldsymbol{r'},\Delta)d\boldsymbol{r}$ yields the "average propagator", $P(\boldsymbol{R},\Delta)$.

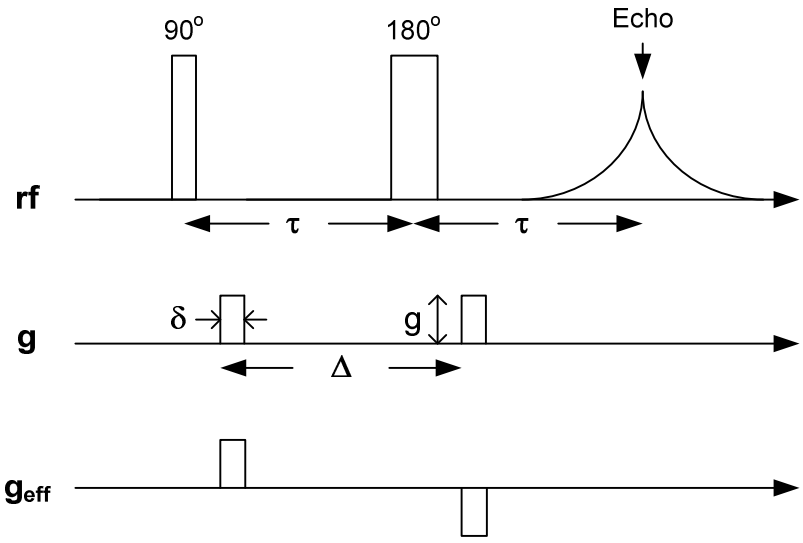

Figure 2.11 Basic Pulsed Gradient Spin Echo (PGSE) sequence to measure spin displacment. **Δ** is the measurement time, $\boldsymbol{\delta}$ and $\boldsymbol{g}$ are the duration and magnitude of the pulsed field gradients.

It is useful to introduce the concept of $\boldsymbol{q}$-space, the dynamic analogue of the static reciprocal space, $\boldsymbol{k}$-space, where

$$\boldsymbol{q} = \frac{\gamma\delta\boldsymbol{g}}{2\pi} \quad (2.33).$$

Now we can write

$$S(\boldsymbol{q},\Delta) = \int P(\boldsymbol{R},\Delta)\,exp[i\gamma\delta\boldsymbol{q}\cdot\boldsymbol{R}]d\boldsymbol{R} \quad (2.34).$$

This equation shows that $P(\boldsymbol{R},\Delta)$ is obtained from a Fourier transform of $S(\boldsymbol{q},\Delta)$ with respect to $\boldsymbol{q}$.

For random diffusive displacements and considering motion in only one direction, the average displacement propagator takes the form of a Gaussian distribution of displacements

$$P(\boldsymbol{R},\Delta) = \frac{1}{2\sqrt{\pi D\Delta}} exp\left[-\frac{\boldsymbol{R}^2}{4D\Delta}\right] \quad (2.35).$$

The Fourier transform of this gives us the expected signal amplitude; an exponential decay, characterized by a purely diffusive coefficient D

$$E(\boldsymbol{q}) = \frac{S(\boldsymbol{q})}{S_0} = exp(-D(2\pi\boldsymbol{q})^2\Delta) \quad (2.36)$$

here S is the signal amplitude obtained at a given $\boldsymbol{q}$ and S_0 is the signal obtained at $\boldsymbol{q} = 0$. The well-known Stejskal-Tanner equation [30] includes a correction of the diffusion time of $-\delta/3$ to account for the finite duration of the gradient pulse. Therefore a plot of $Ln(E(\boldsymbol{q}))$ versus $(2\pi q)^2(\Delta - \delta/3)$ should result in a linear relationship whose slope is the diffusion coefficient of the sample.

It is also possible to measure velocity using this method. Motion of the spins between the dephasing and rephasing gradient pulses result in a phase shift. In the case of diffusion, this motion is random and results in the attenuation of the net magnetization, while in the presence of bulk, coherent flow, ignoring diffusive effects, the average propagator is

$$P(\boldsymbol{R},\Delta) = \delta(\boldsymbol{v}\Delta) \quad (2.37)$$

here $\boldsymbol{v}$ is the velocity of the system. This results in the signal attenuation because of coherent flow as

$$E(\boldsymbol{q}) = exp[i2\pi\boldsymbol{q}\cdot\boldsymbol{v}\Delta] \quad (2.38).$$

Therefore, if there are evenly spaced $\boldsymbol{q}$-increments ($\boldsymbol{q}_{\text{inc}}$) the phase shift between successive experiments is

$$\phi_{inc} = \boldsymbol{q}_{inc}\cdot\boldsymbol{v}\Delta \quad (2.39).$$

Combining the attenuation due to diffusion and phase shift for bulk flow yields the following relationship for signal attenuation

$$E(\boldsymbol{q}) = exp[i2\pi\boldsymbol{q}\cdot\boldsymbol{v}\Delta - D(2\pi\boldsymbol{q})^2\Delta] \quad (2.40).$$

Figure 2.12 shows how attenuation due to random diffusion and a bulk velocity affect the signal. Diffusion causes the broadening of the probability function, while the bulk velocity shifts the probability function towards higher and higher displacements.

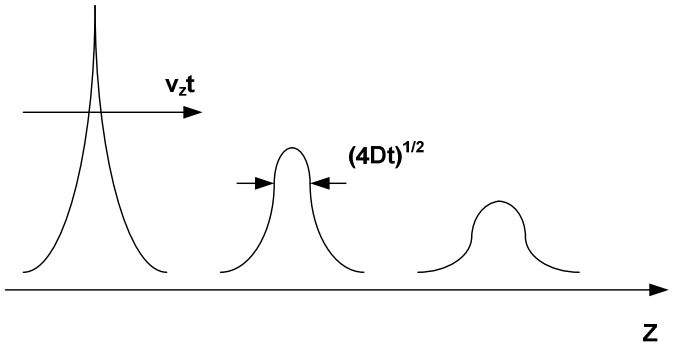

Figure 2.12 Change in the probability function $\boldsymbol{P}(\boldsymbol{R},\boldsymbol{\Delta})$ as an ensemble of spins experiences Brownian motion and convective flow, with increasing time from left to right.

The phase shift (ϕ) experienced at a time t by a nuclear spin i following the path $\boldsymbol{r}_i(\mathrm{t}')$ in a gradient $\boldsymbol{g}(\mathrm{t}')$ is written [1]

$$\phi_i(t) = \gamma\int_0^t \boldsymbol{g}(\mathrm{t}')\cdot\boldsymbol{r}_i(\mathrm{t}')dt' \qquad (2.41)$$

by defining an effective gradient $\boldsymbol{g}^*(t)$ which is inverted by each successive 180° rf pulse: a very useful method to account for the effect of different derivatives of displacement, *i.e.* position ($\boldsymbol{x}$), velocity ($\boldsymbol{v}$), acceleration (**a**), *etc.*, in terms of the final phase modulation of the spin echo [1]

$$E(t) = \exp\left(i\gamma \boldsymbol{x} \int_0^t \boldsymbol{g}^*(t')d't + i\gamma \boldsymbol{v} \cdot \int_0^t t' \boldsymbol{g}^*(t')dt' + \frac{1}{2} i\gamma \mathbf{a} \cdot \int_0^t t'^2 \boldsymbol{g}^*(t')dt' + \cdots\right)$$

(2.42).

This allows for a powerful tool in designing appropriate gradient sequences to measure the different derivatives of displacement, for example if we look at the PGSE sequence (figure 2.11) we see that $\int_0^t \boldsymbol{g}^*(t')dt' = 0$, while for a sequence where we would be interested in the acceleration and higher derivatives of displacement, we need $\int_0^t \boldsymbol{g}^*(t')d't = 0$ and $\int_0^t t' \boldsymbol{g}^*(t')dt' = 0$. A sequence like this known as the velocity compensated PGSE sequence is presented in figure 2.13 and serves to measure incoherent or random motion.

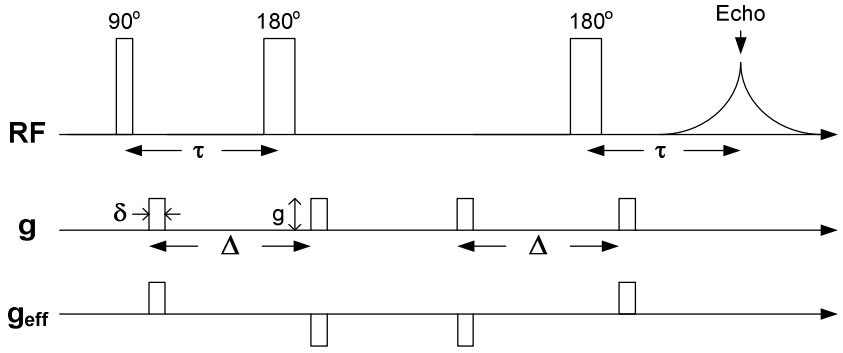

Figure 2.13 Velocity compensated PGSE sequence causing the refocusing of coherent motion while measuring the effects of incoherent motion during experimental time **Δ**.

The ***q***-space pulse sequences presented above to measure spin displacement can be combined with NMR imaging methods to obtain an image where each pixel has ***q***-space information, allowing for the imaging of coherent and incoherent motion. Bear [31] discussed methods of monitoring hydrodynamic dispersion within porous media and states that an "ideal tracer" is one that is inert with respect to its liquid and solid surroundings, and which does not affect the liquid's properties, nor should it interfere with the viscosity or density of the liquid. These criteria are well satisfied by NMR propagator analysis, which explains the enormous amount of interest in porous media investigation using these techniques. The fundamentals of NMR presented above serve as an overview for the NMR pulse sequences used to measure different transport phenomena; whenever an interesting NMR phenomena presents itself in this particular thesis additional elements of NMR theory will be presented where those phenomena occur. To illustrate this the next section will address the important phenomena of diffraction due to spherical boundaries, since for the colloidal particles used in this research the hexadecane oil is trapped inside a spherical particle.

Diffraction Phenomena due to Spherical Boundaries

Given the Lagrangian nature of transport measurements used in NMR, whenever a restriction hinders spin displacement, such as coherent motion (bulk motion) or incoherent motion (Brownian motion), a diffraction pattern can emerge in the ***q***-space data; whether this happens depends on the homogeneity of the sample, *i.e.* enough spins experience the same behavior so that when averaged it is apparent. The length scale and

time scale that these occur give valuable information about the structure of the sample being probed and have been demonstrated in characterizing different structures [32-35]. These structures can be due to rigid porous media (as in model bead packs) boundaries, non-rigid porous media (as in some gels) boundaries or due to the interaction of suspending fluid particles or colloidal particles interactions, *i.e.* evolving boundaries. How geometrical restriction influences Brownian dynamics and the consequent signal attenuation has been reviewed [36].

The application of a pressure gradient across a sample and therefore bulk motion in liquid samples causes non-isotropic stresses to emerge in the system causing preferred displacement in the flow direction. These higher displacements can cause structural features previously invisible due to the relative slowness of thermal motion to emerge. However, these higher displacements can also cause in-flow, out-flow artifacts. In the current research to eliminate these artifacts only thin slices (1mm or 10mm) in the middle of the rf coil were excited, with additional care taken that the mean fluid displacements on the timescales of the measurements were very small compared to the overall length of the coil (20mm). Because the colloidal particles used in this research are spherical particles with a mean radius $a = 1.25 \pm 0.46 \mu m$ filled with hexadecane oil ($D = 4.6 \times 10^{-10} m^2/s$), it is important to verify what effect the diffusion of the oil inside the spheres has on the NMR echo attenuation of the oil signal. The effect of spherical boundaries in PGSE experiments has been obtained by Murday and Cotts [37] and can be written [1]

$$E(q) = exp(-2\gamma^2 g^2 \sum_{m=1}^{\infty} f(\alpha_m)) \quad (2.43)$$

with

$$f(\alpha_m) = \frac{1}{\alpha_m^2(\alpha_m^2 a^2 - 2)}\left[\frac{2\delta}{\alpha_m^2 D} - \frac{2+\exp[-\alpha_m^2 D(\tau-\delta)]-2\exp[-\alpha_m^2 D\delta]-2\exp[\alpha_m^2 D\tau]+\exp[-\alpha_m^2 D(\tau+\delta)]}{[\alpha_m^2 D]^2}\right]$$

(2.44)

where α_m are roots of the Bessel function equation

$$\alpha_m a J_{\frac{3}{2}}'(\alpha_m a) - \frac{1}{2} J_{\frac{3}{2}}(\alpha_m a) = 0 \quad (2.45).$$

For the short time-scale limit ($\Delta \ll a^2/2D$)

$$E(q) = exp(-4\pi^2 q^2 D\Delta) \quad (2.46)$$

while the long time-scale limit ($\Delta \gg a^2/2D$)

$$E(q) = exp\left(-4\pi^2 q^2 \left(\frac{1}{5}a^2\right)\right) \quad (2.47).$$

For the colloidal particles in this research, $a^2/2D$ = 1.7ms, while the shortest experimental time $\Delta = 25$ms, allowing for the reasonable approximation that all experiments are conducted in the long time-scale limit. When the long time-scale behavior is compared with the echo due to the free diffusion using PGSE [1]

$$E(q) = exp(-q^2 D\Delta) \quad (2.48).$$

It is possible to express the weak gradient apparent diffusion coefficient as $a^2/5\Delta$ [1]; figure 2.14 shows this curve.

It has been shown [1] that the PGSE signal in the very long time limit is

$$E_\infty(\boldsymbol{q}) = |S(\boldsymbol{q})|^2 \quad (2.49)$$

or precisely the power spectrum of the reciprocal lattice [10]. The above analysis has used a single sphere radius (a), but what if there is a Gaussian distribution of sphere radii with mean radius a_0 = 1.25μm and standard deviation (*SD*) = 0.46μm.

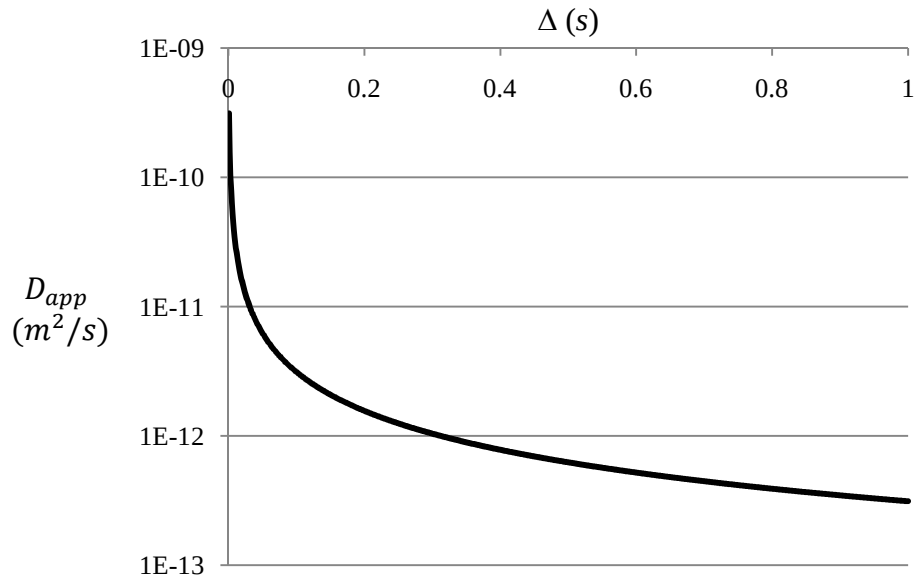

Figure 2.14 The weak gradient apparent diffusion coefficient $\boldsymbol{D_{app} = a^2/5\Delta}$ as a function of $\boldsymbol{\Delta}$ [sec].

In this scenario it is possible to obtain the probability distribution where each a has a Gaussian probability associated with it but instead of being a point is itself a function of displacement. By this method it is possible to obtain figure 2.15.

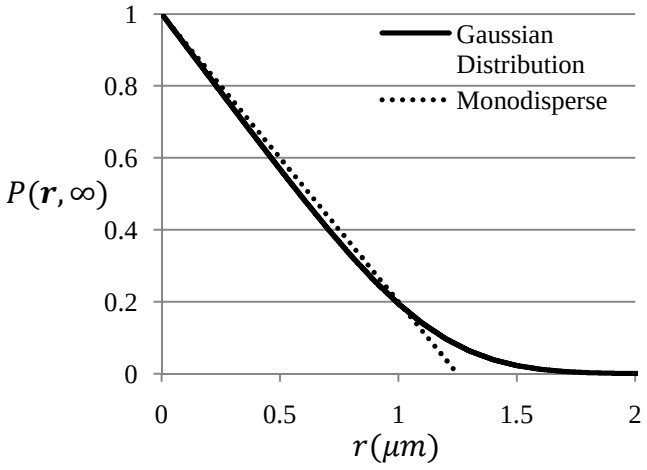

Figure 2.15 Probability distribution ($\boldsymbol{P(r, \infty)}$) of hexadecane inside spheres as $\Delta \rightarrow \infty$ for a monodisperse and a Gaussian distribution ($\boldsymbol{a_0}$ = 1.25μ$\boldsymbol{m}$ and *SD* = = 0.46μ$\boldsymbol{m}$) of sphere sizes. Respective second central moments equal to: 2.61 & 3.14×10^{-13}m^2/s**.**

This shows the formation of a long tail causing the second moment (variance) of the probability distribution to increase from 2.61 to 3.14×10^{-13}m^2/s.

There are two general approaches to sizing the particles which rely on restricted diffusion. These are the Gaussian Phase Distribution (GPD) Model [37] and the Short Gradient Pulse (SGP) Method [38], while an alternative T_2 relaxation method is possible [39]

$$\frac{1}{T_2} = \frac{1}{T_{2,bulk}} + \rho\frac{S}{V} = \frac{1}{T_{2,bulk}} + \rho\frac{3}{a} \quad (2.50)$$

where $T_{2,bulk}$ is the T_2 appropriate for the dispersed phase as a bulk liquid, *S/V* is the surface to volume ratio of the cavity, which is $3/a$ for a sphere, and ρ is the surface relaxivity. If $\frac{\rho a}{D} \ll 1$, the distribution of restricted cavity sizes will result in a distribution of T_2 values. Using the Gaussian probability distribution

$$P(a) = \frac{1}{\sqrt{\pi\sigma^2}} exp\left[\frac{-(a-a_0)^2}{\sigma^2}\right] \quad (2.51)$$

it is also possible to obtain a model relating the NMR echo attenuation with the variance and mean radii of the oil particle distribution by combining this equation with Eqn. 2.52[1]

$$\mathrm{Ln}(E) = -\alpha^2 a_0^2[1+\sigma^2\alpha^2]^{-1} - \frac{1}{2}\mathrm{Ln}\,[1+\sigma^2\alpha^2] \quad (2.52)$$

where $\alpha^2 = \frac{1}{5}\gamma^2\delta^2 g^2$. This model was fit to the stationary flow data at different experimental times Δ, see Table 2.1. which shows the fitting parameters (a_0 and *SD*) for the echo attenuation data for a stationary 22%wt colloidal dispersion from PGSE experiments with G_{max} = 1.7T/m, $\boldsymbol{q}$-pts: 64, *SW*: 5kHz, δ = 4ms.

Table 2.1

$\Delta(ms)$:	$a_0(\mu m)$	$SD(\mu m)$
25	2.00	0.78
50	1.90	1.00
100	1.35	1.20
150	1.52	0.99
200	1.62	1.23
250	1.69	1.22
Microscopy:	**1.25**	**0.46**

The standard deviation of the data is on average $\sigma_{model} > \sigma_{microscopy}$. The mean is approximately the same at Δ = 100ms, deviates significantly at lower Δ data because the long-time limit may not be strictly adhered to, while at higher ***q***-values significant noise affects the data. It is also important to note that δ = 4ms, which smears out the location of the spins during the PGSE sequence, causing a broadening of displacement associated with a particular spin and a well-known over-estimation of both a_0 and σ. To obtain a better estimation it is necessary to use sub-micron δ, which is unfeasible for this particular study. Additionally, a Gaussian fit is a close approximation of the actual distribution, but not the exact probability distribution of the spins in the sample, see figure 2.15, causing additional deviation.

With the behavior at the two limits of free and restricted diffusion it is possible to present these two extreme behaviors for the probability distributions of oil inside the spherical colloidal particles, see figure 2.16.

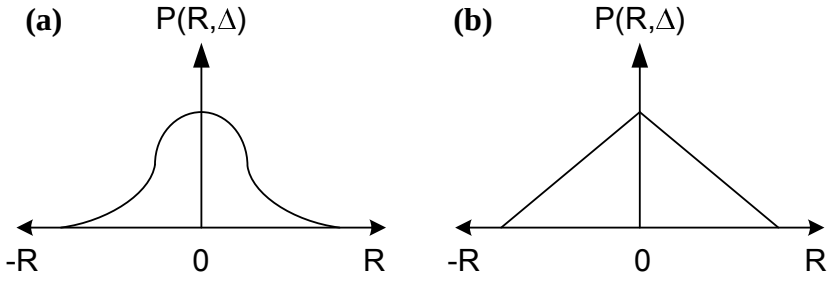

Figure 2.16 The probability distributions for the short-time limit (a) ($\boldsymbol{\Delta \ll a^2/2D}$) when the oil experiences free diffusion and therefore a Gaussian distribution and the long-time limit (b) ($\boldsymbol{\Delta \gg a^2/2D}$) when the oil molecule dynamics inside the spheres is averaged out due to traversing the sphere space multiple times.

Knowledge of these behaviors of the oil molecules is critical in the understanding of the colloidal dynamics particularly in the no-flow conditions.

COLLOIDAL TRANSPORT THEORY

Colloids are a mixture of one substance dispersed in another and are characterized by the phase of each substance. For solids dispersed in a liquid the colloids are known as colloidal dispersions or colloidal suspensions and these colloidal systems are of interest in this thesis. In colloidal suspensions, the particles in a suspending fluid are small enough that Brownian forces affect their dynamics, *i.e.* inertial effects due to interactions with the stochastically moving suspending fluid molecules, which move due to thermal motion (Brownian motion [40-42]). The forces which determine colloid particle dynamics are hydrodynamic, Brownian and interparticle [43]. The hydrodynamic forces are due to the propagation of different particle interactions through the fluid including those due to the application of an external shear field. The Brownian forces are due to the stochastic motion of the suspending fluid molecules impacting the suspended particle. The interparticle forces can be divided into those due to the excluded volume repulsion, electrostatic interaction, van der Waals forces (short-range and attractive), entropic forces and steric forces (either steric repulsion or attractive depletion) [44]. If a colloidal dispersion is unstable it can flocculate, *i.e.* form aggregates of colloidal particles, due to the removal of the electrostatic barrier separating particles, the addition of flocculant (charged polymer), depletants (non-adsorbed polymers) or due to colloid deformation [44]. Since colloidal particles can have significant range of size, shape and surface properties a good starting point in understanding colloidal dynamics is the study of monodisperse hard-sphere colloidal suspensions. This is the simplest colloidal dispersion and can be fully characterized by the volume fraction (ϕ) and the particle Péclet number

(Pe_p) and can be used to form the building blocks for understanding more complex colloids [45, 46]. In this work ϕ and Pe_p are defined as

$$\phi = \left(\frac{4\pi a^3}{3}\right) n \quad (3.1)$$

$$Pe_p = \frac{\dot{\gamma} a^2}{D_{SES}} \quad (3.2)$$

where a is the mean particle radius, n is the number density, $\dot{\gamma}$ is the shear rate and D_{SES} is the Stokes-Eintein-Sutherland [45] diffusivity, and is written

$$D_{SES} = \frac{k_B T}{6\pi\eta_s a} \quad (3.3)$$

where k_B is the Boltzmann constant, T is the absolute temperature and η_s is the viscosity of the suspending fluid. The Péclet number gives the ratio of the convective to diffusive forces and characterizes their relative importance.

Ideal hard-sphere colloids have short-range repulsive interparticle interactions and no long-range electrostatic interactions [47]. To achieve hard-sphere colloidal suspensions in practice, for experiments outside a computer simulation, it is almost always required that the surface of the colloidal spheres be manipulated [47] and that some charge be present on the surface [47, 48]. This charge tends to be large enough to be short-range repulsive but small enough not to cause long-range effects, *i.e.* the effects of van der Waals forces are negated by allowing all the spheres to have the same charge. The theoretical work in this field is immense and only the basic understanding of hard-sphere colloidal dynamics as it relates to this thesis work will be covered in this chapter. For further information an interested reader can find the following references useful [44, 49, 50]. This chapter is organized such that initially the theoretical basis for colloidal

transport is presented, then the background required to understand the colloidal dynamics in the different geometries is investigated and finally the colloidal dispersion used in this work is presented and characterized.

Theoretical Background

A good starting point for understanding colloidal transport is the generalized Langevin equation which is a stochastic ordinary differential equation and the simplest theory of Brownian motion based on the phenomenological Langevin equation [51]

$$m\frac{d\boldsymbol{U}(t)}{dt} = -m\gamma\boldsymbol{U}(t) + \boldsymbol{R}(t) \qquad (3.4)$$

where m is the mass of the colloid, $\boldsymbol{U}(t)$ is the velocity of the colloid, $\gamma = \frac{6\pi\eta a}{m}$ is the frictional constant and $\boldsymbol{R}(t)$ is the stochastic Brownian force term. Eqn. (3.4) says that the force/inertia exerted by the suspending fluid molecules on the colloidal particle equals a frictional term ($m\gamma\boldsymbol{U}(t)$) which opposes the motion of the particle plus the stochastic force $\boldsymbol{R}(t)$ which causes the motion. Generally Langevin equations can be solved by numerical methods [52] or by postulating the appropriate Fokker-Planck equation, *i.e.* a stochastic partial differential equation which characterizes the evolution of the probability distribution function (pdf) with time. For the Langevin equation presented above the latter approach is used where the stochastic random motion $\boldsymbol{R}(t)$ is postulated as a Gaussian pdf which is the proper pdf for Brownian motion, a Wiener process [53]. $\boldsymbol{R}(t)$ therefore has the following properties [51]

$$\langle\boldsymbol{R}(t)\rangle = 0 \qquad (3.5a)$$

$$\langle\boldsymbol{R}(t')\cdot\boldsymbol{R}(t)\rangle = \Gamma\delta(t-t') \quad (3.5b)$$

i.e. it averages to zero and there is no correlation between the Brownian force if $t \neq t'$. The bracket $\langle ... \rangle$ indicates an ensemble average. It can be seen that combining Eqn. 3.4 and 3.5 leads to [51]

$$\langle \boldsymbol{U}(0) \cdot \boldsymbol{U}(t) \rangle = \langle U^2 \rangle e^{-\gamma|t|} \quad (3.6)$$

where $\langle \boldsymbol{U}(0) \cdot \boldsymbol{U}(t) \rangle$ is known as the Velocity Autocorrelation Function (VAF) [54] and indicates the correlation of the velocity of an ensemble average of particles at the start of an observation (t = 0) and at some later time (t > 0). If the velocity does not change over time the normalized VAF equals 1, while if the ensemble changes in velocity direction, but not magnitude, to oppose the initial direction the normalized VAF will equal -1. It is clear from Eqn. 3.6 that for Brownian motion the VAF is expected to decay exponentially towards zero. Since the VAF measures the "memory" of the system about its previous state it is not until the VAF goes to zero that we can say that the entire particle ensemble is experiencing Markovian, or "memoryless", stochastic motion. The time it takes the ensemble to lose "memory" of its previous state can be characterized by a correlation time (τ_c) which relates inversely to the friction constant ($\tau_c = \gamma^{-1}$), where at times t < τ_c the system is correlated, while at times t >> τ_c the system is uncorrelated.

When both convection and diffusion occur in a system it is possible to use conservation of probability to derive the governing differential equation leading to the Fokker-Planck or Smoluchowski equation for velocity

$$\frac{dP(\boldsymbol{x},t)}{dt} = \gamma \frac{d}{dU(t)} U(t) P(\boldsymbol{x}, t) + \frac{\Gamma}{2} \frac{d^2 P(\boldsymbol{x},t)}{dU(t)^2} \quad (3.7)$$

where the 1st term is due to convection (drift term), while the 2nd term is due to diffusion.

Although PGSE NMR cannot probe the correlated regime of small molecule Brownian motion (τ_c~10^{-10}sec), it can measure this correlation regime for macromolecules and colloids [1], for example the thermal motion of 100nm diameter spherical colloids has a interaction time of 100μsec [54].

An important concept in characterizing probability distribution functions (pdf) are the moments [14] which are generally categorized as raw moments

$$\mu_n' = \langle x^n \rangle$$

and central moments

$$\mu_n = \langle (x-\mu)^n \rangle = \int_{-\infty}^{\infty} (x-\mu)^n P(x) dx \quad (3.8)$$

the difference being that the raw moment is the moment about zero while the central moment is about the mean $\mu = \mu_1'$, x is the variable of interest which is displacement in this study. The moments we will be interested in are the first raw moment (mean), second central moment (variance) and third central moment (skewness). For NMR theory it is important to note that the Cauchy-Lorentz distribution, associated with forced resonance, has no mean defined and therefore has no moments as defined above [55]. The second central moment, $\mu_2 = \langle (\boldsymbol{x} - \langle \boldsymbol{x}^2 \rangle)^2 \rangle$, where $\boldsymbol{x}$ is the position vector, is of particular interest for the work presented in this thesis. If $\langle \boldsymbol{x}^2 \rangle = 0$ then $\mu_2 = \langle \boldsymbol{x}^2(t) \rangle$ and the second central moment (or the variance) can be related to the velocity autocorrelation function ($\langle \boldsymbol{U}(0) \cdot \boldsymbol{U}(t') \rangle$), by

$$\langle \boldsymbol{x}^2(t) \rangle = 2 \int_0^t (t-t') \langle U(0) \cdot U(t') \rangle dt' \quad (3.9).$$

By combining equations (3.6) and (3.9) and integrating we obtain

$$\langle \boldsymbol{x}^2(t)\rangle = \frac{2\langle U^2\rangle}{\gamma}\left[t - \frac{1}{\gamma}(1 - \exp(-\gamma t))\right] \quad (3.10)$$

where in the short time limit t << τ_c, the "ballistic motion" regime where particles have linear trajectories, we can use a Taylor expansion of Eqn. (3.10) to obtain

$$\langle \boldsymbol{x}^2(t)\rangle = \frac{2\langle U^2\rangle t}{\gamma} = \langle U^2\rangle t^2 \quad (3.11)$$

In the long time limit t >> τ_c, we obtain [54]

$$\langle \boldsymbol{x}^2(t)\rangle = \frac{2\langle U^2\rangle t}{\gamma} = 2Dt \quad (3.12).$$

Eqn. (3.12) is the classical Einstein relation and is an appropriate description for the unrestricted free diffusion of colloidal particles. More generally we can write [56]

$$\langle \boldsymbol{x}^2(t)\rangle \sim K_\alpha t^\alpha \quad (3.13)$$

where K_α is a constant. We see that Eqn. 3.11 and Eqn. 3.12 can then be written as $\langle \boldsymbol{x}^2(t)\rangle = K_2 t^2$ and $\langle \boldsymbol{x}^2(t)\rangle = K_1 t$; with this generalized notation we can define any diffusive motion relative to α = 1, that is, if $0 < \alpha < 1$ it is subdiffusive while if $\alpha > 1$ it is superdiffusive. This is a useful representation because it allows for the extension to anomalous diffusive regimes [56]. For example, different diffusive behavior occurs on different time scales which might be described by a Levy-flight type ($1 < \alpha < 3$ [56]) Continuous Random Time Walk (CRTW) [56] model. These are processes which not only capture Brownian motion and drift, but also divergent mean jumps at a longer time scale, which at long enough observation time scales can themselves appear stochastic.

A useful extension is to treat hard-sphere Brownian suspensions as isotropic fluids, which experience restriction in motion due to particle-particle collisions, with a correlation time of interaction (τ_I). For τ_c<< t < τ_I *i.e.* at time less than the interaction

time but larger than the characteristic decay time of the fluid (τ_c), the system experiences unrestricted free diffusion

$$\langle \boldsymbol{x}^2(t)\rangle = 2D_{SES}t \quad (3.14).$$

For the interacting system the instantaneous velocity of a particle can be written as the sum of friction and interparticle interaction terms, giving a VAF of the form [54]

$$\langle \boldsymbol{U}(0)\cdot\boldsymbol{U}(t)\rangle = \langle U^2\rangle\left[e^{-\gamma t} + \alpha_I e^{-t/\tau_I}\right] \quad (3.15)$$

where α_I is determined by the interparticle potential and can be modeled as a particle bound in a harmonic potential [54]

$$\alpha_I = (\omega_I/\gamma)^2 \quad (3.16)$$

where ω_I is the effective angular frequency of the interaction. When $t \sim \tau_I$ the particle experiences the interaction forces, and for times t >> τ_I the dynamics reach a new diffusion regime

$$\langle \boldsymbol{x}^2(t)\rangle \cong 2D_I t \quad (3.17)$$

with $D_I = D_{SES} - \alpha_I\tau_I$, where D_I is the long-time self-diffusion coefficient of the particles in an "interacting Brownian system". This model indicates that the VAF for the colloidal particles has a weak long-lived negative tail similar to the case for a monoatomic liquid [54]. Therefore the Brownian particles can be viewed as temporarily trapped in a repulsive cage formed by the instantaneous configuration of its neighbors [57].

This view of a colloidal system as an isotropic liquid allows for a useful framework for the analysis of the probability distribution of displacement (the propagator) as a function of time. This can be extended to a system with shear. Shear

supplies energy for microstructural re-arrangements, allowing particles to oscillate between restricted and un-restricted diffusive regimes with intermittent larger displacements due to local structure/group motion and Taylor dispersion.

Taylor dispersion [58-60] is the process where colloidal or suspending fluid particles migrate across streamlines during shear flow due to Brownian motion. The time-scale for this process is defined in a capillary by the ratio between the square of the capillary radius and the particle diffusivity D', or t = R^2/D'. In the short time limit, t << R^2/D', the dispersion $D^*(t)$ is time dependent and can be represented by a Taylor series [58]:

$$D^*(t) = D' + \frac{1}{6}v^2 t + \frac{\frac{4}{3}D'v^2}{R^2t^2} + \cdots \quad (3.18)$$

while in the long time (or Taylor-Aris [60]) limit, t >> R^2/D') the dispersion coefficient asymptotes to

$$D^* = D' + \frac{v^2R^2}{48D'} \quad (3.19).$$

For the microcapillary work presented in this thesis R = 126x10^{-6} m, D_{SES} = 1.73x10^{-13}m^2/s and D_W = 2.20x10^{-9}m^2/s at 20^{o}C. Therefore R^2/D_{SES} = 9.2x10^4 seconds and R^2/D_W = 7.2 seconds, *i.e.* all experiments conducted are in the short time limit.

Memory Functions

A limitation of the Langevin equation presented in Eqn. 3.4 and used in the above analysis lies in the assumption that the systematic force ($m\gamma \boldsymbol{U}(t)$) is determined only by the instantaneous values of the particle velocity, implying no memory of the previous particle dynamics. A more general approach introduces the concept of memory functions, which can fully describe complex time dependent dynamical relations that

otherwise could be lost. To extend Eqn. 3.4, the equation of motion for colloidal particles should be [51]

$$m\frac{d\boldsymbol{U}(t)}{dt} = -m\int_0^t \gamma(t-t')\boldsymbol{U}(t')dt' + \boldsymbol{R}(t) \quad (3.20).$$

If a small external force ***F(t)*** sufficiently weak to be treated by linear theory is added,

$$m\frac{d\boldsymbol{U}(t)}{dt} = -m\int_0^t dt'\,\gamma(t-t')\boldsymbol{U}(t') + \boldsymbol{R}(t) + \boldsymbol{F}(t) \quad (3.21)$$

we obtain the equation of motion for a fluctuation-dissipation equilibrium for the colloidal system. The use of memory functions to derive dynamic models has a long history [51, 54, 61] and they remind us that for "complex" systems the underlying deviations of models and simulations from experimental observation may be due to the lack of capturing the necessary system memory as a function of time. The memory function in the generalized hydrodynamic formulation is a space-time function, while it is a time dependent phase-space function in the kinetic theory approach. It is in the manner of calculating the memory function that the two approaches differ [51]. A general memory function equation can be written

$$\frac{\partial}{\partial t}A(t) = -\int_0^t dt'\kappa(t')A(t-t') \quad (3.22)$$

where $A(t)$ is the time correlation function and $\kappa(t')$ is the memory function. The latter determines how much is remembered from previous time. The form that $\kappa(t')$ takes depends on the system being investigated. A simple starting point for picking $\kappa(t')$ is to use the initial condition:

$$\kappa(0) = \frac{-\ddot{C}(0)}{C(0)} \quad (3.23a)$$

and requiring

$$\kappa(t) = \kappa(0)f(t) \quad (3.23b)$$

$$f(0) = 1 \quad (3.23c)$$

where $C(0)$ is the initial value and $\ddot{C}(0)$ is the curvature for an arbitrary function $C(t)$. Another way to model a system is to express the memory function decay in terms of coupling to higher-order time-correlation functions which involve more than two dynamic variables; this approach is called mode-coupling and is closer to being a microscopic description.

Using the Liouville equation it is possible to derive a function for the evolution of the autocorrelation function $\boldsymbol{\psi}(t)$ known as the Memory function Equation (ME) or master equation [54]

$$\frac{d\boldsymbol{\psi}(t)}{dt} = -\int_0^t dt'\, \kappa(t')\boldsymbol{\psi}(t-t') \quad (3.24)$$

where $\kappa(t)$ is the memory function

$$\kappa(t) = \frac{\langle \dot{A}^*(0)(1-\zeta)e^{i(1-\zeta)Lt}\dot{A}(0)\rangle}{\langle |A(0)|^2\rangle} - 2\varphi(0)\delta(t) \quad (3.25).$$

This is one of the major results in the statistical mechanics study of many-body systems [54]. Solving the ME is a complex problem, however using a Continued Fraction Representation (CFR)[54] it is possible to express the Laplace transform of the normalized autocorrelation function ($\tilde{\psi}(s)$) as

$$\tilde{\psi}(s) = \int_0^\infty dt e^{-st}\frac{\langle \mathbf{v}(0)\cdot\mathbf{v}(t)\rangle}{\langle v(0)^2\rangle} = \cfrac{1}{s+\cfrac{\langle \dot{v}(0)^2\rangle/\langle v(0)^2\rangle}{s+\cfrac{\langle \ddot{v}(0)^2\rangle}{\langle \dot{v}(0)^2\rangle}\cfrac{\langle \dot{v}(0)^2\rangle}{\langle v(0)^2\rangle}}}} \quad (3.26)$$

where $\langle v(0)^2 \rangle = 3v_0^2$. This form serves as a basic starting point for the solution of model calculations.

Statistical Mechanics and Continuum Mechanics Description

The macroscopic descriptions of dissipation phenomena are through diffusion, viscosity and thermal conduction. In the absence of external perturbations, spontaneous microscopic fluctuations always occur in a system at finite temperature. These are dissipated in a similar fashion as external disturbances. This interplay between perturbation and dissipation is described by the fluctuation dissipation theorem [23, 54], a powerful tool in non-equilibrium statistical mechanics. For long-wavelength and low frequency fluctuations, the fluid behaves like a continuum, *i.e.* it can be described by equations of hydrodynamics. At wavelengths comparable to the inter-particle distances, the local structure of the fluid becomes important and is described by an assembly of interacting particles, *i.e.* particle dynamics. The basic assumption of hydrodynamics is that changes in the fluid take place sufficiently slowly that the system can be considered to be in a state of local thermodynamic equilibrium. This leads to a closed set of equations describing the space-time variations of the conserved variables. This becomes an explicit description when thermodynamic derivatives and transport coefficients are specified. Unless far removed from the low frequency, long wavelength limit it is appropriate to extend the hydrodynamics description by retaining the basic structure of the equations, but replacing the thermodynamic derivatives and transport coefficients by functions which can vary in space or in space and time leading to the generalized hydrodynamic description. When far enough removed from the low frequency, long

wavelength limit a particle dynamics description is essential, where the spatial and time variations are comparable to the collision mean free path and mean time between collisions. The mean free path is described by kinetic theory as [62]

$$\lambda = \frac{a}{3\sqrt{2}\phi} \quad (3.27)$$

where for a finite volume fraction [62]

$$\lambda = \frac{a}{3\sqrt{2}}\left(\frac{1}{\phi} + \frac{1}{\phi_m}\right) \quad (3.28)$$

where ϕ_m is the maximum packing fraction. Particle dynamics concerns the relation between particle interactions and motion on one hand and macroscopic properties of the fluid on the other. The combination of hydrodynamic equations with molecular models for the functions which replace the thermodynamic derivatives and transport coefficients results in a hybrid description of fluid dynamics with a considerable range of validity. One of the principle goals of statistical mechanics is to be able to calculate all the dynamical properties in terms of only the interaction potential and allow for a unified description for all wavelengths and frequencies of particle velocity fluctuation.

An interesting initial approach for describing colloidal particle dynamics is the use of the Boltzmann equation, which is the basic equation of kinetic theory of dilute gases and of fundamental importance in non-equilibrium statistical mechanics. The Boltzmann equation uses probabilistic ideas to make a connection between molecular motions and irreversible thermodynamics. The average properties of the ensemble of particles are examined using the conservation equation of the one particle distribution

function $f = f(x, p, t)$ in phase space, where x is position, p is momentum and t is time. This particle distribution function changes due to motion without collision (streaming) and through collisions. The Boltzmann equation is written

$$\frac{df}{dt} = \frac{\partial f}{\partial t}\Big|_{stream} + \frac{\partial f}{\partial t}\Big|_{coll} \quad (3.29a)$$

where

$$\frac{\partial f}{\partial t}\Big|_{stream} = \frac{\partial f}{\partial \boldsymbol{x}} \cdot \frac{\boldsymbol{p}}{m} + \frac{\partial f}{\partial \boldsymbol{p}} \cdot \boldsymbol{F} \quad (3.29b)$$

$$\frac{\partial f}{\partial t}\Big|_{coll} = \iint g(\boldsymbol{p} - \boldsymbol{p}', \boldsymbol{q})[f(\boldsymbol{x}, \boldsymbol{p} + \boldsymbol{q}, t) f(\boldsymbol{x}, \boldsymbol{p}' - \boldsymbol{q}, t) - f(\boldsymbol{x}, \boldsymbol{p}, t) f(\boldsymbol{x}, \boldsymbol{p}', t)] dp' dq$$

(3.29c)

where $\boldsymbol{F}$ is the external force on the particle, $\boldsymbol{q}$ is a dummy variable and "primes" refer to post-collision momentum. The form of the collision term is known due to the "Stosszahl Ansatz" or molecular chaos, assumption that there are only two-body collisions and no-correlation prior to collision. An important result of the Boltzmann equation is that the entropy of an isolated system will increase due to reversible processes. The Boltzmann equation can be used to determine the well-known Maxwell distribution for molecules at thermal equilibrium

$$f = n\left[\frac{m}{2\pi kT}\right]^{3/2} exp[-mU^2/2kT] \quad (3.30).$$

Using ergodic theory, *i.e.* the long time average of a function along the trajectories exists almost everywhere and is related to the ensemble average, the macroscopic properties of the systems have values close to thermodynamic equilibrium. This allows for the derivation of the continuum equation of motion from the Boltzmann equation using the Chapman-Enskog method [63]

$$\frac{\partial \rho}{\partial t} + \nabla \cdot (\rho \mathbf{v}) = 0 \quad (3.31a)$$

$$\rho \frac{\partial \mathbf{v}}{\partial t} + \nabla \cdot (\rho \mathbf{v}\mathbf{v}) = \rho \mathbf{g} + [\nabla \cdot \boldsymbol{\sigma}] \quad (3.31b)$$

$$\frac{3}{2} nk \frac{\mathrm{dT}}{dt} = -\boldsymbol{\sigma} : \nabla \mathbf{v} + \nabla \cdot \mathbf{q} \quad (3.31c)$$

where ρ is the fluid density, $\mathbf{g}$ is the gravitational force, $\boldsymbol{\sigma}$ is the molecular stress tensor and $\mathbf{q}$ is the heat flux. The derivation of these continuum equations from the statistical mechanics based Boltzmann equation is central in the statistical mechanics modeling of macroscopic behavior. These three continuum equations are the equation of mass, equation of motion and equation of energy and can be derived independently using the differential volume approach [64].

If it is assumed that the fluid has a constant ρ the equation of mass becomes

$$\nabla \cdot \mathbf{v} = 0 \quad (3.32).$$

Additionally, for a Newtonian fluid the molecular stress tensor can be written [64]

$$\boldsymbol{\sigma} = -p\boldsymbol{\delta} - \mu(\nabla \mathbf{v} + (\nabla \mathbf{v})^T) \quad (3.33)$$

where μ is the fluid viscosity. Using these equations with the conservation equations we obtain the well-known Navier-Stokes equation

$$\rho \frac{\partial \mathbf{v}}{\partial t} + \rho(\mathbf{v} \cdot \boldsymbol{\nabla} \mathbf{v}) = -\nabla p + \mu \nabla^2 \mathbf{v} \quad (3.34).$$

Furthermore, when inertial forces are small compared with viscous forces, *i.e.* $\mathrm{Re} \to 0$, we obtain the Stokes equation

$$\nabla p = \mu \nabla^2 \mathbf{v} \quad (3.35)$$

which are linear and reversible in time and are of critical importance in colloidal particle theory because they form the foundation for a large proportion of theoretical and numerical approaches used to study colloidal systems.

For a multiphase system it is possible to apply averaged transport theory where the hydrodynamic conservation equations are averaged on a scale large compared to the fluid particles, allowing for the addition of stress and interfacial force terms to account for the presence of the particles. The averaged equations of mass, momentum and energy where the subscript i denotes a phase are [65]

$$\frac{\partial \alpha_i \langle \rho_i \rangle}{\partial t} + \nabla \cdot \alpha_i \langle \rho_i \rangle \langle \mathrm{v}_i \rangle = 0 \quad (3.36a)$$

$$\frac{\partial \alpha_i \langle \rho_i \rangle \langle \mathrm{v}_i \rangle}{\partial t} + \nabla \cdot \alpha_i \langle \rho_i \rangle \langle \mathrm{v}_i \rangle \langle \mathrm{v}_i \rangle = \nabla \cdot \alpha_i (\langle T_i \rangle + T_i^{Re}) + \alpha_i \langle \rho_i \rangle \mathbf{g} + M_i \quad (3.36b)$$

$$\frac{\partial}{\partial t} \alpha_i \langle \rho_i \rangle \beta_i + \nabla \cdot \alpha_i \langle \rho_i \rangle \langle \mathrm{v}_i \rangle \beta_i = \nabla \cdot \alpha_i [(\langle T_i \rangle + T_i^{Re}) \cdot \mathrm{v}_i - \langle q_i \rangle - q_i^{Re}] + E_i + W_i$$

$$+ \alpha_i \langle \rho_i \rangle (r_i + g \langle \mathrm{v}_i \rangle) \quad (3.36c)$$

where α_i is the volume fraction, $\langle \rho_i \rangle$ is the average density, $\langle \mathrm{v}_i \rangle$ is the average velocity, $\langle T_i \rangle$ is the average stress, T_i^{Re} is the Reynolds stress, $\mathbf{g}$ is the gravitational force, M_i is the interfacial force density, $\beta_i = \langle u_i \rangle + \frac{1}{2} \langle \mathrm{v}_i \rangle^2 + u_i^{Re}$ where u_i is the internal energy density and u_i^{Re} is the fluctuation kinetic energy, $\langle q_i \rangle$ is the average heat flux, q_i^{Re} is the Reynolds energy flux, E_i is the interfacial energy flux, W_i is the interfacial work. The additional stresses and interfacial forces must be represented by constitutive equations that account for the effects of the particle velocity fluctuations. These velocity

fluctuations are analogous between gas molecules modeled as “billiard” balls and colloidal suspension particles, where for the former it is due to collisions while for the latter it is due to both collisions and hydrodynamic interactions.

The use of additional stress terms in the equation of motion to account for particle velocity fluctuations due to hydrodynamic interactions is one way to analyze colloidal suspensions, an alternative is to apply the linear Stokes equations. This can be done by modeling the impact of particles on the velocity field by modeling them as point forces. This method is known as a Stresslet (or Stokeslet when applied to the Stokes equation) Model [66, 67] involves application of singularities. It is a “far-field” approximation since far from a sphere it gives a correct contribution to the stress on the fluid. This leads to incorporating a point force in the Stokes equation as

$$\nabla p = \mu \nabla^2 \mathbf{v} + \delta(\mathbf{x})\mathbf{F} \quad (3.37).$$

The Stokes equation can be solved by finding the appropriate Green’s functions

$$p(\mathbf{x}) = \frac{\mathbf{F}\cdot\mathbf{x}}{4\pi|\mathbf{x}|^3} \quad (3.38a)$$

$$\mathbf{v}(\mathbf{x}) = \mathbf{I}\cdot\mathbf{F} \quad (3.38b)$$

where $\mathbf{I} = \frac{1}{8\pi\mu x}\left(\delta(\mathbf{x}) - \frac{\mathbf{x}\cdot\mathbf{x}}{x^2}\right)$ is the Oseen tensor and **F** is the magnitude of the point force acting at the origin. These results can be generalized to n particles by summation, for example for spherical particle i impacted by the presence of n spherical particles [68]:

$$\mathbf{v_i}(\mathbf{x}) = \mathbf{v_0} + a\mathbf{v_0}\cdot\sum_{\mathbf{j}\neq\mathbf{i}}^{\mathbf{n}} \mathbf{I}(\mathbf{x_i} - \mathbf{x_j}) \quad (3.39).$$

The Stokeslet model can be used to solve the two particle problem which dominates dilute suspensions, however due to the linearity of the Stokes equations there is no source of irreversibility and therefore particles cannot cross streamlines after collisions.

Reversibility and Irreversibility

Equations describing colloidal particle dynamics combine deterministic and stochastic forces in the description of the particle momentum, requiring the use of stochastic calculus. While the deterministic component has a memory of the states it occupies and can be predicted at any time, *i.e.* is reversible, the stochastic component represents a loss of memory with time and therefore a loss in predictability, *i.e.* is irreversible. This randomness is contrary to the mathematical rules governing Newton's laws and Maxwell's electromagnetic theory, therefore fundamentally requiring the addition of probability theory and the tools of statistical mechanics to model colloidal systems.

A description of whether a system is experiencing reversible or irreversible motion is of fundamental importance and a useful mathematical definition can be found in chaos mathematics [69-71]. Chaos means deterministic behavior that is very sensitive to initial conditions, *i.e.* infinitesimal perturbations lead to large variations in behavior. In dynamical systems theory the measure of chaos is the Lyapunov exponent (λ); ($\lambda = f(\lambda_1, \lambda_2, \dots, \lambda_N)$ where $\lambda_1 > \lambda_2 > \lambda_3$ ...). The time it takes a system to become chaotic (the Lyapunov time) is defined as $1/\lambda_1$, where λ_1 is the maximal Lyapunov exponent.

The Lyapunov exponent is calculated by considering an initial state in phase space, tracking the particle trajectories evolution in time, perturbing the system by adding an incremental random initial displacement and tracking the particle trajectories, and repeating this process as necessary. The differences or spread in evolved particle position after the initial perturbations are a measure of whether or not chaotic behavior is present in the system. The mathematical definition is [70, 71]

$$|\delta \boldsymbol{X}(t)| \approx e^{\lambda t}|\delta \boldsymbol{X}_0| \quad (3.40a)$$

$$\lambda = \lim_{t\to\infty} \frac{1}{t} \mathrm{Ln} \frac{|\delta X(t)|}{|\delta X_0|} \quad (3.40b)$$

where $\delta \mathbf{X}_0$ is the initial difference between the starting point of two trajectories in phase space, while $\delta \boldsymbol{X}(t)$ is the difference between those trajectories at time t. It is clear from Eqn. (3.40a) that when $\lambda > 1$ the system tends towards chaotic motion and that the definition of the Lyapunov time is the time it takes trajectories in phase space to be separated by e^1. This definition is interesting when analyzing probability distribution functions describing the displacement in a system due to stochastic processes as measured by velocity compensated PGSE experiments, because the spreading of these distributions with time measures the growth of irreversibility in the system which is analogous to the growth of chaos. This kind of analysis will serve as a useful framework for analyzing the colloidal transport in a microcapillary in Chapter 4.

Chaotic behavior has been noted in the modeling of the three body interaction problem via the Stokelets model [68] and Stokesian dynamics simulations [72]. In concentrated suspensions, Pine *et al.* [72] showed that a critical strain is associated with the time for onset of irreversibility. Even for dilute systems ($\phi < 0.10$) where only

binary collisions are predicted to occur, surface roughness [73, 74], interparticle or Brownian forces [75-77] and the impact on the particle distribution function (a measure of the microstructure of the suspension) cause particles to cross streamlines after collision, generating irreversible dynamics. Wang *et al.* [78] and Janosi *et al.* [68] performed simulations on three-particle interactions, showing that the fore and aft symmetry of two particle interactions is disturbed by the presence of a third particle. The show that the trajectories of three particles in Stoke's flow can be chaotic and therefore irreversible for perfectly smooth spheres. This is the classical three body problem.

Simulation Methods

Simulating particle transport in a colloidal dispersion requires the use and understanding of fundamental principles, so it is useful to describe the numerical simulation methods before the current understanding of colloidal dynamics is presented. This is also useful due to the pervasiveness of simulations in the advancement of the field, particularly those using Stokesian Dynamics (SD) [46, 52, 75, 79].

Flow of colloidal suspensions is a challenging fluid mechanics problem which can be solved analytically for a single particle, semi-analytically for two particles, but requires numerical solution when dealing with three or more particles. Simulations that explicitly take account of the hydrodynamic interactions (HI) between suspended particles are a useful tool for the study of particle suspensions, but simulations without HI or simplified HI such as Brownian Dynamics (BD) and kinetic theory-like treatments are pervasive in the study of equilibrium and non-equilibrium molecular dynamics

simulations and give useful approximations [80]. BD [80, 81], the pioneering simulation method for colloidal suspensions, is a stochastic simulation of the time evolution of the N-body Smoluchowski equation

$$\frac{\partial P(\boldsymbol{x}^N,t)}{\partial t} + \boldsymbol{\nabla} \cdot \boldsymbol{j}_N = 0 \quad (3.41).$$

Here $P(\boldsymbol{X}^N, t)$ is the probability distribution function and $\boldsymbol{j}_N$ is the particle flux vector for an N-body system defined as

$$\boldsymbol{j}_N = -\boldsymbol{D} \cdot \boldsymbol{\nabla} P(\boldsymbol{x}^N, t) \quad (3.42)$$

where the diffusivity $\boldsymbol{D}$ is related to the hydrodynamic resistance function ($\boldsymbol{R}_{FU}$) by the Stokes-Einstein relation, $\boldsymbol{D} = kT\boldsymbol{R}_{FU}^{-1}$. Eqns. 3.41 with 3.42 corresponds to the N-body Langevin equation which can be written analogous to the single particle Langevin equation (Eqn. 3.4) with the addition of an interparticle potential term $\boldsymbol{F}^{IP}$

$$\boldsymbol{m} \cdot \frac{d\boldsymbol{U}}{dt} = \boldsymbol{F}^H + \boldsymbol{F}^B + \boldsymbol{F}^{IP} \quad (3.43).$$

The hydrodynamic ($\boldsymbol{F}^H$), Brownian ($\boldsymbol{F}^B$) and potential forces ($\boldsymbol{F}^{IP}$) are defined by

$$\boldsymbol{F}^H = -\boldsymbol{R}_{FU} \cdot \boldsymbol{U} \quad (3.44a)$$

$$\langle \boldsymbol{F}^B \rangle = 0 \quad (3.44b)$$

$$\langle \boldsymbol{F}^B(0) \cdot \boldsymbol{F}^B(t) \rangle = 2kT\boldsymbol{R}_{FU}\delta(t) \quad (3.44c)$$

$$\boldsymbol{F}^{IP} = -\nabla V_p(\boldsymbol{x}) \quad (3.44d).$$

In Eqn 3.43 $\boldsymbol{m}$ is the generalized mass/momentum-of-inertia matrix (6Nx6N), **U** is the vector (6N) of the particles' translational/rotational velocity and $\boldsymbol{R}_{FU} = 6\pi\eta a\boldsymbol{I}$ or the Stokes drag law. These types of non-equilibrium molecular dynamics simulations or Brownian dynamics simulations can be used to produce qualitatively correct behavior at low *Pe* [80]. For more accurate simulations it is necessary to add hydrodynamic interactions where $\boldsymbol{F}^H$ is modified as [46, 80]

$$\boldsymbol{F}^H = -\boldsymbol{R}_{FU} \cdot (\boldsymbol{U} - \langle \boldsymbol{U} \rangle) + \boldsymbol{R}_{FE} : \langle \boldsymbol{E} \rangle \quad (3.45)$$

where $(\boldsymbol{U} - \langle \boldsymbol{U} \rangle)$ gives the relative velocity of a particle to the ensemble average and $\langle \boldsymbol{E} \rangle$ is the rate of strain and $\boldsymbol{R}_{FE}$ is the force/torque on the particle due to the shearing motion or rate of strain. The bulk rate of strain $\langle \boldsymbol{E} \rangle$ and the imposed flow $\langle \boldsymbol{U} \rangle$ are defined as

$$\langle \boldsymbol{E} \rangle = (1/2)[\langle \boldsymbol{\nabla U} \rangle + \langle \boldsymbol{\nabla U} \rangle^T] \quad (3.46a)$$

$$\langle \boldsymbol{U} \rangle = \langle \boldsymbol{\nabla U} \rangle \cdot \boldsymbol{x} \quad (3.46b).$$

The probability flux vector $(\boldsymbol{j}_N)$ for the Smoluchowski equation (Eqn. 3.39) is re-written in this case as

$$\boldsymbol{j}_N = \langle \boldsymbol{U} \rangle P_N(\boldsymbol{X}^N, t) + \boldsymbol{R}_{FU}^{-1} \cdot [\boldsymbol{R}_{FE} : \langle \boldsymbol{E} \rangle + \boldsymbol{F}^P - kT\boldsymbol{\nabla} ln P_N(\boldsymbol{X}^N, t)\ ] P_N(\boldsymbol{X}^N, t) \quad (3.47).$$

At equilibrium $\langle \boldsymbol{E} \rangle = 0$ and $F^P = kT\boldsymbol{\nabla} ln P_N(\boldsymbol{X}^N, t)$ and we obtain

$$\boldsymbol{j}_N = \langle \boldsymbol{U} \rangle P_N(\boldsymbol{X}^N, t) \quad (3.48).$$

With the equations of motion for BD and SD explicitly defined above, it is useful to look at the macroscopic stress $\langle\Sigma\rangle$ in the colloidal dispersion. This can be written as the sum of the suspending fluid component and the colloidal particles as

$$\langle\Sigma\rangle = \langle\Sigma\rangle^f + \langle\Sigma\rangle^p \quad (3.49)$$

where the solvent contribution, $\langle\Sigma\rangle^f$, is due to hydrostatic pressure and Newtonian viscosity contributions and is isotropic

$$\langle\Sigma\rangle^f = -\langle P_f\rangle \boldsymbol{I} + 2\eta\langle \boldsymbol{E}\rangle \quad (3.50).$$

The particle contributions are due to the hydrodynamic stress $\langle \boldsymbol{S}^H\rangle$, the Brownian stress $\langle \boldsymbol{S}^B\rangle$ and the interparticle stress $\langle \boldsymbol{S}^P\rangle$

$$\langle\Sigma\rangle^p = n[\langle \boldsymbol{S}^H\rangle + \langle \boldsymbol{S}^B\rangle + \langle \boldsymbol{S}^{IP}\rangle] \quad (3.51).$$

Each stress component is explicitly given by

$$\langle \boldsymbol{S}^H\rangle = -\langle \boldsymbol{R}_{SU}\cdot\boldsymbol{R}_{FU}^{-1}\cdot\boldsymbol{R}_{FE} - \boldsymbol{R}_{SE}\rangle : \langle \boldsymbol{E}\rangle \quad (3.52a)$$

$$\langle \boldsymbol{S}^B\rangle = -kT(\boldsymbol{I} + \langle \boldsymbol{\nabla}\cdot(\boldsymbol{R}_{SU}\cdot\boldsymbol{R}_{FU}^{-1})\rangle) \quad (3.52b)$$

$$\langle \boldsymbol{S}^{IP}\rangle = -\langle(\boldsymbol{x}\boldsymbol{I} + \mathbf{R}_{\mathrm{SU}}\cdot\mathbf{R}_{\mathrm{FU}}^{-1})\cdot\boldsymbol{F}^{IP}\rangle \quad (3.52c).$$

Here $\boldsymbol{R}_{SU}$ and $\boldsymbol{R}_{SE}$ are the resistance tensors coupling the stresslet to particle velocity and imposed rate-of-strain. The explicit difference between a SD and BD is that the latter neglects hydrodynamic interactions, $\boldsymbol{R}_{SU} = \boldsymbol{R}_{FE} = \boldsymbol{R}_{SE} = 0$ and $\boldsymbol{R}_{FU} = 6\pi\eta a\boldsymbol{I}$ [80] and leads to the much less interesting stress terms

$$\langle \boldsymbol{S}^{H} \rangle = 0 \quad (3.53a)$$

$$\langle \boldsymbol{S}^{B} \rangle = -kT\boldsymbol{I} \quad (3.53b)$$

$$\langle \boldsymbol{S}^{IP} \rangle = -\langle (\boldsymbol{xI}) \cdot \boldsymbol{F}^{IP} \rangle \quad (3.53c).$$

BD simulations typically use a 1st order integration of the stochastic differential equations, with the critical approximation that the HI can be represented by a pairwise-additive sum of two-particle mobility tensors, [81] or can be ignored altogether. Despite this oversimplification of the HI, BD simulations give important qualitative insights into the dynamics of colloidal suspensions, and can be quantitative [82].

SD [52] uses a much better approximation to the HI than BD, obtained by truncating the multipole hierarchy at the L = 1 order of spherical harmonics rather than L = 0. An important consequence of including particle torques and stresses is that interactions between distant spheres are given exactly, even in the presence of an external shear. Another innovation of SD is the incorporation of short-range "lubrication" forces. When two particles are near contact, the HI are dominated by forces originating from flow in the gap between the particles. Although HI are not additive in general, lubrication forces are an exception and can be added, pair by pair, to the far-field forces. Including lubrication forces in this way allows a truncated multipole expansion to accurately represent the HI in all particle configurations. In practice no general numerical method can afford the computational cost of resolving the flow in the narrow gaps between closely-spaced particles, so lubrication forces always need special attention. Even SD is too time consuming for dynamical simulations of more than a few

hundred particles. Approximations have been made for high volume fraction $\phi > 0.50$ which are dominated by lubrication forces, and therefore long-range HI are ignored and the mobility tensor is calculated on the basis of lubrication forces alone [83], this has allowed the simulation of a few thousand colloidal particles [84]. Limitations of SD include that the suspending fluid is assumed Newtonian and required creeping flow condition ($Re = 0$). It is also difficult to extend it to suspensions of non-spherical particles, or to suspensions bounded by container walls. These issues are being addressed [83, 85, 86] and SD remains a robust, physically-motivated algorithm, which is straightforward although difficult to code. The Stokes equations can also be solved by boundary-element methods, which are more flexible than SD and can be applied to non-spherical or deformable particles [87-89] however these are even more computationally demanding than SD, with approx. 100 deformable drops in a shear flow being simulated so far [90].

In reality, HI develop in time and space from purely local stresses generated at the solid-fluid surfaces, which then propagate throughout the fluid by diffusive momentum transport. Several computational schemes attempt to exploit this spatial locality; Lattice-Boltzmann [91-93], finite-element methods [94-98] and particle-based schemes such as dissipative particle dynamics [99]. However, for low *Re* flows, the computational gains arising from spatial locality are offset by the additional time scale required to follow the motion of the fluid. Other quasi-particle methods including Monte Carlo [100] and smooth particle hydrodynamics [101, 102] can be employed to model particle-fluid systems. It is important to note that Lattice-Boltzmann simulations have been found

under certain conditions to have a significant advantage over SD for flows in porous media [103] and for some colloidal suspensions [104].

Colloidal Suspension Viscosity Dependence on *Pe* and ϕ

For hard-sphere colloidal suspensions the rheology ranges from Newtonian at low ϕ, to non-Newtonian, exhibiting shear thinning, shear thickening [44, 50, 84] and normal stress differences [46, 105, 106], at high ϕ, and eventual jamming at a maximum packing [107, 108]. The viscosity as ϕ increases can be described by different rheology models. At low enough ϕ (< 0.03) it is sufficient to only analyze the motion of the fluid around a single sphere and the effects of the individual spheres are additive; this regime is described by the Einstein equation [41]

$$\eta_r = 1 + 2.5\phi \quad (3.54)$$

where η_r is the effective viscosity $\eta_{eff}(Pe)$ at a certain shear rate divided by the viscosity of the suspending medium η_s. This equation has been extended (ϕ < 0.10) by Batchelor [109] to include binary collisions

$$\eta_r = 1 + 2.5\phi + 6.2\phi^2 \quad (3.55).$$

As the volume fraction increases up to $\phi < 0.30$, colloidal suspensions have been measured to be essentially Newtonian [105], while as the volume fraction increases above this value non-Newtonian effects such as shear thinning occur which can be described by the Krieger-Dougherty equation [110]

$$\eta_r = \left(1 - \frac{\phi}{\phi_{max}}\right)^{-2.7\phi_{max}} \quad (3.56).$$

ϕ_{max} is the maximal packing of the spheres, in this work this value is ϕ_{max} = 0.68. At still higher volume fractions shear thickening occurs at high shear rates.

Theoretically, the relative viscosity (η_r) is composed of hydrodynamic and Brownian contributions and can be written as [111]

$$\eta_r = 1 + \eta_H + \eta_B \quad (3.57).$$

These contributions have a dependence on Pe_p such that at low Pe_p, the Brownian stresses and viscosity (η_B) decreases rapidly while the hydrodynamic stresses increase linearly, with a constant viscosity contribution (η_H). This contribution is however not enough to offset the decline in η_B and therefore there is a decrease in η_r, *i.e.* shear thinning. At high Pe_p, Brownian stresses become negligible and the hydrodynamic stresses contribute increasingly to the overall stress as the particles are pushed into close contact and lubrication forces dominate the hydrodynamic interactions and η_r increases, *i.e.* shear thickening. Brady *et al.* [112] were the first to simulate these shear thinning and thickening phenomena using Stokesian dynamics simulations. Whether or not shear thinning and thickening occur for a hard-sphere suspension is dependent on ϕ.

At high enough volume fraction hard–sphere colloidal suspensions will transition to a glassy state at $\phi \sim 0.58$ [44]. Before this transition a coexistence region has been predicted [113] and observed [114] to exist at $0.494 < \phi < 0.545$. The main difference between prediction and observations was that the former predicted a face centered cubic (fcc) arrangement but the latter observed an intermediate between fcc and hexagonal closest packing (hcp) arrangement [115, 116].

The nucleation kinetics at the glass transition has been extensively studied [117-121]. Charged colloids that interact through screened Coulombic forces can also crystallize. However, due to the repulsive Coulombic interaction, the transition to a colloidal crystal can occur even at dilute volume fractions if the screening (Debye) length is sufficiently large relative to the colloid size [122, 123]. Polydispersity effects on crystallization structure and kinetics are difficult to quantify experimentally. Suspensions of polydisperse hard-spheres are predicted to crystrallize if the standard deviation of the size distribution is below a maximum of 10% [124]. It has been shown that as a suspension approaches this theoretical limit the crystallization kinetics retard dramatically [125]. However, for suspensions with hard-sphere-like interactions at volume fractions below the coexistence region, only string-like order has been observed [126]. This has been confirmed by Stokesian dynamics simulations looking at the triplet-distribution function [127]. In contrast to simulation results, there have been no experimental reports of close-packed layer ordering or string organization below the coexistence volume fraction for hard spheres. However, in the two-phase region layer ordering has been reported [126]. Most shear-induced ordering experiments have been conducted with nearly monodisperse suspensions (standard deviation in particle size <5% of the mean is typical). Such tight constraints on size distribution are consistent with end-use applications involving self-assembly. Earlier we noted that, at equilibrium, polydispersity dramatically affects the crystallization boundaries and kinetics. Brownian dynamics simulations suggest that polydispersity similarly inhibits the production of ordered phases in steady-shear flow [128].

In systems with short-repulsive forces even lower volume fractions for glassy transition than discussed above have been observed [24, 25]. For a system similar to the one used in this dissertation work [129] a yield stress was observed at $\phi = 0.46$, indicating a soft glassy state. Glassy states are characterized by the particles being effectively trapped in cages formed by their neighbors, the presence of yield stress, and thixotropic behavior.

The yield stress is associated with both a jamming process and the glass transition, where some researchers have argued that jamming and glass transitions are the same process, and have many analogies with jamming in granular materials. The thixotropic behavior can be thought of as a competition between "rejuvenated" and "aging" regimes. Shearing of the suspension allows the exploration of the full energy landscape of potential energy wells associated with the particle cages, while the aging results in kinetic processes with the particles gradually favoring occupancy of the deepest energy wells [130-133]. The transition to glassy states has been successfully described by defining τ_α and τ_β relaxation times, where the short-time (β) relaxation is a many-body process during which particles remain within a cage of nearest neighbors, while the long-time (α) relaxation corresponds to particles escaping their cages. As the glass transition is approached, the cages become tighter, and both τ_α and τ_β become longer [134].

Standard Mode Coupling Theory

Because of the inability of many rheology models to extend their results obtained at lower ϕ to the glass transition regime ($\phi \geq 0.58$), the standard Mode-Coupling

Theory (MCT) [134, 135] has recently been shown to predict near-quantitative explanation of numerous dynamic measurements at the glass transition in quiescent colloidal suspensions. This difference is due to the fact that at the approach to ϕ_g the only quantity that diverges is the structural relaxation time, while rheological models predict multiple quantities (pressure, stresses *etc.*) diverging. Fuchs *et al.* [134] have sought to extend this standard MCT to the case of steady shear while still retaining one of its largest appeals, that the only input is the static structure factor or equal-time density correlator S_q and that at t << 0 the system is governed by the Boltzmann distribution. Another important note is that most MCT approaches neglect Hydrodynamic Interactions (HI) due to the presence of an incompressible solvent surrounding the Brownian particles; the main justifications for this are that close to ϕ_g the HI mainly renormalize the time scale of local diffusive transport, while the structural relaxation time is a divergent multiple of this and therefore makes the HI unimportant. MCT also only applies to the low shear rates [134] because at high shear HI are very important, *i.e.* shear thickening.

For the work presented here, the bulk volume fraction (ϕ_b) is $\phi_b = 0.08$ & 0.22 and therefore the models above indicate that Newtonian rheology should exist. However there are two important factors that indicate that this rheological description is too simplistic. The first is the shear induced migration of colloidal particles due the particle pressure which has been shown experimentally [105, 136] and by modeling [46] to occur for colloidal suspensions, allowing substantially higher ϕ than the ϕ_b to occur in a system. In the microcapillary work presented in this thesis $\phi(r)$ as high as $2\phi_b$ have

been measured close to the center of the capillary, *i.e.* pushing it into the non-Newtonian regime. The second development is Stokesian dynamics simulations by Bergenhloltz *et al*. [137] indicating that the non-Newtonian rheology seen at high concentrations (shear thinning and shear thickening) is also present at dilute concentrations, although these effects are difficult to measure mechanically.

All the rheological changes discussed so far reflect the striking transitions in a suspensions' microstructure, which most commonly in the colloidal literature refers to the pair-distribution function $g(\boldsymbol{r})$. The probability of finding a pair of particles at a separation of $\boldsymbol{r}$, which can be written as [127]

$$P(\boldsymbol{r}|0) = ng(\boldsymbol{r}) \quad (3.58)$$

where n is the average number density. The coordinates of the reference particle (particle 1) are set at the origin of the coordinate system, and $\boldsymbol{r}$ is the vector from this particle to any other particle center (particle 2) in the suspension. Eqn. 3.58 can be extended to define higher order distribution functions, for example the triplet-distribution function can be written as [127]

$$P(\boldsymbol{r}, \boldsymbol{s}|0) = n^2 g(\boldsymbol{r}, \boldsymbol{s}) \quad (3.59)$$

where $\boldsymbol{s}$ is the vector from particle 1 to particle 3. The issue of flow-induced structure is omnipresent in any consideration of the rheology of colloidal suspensions.

Microstructure

In the absence of flow, a wide range of colloidal organizations can be encountered in a colloidal suspension depending on the relative values of Brownian, repulsive and

attractive forces [44, 138, 139]. When Brownian forces dominate and the volume fraction is below the fluid-solid threshold, the particles organize as in a disordered liquid whose equilibrium behavior can be predicted by thermodynamics theory and simulation [44]. If attractive interparticle forces dominate, then at low ϕ the colloids aggregate or gel into scale invariant, self-similar clusters with fractal structure [140], while at high ϕ these gels exhibit long-range heterogeneous void structure [141, 142]. Although still incomplete, understanding of the quiescent gelation transition has received considerable attention recently [143, 144].

The application of external forces (for example due to pressure driven flow) to a colloidal suspension causes many interesting yet not fully understood microstructural effects and these form a large motivation for the present work. Most types of suspensions display an anisotropic organization when subjected to shear flow [145]. These structural effects during flow are strongly affected by the delicate balance among interparticle forces, Brownian motion and hydrodynamic interactions. The resulting non-equilibrium microstructure is in turn a principle determinant of the suspension rheology [50], with gelation and phase boundaries dependent on the strength of flow. The microstructure rearranges to accommodate the applied hydrodynamic and colloidal forces. At sufficiently high ϕ the interactions between colloids are comparable to forces induced by the hydrodynamics, manifesting itself as shear thinning behavior. While under strong enough flow conditions, the hydrodynamic interactions dominate, leading to the dominance of lubrication forces at high enough shear. This causes the formation of flow induced density fluctuations, or hydroclusters, which manifest themselves

macroscopically as shear thickening behavior, and dominate the microstructure when $Pe_p \rightarrow \infty$. Hydrocluster formation induced by hydrodynamic interactions were first measured using light scattering dichroism [146, 147] and small angle neutron scattering [148]. More detailed information on the development of these hydroclusters was obtained from computer simulations [45, 52, 75, 84, 149]. In computer simulations of the shear-induced microstructure at high Pe_p, the incorporation of hydrodynamic interactions is crucial. Simulations without hydrodynamics (Brownian Dynamics (BD)) and with hydrodynamics (Stokesian Dynamics (SD)) for a hard-sphere suspensions at ϕ = 0.45 for Pe_p 0.1, 10 and 1000 [149] show that at Pe_p = 1000, with SD a distorted liquid-like structure exists, while for BD the particles arrange into strings along the flow direction. Thus BD can only predict shear thinning, but SD can predict both shear thinning and shear thickening. These simulations show that the particles are squeezed together until only a thin liquid layer separates them, causing large hydrodynamic lubrication forces in the contact zone between particles. However due to the extreme sensitivity of the lubrication forces on interparticle distance, the interparticle potential and particle roughness effects are areas where further study is necessary to understand their impact on microstructure development [150-152].

Distortion of the microstructure will occur when the reciprocal of the shear rate is smaller than the time for diffusion. The separation of these weak and strong flow regimes is at $Pe_p \sim 1$. At $Pe_p > 1$, a distortion of the liquid-like structure can be expected. At low Pe_p ($Pe_p << 1$), the microstructure is isotropic, where light scattering experiments reveal a ring-like (Debye-Scherrer) pattern [126]. As Pe_p increases the microstructure is

distorted, as the particles are pushed together along the compression axis of the flow field, while being further separated along the extensional axis. This means that the angular pair distribution function $g(\theta)$ has a preference for particles to occupy the compressional quadrant upstream from a test particle [153, 154], see figure 3.1. This asymmetry has been shown to become less pronounced using simulations of non-colloidal suspensions in simple shear flow as ϕ decreases from $\phi = 0.65 \rightarrow 0.40$ [155]. Gadala-Mari and Acrivos [156] were the first to provide experimental evidence that concentrated suspensions develop this anisotropic structure. An interesting note is that if the flow direction is reversed a temporary reversal of regions in figure 3.1 occurs until the microstructure has re-arranged to accommodate the new flow condition. This behavior is a large motivation for the use of oscillating flow to manipulate the colloidal suspension microstructure.

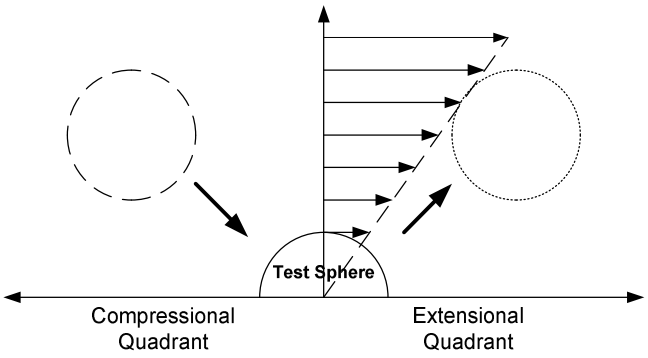

Figure 3.1 Diagram shows a sphere occupying the compressional and extensional quadrants relative to a test sphere. Anisotropy arises when particles preferentially occupy one rather than the other. When the flow direction is reversed, the quadrants reverse, and the spheres cannot instantaneously change quadrants. Therefore anomalous dynamics can be observed while the microstructure adapts to the imposed shear field. Reproduced from [16].

It is important to note that the shear deformation of the colloidal liquid structure is a smooth process with no long-range string or layer ordering [157] and the major

difficulty in colloidal transport is to account correctly for the hydrodynamic interactions. To correctly account for multibody hydrodynamic interactions, an important tool as mentioned above is the Stokesian Dynamics (SD) technique, which correctly accounts for hydrodynamic interaction of particles in close contact [52, 75, 158, 159].

Using this technique Bergenholtz *et al.* [160] showed that the non-Newtonian behavior and therefore anisotropic microstructure of the colloidal suspensions is present even at dilute ϕ. This is an important conceptual point, because NMR measurements do not measure boundary effects as classical rheometry does, but measures the particles as they transport through their environment. Therefore if microstructural anisotropy effects occur even at dilute ϕ it is not unexpected that this underlying anisotropy should contribute to the NMR experiment.

Since surface roughness is an important component in the formation of the asymmetry discussed above, it is necessary to address it. When two particles come within 10^{-2} to 10^{-3} radii, surface roughness can cause contact prohibiting the formation of closed orbits [161]. Analytical and experimental studies have examined the effects of surface roughness [162-164] showing that surface roughness causes the loss of fore and aft symmetry of the relative trajectory of two spheres, this can serve as the sole source of irreversibility and can decrease the viscosity of the suspension [150, 165].

Particle Pressure & Shear Induced Migration

Although less studied than the viscosity, it is accepted that colloidal suspensions exhibit normal stress differences. Normal stress measurements are very difficult in

practice; although finite stresses exist for colloidal suspensions, their magnitudes are small because rheometric measurements monitor fluid response due to the bulk stress which are on the order of instrument limitations [166-168]. Additionally, only the normal stress differences are reported in practice because of the inability to resolve the isotropic component of the normal stress due to the hydrostatic pressure.

The particle pressure (separate from the suspending fluid pressure) only develops due to the relative particle motions in viscous hydrodynamically dominated suspensions and it is the driving force for particle migration seen in non-colloidal and concentrated suspensions [46]. These particle fluctuations in a suspension due to shear induced interactions imply a suspension temperature $\langle u' \cdot u' \rangle_P$, which has previously been used to relate particle pressure to this fluctuation motion in the form

$$\Pi \sim \frac{\eta \sqrt{\langle u' \cdot u' \rangle_P}}{L} \quad (3.60)$$

where L is the relevant length scale for the system of interest [106, 169]. An important bulk fluid mechanical consequence of the normal stresses in colloidal systems is their role in driving secondary flows.

It has been known at least as far back as the 1950s [170] that flow-induced interactions cause a pressure to be exerted by the disperse phase. Flow models using particle pressure have been applied in suspensions [169, 171], with a primary motivation to examine particle migration phenomena. Additionally, experimental studies [136, 172, 173] have used the concept of particle pressure to describe observations in sheared Brownian suspensions. The bulk stress of a suspension is written as shown in Eqn. 3.49 in terms of the fluid and particle contributions. The bulk suspension pressure is

$$\langle P \rangle = -(1/3)\langle \Sigma_{ii} \rangle \quad (3.61).$$

For an incompressible suspension $\langle P \rangle = P_0$, *i.e.* the bulk suspension pressure is constant. The particle pressure (Π) and fluid pressure (Π^f) can be written as [46]

$$\Pi = -\frac{1}{3}\langle \Sigma_{ii}^{p} \rangle \quad (3.62a)$$

$$\Pi^{f} = -\frac{1}{3}\langle \Sigma_{ii}^{f} \rangle \quad (3.62b).$$

By using the subscripts (i = 1, 2, 3) to refer to the flow, velocity gradient and vorticity directions Eqn. 3.62a becomes:

$$\Pi = -(1/3)[\Sigma_{11}^{P} + \Sigma_{22}^{P} + \Sigma_{33}^{P}] \quad (3.63).$$

Note that for a cylindrical coordinate system (r, θ, z), *i.e.* to model flow in a capillary, the subscripts 1,2 and 3 refer to the z-, r- and θ-directions, see figure 3.2.

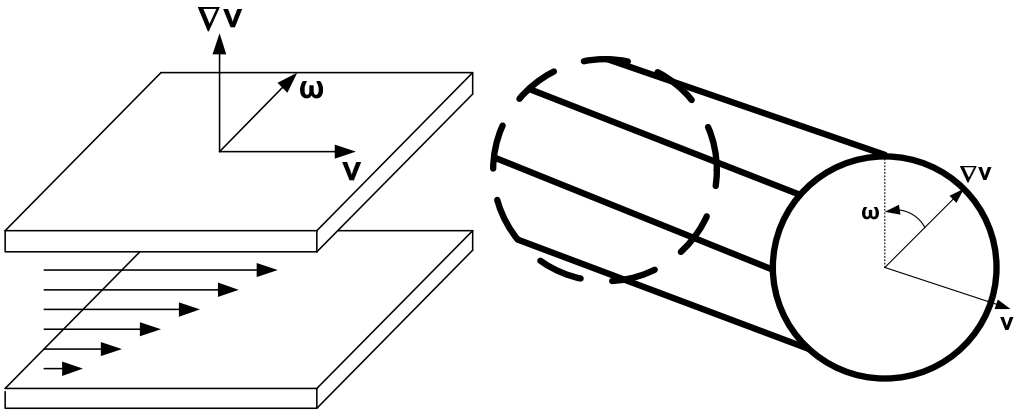

Figure 3.2 Diagrams showing the flow (**v**), gradient (**∇v**) and vorticity (***ω***) directions for a parallel plate geometry and a pipe geometry.

Using this notation the normal stress differences, which measure the structure of the system, are defined as [174]

$$N_1 = \langle \Sigma_{11} - \Sigma_{22} \rangle \quad (3.64a)$$

$$N_2 = \langle \Sigma_{22} - \Sigma_{33} \rangle \quad (3.64b).$$

For colloids suspended in a Newtonian fluid only the particle stress $\langle \Sigma^{P} \rangle$ contributes to N_1 and N_2, as a Newtonian fluid is unable to support anisotropic normal stresses. A useful dimensionless number when conducting rheology measurements on structured systems is the Weissenberg number (Wi), where Wi = $\frac{N_1}{\sigma}$ which defines the recoverability of strain [175].

The particle pressure (Π) can be related to osmotic pressure and it has been shown analytically that the particle pressure at $Pe_p = 0$ compares favorably with exact results for the equilibrium osmotic pressure [46, 80]. This relationship between particle and osmotic pressures has been pushed further to non-equilibrium conditions [46], where the varying particle pressure is the driving force for particle migration in shear flow. To this end the hydrodynamic functions developed by Jefferey *et al.* [176] have been used to relate particle pressure to particle motion, *i.e.* these functions relate the particle motions in a linear flow field to their isotropic stress contribution. The Brownian contribution is described in terms of these hydrodynamic functions, such that at $Pe_p = 0$ only the Brownian component contributes to the particle pressure. The microstructural anisotropy necessary for the development of particle pressure in a colloidal system results in the measured and simulated bulk suspension normal stress differences. The requirement for a nonzero hydrodynamic contribution to Π in a suspension flow introduces a microstructural anisotropy of a form that breaks fore-aft symmetry [174], see figure 3.1 for reference.

Modeling Shear Induced Migration

To constrain Brownian particles at any finite ϕ requires exerting a normal stress, which is the osmotic pressure

$$\boldsymbol{j}_n = -M\nabla\Pi \quad (3.65).$$

Here $\boldsymbol{j}_n$ is the number flux of the particles, the mobility (M) is the inverse of friction and is given by $M = (6\pi\eta a)^{-1}$ for an isolated sphere, but is generally dependent on ϕ and can be written as $\widetilde{M}(\phi) \sim(\phi \cdot M)$. In pressure driven flow in a pipe, particles not only diffuse but also experience shear-induced migration, which in contrast to Fickian diffusion generates a concentration gradient. It is the particle normal stresses that play the primary role in the cross-stream migration that results in variation of ϕ across a flow geometry [171]. The flux of particles at a finite concentration can be written as

$$\boldsymbol{j} = -\widetilde{M}(\phi)\left[\frac{\partial\Pi}{\partial\phi}\nabla\phi + \frac{\partial\Pi}{\partial\dot{\gamma}}\nabla\dot{\gamma}\right] \quad (3.66)$$

with the first term the Fickian diffusion term rewritten from Eqn. 3.65, while the second is the shear induced diffusion term derived by Leighton *et al.* [177], and where $\widetilde{M} = (4\pi a^2/3)M$, $\Pi = \Pi(\phi, \dot{\gamma}, kT)$. If $\dot{\gamma} \neq 0$, the relative motion of the two phases (colloids and suspending fluid) is induced by both the shear induced migration and Fickian diffusion. Eqn. 3.66 defines the flux of particles in a colloidal suspension as a function of $\dot{\gamma}$ and ϕ which allows for the modeling of shear-induced migration.

The model of Morris and co-workers [105, 171, 178] based on particle pressure analysis has been used to model the particle volume fraction as a function of radial position $\phi(r)$ in fully developed capillary flow [105, 136, 178]. A general description of the particle migration relative to the bulk flow is given by [105]

$$\frac{\partial \phi}{\partial t} + \langle \boldsymbol{U} \rangle \cdot \nabla \phi = -\frac{2a^2}{9\eta} \nabla \cdot \left[f(\phi) \nabla \cdot \Sigma^{\mathrm{P}} \right] \quad (3.67)$$

where $\langle \boldsymbol{U} \rangle$ is the ensemble-average velocity of the bulk suspension, a is the particle radius, η is the suspension viscosity, $f(\phi)$ is the hindered settling function, and Σ^{P} is the particle contribution to the bulk stress. Eqn. 3.67 can be used to determine the particle phase migration as a function of time and space for different geometries of interest. For fully developed particle migration under steady state conditions the LHS of (3.67) equals zero leading to

$$0 = -\frac{2a^2}{9\eta} \nabla \cdot \left[f(\phi) (\nabla \cdot \Sigma^{\mathrm{P}}) \right] \quad (3.68).$$

For axisymmetric capillary flow, Eqn. 3.68 can be written as [178]

$$0 = -\frac{2a^2}{9\eta} \frac{\partial}{\partial \mathrm{r}} \cdot \left[f(\phi) \left(\frac{\partial \Sigma^{\mathrm{P}}_{\mathrm{rr}}}{\partial \mathrm{r}} + \frac{\mathrm{N_r}}{\mathrm{r}} \right) \right] \quad (3.69)$$

where $N_r = \Sigma^{\mathrm{P}}_{\mathrm{rr}} - \Sigma^{\mathrm{P}}_{\theta\theta}$. Equation 3.69 simplifies to

$$\left[\frac{\partial \Sigma^{\mathrm{P}}_{\mathrm{rr}}}{\partial \mathrm{r}} + \frac{\mathrm{N_r}}{\mathrm{r}} \right] = 0 \quad (3.70).$$

Using $N_r \approx -0.3\eta_0 \eta_n(\phi) \dot{\gamma}(r)$ [171] in conjunction with the momentum equation for capillary flow [64], where η_0 is the suspending fluid viscosity, η_n is the normal stress viscosity, and $\eta_s = \eta/\eta_0$

$$0 = \frac{dP}{dz} + \eta_0 \eta_s \frac{1}{r} \frac{d}{dr} \left(r \frac{\partial U_z}{\partial r} \right) \quad (3.71)$$

Eqn. 3.70 is solved to obtain $\phi(r)$ for fully developed flow. At steady flow conditions the pressure gradient (dP/dz) is constant. By writing $\dot{\gamma} = \partial U_z/\partial r$, Eqn. 3.71 can be rewritten as

$$\dot{\gamma}(r) = \left[\frac{(\frac{dP}{dr})r}{2\eta_0\eta_s}\right] \quad (3.72)$$

where

$$\eta_0\eta_s = \eta_0\left[1 + \frac{2.5\phi}{(1-\phi/\phi_m)} + 0.1\frac{\phi^2}{(1-\phi/\phi_m)^2}\right] \quad (3.73)$$

is the suspension viscosity as used by Frank *et al.* [105].

Any correction addressing the model's cusping phenomena as done for small channels is not necessary since at low $Pe$the shear-induced particle pressure vanishes, but the Brownian contribution does not. Given that for our system (a/R)$\sim(1/100)$ [105] its effect would have been minimal except for a relatively small region at r $\sim$ 0. To solve Eqn. 3.70, the particle contribution to the bulk stress (Σ^P) is required, and we follow Frank *et al.* [105] using the expression

$$\frac{\Sigma^P_{rr}}{-kT/\frac{4}{3}\pi a^3} = a(\phi) + \frac{2Pe}{9\left[\frac{1}{b_r(\phi,Pe)}+\frac{1}{c_r(\phi)}\right]} \quad (3.74)$$

where

$$a(\phi) = \frac{3\phi}{(1-\phi/\phi_m)} \quad (3.75a)$$

$$b_r(\phi, Pe_{SES}) = \frac{A\lambda_r^B Pe_{SES}\phi}{(1-\phi/\phi_m)^3} \quad (3.75b)$$

$$c_r(\phi) = \lambda_r^H \eta_n(\phi) \quad (3.75c)$$

and $\phi_m = 0.68$ is the maximum packing volume fraction. The normal stress viscosity (η_n) suggested by Morris and Boulay [171] for non-Brownian suspensions is given by

$$\eta_n = \frac{0.75\left(\frac{\phi}{\phi_m}\right)^2}{(1-\phi/\phi_m)^2} \quad (3.76).$$

To obtain $\phi(r)$ Eqn. 3.72 and Eqn. 3.74 are solved simultaneously using a simple numerical solution scheme. The main fitting parameters are (A, λ_r^B, λ_r^H) of Eqn. 3.75. Parameter A determines the transition from the low to high Pe behavior and in this study A = 0.4 as reasoned by Frank *et al.* [105]. λ_r^B and λ_r^H allow for the modeling of normal stress differences predicted analytically and observed in simulation. These anisotropy factors respectively address the limits of a Brownian dominated suspension and a hydrodynamically dominated suspension. Again following Frank *et al.* [105] we use $\lambda_r^B = 1.8$ and $\lambda_r^H = 0.75$ based on the work of Phung *et al.* [79]. By fixing these three parameters the comparison of the model to the data is fully determined by Pe and the bulk volume fraction ϕ, where the parameters iterated are $\phi(0) = \phi_0$ and dP/dz. To solve for $\phi(r)$ numerically, Eqn. 3.70 is rewritten as

$$\frac{\Sigma_{rr}^P(\phi_i, r_i) - \Sigma_{rr}^P(\phi_{i-1}, r_{i-1})}{r_i - r_{i-1}} - \frac{0.3\eta_0\eta_n(\phi_i)\dot{\gamma}(\phi_i, r_i)}{r_i} = 0 \quad (3.77)$$

and is solved by using the robust bisection method [179] to obtain ϕ_i for $r_i = ih$, where i = [1,2,…,N]. N is the number of iteration steps and therefore defines the resolution of the fit to h = R/N, where the radius of the capillary R = 126μm. This iteration process has

been used previously [136] for flow of colloidal suspensions $\phi = 0.04, 0.08, 0.22$ & 0.43 at *Pe* = 42 and fit the data reasonably well considering that this flow was not fully developed (L/R ~ 60) for the lower concentrations ($\phi = 0.04$ & 0.08). This iteration process is used to fit $\phi(r)$ vs. r data for the microcapillary data presented in this work. An important note on colloidal suspensions is that unlike non-colloidal suspensions where the entrance length is only dependent on ϕ, the entrance length for colloidal suspensions is dependent on both $\dot{\gamma}$ and ϕ. This entrance length dependence has been investigated by Semwogerere *et al.* [105] and those results are used to determine whether the entrance length for the systems investigated in this thesis are fully developed or not.

Preparation of Model Colloidal Suspensions

The core-shell latex colloidal particles used in the work presented in this thesis were constructed using the method of Loxley and Vincent [180]. Hexadecane, poly-methylmethacrylate (PMMA MW 350,000) and poly (vinyl alcohol) (PVA) MW 95000, 95% hydrolyzed were purchased from Fisher Scientific. Dichloromethane and acetone of analytical quality were used, as was de-ionized (DI) water. An oil phase containing 3.0g of PMMA, 60mL of dichloromethane, 3.8mL of acetone and 5mL of hexadecane was prepared. The oil phase was added drop-wise to 80mL of 2% PVA solution. A Heidolph Silent Crusher M homogenizer was used to stir the mixture at a high-shear rate, creating an oil-in-water emulsion. By stirring at 12,000 rpm for 1hr the desired 2.5μm diameter particles were produced. The emulsion was then added to 120mL of 2%PVA and gently stirred overnight in a fumehood to allow all the volatile solvent to evaporate. As the

dichloromethane evaporates the polymer-rich phase migrates to the oil/water interface, and as all of it evaporates a hard-shell of PMMA is formed separating the oil (Hexadecane) from the water phase. The PVA molecules in the water-phase adhere to the surface of the spheres creating a short range repulsive charge, exhibiting hard-sphere like behavior [48]. In practice each batch created has a volume-fraction $\phi = 0.04$ and an average particle diameter of $d = 2.49 \pm 0.93\mu m$; the particle distribution can be seen in figure 3.3 and was obtained by light microscopy, using frame capture at 42 frames per sample slide. An in-house edge detection type algorithm using MATLAB® was used to analyze each image to obtain particle diameters. Field-emission microscopy images were also obtained and corroborated the sizes obtained by using the light microscopy method. Samples were selected randomly from different locations within a suspension sample to represent as random a sampling as possible.

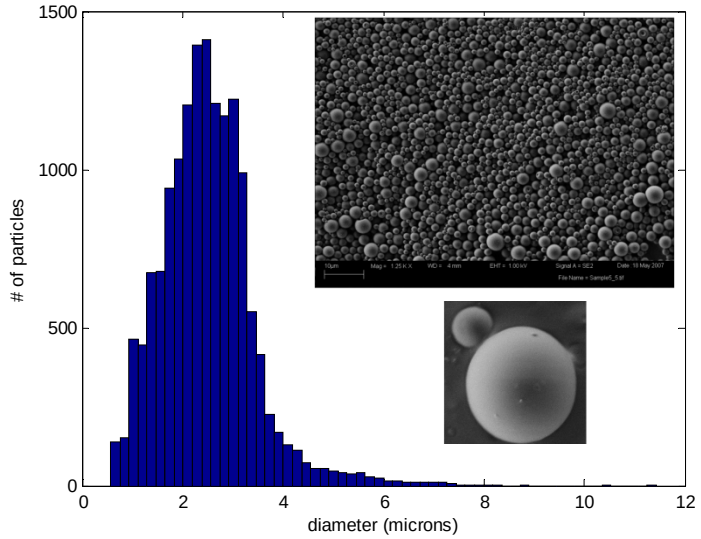

Figure 3.3 Clockwise, starting in upper left corner. A particle size distribution of colloidal suspension obtained using light microscopy. A Field Emission Microscopy (FEM) image of two neighboring particles. FEM image of a collection of particles.

To remove any air bubbles in the colloidal suspensions, it is important to degas the suspension under vacuum overnight before they are to be used; in practice the colloidal suspensions were degassed before and after any centrifugation.

To obtain the different volume fractions ($\phi = 0.08$ & 0.22) used in this work batches were combined and centrifuged using a Sorvall RC 5C high speed centrifuge at 8000 rpm and 15,000 rpm for 10 minutes each. This second higher centrifugation rate was used to obtain any particles left behind after the initial transfer of particle from the centrifugation tubes. Since the colloidal particles have a slightly lower density than the suspending fluid, the lower dilute phase can be removed and the remaining concentrated upper particle phase re-suspended, producing the desired volume fraction. Volume fractions were calculated based on the known input of materials in the construction of the particles, the volume of liquid removed after centrifugation, and the volume of liquid added to re-suspend. By using a hematocrit centrifuge (IEC MB Centrifuge, Damon/IEC Division) it was possible to measure the concentration of the suspension at any point in time, both right after preparation and after different experimental runs. This method was to fill a 1mm diameter capillary, seal the bottom and measure the height of the fluid. Then multiple capillaries (10) were subjected to high centrifugal forces over a period of 30 minutes and the resulting height of the packed particle layer was measured. This allowed the calculation of a volume fraction by dividing the final colloid height with the initial colloidal suspension height, while taking into account a maximum fraction of 0.68. This allows for a simple and convenient way of observing changes in the colloidal

suspension volume fraction during experimental runs, as the effluent samples can be tested while experiments are occurring.

Since the chemical shift between the oil and water peaks of the colloidal suspension is ~ 3.5 ppm, and there is significant overlap between the water and oil peaks, it was necessary to dope the samples with a paramagnetic T_1 reducing agent, Magnevist (Berlex Laboratories), which was added at a concentration of 11.7μL per mL of suspension. Since the oil is encased inside a hard-sphere, the enhanced relaxation only occurs to the suspending fluid (water peak). This explains why in some long time ($\Delta >$ 250ms) transport experiments only the oil (colloid) peak is available since by this time the water (suspending fluid) signal has relaxed.

The colloidal particles as mentioned above have a slightly lower density than the suspending fluid and therefore the suspensions cream slowly, on the order of days. This required that the suspensions be agitated constantly when not flowing. This was done by using a magnetic stirrer for any suspension not being experimented on. Care was taken to make sure that flow geometries (including any tubing into or out of the magnet) were small enough that during an experiment their transit time through the flow system and agitation while in the system was sufficient. This was an important design criteria for all the experimental setups used. Since the experimental observation times (on the order of ms) and overall experimental times were short relative to the time of creaming and because of the setup design, creaming had no impact on the experimental results presented here.

Rheology Background and Measurements

Rheology is the study of the flow and deformation of matter and there are multiple references available for further information on this research field [1-3]. The applications of rheology are immense, including in geology and mining, concrete technology, solid mechanic, plastics industry, tribology (study of lubrication) and the food industry. Information about the rheology of materials is used to design/select equipment such as pumps, pipelines, extruders, mixers and heat exchangers. It is also used to obtain information about atomic and molecular scale phenomena and obtain constitutive relations. There are two extremes of material flow, Newtonian fluids and elastic solids, and many materials have the characteristics of both. For an elastic spring two characteristic properties are the stress (σ) or the force over area (F/A), and the strain (γ) or the increase in length over the original length (δL/L). An additional important quantity is the shear rate ($\dot{\gamma}$) or the rate of change in strain over the change in time ($d\gamma/dt$). The viscosity of a material (η) is simply the stress over the shear rate ($\eta = \tau/\dot{\gamma}$), therefore most rheometrical devices are designed to apply a controlled stress to a material and measure the strain or vice-versa. Typical viscosities of fluids tested by rheometers can range over many orders of magnitude (for example acetic acid $\eta = 10^{-5} Pa \cdot s$ to asphalt binder $\eta = 10^{5} Pa \cdot s$). The different types of fluid behavior include Casson plastic, Bingham plastic, pseudoplastic (or shear thinning), Newtonian and dilatant (or shear thickening), shown in figure 3.4. A simple phenomenological model for these fluids is the Herschel-Bulkley model

$$\sigma = K\dot{\gamma}^{n} + \sigma_0 \quad (3.78)$$

here K (the consistency index) is similar to viscosity (η), n is the power law constant and σ_0 is the yield stress. For shear thinning ($0 < n < 1$), Newtonian ($n = 1$) and shear thickening fluids ($n > 1$) $\sigma_0 = 0$, while for Casson plastic ($\sigma_0 > 0$ and $0 < n < 1$) and Bingham plastic fluids ($\sigma_0 > 0$ and $n = 1$) there is a finite yield stress. It is important to note that when the applied stress is less than the yield stress the material will not flow and behaves as a solid (*e.g.* butter). Shear thinning is an important property of high concentration colloidal suspensions ($\phi > 0.37$ [105]) and is due to anisotropic particle alignment with the flow streamlines, a similar property that occurs in many polymeric fluids.

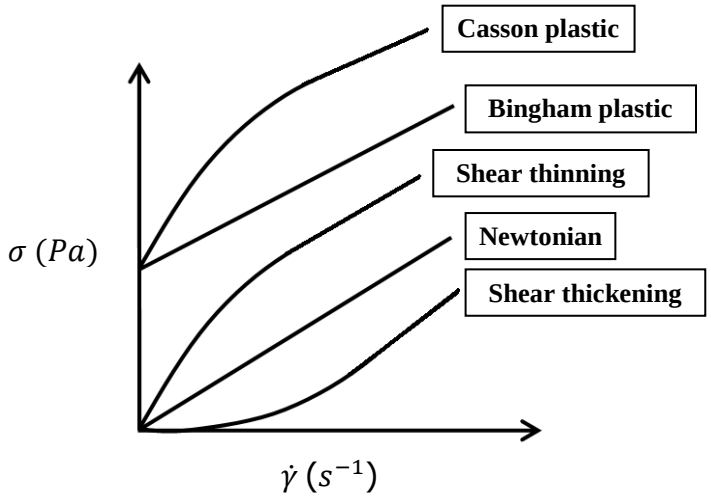

Figure 3.4 The Viscosity behavior of different fluids on a shear stress ($\boldsymbol{\sigma}$) vs. shear rate ($\dot{\boldsymbol{\gamma}}$) plot.

Another important rheological behavior is viscoelasticity, which is present in all materials to some extent, and is the combination of viscous and elastic behavior. Elasticity deals with the mechanical properties of elastic solids (Hooke's law) where E = σ/γ or the stress divided by the strain on the material. From the theory of hydrodynamics, Newton's law states that the viscosity is equal to the stress over the shear rate. The

stress-strain relationship is more complex than that explained by the simple models using Hooke's law or Newton's law. Elastic materials store energy while viscous materials dissipate energy, viscoelastic materials both store and dissipate a portion of the energy. Viscoelastic experiments can be broken down into static tests (such as a stress relaxation test (Maxwell model) or creep test (Kelvin-Voigt model)) and dynamic tests (controlled strain and controlled stress). To understand viscoelastic measurements it is necessary to introduce the phase angle (δ) which is the angle between the stress (σ) and the strain (γ), which for a Hookean elastic solid $\delta = 0$, while for a viscous liquid $\delta = 90^o$ and for Viscoelastic materials $0 < \delta < 90^o$; this allows for the definition of a storage modulus $G'(\omega) = \sigma_0 \cos(\delta)/\gamma_0$, a loss modulus $G''(\omega) = \sigma_0 \sin(\delta)/\gamma_0$ and a loss tangent $\tan(\delta) = G''(\omega)/G'(\omega)$. In a dynamic experiment the stress is referred to as the complex stress σ^*, which can be separated into two components, $\sigma^* = \sigma' + i\,\sigma''$, where σ' is the elastic stress and σ'' is the viscous stress, these stresses can be calculated once the complex stress and the phase angle have been measured because $\sigma' = \sigma^* cos(\delta)$ and $\sigma'' = \sigma^* sin(\delta)$. In a similar fashion the complex modulus, the overall material resistance to deformation, can be written as a combination of the elastic or storage modulus and the viscous or loss modulus; *i.e.* $G^* = G' + iG''$, where $G' = G^* cos(\delta)$ and $G'' = G^* sin(\delta)$. It is important to also note that the $tan(\delta) = G''/G'$ is a measure of the damping ability of the material. Additionally it is important to note that the viscosity measured in an oscillatory experiment is the complex viscosity, which contains an elastic component and a term similar to the steady state viscosity and is defined as $\eta^* = \eta' - i\,\eta'' = G^*/\omega$. It is critical in any rheometry experiment to understand how

the system behaves not only as a function of the stress or strain applied but also to understand its time-dependent behavior. This makes rheometry experiments of complex materials such as colloidal fluids very complicated. The same series of experiments on the same material at different times can generate different results and emphasizes the importance of initial conditions in the measurements.

The colloidal suspensions used in the flow studies presented in later chapters were investigated using a AR-G2 rheometer. The results of steady state flow experiments using a 60mm diameter parallel plate setup with a 1mm gap and fluid trap at a temperature of 20^{o}C is shown in figure 3.5. The scheme for these experiments was as follows: pre-shear the sample for 2 minutes at $10s^{-1}$, perform steady state flow experiments from high to low shear ($600 – 0.001\ s^{-1}$) and then low to high shear $0.001s^{-1}$-$600s^{-1}$; to test for "thixotropy", *i.e.* a time-dependent change in viscosity. Then perform peak hold experiments at fixed shear rates of 0.0001, 0.001, 0.01, 0.1, 1.0, 10, 100 s^{-1} for two minutes each and repeat the steady state flow experiments. The peak-hold experiments showed no evidence of "thixotropy", but confirmed the effects shown in figure 3.5, where a dramatic growth in error occurred for $\sigma < 0.5\ Pa$, indicating rheological instrument sensitivity limitations due to environmental effects, *i.e.* building vibrations, air flow disturbances *etc*.

The choice of using the parallel plate rather than the cone-and-plate setup (the latter produces a homogeneous shear field across the sample and therefore is in theory better if the colloids migrate to regions of low shear) is because in practice the cone-and-plate setup has a truncation at its end, where particles tend to accumulate and distort

experiments. The reason for using a 1 mm gap is because of heuristics; although a smaller gap would still allow for the approximation of a continuum (*i.e.* gap size >> colloidal particle diameter) it is recommended for parallel plates not to use a gap less than 1/100 the plate diameter due to possible imperfections in the alignment of the two flat surfaces of the parallel plates. Tests on glycerol confirmed these effects, with a 1mm gap producing good results. To appreciate how the viscosity is measured the following equation is presented, for a parallel plate setup: $\eta(t) = \frac{M(t)}{2\pi R^3 \dot{\gamma}}\left(3 + \frac{dlnM(t)}{dln\dot{\gamma}}\right)$, where $M(t)$ is the torque. Since normal stress differences are of significant importance to understanding the shear induced migration of colloidal particles, it is informative to see how these may be measured by the cone-and-plate and parallel-plate geometries respectively [181]

$$N_{11}(t) = \frac{2F_z(t)}{\pi}(R_o^2 - R_i^2) \quad (3.79)$$

$$N_{11}(t) - N_{22}(t) = \frac{F_z(t)}{\pi R^2 \dot{\gamma}}\left(2 + \frac{dln(F_z(t))}{dln\dot{\gamma}}\right) \quad (3.80)$$

where $F_z(t)$ are the normal force measured. These equations show that the first normal stress difference can be directly measured using a cone-and-plate geometry, but as noted above the magnitude of these stresses is of the order of the instrument sensitivity and are made difficult due to the inability of Newtonian fluids to support normal stress differences. This generated no amplitude for the normal forces measured in the experiments shown in figure 3.5.

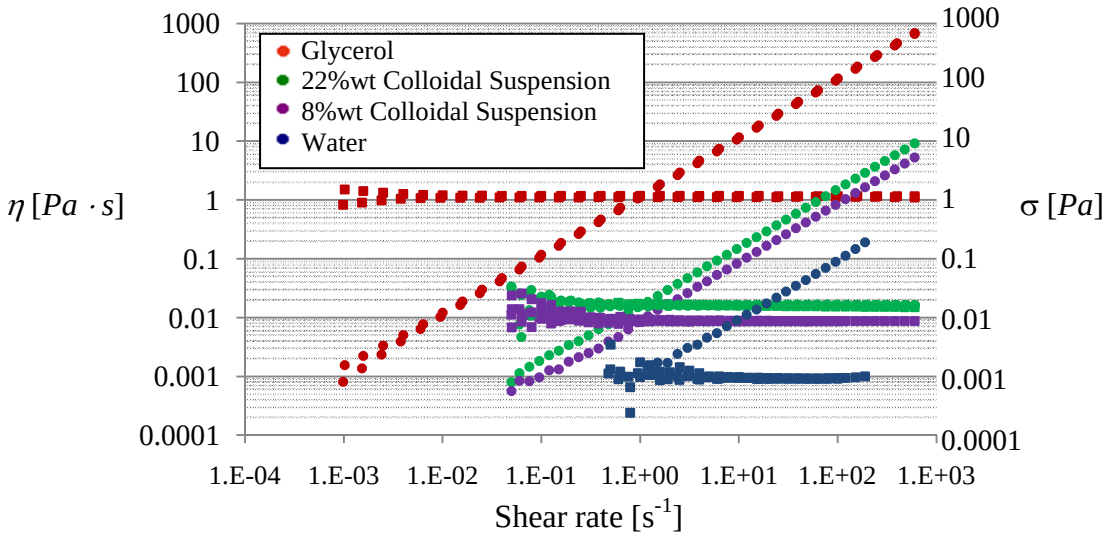

Figure 3.5 Viscosity ($Pa \cdot s$) and shear stress (Pa) plotted against the shear rate (s^{-1}) for glycerol, water, 8% and 22%wt hard-sphere colloidal suspension. Below a shear stress of ~0.5 Pa spreading occurs for all fluids tested indicating the lower limit of sensitivity of this rheological setup. Above this value all fluids behave approximately Newtonian (*i.e.* constant viscosity as a function of shear rate).

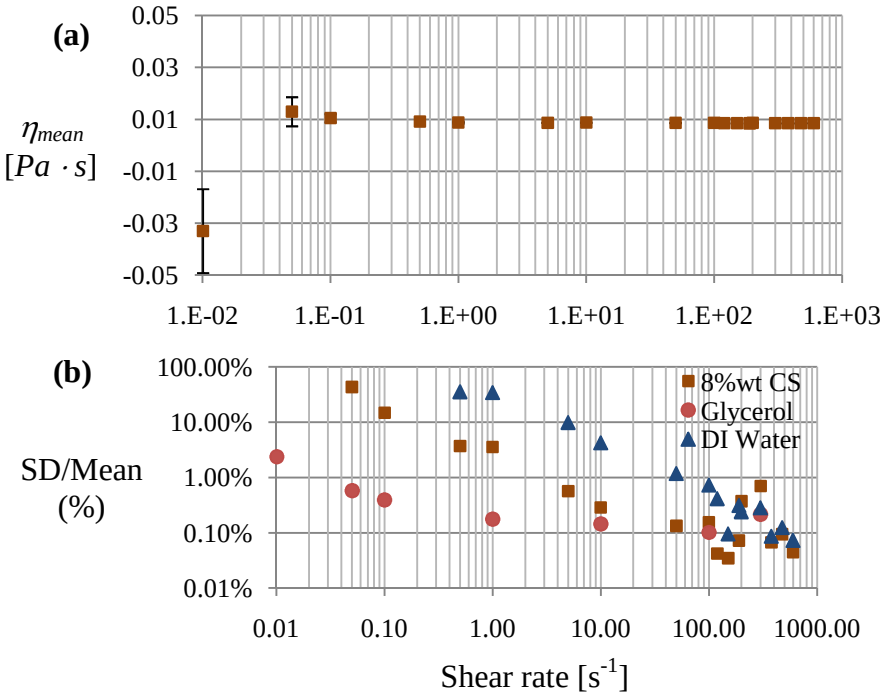

Figure 3.6 Peak hold experiments. (a) Shows the mean viscosity, η_{mean}, for each peak hold experiment for a 8%wt colloidal suspension. The error bars represent the spread of the data. (b) Shows the standard deviation divided by the mean for the viscosity. The change from a random distribution to linear one, at shear rate < $100s^{-1}$ corresponds favorably with the experimental error of the instrument, with ~10% SD/Mean representing the instrument limitation. It is obvious that the higher the viscosity of the fluid the larger the shear rate/shear stress range that can be investigated.

COLLOIDAL TRANSPORT IN A MICROCAPILLARY

Introduction

The fluid dynamics of colloidal suspensions are important in a myriad of industrial and environmental processes and have therefore received much attention in the scientific literature [45, 50]. The simplest colloidal suspension to understand is that of monodisperse hard spheres where the particles interact through hydrodynamic and Brownian forces. These suspensions can be fully characterized by the particle Péclet number (Pe_p) and the particle volume fraction (ϕ) [45]. Detailed experimental, analytical and simulation studies have been conducted to investigate the behavior of hard sphere colloidal suspensions over the full range of volume fraction (ϕ), from dilute to close packed, and for Pe_p numbers encompassing the rheological behavior from weak flow conditions ($Pe_p \sim 1$) to strong flow conditions ($Pe_p >> 1$) [75, 137]. This study will focus on the flow dynamics at the strong flow condition ($Pe_p >> 1$) for a $\phi = 0.22$ hard sphere suspension. Pe_p and ϕ are defined as:

$$Pe_p = \frac{\langle \dot{\gamma} \rangle a^2}{D_{SES}} \quad (4.1)$$

$$\phi = \frac{4\pi a^3 n}{3} \quad (4.2)$$

the standard Stokes-Einstein-Sutherland D_{SES} form of the colloidal diffusivity is used, η_0 is the viscosity of the suspending fluid, a is the mean radius of the colloidal spheres, k_B is the Boltzmann constant, T is the temperature. The averaged shear rate $\langle \dot{\gamma} \rangle$ is used to define the velocity $a\langle \dot{\gamma} \rangle$ and n is the number density. To obtain the averaged shear rate

the following equation is used, $\langle\dot{\gamma}\rangle = \frac{4}{3}\pi v_{max} R$, where v_{max} is the maximum velocity in the capillary and R is the radius of the microcapillary.

Additional dimensionless numbers used to characterize the flow are the tube Péclet number (Pe_t), particle *Reynolds* number (Re_p) and the tube *Reynolds* number (Re_t)

$$Pe_t = \frac{2R\langle v\rangle}{D_w};\ Re_p = \frac{a^2\langle\dot{\gamma}\rangle\rho}{\eta_0};\ Re_t = \frac{2R\langle v\rangle\rho}{\eta_0} \quad (4.3)$$

where $\langle v\rangle$ is the average velocity in the capillary, D_w is the diffusion coefficient of water and ρ is the density of the fluid in the capillary.

In this study NMR transport measurements were conducted on a stationary system (Q = 0.000mL/hr) as well as for the same system at three different volumetric flow rates Q = 0.125, 0.250 and 0.500mL/hr. These flow rates correspond to the following flow conditions (Table 4.1)

Table 4.1

Q: 0.125mL/hr, Pe_p: 135, Pe_t: 80, Re_p: 2.3×10^{-5}, Re_t: 0.18
Q: 0.250mL/hr, Pe_p: 270, Pe_t: 160, Re_p: 4.6×10^{-5}, Re_t: 0.35
Q: 0.500mL/hr, Pe_p: 540, Pe_t: 321, Re_p: 9.3×10^{-5}, Re_t: 0.70

As can be seen in Table 4.1, all the flow conditions can be characterized as strong flow ($Pe >> 1$) and that inertial forces are small compared with viscous forces ($Re < 1$). This allows for a reasonable approximation of the flow as being governed by Stokesian dynamics[52] ($Re << 1$), particularly at the particle scale.

Materials and Methods

The colloidal suspensions used in this study were prepared and characterized as explained in chapter 3 and are characterized by $\phi = 0.22$ and $a = 1.25\mu$m, where $D_{SES} = 1.73\times10^{-13}$m^2/s. The experimental setup (figure 4.1) consists of a syringe pump (22 Harvard Science®) with a 5mL syringe (BD Medical®) pumping the fluid through 2m of a 1mm diameter PTFE tubing (GE Healthcare®). This was connected to a 50 cm long 252μm I.D. capillary (Polymicro®) by epoxy. The microcapillary then opened into another piece of PTFE tubing (2.5m of 1mm diameter), which was fixed to it by epoxy. To stabilize the microcapillary inside the rf coil it was threaded through a 1mm ID glass capillary and a 5mm ID NMR tube sealed at each end by flexible silicone tubing allowing a rigid structure. At the outlet of this flow setup was a gradiated cylinder to collect the effluent, the concentration of the effluent could then by tested in a centrifuge to measure when a steady state had been reached.

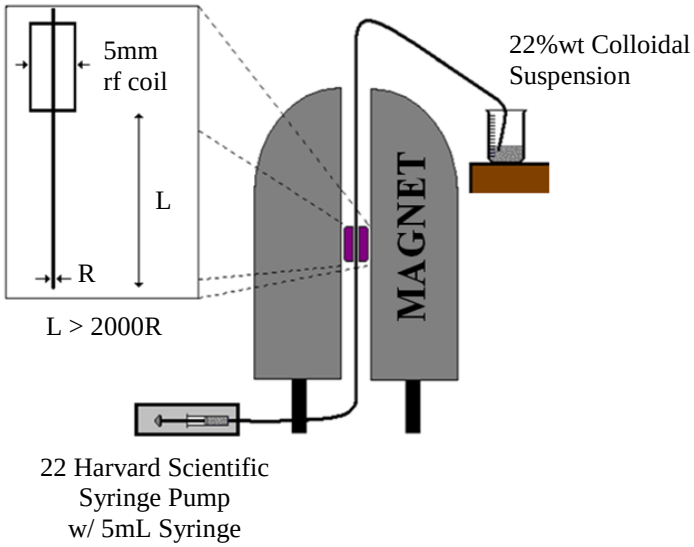

Figure 4.1 A schematic of the experimental setup for the microcapillary experiment.

The NMR experiments were conducted using a Bruker 250MHz superconducting magnet, using a Mirco5 probe base and depending on experiment using a Micro5 ($\mathbf{g}_{max}$: 1.7T/m in three orthogonal (X,Y,Z) gradient directions) or a Diff30($\mathbf{g}_{max}$: 11.3T/m, unidirectional (Z) gradient direction) gradient coils. The flow setup is placed inside a 5mm rf coil at a distance > 2000 × R from the beginning of the microcapillary section of the flow setup. This is to make sure that all dynamical experiments are conducted on the steady state regime of colloidal migration due to shear induced migration [173]. To study the fluid dynamics of the colloidal suspension inside the capillary, spectrally resolved Pulsed Gradient Spin Echo (PGSE) Nuclear Magnetic Resonance (NMR) techniques [1] are used. These allow for the simultaneous investigation of the dynamics of both the colloid and suspending fluid phases of the hard-sphere colloidal suspensions. The dynamics are measured for a stationary colloidal suspension and at the strong flow conditions (Q = 0.125mL/hr, 0.250mL/hr and 0.500mL/hr) inside the capillary (R = 126μm) for experimental times (Δ) from 25ms to 700ms. The NMR pulse sequences used in the study of the microcapillary are seen in figure 4.2. An important step before dynamic experiments on the colloidal suspensions was the use of NMR imaging experiments to verify the orientation of the capillary inside the rf coil as well as experiments on DI water flow through the capillary using the same NMR pulse sequences used.

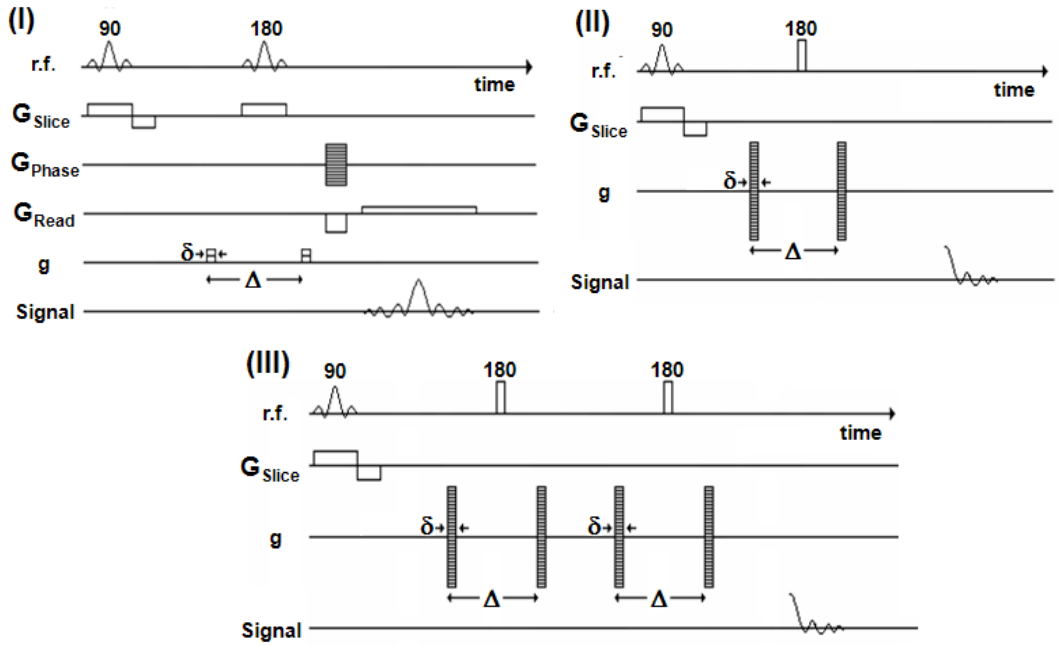

Figure 4.2 Shows the NMR timing sequences for (I) velocity map, (II) PGSE and (III) velocity compensated PGSE pulse sequences.

Results

To characterize the velocity flow through the microcapillary velocity maps were obtained for the flow of DI water and a 22%wt colloidal suspension at a flow rate Q = 0.250mL/hr and Q = 0.500mL/hr, see figure 4.3. These velocity maps are averaged over a 10mm slice and have in-plane resolution of 11.7×11.7 μm^2. As can be seen a truncation occurs in one of the directions for some of the velocity maps (4.3a,c,d); this is the phase direction. To characterize the rheology, velocity profiles were extracted from the read direction (see chapter 2) of the velocity maps and fitted with a power law model [182],

$$v_z(r) = v_{z,max}\left[1 - (r/R)^{\left(\frac{1}{n}\right)+1}\right] \quad (4.4)$$

where n is the power law exponent. For a shear thinning fluid $n < 1$, for a Newtonian fluid $n = 1$ and a shear thickening fluid $n > 1$.

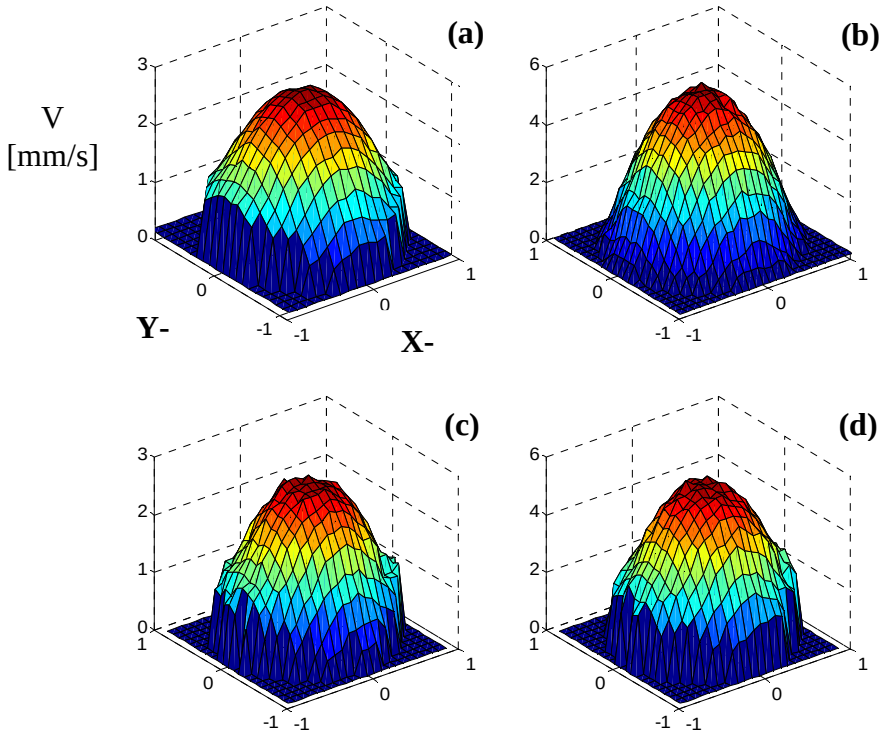

Figure 4.3 Velocity maps for (a) DI water at 0.25mL/hr, (b) DI water at 0.50mL/hr, (c) 22%wt colloidal suspension at 0.25mL/hr, (d) 22%wt colloidal dispersion at 0.50mL/hr. The phase direction is X-direction, read direction is the Y-direction.

The fits were obtained using a least square fit of the difference between the data points and the model. The velocity profile for DI water is best fit with $n = 1$, confirming the Newtonian rheology and verifying the experimental method, while the 22%wt colloidal suspension was best fit with $n = 0.71$ (Q = 0.25mL/hr) and $n = 0.85$ (Q = 0.50mL/hr), indicating a non-Newtonian shear thinning rheology. At first glance this seems to contradict the results from characterizing the colloidal suspension using a parallel plate setup with an AR-G2 rheometer (see chapter 3), which indicated an approximate Newtonian rheology for $\dot{\gamma} > 0.5s^{-1}$, where for $\dot{\gamma} < 0.5s^{-1}$ instrumental

limitations did not allow any conclusive statement about the rheology. A more phenomenological rheological model for fitting the velocity profile of colloidal suspensions is the Carreau equation [182],

$$\eta = \eta_\infty + (\eta_0 - \eta_\infty)[1 + (\lambda\dot{\gamma})^2]^{\frac{n-1}{2}} \quad (4.5)$$

where η_∞ is the infinite-shear-viscosity, η_0 is the zero-shear-viscosity, λ is a material property defining the onset of shear thinning. This model allows for a Newtonian plateau at high and low shear rates, separated by a transition, which captures the shear thinning behavior of colloidal suspensions. The measured shear range (figure 4.4) based on the colloidal suspension velocity profiles obtained using $\dot{\gamma} = \frac{\Delta V_z(r)}{\Delta r}$ is always higher than $\dot{\gamma} > 0.5s^{-1}$ due to experimental factors, which corresponds to approximately Newtonian Rheology for the 22%wt colloidal suspension; however as shown by Bergenholtz *et al.* [137] the non-Newtonian aspects of colloidal suspension rheology are ever present although rheological measurements due to experimental resolution and error do not capture them. The deviation from Newtonian behavior in the microcapillary is due to shear induced migration due to normal stress differences [46, 136, 173], an effect which is difficult if not impossible to measure in low concentration suspensions using traditional rheology techniques because the magnitude of these stresses is on the order of instrument limitation [46]. The maximal velocities of the colloidal suspensions relative to those of DI water are respectively 0.87 and 0.96 for Q = 0.25mL/hr and 0.50mL/hr. With the same volumetric flows through the capillaries at each flow rate and assuming a power law model fit, then the appropriate power law constant using Eqn. 4.4 are n = 0.59 and 0.85 for the colloidal suspensions at Q = 0.25 and 0.50mL/hr respectively.

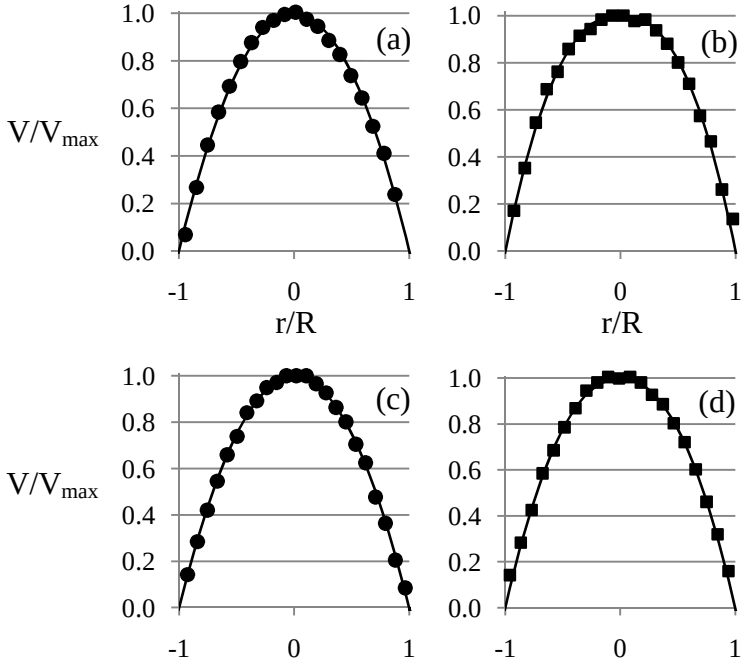

Figure 4.4 Normalized velocity profiles obtained from velocity maps and fit with power law model with power law constant n, (a) DI water at 0.25mL/hr, n: 1.00 (b) colloidal suspension at 0.25mL/hr, n: 0.71 (c) DI water at 0.50mL/hr, n: 1.00 (d) colloidal suspension at 0.50mL/hr, n: 0.85.

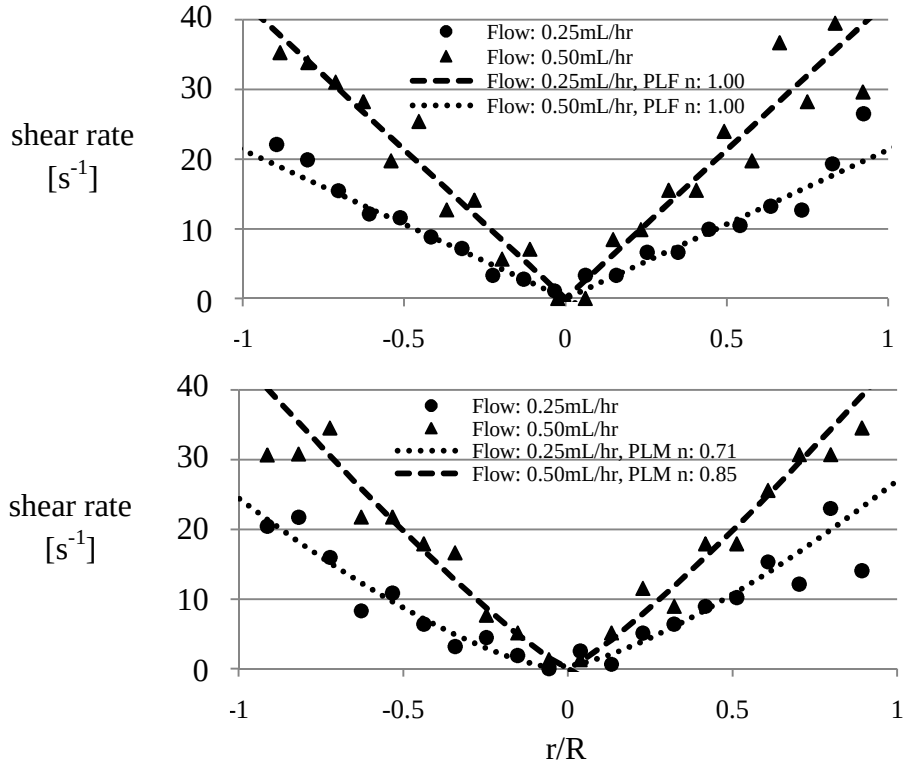

Figure 4.5 Measured shear rates from the velocity profiles obtained from the velocity maps, (top) DI water and (bottom) 22%wt colloidal suspension, all fitted with power law models (n: power law constant).

These results indicate that for Q = 0.50mL/hr the rheology of the colloidal suspension is captured by the shear thinning power law model while for Q = 0.25mL/hr a less good fit is found. This may be indicative of different microstructural regimes whose steady state is shear dependent.

The microcapillary fluid transport was characterized by using DI Water. A time series of propagators was obtained showing the effects of Taylor dispersion on the probability distribution (see figure 4.7); this series shows the initial progression towards a Gaussian probability distribution as well as wall effect causing a higher probability of finding water molecules at small displacements. This effects has previously been studied using PGSE NMR [58]. Using Taylor dispersion the dispersion coefficients (D^*) the short time and long time limits are characterized by the following equations [58]

(Pre-asymptotic regime) $t \ll R^2/D_0; \quad D^* = D_0 + \frac{1}{6}\langle U\rangle^2 t + \frac{4}{3}\frac{D_0\langle U\rangle^2}{R^2 t^2} + \cdots$ (4.6a)

(Asymptotic regime) $t \gg R^2/D_0; \quad D^* = D_0 + \frac{\langle U\rangle^2 R^2}{48 D_0}$ (4.6b)

For DI water R^2/D_0 = 7.2s and for the colloidal suspension R^2/D_{SES} = 23.1hrs, while the longest experimental time used is Δ = 0.7s, therefore the systems being studied are in the pre-asymptotic regime. Figure 4.6 shows results from PGSE and Velocity compensated PGSE (or VPGSE) experiments to obtain the dispersion coefficient for DI water flowing at Q = 0.25mL/hr and 0.50mL/hr in a parallel (Z) and perpendicular (X) direction to the axial flow direction (Z). Figure 4.6. shows that for times Δ < 0.5s the dispersion is in the pre-asymptotic regime and is modeled reasonably well using Eqn. 4.6a,b although the quantitative values at the longer Δ ≥ 100ms is consistently high.

Figure 4.7 shows a series of propagators obtained for Q: 0.25mL/hr at Δ = 25, 50, 150, 250 & 500ms in the axial-to-flow (Z) direction. These propagators indicate a narrowing in the distribution of displacement with time. The initial propagator (Δ = 25ms) has the shape of a Heaviside hat function convoluted with a Gaussian function, corresponding to Poiseuille flow with diffusion. As time evolves a higher probability appears at the lower displacement (close to the wall) which is due to the restriction of the wall. At the final time (Δ = 500ms) the propagator is still evolving towards a Gaussian distribution, which is beyond the experimental times in this experiment (R^2/D_0 = 7.2s), but has been seen in experiments similar to these using PGSE NMR [58].

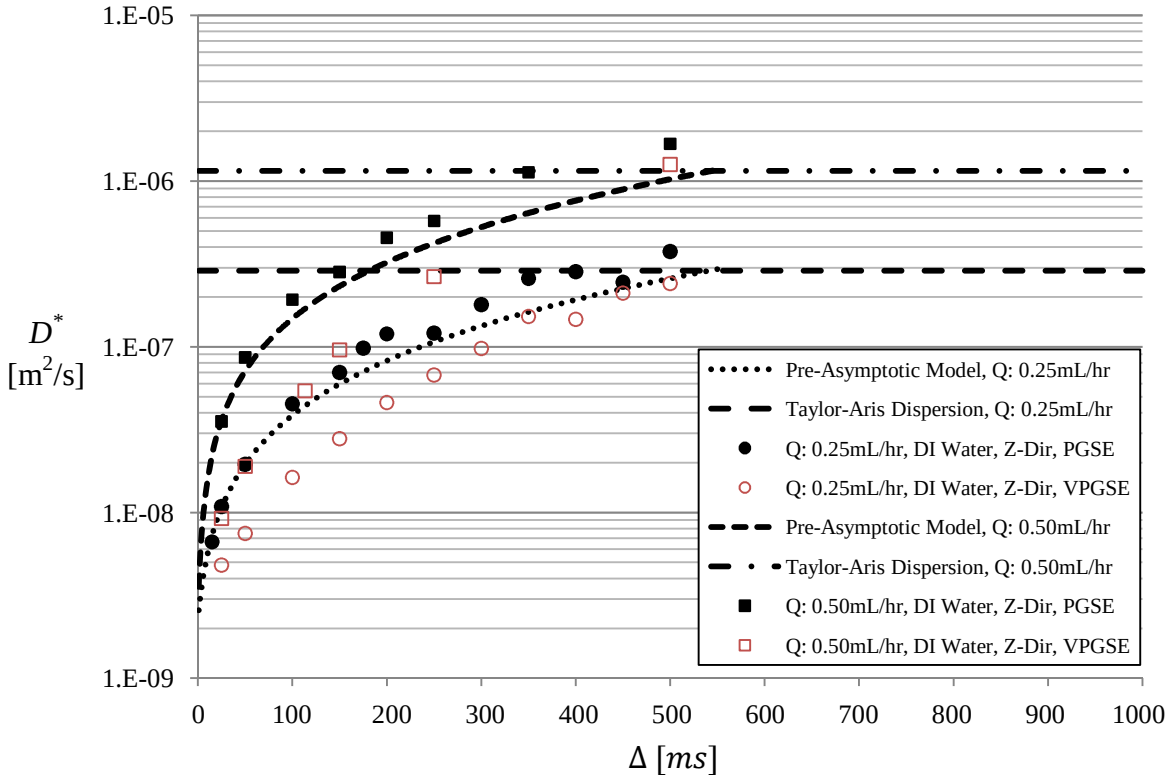

Figure 4.6 Dispersion coefficients obtained by using Stejskal-Tanner plots.

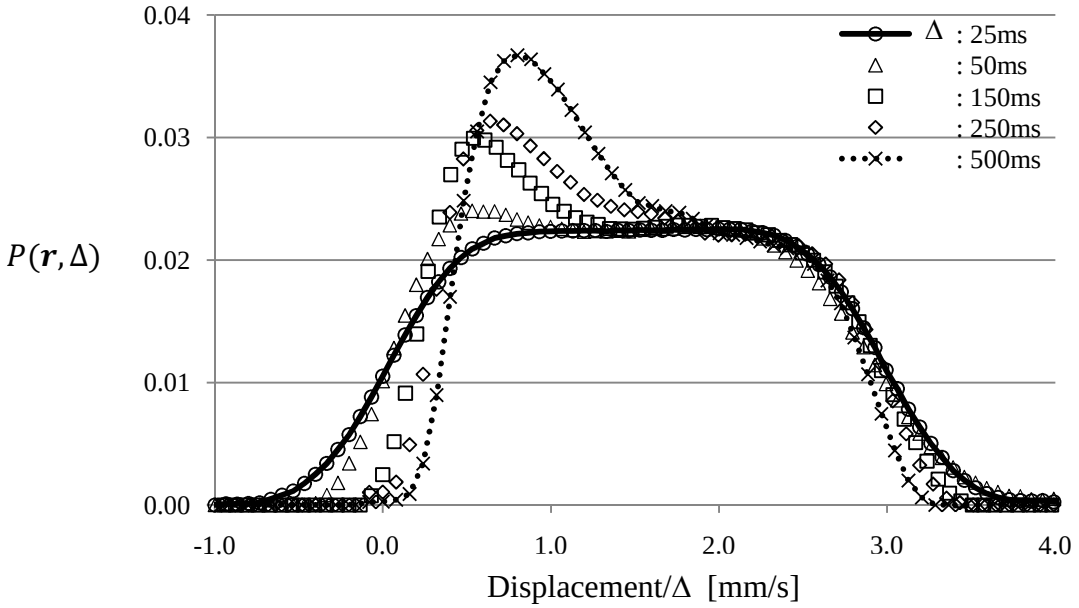

Figure 4.7 The propagators of DI water in the axial-to-flow (Z) direction at different experimental times Δ = 25, 50, 150, 250 and 500ms.

For the colloidal suspension there are two phases that experimental data can be acquired for: the colloids (oil signal) and the suspending fluid (water signal). PGSE propagator information for both phases can be acquired simultaneously due to a similar degree of dispersion with time, see figure 4.8. However when acquiring velocity compensated PGSE propagators the significant difference in the diffusion of the suspending fluid (D_W = 2.2×10^{-9}) and the colloids (D_{SES} = 1.7×10^{-13}), which differ by ~ 10^4 corresponding to ~ 10^2 times larger displacements due to free diffusion on the same time scale, causes an inability to acquire data from both phases simultaneously. Since the phase of interest in the colloidal suspension is the colloidal phase and its time scale of displacement due to Brownian motion is on a time scale which NMR can probe (see chapter 3), only data for the velocity compensated propagators for the colloids will the presented.

Figure 4.8 shows the dispersion coefficients obtained by PGSE for the colloids (oil peak) and suspending fluid (water peak) for 22%wt Colloidal dispersions flowed at Q = 0.25 and 0.50mL/hr through the microcapillary. For Q = 0.25mL/hr a clear transition occurs where initially (Δ < 200ms) the colloids have a lower dispersion coefficient than the suspending fluid, however at long times (Δ > 350ms) the reverse is true, *i.e.* the dispersion coefficient for the colloids is higher than the suspending fluid. During the intermediate time (200ms < Δ < 350ms) the dispersion coefficients are approximately the same. This clear transition is contrasted at Q = 0.50mL/hr, where the dispersion coefficient of the suspending fluid is higher than the dispersion coefficient of the colloids, although short time transitions seem to be occurring. When the dispersion coefficients of the colloidal dispersion (figure 4.8) are compared with the dispersion coefficients for DI water (figure 4.6) flowing through the same microcapillary it is evident that the dispersion coefficients of the latter are higher than those of the water in the colloidal suspension. This indicates that the latter is a more restricted fluid, *i.e.* the colloids are much less mobile than the DI water, both due to a small diffusion coefficient and because of structural ordering. This causes restricted diffusion of the suspending fluid, which have to traverse longer distances around obstacles to cause the same net displacement as the free diffusing DI water molecules. This causes the dispersion to be less than the expected dispersion using Eqn. 4.6a,b.

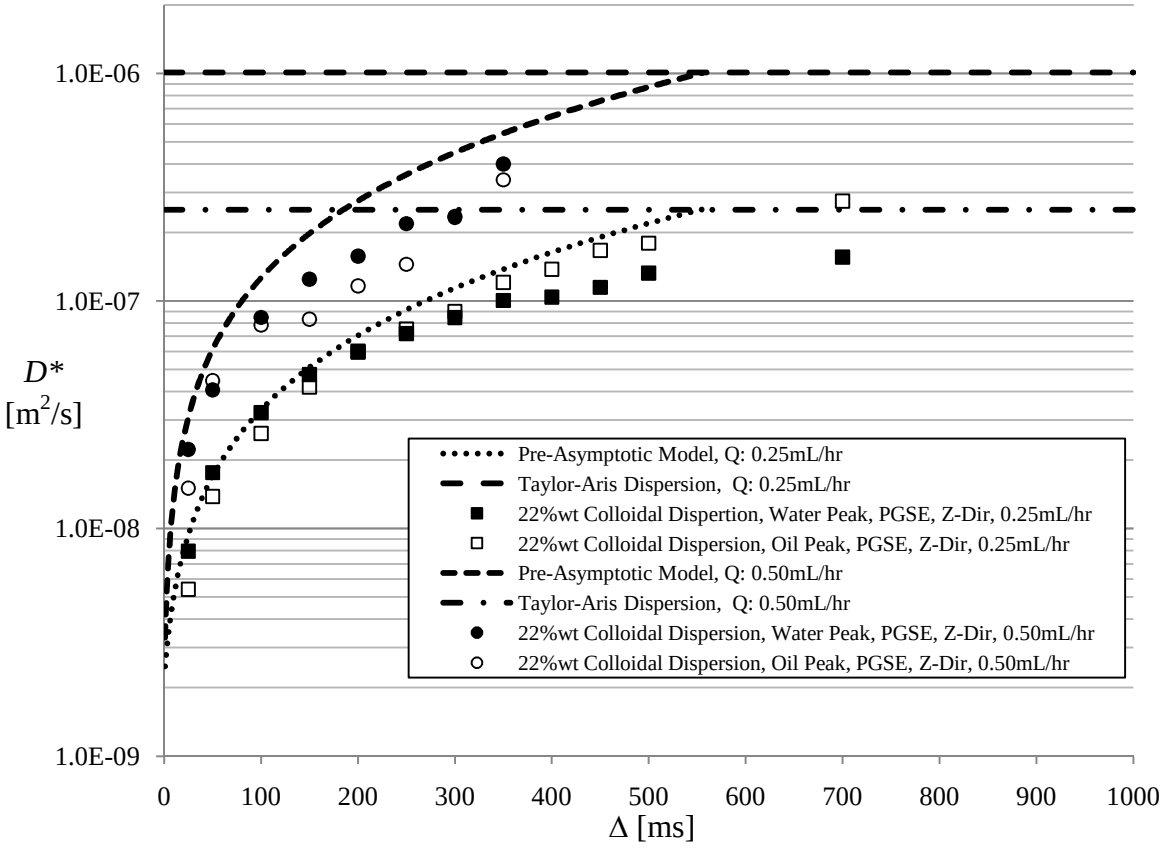

Figure 4.8 The dispersion coefficients for the colloids (oil peak) and suspending fluid (water peak) acquired simultaneously using PGSE experiments at different experimental times (Δ) for Q = 0.25mL/hr and 0.50mL/hr.

Figure 4.9 shows the propagators at Δ = 25, 50, 150 and 250ms for DI water, the colloid and suspending fluid of the colloidal suspension and a combined propagator defined as

$$P_{combined}(r) = (1-\phi)P_{suspending\ fluid}(r) + \phi P_{colloid}(r) \quad (4.7).$$

Here $P_{suspending\ fluid}(r)$ is the probability distribution (propagator) of the suspending fluid and $P_{colloid}(r)$ is the propagator of the colloids in the colloidal suspension. From figure 4.9 it is evident that the colloids have a higher probability of occupying regions of high displacement (center of capillary) than regions of low displacement (close to wall).

The colloids are not affected by Taylor dispersion on the time scales being investigated which causes their probability distribution to remain approximately constant with time. The suspending fluid, which is affected by Taylor dispersion, has a narrowing of its distribution with time. At small displacements the suspending fluid behaves as the DI water, with an increase in probability at small displacement due to wall reflections, while at higher displacement a region of high probability is seen to form at Δ = 50ms (figure 4.9b). This progresses to a similar distribution as for DI water as Δ = 250ms. This behavior is due to the restricted diffusion of the suspending fluid caused by the colloidal particles which occupy the center of the capillary at a higher ϕ than close to the wall. This is demonstrated in figure 4.10 where the concentration profile as a function of radial position has been extracted from the propagators and the velocity maps, *i.e.* the propagators give the concentration at a certain displacement (colloid/suspending fluid signal) while the velocity map allows for these displacements to be assigned to a radial position [136].

A normal stress difference based steady state migration model based on the work of Morris *et al.* [105, 171, 173] has been plotted from comparison to the data for different particle Peclet numbers, Pe_p = 0, 10, 100 and 1000 (see code in Appendix A). It can be seen that this model deviates from the data both at the wall and in the center of the capillary. At the center of the capillary the model allows for a non-physical cusping which is incorrect because the particles are finite and an increase in particle-particle interactions which follows an increase in ϕ.

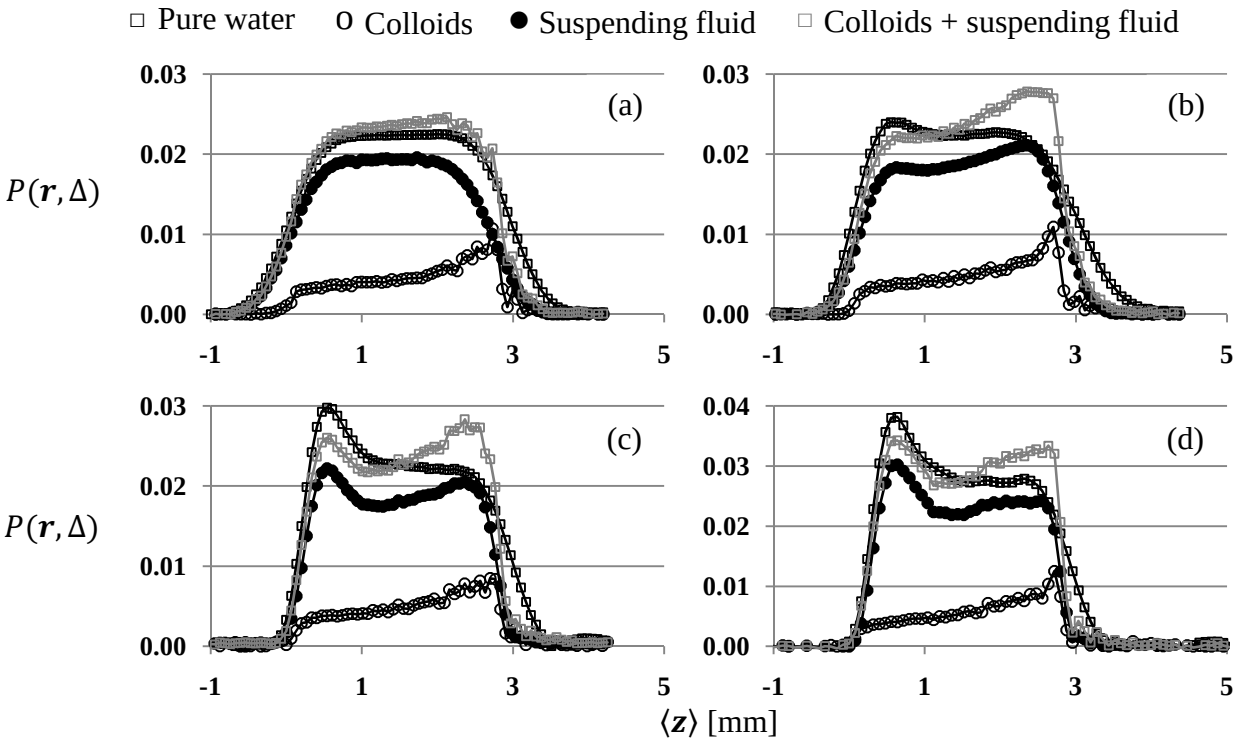

Figure 4.9 Probabilities of displacement normalized with time (Δ) for DI water, colloids, suspending fluid and colloids + suspending fluid at (a) Δ = 25ms, (b) Δ = 50ms, (c) Δ = 150ms, (d) Δ = 250ms for Q = 0.25mL/hr.

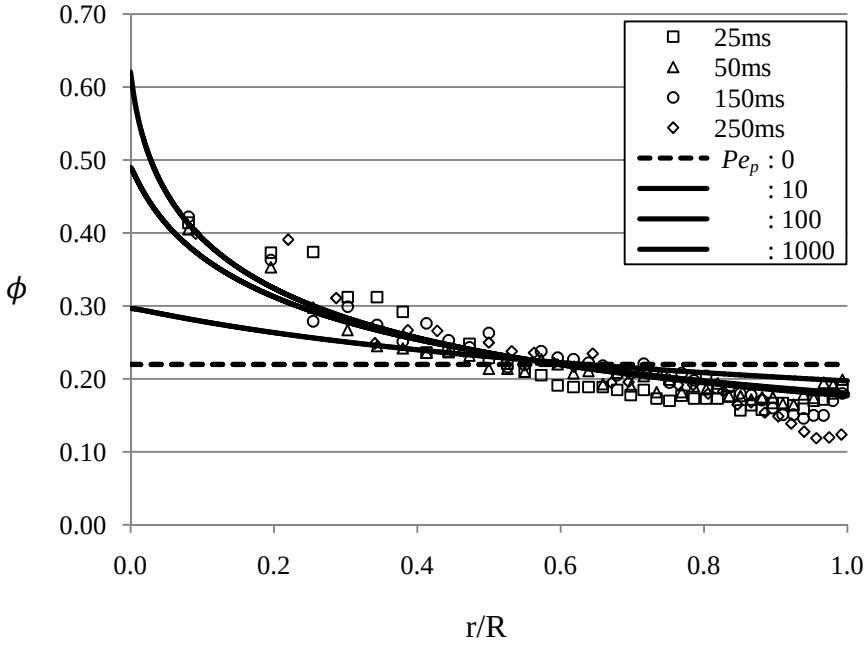

Figure 4.10 The colloid volume fraction $\boldsymbol{\phi}$ as a function of radial position (r/R) obtained from propagators and velocity maps at Q = 0.25mL/hr, for Δ = 25, 50, 150 and 250mL, the solid lines are for model of shear induced migration for different Péclet numbers [Frank *et al.*], Pe_p = 0, 10, 100 and 1000.

The former effect has been addressed by Morris and coworkers, while the latter effect has not been addressed. The effect of particle-particle interactions should be to decrease the diffusion or mobility as the particles get closer to the center, which should counteract the particle-migration driving force towards the center. This effect should explain the more gaussian-like distribution rather than a cusping of the concentration profile. At the wall it can be seen that as Δ increases, the probability of finding a particle which has experienced no or small displacement decreases, corresponding to a ~1/3 drop in ϕ from Δ = 25 to 250ms. This effect is consistent with some particles initially close to the wall moving away from the wall region given enough strain due to the high shear (see figure 4.5).

Interestingly, closest to the wall, corresponding to r/R = 0.96 – 1.00 or $\sim 5\mu m$, ϕ increases with increasing r/R. Work on near-wall dynamics of concentrated suspensions is virtually unexplored both experimentally and theoretically [183]. However, recent work on the dynamics of concentrated hard-sphere colloids near a wall [183], showed that the hydrodynamic drag that slows a particle in the vicinity of the wall is progressively weakened at high ϕ due to a counterbalance by hydrodynamic interactions. This work conducted at $Pe_p = 0$ indicates that for approximately $\phi \geq 0.1$ this shielding of the wall effect should become significant, while once above $\phi \sim 0.35$ diffusion in bulk or close to the wall are indistinguishable.

The results shown in figure 4.10 and discussed above show the strong dependence of ϕ on radial position. This is important because when investigating these systems using velocity compensated PGSE techniques the signal is an average of the different

regional dependent dynamics weighted by ϕ. Velocity compensated PGSE allows for the investigation of the irreversible or stochastic motion occuring in the colloidal suspension. Initially we look at the colloidal suspension at no flow conditions. Brady *et al.* [184] have shown by simulation that the onset of non-Newtonian behavior in a hard sphere colloidal suspension is manifest in normal stress differences. These stress differences have been used to explain the observed migration of colloidal particles leading to more concentrated regions where lower shear rates exist [105, 136, 173].

Figure 4.11 shows the results for the velocity compensated dispersion coefficient at no flow conditions in both the parallel- and perpendicular-to-flow directions. It shows how well these coefficients correspond to the effects of the finite-variance due to the hexadecane oil inside the colloidal particles (presented in detail in chapter 2.4) as well as the contribution from Brownian diffusion. It can be seen that the measured dispersion coefficients fit well with the expected results except at long times ($\Delta \geq 400$ms). To clarify any potential effect that particle-particle collision may be having on these results a simple kinetic theory model for hard-spheres is used. Kinetic theory models the spheres without any hydrodynamic interaction with a free mean path (λ) defined as

$$\lambda = \frac{1}{4\sqrt{2}\pi a^2 n} \qquad (4.8).$$

This can be combined with the variance obtained assuming unrestricted diffusion with D_{SES} = 1.73×10^{-13}m^2/s or $\langle x^2 \rangle = 2D_{SES}\Delta$ = 3.46×10^{-13}*Δ [m^2] to predict the probability of collisions using the fact that particles must displace length λ in order for the first collision to occur

$$P_{collision}(\Delta) = erfc\left({}^{\sigma}/_{\sqrt{2}\lambda}\right) \quad (4.9).$$

Here σ is the standard deviation of the gaussian pdf and $erfc(x)$ is the complementary error function

$$erfc(x) = 1 - \mathrm{erf}(x) = \frac{2}{\sqrt{\pi}}\int_x^{\infty} e^{-t^2}dt \quad (4.10).$$

This simple kinetic theory model allows us to draw the accumulation of initial particle collisions on figure 4.11, demonstrating a link between the rise of particle collisions in the system with the deviation of the dispersion coefficient (D^*) from the expected behavior given by the model which combines the finite variance and Brownian diffusion. It is well known that a weak "long-lived" tail exists in the VAF of monatomic liquids [54] and should exist in Brownian particle fluids, which can be explained by the addition of repeated ring collisions into memory functions.

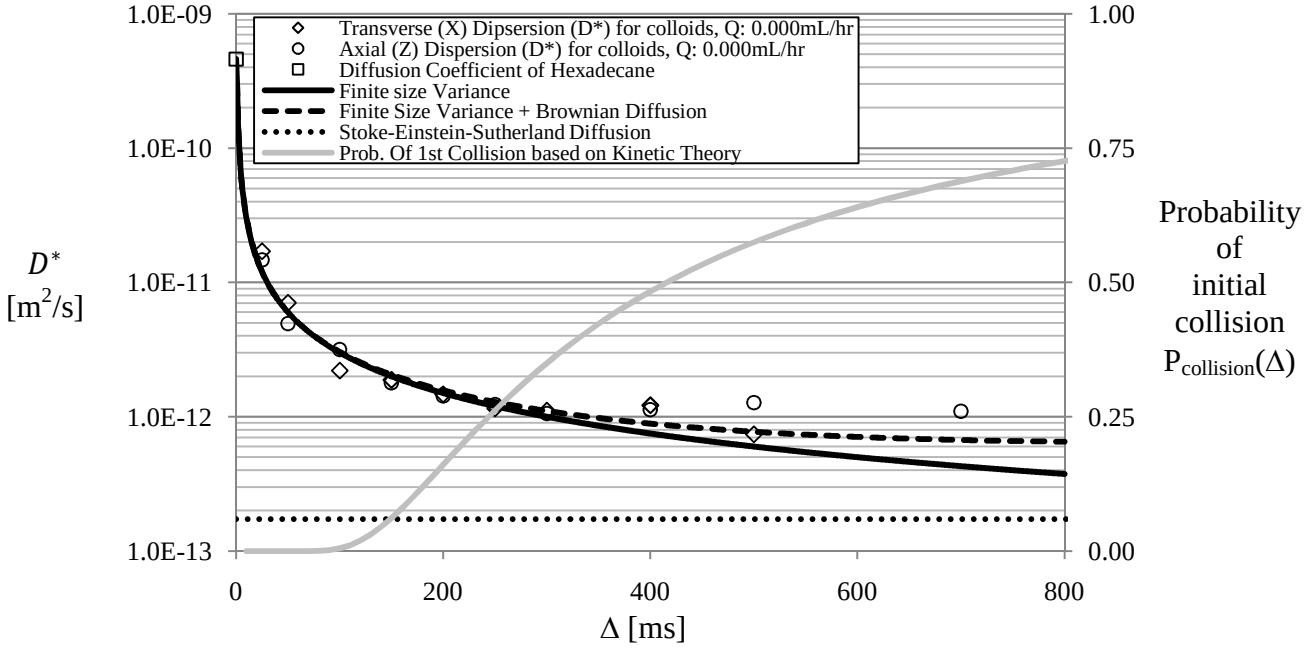

Figure 4.11 Dispersion of colloids at Q: 0.000mL/hr in the radial (X) and axial (Z) directions relative to capillary geometry. Guidelines include the effects of a finite variance in oil displacement due to restriction inside the colloids, variance due to Brownian diffusion, and the probability of initial collision based on kinetic theory of hard spheres.

It is clear from figure 4.11 that for $\Delta \leq 300ms$, the simple model shows that the variance observed is mainly due to the restriction of the oil inside the colloids, with the variance due to Brownian diffusion having a limited contribution. Additionally based on kinetic theory less than 1/3 of the particles have experienced a collision. By measuring the velocity compensated propagators for the stationary sample (figure 4.12) it is observed that the width of the distribution is essentially stationary for Δ = 25 to 300ms [see Appendix B, for the 1st, 2nd and 3rd moments of these probability distributions]. Additionally, drying the sample, *i.e.* dramatically increasing the colloid particle restriction and removing the Brownian component, emphasizes the effect of the oil molecule restriction inside the spheres. It shows the same distribution as the non-dried sample, although the dried sample shows no change with time. The shape of the propagators in figure 4.12 approaches the shape predicted in figure 2.14 (chapter 2) due to a Gaussian distribution of sphere sizes, which caused the variance to increase from 2.61 to $3.14\times10^{-13}m^2/s$, which corresponds favorably with the results presented in figure 4.13 for the variance obtained from the propagators.

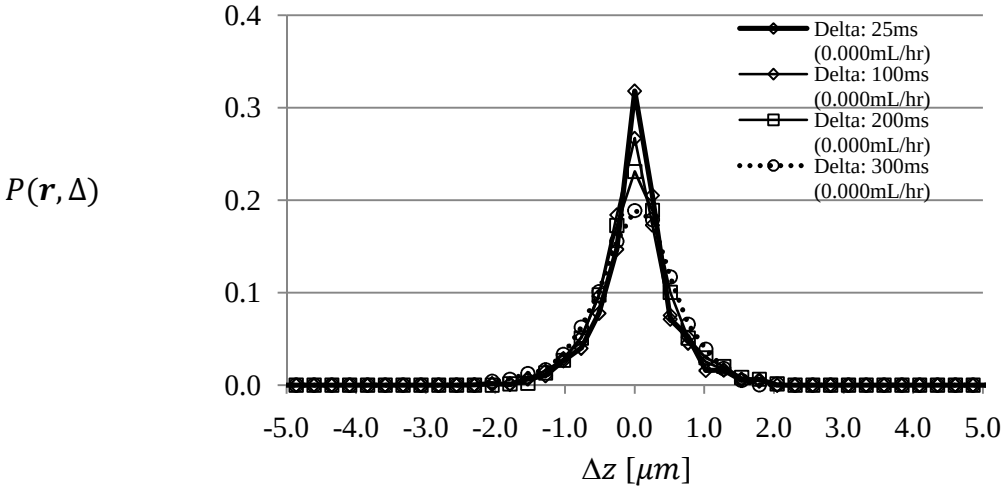

Figure 4.12 The propagators for colloids $\boldsymbol{\phi}$ = 0.22 at Q = 0.000mL/hr, for Δ = 25, 100, 200 and 300ms.

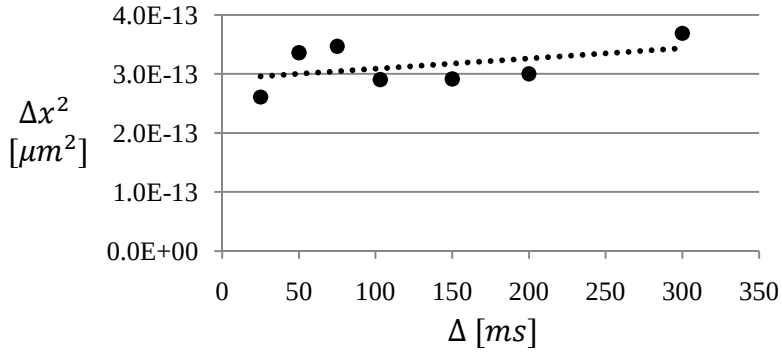

Figure 4.13 2nd Moment of the propagators for colloids at Q = 0.000mL/hr, for Δ = 25, 50, 75, 100, 150, 200 and 300ms, the dotted line is a linear fit indicating the linear slope of the variance with time as $0.55\boldsymbol{D_{SES}}$ *i.e.* restricted diffusion.

Figure 4.13 shows the variance as a function of time obtained from the propagators presented in figure 4.12 as well as propagators not shown, these indicate a variation with time that is $0.55D_{SES}$, indicative of restricted diffusion. It is interesting that there is initially a larger slope Δ = 25 – 50ms, but as the initial collisions (see figure 4.11) start (Δ > 50ms) there is a dip in the variance and then it stabilizes. This may be a result of the initial free diffusion of spheres with the effects of collision decreasing and even reversing in direction the net displacement of the particles. However due to the minute displacements being observed and the few data points used to obtain these variances (see figure 4.12), these effects are within experimental error.

To study the effects that shear has on the colloidal system, velocity compensated PGSE experiments were conducted while applying three different volumetric flow rates: Q = 0.125mL/hr, 0.250mL/hr and 0.500mL/hr. The propagators obtained are presented in figure 4.14 over a varied range of Δ = 25 to 200ms. The interesting feature of these propagators is the rapid broadening of the distributions at high enough Δ times. Since the

width of the propagators is measured by the variance, the variance of these propagators is presented in figure 4.15, with the variance at no flow condition presented for comparison. These indicate a significant deviation in the variance occurring at Δ = 50, 100 and 200ms for the Q = 0.500, 0.250 and 0.125mL/hr respectively. This corresponds to an approximate doubling of average strain $\langle\gamma\rangle = \langle\dot{\gamma}\rangle\Delta$ with the doubling of Q and hence $\langle\dot{\gamma}\rangle$. Since applied strain is associated with energy input into the system, it is reasonable from these results to assume that there is an energy threshold above which a marked increase of irreversible motion should occur. This strain threshold to the onset of irreversibility has been previously shown experimentally and confirmed by Stokesian dynamics simulation for a non-colloidal system of hard sphere colloidal suspension [72]. Where the Lyapunov exponent **(**as discussed in chapter 3**)** was used to characterize the onset of irreversibility. An analogous approach is used in this study, where instead of the Lyapunov exponent the Lyapunov time is presented. The Lyapunov time **(**$t_{Lyapunov}$**)** is the length of time for a dynamic system to become chaotic [185], reflecting the limits of system predictability. It may be written as $t_{Lyapunov} = (\lambda_1)^{-1}$, where λ_1 is the maximal Lyapunov exponent and is written [186]

$$\lambda_1 = \lim_{t\to\infty} \frac{1}{t} ln \frac{|\delta X(t)|}{|\delta X_0|} \quad (4.11)$$

If we imagined a system where the colloidal particles only follow the streamlines setup by a low *Re* flow field of the suspending fluid (a conservative steady state system) λ_1 will equal zero. The equations of motion for each particle will only become unpredictable due to Brownian motion or particle-particle interactions causing a translational motion across streamlines.

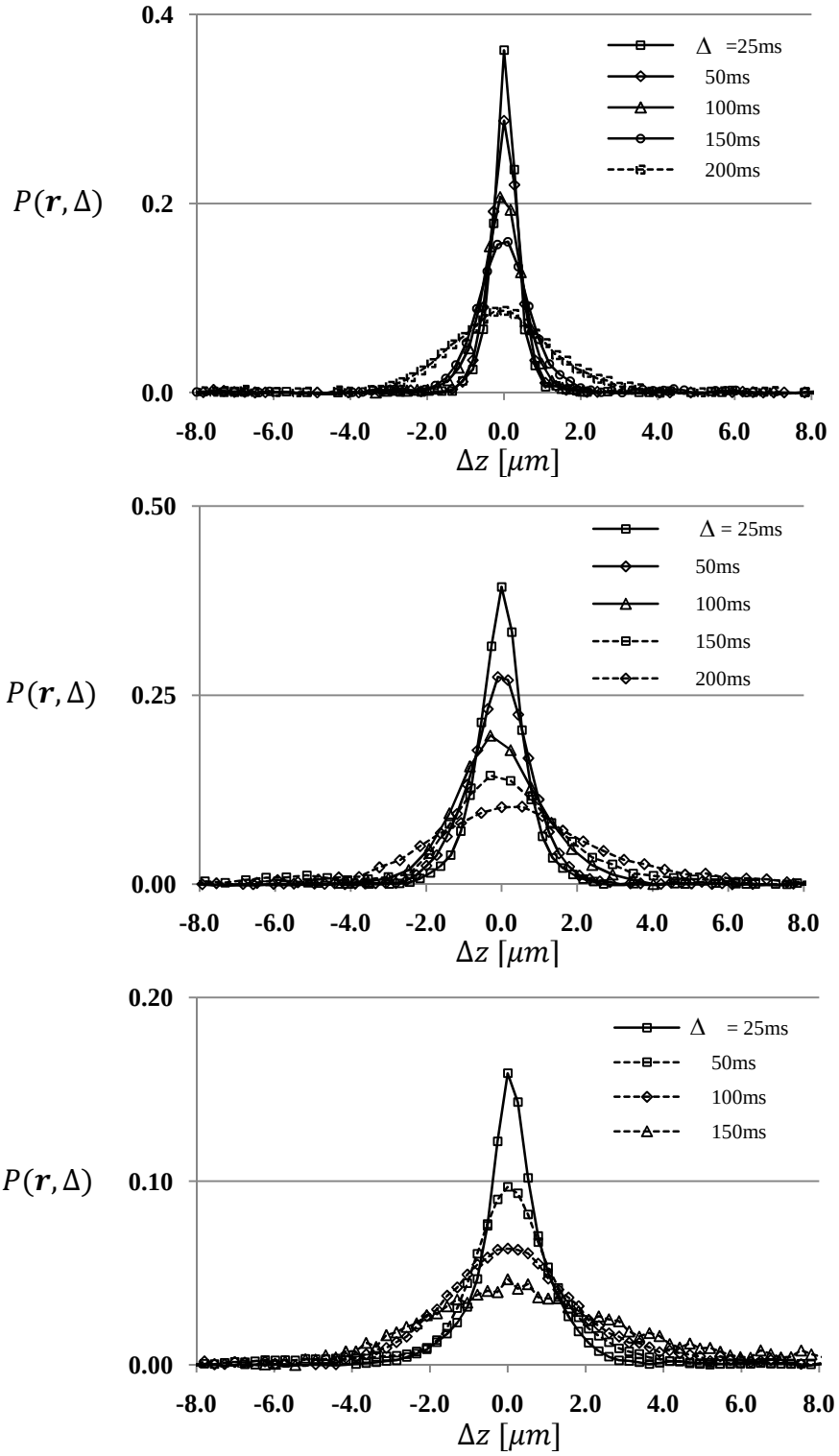

Figure 4.14 Propagators for the colloids (oil) from velocity compensated PGSE experiments at (a) Q = 0.125mL/hr, (b) Q = 0.250mL/hr and (c) 0.500mL/hr for different experimental times (Δ). The solid and dashed lines correspond respectively to the "pre-breakout" and "post-breakout" data.

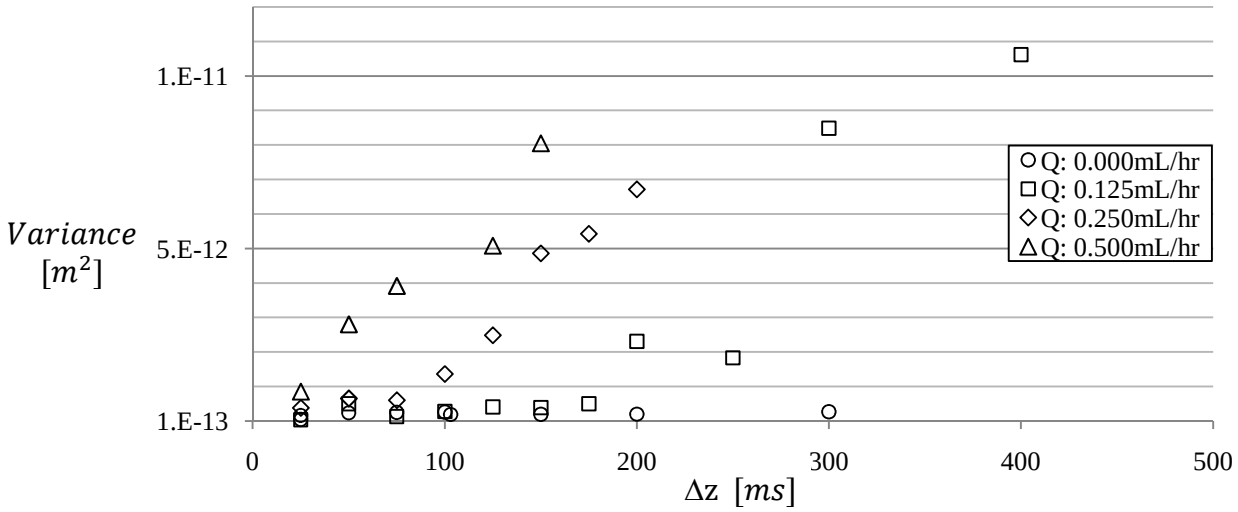

Figure 4.15 Shows the calculated variances from the velocity compensated propagators obtained for four flow conditions; 0.000mL/hr, 0.125mL/hr, 0.250mL/hr and 0.500mL/hr; a relatively clear transition occurs for the sheared systems at ~200ms, ~100ms and ~50ms, but no such transition occurs for the no flow system at these time scales.

Since we know that Brownian motion is a small contributor on the time scales that we are investigating ($\Delta < 700$ms) the main source of unpredictability for our system is due to particle-particle interactions. Figure 4.14 and 4.15 show the timescale (and therefore λ_1) of the growth in unpredictability (or irreversible) motion for the system being investigated. Since the Lyapunov time is defined in phase space by trajectories separated by an exponential magnitude, it is necessary for a clear definition for the current system as to what constitutes a perturbation of initial conditions and what constitutes an exponential separation.

For this system the initial conditions are characterized by the probability distribution of displacement at the no flow condition, as $\Delta \to 0$, which characterizes the initial structure and size distribution of the colloidal suspension with no shear applied. The initial perturbations are supplied by the shear whose magnitude is radially dependent;

this assumes that all discrete volume elements experiencing different shear have the same distribution of colloidal particles as the total distribution. Then the trajectory of each volume element is defined by the probability distribution, *i.e.* if it stays the same the system is conservative ($\lambda_1 = 0$), but if it broadens the system is experiencing irreversible motion ($\lambda_1 > 0$). To measure the change in the probability of displacement the variance will be used, with variance being the square of the standard deviation for the pdf. Then if the standard deviation has grown by 2.7 (or e) or the variance has grown by 7.4 (or e^2) the system has reached the Lyapunov time and is considered chaotic. By this definition the Lyapunov time at Q = 0.500, 0.250 and 0.125mL/hr falls in the ranges 25-50ms, 100-125ms and 200-300ms respectively.

To investigate the effect of Taylor dispersion and hydrodynamic interactions on the overall dispersion, the perpendicular-to-flow direction dispersion coefficients are presented in figure 4.16. These show that shear increases the dispersion in the perpendicular-to-flow direction. An interesting exception is at low Δ where the effects of the variance due to oil inside the spheres is still strong. It is shown that with increasing Δ, *i.e.* strain $\gamma = \langle\dot{\gamma}\rangle \cdot \Delta$, the variance decreases. This is due to ordering/restriction as there is a radial dependence for ϕ with a fairly high concentration in the central region and falls in line with the discussion of the Lyapunov time, where once the system has passed this time a difference of dispersion with flow rate can be seen in figure 4.16. As is expected the dispersion in the perpendicular-to-flow direction is much less than that for the parallel-to-flow direction (see figure 4.17), with $\sim 50\%$ higher dispersion for $\Delta \geq 150ms$ with doubling of Q.

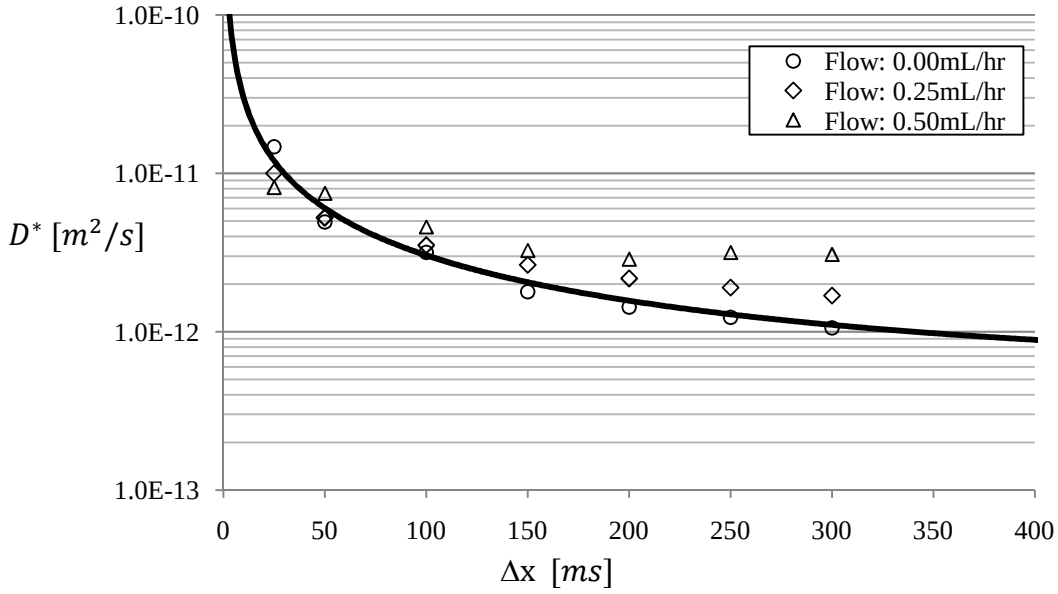

Figure 4.16 Dispersion coefficient (D*) for velocity compensated PGSE experiments in the transverse (X) direction, where the fit is $\boldsymbol{D^* = a^2/5\Delta}$ [8].

This can be contrasted with the parallel-to-flow direction shown in figure 4.17, which is presented with lines corresponding to $D^* = K \cdot \Delta^{1.2}$, $D^* = K \cdot \Delta Ln(\Delta)$ and $D^* = K \cdot \Delta^{1.4}$, where K scales with $\langle u \rangle^3$ [187]. These indicate that in the parallel-to-flow direction the system is affected by Taylor-like dispersion, where an enhanced diffusion might be caused by particle-particle interaction. An interesting phenomena is the $\langle u \rangle^3$ dependence, which is encountered in inviscid turbulent fluids where the energy is dissipated at a rate ϵ which is equal to the supply rate where [188, 189]

$$\epsilon = \frac{\langle u \rangle^3}{l} \quad (4.12)$$

where l is the width of the flow. This process leads to dispersion scaling with the supply of energy to the system in the form of strain.

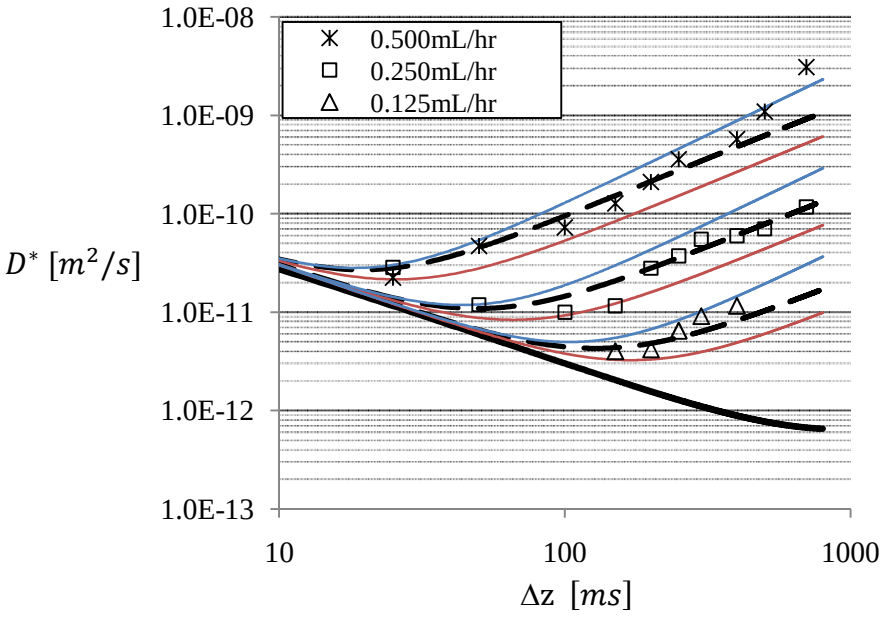

Figure 4.17 Dispersion (*D**) coefficients for the colloids (Oil) from the velocity compensated PGSE experiments at Q = 0.125, 0.250 and 0.500mL/hr. The solid black line indicates D* from the variance due to finite internal size of particles and due to free Brownian motion. The three lines around each data set are in ascending order: $D^* = K \cdot \Delta^{1.2}$, $D^* = K \cdot \Delta Ln(\Delta)$ and $D^* = K \cdot \Delta^{1.4}$, where K scales with $\langle \boldsymbol{u} \rangle^3$ and is an arbitrary fitting factor.

To emphasize the strain dependence on the evolution of the propagators, the propagators at Q = 0.125, 0.250 and 0.500mL/hr at Δ = 25, 50 and 75 ms are presented in figure 4.18. The idea that passed a strain threshold a dramatic increase in irreversibility occurs in the system, introduces the ideas of micro-structural length scales which cause a restriction to the motion at small strains, but at large strains allow particles to more freely cross streamlines, and therefore a rapid increase in dispersion should occur. To address this phenomena it is useful to introduce two system correlation relation times (α and β). This approach has been previously used to model systems of colloidal dispersions approaching glass transition, a regime which causes difficulties in the implementation of Stokesian dynamics simulations due to the divergence of multiple quantities [134]. This

regime has been successfully modeled using mode coupling theory [134], which does not include hydrodynamic interactions.

If an analogous analysis is used to understand the strain dependence, the initial system can be assumed to experience a short time relaxation due to restricted diffusion quantified by β, while at longer times a α relaxation dominates the system as the microstructure experiences shear induced rearrangements. This picture allows for the modeling of dispersion of the system as either

$$D^* \sim K\Delta^{\alpha} + a^2/5\Delta \quad (4.13)$$

or

$$D^* \sim K\Delta ln(\Delta) + a^2/5\Delta \quad (4.14)$$

These models were used to create the lines in figure 14.17, where K depends on the mean velocity to the third power, while α = 1.2 to 1.4 in Eqn. (4.13) forms an envelope around the data with Eqn. 4.14 fitting in between.

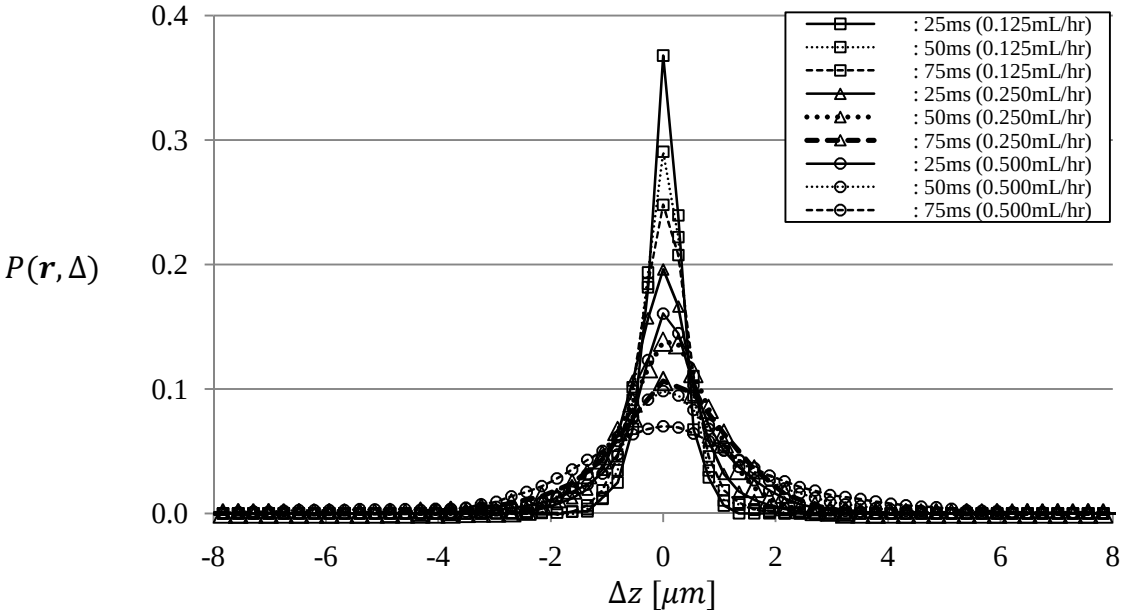

Figure 4.18 Velocity compensated PGSE propagators for Q = 0.125, 0.250 and 0.500mL/hr at Δ = 25, 50 and 75ms.

Conclusions

A detailed dynamic NMR study has been conducted to study a 22%wt colloidal suspension in a microcapillary with both no-flow and flowing conditions; Q = 0.000, 0.125, 0.250 and 0.500mL/hr. Velocity maps for DI water and the colloidal suspensions were obtained at Q = 0.250 and 0.500mL/hr, while propagators in the parallel-to-flow direction were obtained for DI water and both phases of the colloidal suspension as a function of experimental time Δ = 25 – 250ms. By combining the information from the propagators and velocity map, concentration profiles in a flowing system, Q = 0.250mL/hr, were obtained as a function of observation time Δ = 25 – 250ms. This showed wall and particle-particle induced effects which affect this profile and cause a deviation from expected results based on a normal-stress based model. To further study the incoherent motion of the colloidal suspension velocity compensated PGSE experiments were conducted. These showed that at no-flow conditions small displacements due to Brownian motion were observed on the time scales being investigated. These also showed that by modeling the restricted diffusion inside a spherical boundaries with Gaussian distribution fit well with the observed decrease in dispersion over time for the no-flow condition colloidal suspension. For the flowing systems a strain dependent growth in irreversibility was observed for all flow rates tested. The time it took each system to reach a chaotic state was quantified using the Lyapunov time and was found to scale with strain, with times of 25-50ms, 100-125ms and 200-300ms corresponding to Q = 0.500, 0.250 and 0.125mL/hr. To address the strain dependence of the growth in irreversibility, ideas from mode-coupling theory were used

to characterize the colloids experiencing either a restricted diffusion due to neighbors or a break-out type effect allowing for particles to jump between different restricted states.

COLLOIDAL TRANSPORT IN A BIFURCATION

Introduction

The flow and distribution of Newtonian, polymeric and colloidal suspension fluids at low Reynolds numbers in bifurcations has importance in a wide range of disciplines, including applications in microvascular physiology [190, 191] and microfluidic devices [192]. Recently studies of bifurcations have involved "plasma skimming" to separate red blood cells from blood plasma [193, 194] as well as uses in creating reversible and irreversible flow devices [195] and fluid based logic gates [196]. Additionally, the fluid mechanics of hard-sphere colloidal suspensions have received much attention [197] due to the prevalence of suspensions of small particles dispersed in a fluid in a variety of natural and industrial settings. It is the aim of this study to apply dynamic Magnetic Resonance Microscopy (MRM) to examine fluid, and more importantly, particle distribution of colloidal suspensions in a bifurcation. The pure fluids studied are water (Newtonian) and xanthan gum (non-Newtonian) for comparison to the results obtained for the hard-sphere colloidal suspensions. Colloidal suspensions of a polydisperse oil filled core shell suspension [198] with mean radius $a = 1.25 \pm 0.46$ μm at volume fractions ϕ of 0.08 and 0.22 are studied. These model spheres have been used before in conjunction with the use of NMR techniques to study the diffusion properties of the oil inside the particles [199], velocimetry of the steady-shear rheology [200], demonstration of nanoscale NMR velocimetry [201] and in demonstrating irreversible hydrodynamic behavior of low volume fraction colloidal suspensions in a

capillary flow experiment [202]. In addition to conducting MRM experiments, simple Computational Fluid Dynamics (CFD) simulations will be used for comparison with the MRM results for all four fluids and all three spatial components of velocity.

Theory

PGSE NMR & Dynamic NMR Imaging

A more detailed description of the relevant MRM theory can be found in chapter 2. The underlying principle in MRM is that the nuclear spin precession frequency depends on the local magnetic field strength felt by each spin. By applying a magnetic field gradient across a sample, controlled differences in the local magnetic field strength allow for the use of this frequency and the accumulated precession phase to mark spin positions. Only two techniques are able to probe self-correlation at the microscopic level: polarized neutron scattering and pulsed gradient spin echo (PGSE) NMR [1]. These techniques are complimentary because PGSE is limited to dynamic displacements of between 10 nm to 100 μm and time scales between a few milliseconds and a few seconds while neutron scattering has an upper limit of dynamic displacements of 10 nm and best results for time scales less than a few microseconds [1]. PGSE NMR thus serves well for studying the hydrodynamic behavior of colloidal systems of length scales and time scales ranging from those of uncorrelated Brownian motion [203] to correlated motion, caused by particle-wall, particle-particle and fluid-particle hydrodynamic interactions.

The propagator or self-correlation function $P_s(\boldsymbol{r}|\boldsymbol{r}+\boldsymbol{R},\Delta)$ *g*ives the probability that a spin at position $\boldsymbol{r}$ at time t = 0 is at $\boldsymbol{r}+\boldsymbol{R}$ at time $t = \Delta$. We can then define the

averaged propagator $\bar{P}_s(\boldsymbol{R}, \Delta)$ which gives the average probability that any particle has displaced $\boldsymbol{R}$ over time Δ

$$\bar{P}_s(\boldsymbol{R}, \Delta) = \int P_s(\boldsymbol{r}|\boldsymbol{r} + \boldsymbol{R}, \Delta)\, \rho(\boldsymbol{r}) d\boldsymbol{r} \qquad (5.1)$$

$\rho(\mathbf{r})$ is the initial spin probability distribution to find a spin at position **r**.

The form of the PGSE attenuation function can be written as

$$E(\boldsymbol{q}, \Delta) = \int \bar{P}_s(\boldsymbol{R}, \Delta)\, exp[i2\pi \boldsymbol{q} \cdot \boldsymbol{R}] d\boldsymbol{R} \qquad (5.2)$$

where in analogy to neutron scattering $\boldsymbol{q} = (2\pi)^{-1}\gamma \boldsymbol{g}\delta$ is the conjugate variable to spin displacement. Here $E(\boldsymbol{q}, \Delta)$ is the NMR spin echo signal $S(\boldsymbol{q}, \Delta)$ normalized by the signal at $\boldsymbol{q}$ = 0, *S*(0,Δ), which normalizes NMR relaxation effects. Equation (5.2) is the Fourier Transform of the averaged propagator. Therefore, by incrementing $\boldsymbol{q}$ to sample $\boldsymbol{q}$-space and Fourier transforming the normalized spin echo signal, we can obtain the Propagator for a particular flow state. When defining our normalized echo signal (5.2) we have assumed that the gradient pulses are narrow (δ<<Δ), *i.e.* spins do not move significantly during the gradient application. This assumption is also correct if the spin velocities remain constant during δ.

In this research, combined $\boldsymbol{k}$-space and $\boldsymbol{q}$-space imaging spatially resolves the flow yielding velocity images in the bifurcation. When combining $\boldsymbol{k}$- and $\boldsymbol{q}$-space imaging the signal acquired $S(\boldsymbol{k}, \boldsymbol{q})$, is modulated in the space of two vectors: $\boldsymbol{k} = (2\pi)^{-1}\gamma \boldsymbol{G}$t conjugate to spin position and $\boldsymbol{q}$ conjugate to spin displacement over the time Δ. The echo amplitude signal can be written

$$S(\boldsymbol{k}, \boldsymbol{q}) = \iint \rho'(\boldsymbol{r}) P_s(\boldsymbol{r}|\boldsymbol{r} + \boldsymbol{R}, \Delta) exp[i2\pi \boldsymbol{k} \cdot \boldsymbol{r}] exp[i2\pi \boldsymbol{q} \cdot \boldsymbol{R}] d\boldsymbol{R} d\boldsymbol{r} \qquad (5.3)$$

An Inverse Fourier Transform of (5.3) yields

$$\rho'(\boldsymbol{r})P_s(\boldsymbol{r}|\boldsymbol{r}+\boldsymbol{R},\Delta) = \iint S(\boldsymbol{k},\boldsymbol{q})exp[-i2\pi\boldsymbol{k}\cdot\boldsymbol{r}]exp[-i2\pi\boldsymbol{q}\cdot\boldsymbol{R}]d\boldsymbol{q}d\boldsymbol{k} \quad (5.4)$$

If this is normalized by the spatially localized effective spin density, $\rho'(\mathbf{r})$ which includes magnetic relaxation effects we get

$$P_s(\boldsymbol{r}|\boldsymbol{r}+\boldsymbol{R},\Delta) = \frac{\iint S(\boldsymbol{k},\boldsymbol{q})exp[-i2\pi\boldsymbol{k}\cdot\boldsymbol{r}]exp[-i2\pi\boldsymbol{q}\cdot\boldsymbol{R}]d\boldsymbol{q}d\boldsymbol{k}}{\int S(\boldsymbol{k},0)exp[-i2\pi\boldsymbol{k}\cdot\boldsymbol{r}]d\boldsymbol{k}} \quad (5.5)$$

This propagator gives the probability of displacement for every spin in the imaging volume being excited; since each voxel in that volume has a finite number of spins, the displacement for the voxel is the average displacement $\bar{R}(\boldsymbol{r})$ for all the spins inside that voxel. Since the displacement occurs over time Δ, the mean displacement for each voxel is given by

$$\bar{v}(\boldsymbol{r}) = \bar{R}/\Delta \quad (5.6)$$

The calculation of $\bar{v}(\boldsymbol{r})$ for every voxel allows the construction of a velocity image.

It is important to keep in mind that the dynamic data acquired in the velocity images and propagators represents the averaged dynamics inside the bifurcation, because each voltage measure is an independent observation of the system. For the experiments presented in this paper, the velocity images give the velocities averaged over 2hr 16min, while the propagators give the probability of displacement for dynamics averaged over 1hr 8min. In this way the measurements are averaged over thousands of ensembles of the flow.

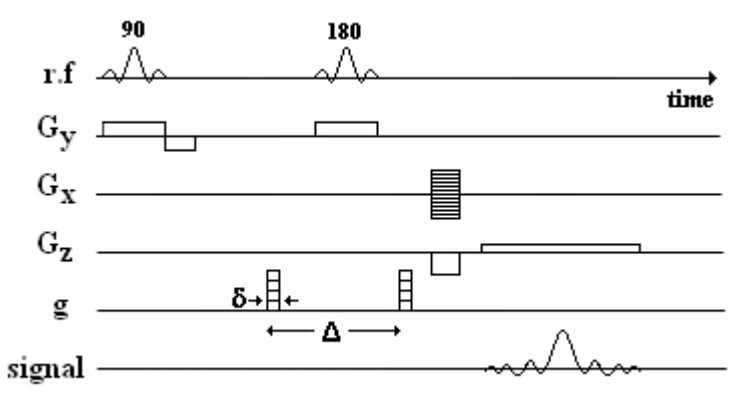

Figure 5.1 Pulse sequence used to acquire the velocity maps. Signal evolves under the influence of both the PGSE gradient g and the resolution gradient G. FOV = 7.5mm, Slice thickness: 0.2mm, Acq_size: [128 by 128], Δ = 25ms, δ = 1ms, SW = 100,000, g_{min} = 100mT/m, g_{max} was varied for different flow rates. 16 Averages, T_R = 1s, T_{Exp} = 2 hr 16 min.

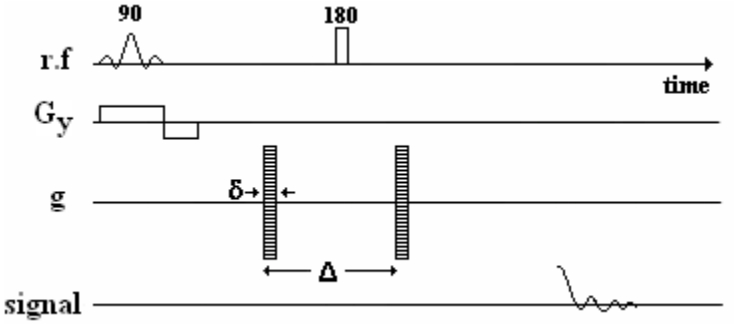

Figure 5.2 Pulse sequence used to acquire the propagators. Signal evolves under the influence of the gradient g. Slice thickness: 0.5 mm, Acq_size: 256, Δ = 25ms, δ = 2ms, SW = 5,000. g_{max} was varied for different flow rates. q-pts: 128. 16 Averages, T_R = 2s, T_{Exp} = 68 min.

PGSE NMR & Particle Distribution

In ***q***-space imaging the volume being excited can be the whole sample inside the rf coil or a limited region inside the coil by using slice selective rf pulses. To determine the particle concentrations entering each bifurcation channel a 500μm slice in the bifurcating channel is excited orthogonal to the axial flow direction, see figure 5.9 for reference. The displacement of spins was encoded in a direction perpendicular (x-direction, for coordinate system used in this study, reference figure 5.5) to the axial flow

direction, with spins inside the larger bifurcation outlet channel being displaced in a negative direction relative to a centerline through the bifurcation inlet channel, while spins inside the smaller bifurcation outlet channel were displaced in a positive direction. Two sets of experiments were conducted at each flow rate. First the colloidal suspension flow was measured to obtain a combined oil and water propagator. The sample was then doped to relax the water phase magnetization so that only the oil particle dynamics were obtained. By comparing the distribution of fluid into each channel for the two propagators, a method for determining the suspension fluid and particle partitioning in each channel is obtained. Assuming each channel has the same size distribution of particles, then the exact concentration of particles entering each channel can be obtained from the data.

Experiment

Apparatus

The NMR experiments were performed using a Bruker DRX 250 NMR system based on a horizontal narrow bore 5.8 T superconducting magnet. A micro 5 (Bruker GmBh, Karlsruhe) gradient coil provides three orthogonal magnetic field gradients with amplitude up to 1.7 Tm^{-1}. The bifurcation used was laser etched from a hard polymer. It consisted of circular capillaries, with inlet diameter 2.50 ±0.01 mm, bifurcating at 45^{o} angles to a small diameter outlet of 0.76 ±0.01 mm, and a large diameter outlet of 1.25 ±0.01 mm. The fluids were pumped through the bifurcation using an HPLC pump (Pharmacia) and a syringe pump (KD Scientific). The HPLC pump was used for the

water and xanthan gum to provide pressure flow control. The colloids were pumped using the syringe pump. The pumps were calibrated using velocity imaging and volumetric throughput measurements of water and no difference was found in between the two pumps.

Materials

Four fluids were used in this work: de-ionized water, 0.25%wt xanthan gum (MP Biomedicals), 8%vol hard-sphere colloidal suspension and 22%vol hard-sphere colloidal suspension. All fluids were doped with Gd^{3+} in Magnevist (Berlex Laboratories) to decrease T_1 relaxation and allow more rapid signal acquisition. An AR-1000 rheometer (TA Instruments) indicated no change in the rheology of the fluids before and after doping. The colloidal suspension consists of oil filled hard shell particles [198], radius $a = 1.25 \pm 0.46\mu m$ suspended in a water phase (figure 5.3 shows the particle distribution) consisting of 2%wt polyvinyl (95% hydrolyzed, avg. M.W. 95000, Acros Organics). The oil phase is composed of hexadecane (Fischer Scientific), while the hard shell is made from poly(methylmethacrylate) (Sigma Aldrich). Field Emission Microscopy (FEM) images of the particles show that they have a smooth surface and a spherical shape. Flocculation was not observed during any steps of processing or characterization and no evidence of flocculation was present during the NMR experiments.

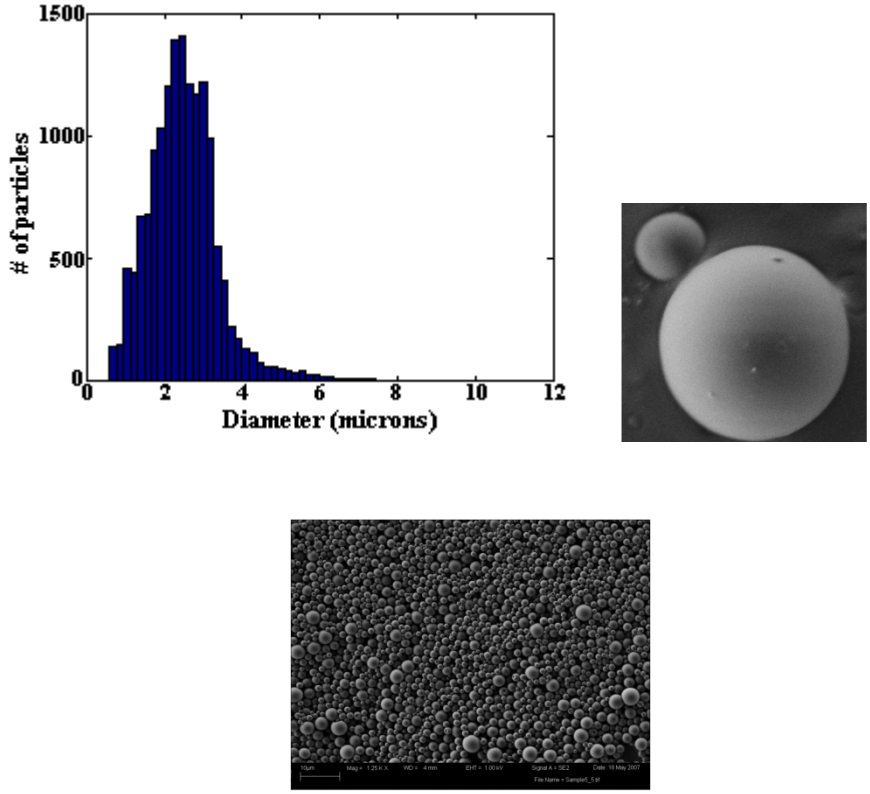

Figure 5.3 Clockwise, starting in upper left corner. A particle size distribution of colloidal suspension obtained using light microscopy. A Field Emission Microscopy (FEM) image of two neighboring particles. FEM image of a collection of particles.

Viscosity models for fluids

The viscosity of an incompressible Newtonian fluid is described by a constant relationship between viscosity and shear. The de-ionized water should exhibit Poiseuille velocity profiles [182] in both of the outlet channels far enough downstream from the entrance. The viscosity of the 0.25% xanthan gum solution is modeled using the power law relationship between viscosity (η) and shear rate ($\dot{\gamma}$), $\eta = m\dot{\gamma}^{n-1}$[182]. This relationship allows for the modeling of velocity profiles in the outlet channels, where the power law constant (n) is determined empirically and compared with literature values [204]. In a hard-sphere suspension particles interact through hydrodynamic and

Brownian forces. A hard-sphere colloidal system is described by the volume fraction ϕ and the particle Péclet number, $Pe_p = \frac{\dot{\gamma} a^2}{D_{SES}}$ where $D_{SES} = kT/6\pi\eta_s a$ is the Stokes-Einstein-Sutherland diffusivity of an isolated spherical particle of radius *a* in a suspending fluid of viscosity η_s. The Pe_p number determines the relative importance of the Brownian and hydrodynamic stresses. At low Pe_p, the Brownian stresses contribute significantly to the overall stress; as the Pe_p number increases shear thinning is observed as the Brownian contribution decreases; while at high Pe_p the hydrodynamic stresses and viscosity contribution increases dramatically as particles are pushed into close contact and lubrication forces dominate the hydrodynamic interactions causing shear thickening [205].

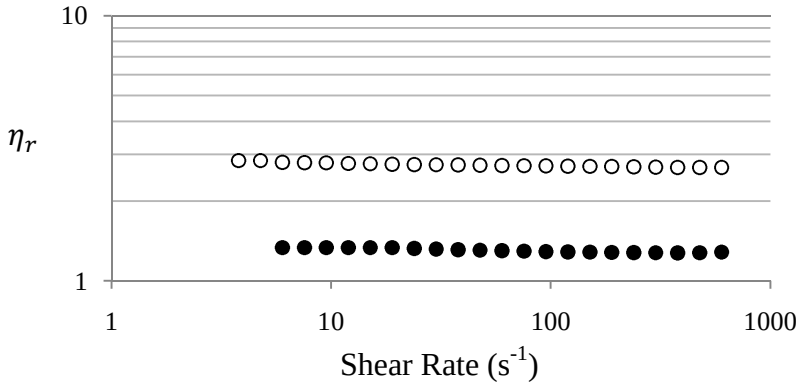

Figure 5.4 Reduced viscosity (η_r) for the 8% and 22% hard sphere colloidal suspensions obtained using a AR-G2 rheometer with a stainless steel 60mm parallel plate setup.

Therefore the total viscosity of a colloidal suspension may either decrease (shear thinning) or increase (shear thickening) at different Pe_p. These non-Newtonian effects seen in concentrated suspensions can also be present in dilute suspensions [160]. Rheology measurements of the 8% hard sphere colloidal suspension and 22% hard sphere

colloidal suspension are presented in figure 5.4, where the relative viscosity $\eta_r = {}^{\eta}/_{\eta_s}$ is plotted against shear rate ($\dot{\gamma}$). The results presented were obtained using an AR-G2 rheometer (AR Instuments) using a stainless steel 60mm parallel plate setup with a fluid trap and using a 1mm gap with the temperature set to 20.0^{o}C. The experiments were run using the following scheme: pre-shear for 2 minutes at 10s^{-1}; run steady state flow experiments high to low shear (600 – 0.001 s^{-1}) and then low to high shear (0.001s^{-1}-600s^{-1}); then to test for thixotropy, *i.e.* time-dependent change in viscosity, peak hold experiments were conducted at (0.001, 0.01, 0.1, 1.0, 10, 100 s^{-1}) for two minutes each; and then the steady state flow experiments were repeated. The peak-hold experiments showed no evidence of thixotropy, but confirmed a growth in experimental error seen in the steady state flow experiments for shear stress τ < 0.05Pa, which also occurred for Newtonian (DI water and Glycerol) samples. This shear stress was therefore used as the lower limit of instrument sensitivity due to environmental effects, *i.e.* building vibrations, air flow disturbances *etc*. As can be seen in figure 5.4 the rheology over the range measured is approximately Newtonian with only a slight decrease in η^* with increasing shear rate; these decreases correspond to 3% and 6% respectively for the 8% and 22% hard sphere colloidal suspensions. The mean values of η^* are respectively 1.28 and 2.68, which correspond favorably with previous simulation and experimental results for hard sphere colloidal suspensions [205]. For comparison with models, for the viscosity of the 8% colloidal suspension we will use the Batchelor expansion [206] of the Einstein relation $\eta = \eta_s(1 + 2.5\phi + 6.2\phi^2)$ which for ϕ = 0.08 gives η^* = 1.24. The computational fluid dynamics (CFD) model used will assume constant particle

concentration throughout the bifurcation so the viscosity will be Newtonian. The 22% colloidal suspension is modeled using a power-law viscosity model with $n > 1$ (shear thickening), to generate a macroscopically consistent CFD model for the fluid distribution experimentally observed in the outlet channels. This is due to the fact that a shear thinning model of the Rheology does not replicate the fluid distribution obtained in this study and although a Carreau model may be more representative of a 22% colloidal suspension, the simpler power law model represents the fluid distribution well and is easier to use for the CFD simulations done in this study and serves as a qualitative comparison with the dynamic magnetic resonance microscopy results. It is well known in the numerical studies of flow contractions that the singularity at the reentrant corner located at the entrance to the smaller duct, where stresses tend to infinity, causes severe difficulties [207].

Methods

The MRM pulse sequences, or NMR timing diagrams, used to acquire the velocity maps and the propagators are shown in figures 5.1 and 5.2. PGSE techniques [1] are used to obtain dynamic images of the fluids inside the bifurcation with spatial resolution of 59 x 59 µm/pixel in plane over a 200 µm thick slice. Velocity in all three spatial directions was examined to determine the impact of secondary flows and to characterize the transport in the bifurcation. The fluids flowed against gravity with the pressure difference applied using a HPLC pump for the water and xanthan gum fluids and by using a syringe pump for the 8% and 22% hard-sphere colloidal suspensions. The velocity data provides direct measurement of the velocity profiles inside each of the

outlet channels as well as the flow partitioning between the two outlet channels. CFD software was used to simulate the flow through a model of the bifurcation for all four fluids. These simulations were then compared with the experimental results obtained using dynamic MRM. For the 22% hard sphere colloidal suspension the percentage distribution of colloid particles into each outlet capillary was determined by examining the spectrally resolved propagator in a direction orthogonal to the axial flow. The fraction of oil signal versus oil and water signal was determined from integration of the chemically resolved spectra for the negative and positive displacement and were divided by each other, respectively being assigned to the large and small branches. These were then multiplied with the outlet concentration (22%) to give the concentration in each branch.

CFD Simulations

A commercially available Computational Fluid Dynamics (CFD) software, ANSYS CFX (v. 11.0) was used to simulate the flow though the experimental bifurcation geometry that was drawn using SolidWorks (v.4.1) (see figure 5.5). A no slip boundary condition at the smooth inner wall of the bifurcation was applied, while the outlets were set at zero relative average pressure. At the inlet, velocity profiles were applied based on the fluid rheological properties and the MRM experimental results. The rheological models presented in section 5.3.3 were used for each fluid. In post processing the simulations, velocity data in all three spatial directions from the mid plane of the geometry was exported to Matlab (R2006a) and used to make velocity maps for the three directions of velocity. These are shown in figure 5.7. Since the MRM data is obtained

over a finite slice thickness some discrepancy is expected between the CFD and MRM results. The velocity images for the axial (V_z) and perpendicular to axial (V_x) flows were scaled the same as the MRM data for those velocity directions. The velocity map in the slice direction (V_y) had velocity magnitudes that were almost two orders of magnitude lower than those obtained in the MRM data and thus have a different scaling, but allow for a qualitative comparison.

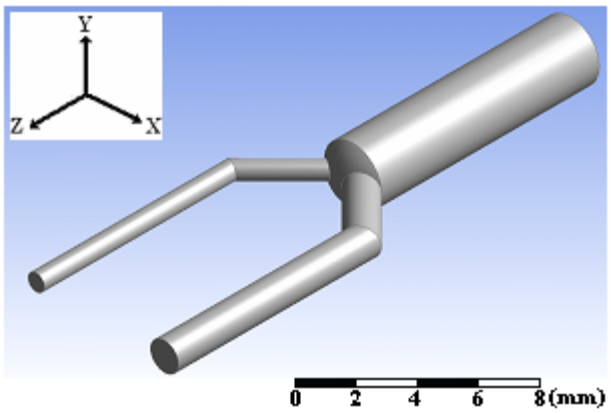

Figure 5.5 Shows the Bifurcation geometry used for the CFD simulations. The orientation of the coordinate system to be used is indicated.

Results and Discussion

This study was conducted with the aim of demonstrating the ability of dynamic MRM techniques to obtain information about complex flows inside a bifurcation and to allow the quantitative determination of fluid and particle separation caused by a bifurcation with different sized outlets and overall acceleration. The CFD results were obtained for qualitative comparison with the MRM, in particular to compare the impact of rheological constitutive equations on the flow partitioning in the bifurcation.

Velocity Maps

Magnetic resonance microscopy velocity images for each fluid were obtained in three velocity directions (V_x, V_y and V_z) for volumetric flows of 10mL/hr, 20mL/hr and 30mL/hr, but due to space considerations only velocity images at 20mL/hr are presented in figure 5.8. Velocity images for a particular velocity direction are scaled the same to allow for a qualitative comparison. When comparing the fluids to the water velocity images it is clear that shear thinning behavior is occurring, *i.e*. a blunted velocity profile, in the 0.25% xanthan gum solution. Additionally it can be seen that the secondary flows for the 22% hard-sphere colloidal suspension are markedly larger and more distinct than those for the other fluids. To further probe the information obtained in the velocity images and investigate the flow partitioning and velocity profiles inside the outlet channels, velocity profiles across the small and large bifurcation outlets were plotted against theoretical fits (Poiseuille & Power Law) by averaging across the first 10 pixels of the velocity map *i.e.* the furthest downstream and most fully developed region after the bifurcation in the axial direction as shown in figure 5.6. Least squares fit to each of the velocity profiles was used. The velocity profiles for water, 8% and 22% hard-sphere colloidal suspensions fit a Poiseuille profile whereas the 22% Xanthan gum behaves as a Power Law fluid with a power law constant $n = 0.44 \pm 0.05$ in agreement with typical values [204]. These velocity profiles were integrated to determine the volumetric flow rates (Q) in each of the bifurcation outlets, giving the flow ratios between the large and small outlet channels (Q_{lg}/Q_{sm}) for all four fluids at the three flow rates tested (10mL/hr, 20mL/hr and 30mL/hr). The results of these calculations can be seen in Table 5.1.

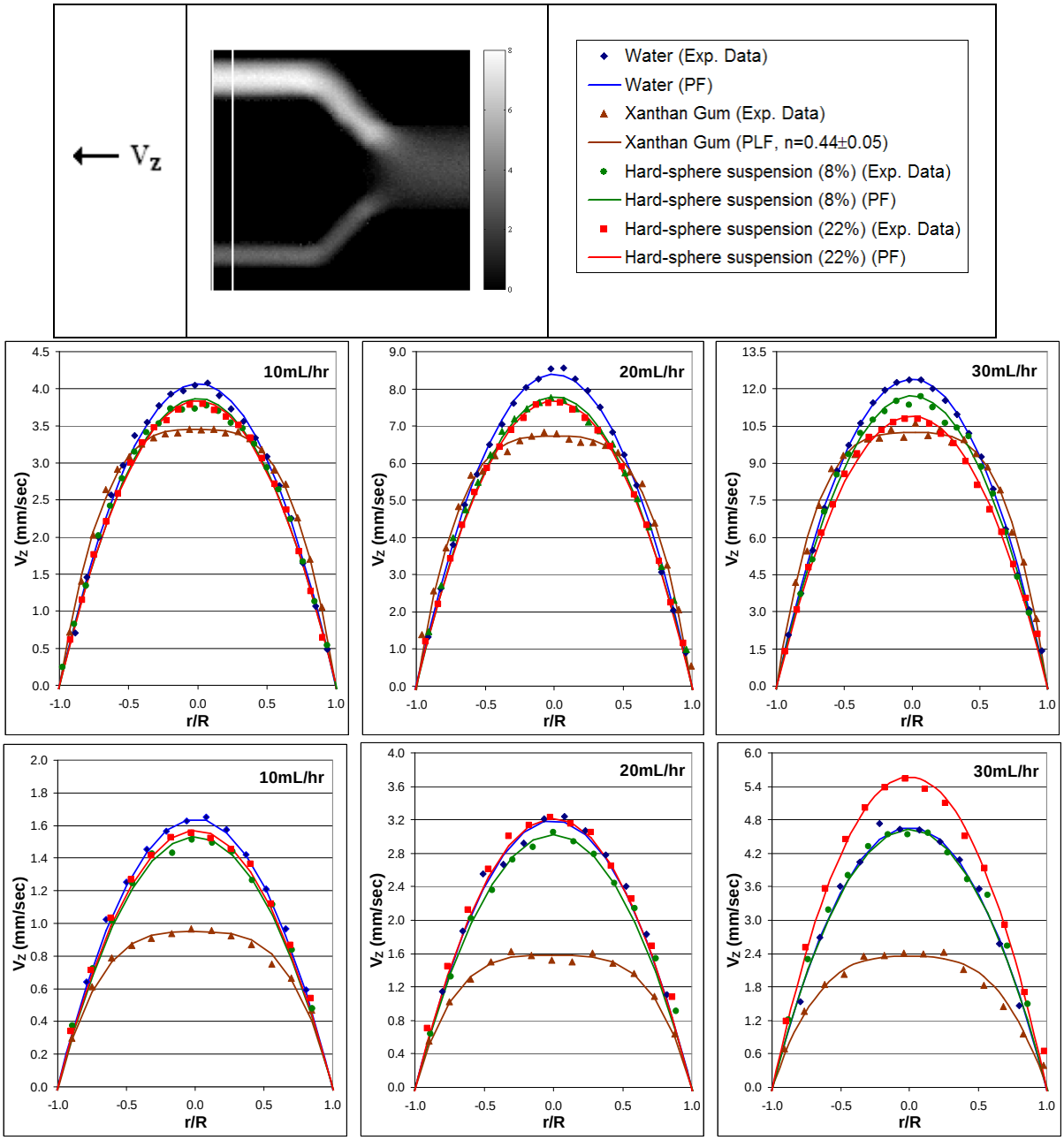

Figure 5.6 The white lines in the top-left image indicate the region of the axial flow (V_z) velocity maps averaged to obtain the velocity profiles. Plots show the velocity profiles for the large (1st Row) and small (2nd Row) bifurcation outlets, at 10mL/hr (1st column), 20mL/hr (2nd column) and 30mL/hr (3rd column). The experimental data (Exp. Data) for the water (diamonds), xanthan gum (triangles), 8% hard sphere colloidal suspension (circles) and 22% hard-sphere colloidal suspension (squares) were fitted (solid lines) with either a Poiseuille Fit (PF) or a Power Law Fit (PLF).

Table 5.1.

Ratio (Q_{Lg}/Q_{Sm})	10mL/hr	20mL/hr	30mL/hr
Water	7.1	7.2	7.2
Xanthan Gum	9.9	11.1	11.6
8% Hard Sphere Colloidal Suspension	7.0	7.0	6.9
22% Hard Sphere Colloidal Suspension	6.8	6.5	5.3

The ratios for water are constant for the three flow rates analyzed and are in good agreement with the theoretical prediction for the Hagen-Poiseuille relation $\mathrm{Q} = \frac{\Delta P}{L}\frac{\pi R^4}{8\mu}$, in terms of hydrodynamic resistance $\frac{\Delta P}{\mathrm{Q}}$ for each channel. The result is $\frac{\mathrm{Q_{lg}}}{\mathrm{Q_{sm}}} = \frac{\mathrm{R_{lg}^4}}{\mathrm{R_{sm}^4}} = 7.3$ for large and small radii. The 8% colloidal suspension maintains a constant volumetric partitioning of flow as the total flow rate varies but with a slightly reduced values from the Hagen-Poiseuille prediction. The xanthan gum shows a trend of increased flow down the larger outlet channel as total flow rate and hence shear rates are increased. This is an expected behavior for a shear thinning fluid. The shear rates are stronger in the larger outlet channel $\dot{\gamma} \propto R$, which generates a lower effective viscosity for the xanthan gum in that channel, leading to lower flow resistance and larger proportion of flow. As the flow rate increases the shear thinning effect is enhanced resulting in increasing flow in the larger channel. The 22% hard-sphere colloidal suspension shows the opposite behavior to xanthan gum despite the fact that slight shear thinning was observed in figure 5.4.

The volumetric flow partitioning toward the larger channel is reduced from the Newtonian case. Surprisingly this is consistent with a shear thickening behavior, with

increased flow resistance in the larger branch. As the flow rates are increased, a decrease of flow down the large outlet channel is observed, while the small outlet channel flow increases, causing a decreasing (Q_{lg}/Q_{sm}) ratio at higher flow rates.

Table 5.2.

	10mL/hr	20mL/hr	30mL/hr
Pe_p (Large Channel) Colloidal Suspension ϕ = 8%/22%	66/28	140/58	190/79
Pe_p (Small Channel) Colloidal Suspension ϕ = 8%/22%	6/3	12/6	20/10

This is a primary result of our study. The bulk rheology of a colloidal suspension does not determine flow partitioning in a bifurcation with flow contractions. For these experiments the Pe_p for both outlet channels at the three flow rates tested (see Table 5.2), ranges from 207 to 652 for the large outlet channel and 142 to 510 for the small outlet channel. These *Pe* numbers are determined from flows after the bifurcation of the fluid and in the bifurcation region, where the fluid bifurcates from a 2.5 mm diameter channel into 1.25 and 0.76 mm channels. There are local regions with higher shear rates, where very high *Pe* number regions exist and the acceleration into the outlet channels particularly at the larger outlet channel, is an explanation for a change in the microstructure of particles in the suspension, causing a jamming effect [107, 108]. To understand this colloidal particle concentration effect it is useful to understand that the overall distribution of fluid into each of the outlet channels is fitted well by a 2D CFD simulation using a shear thickening power law relationship for the viscosity, see figure 5.7.

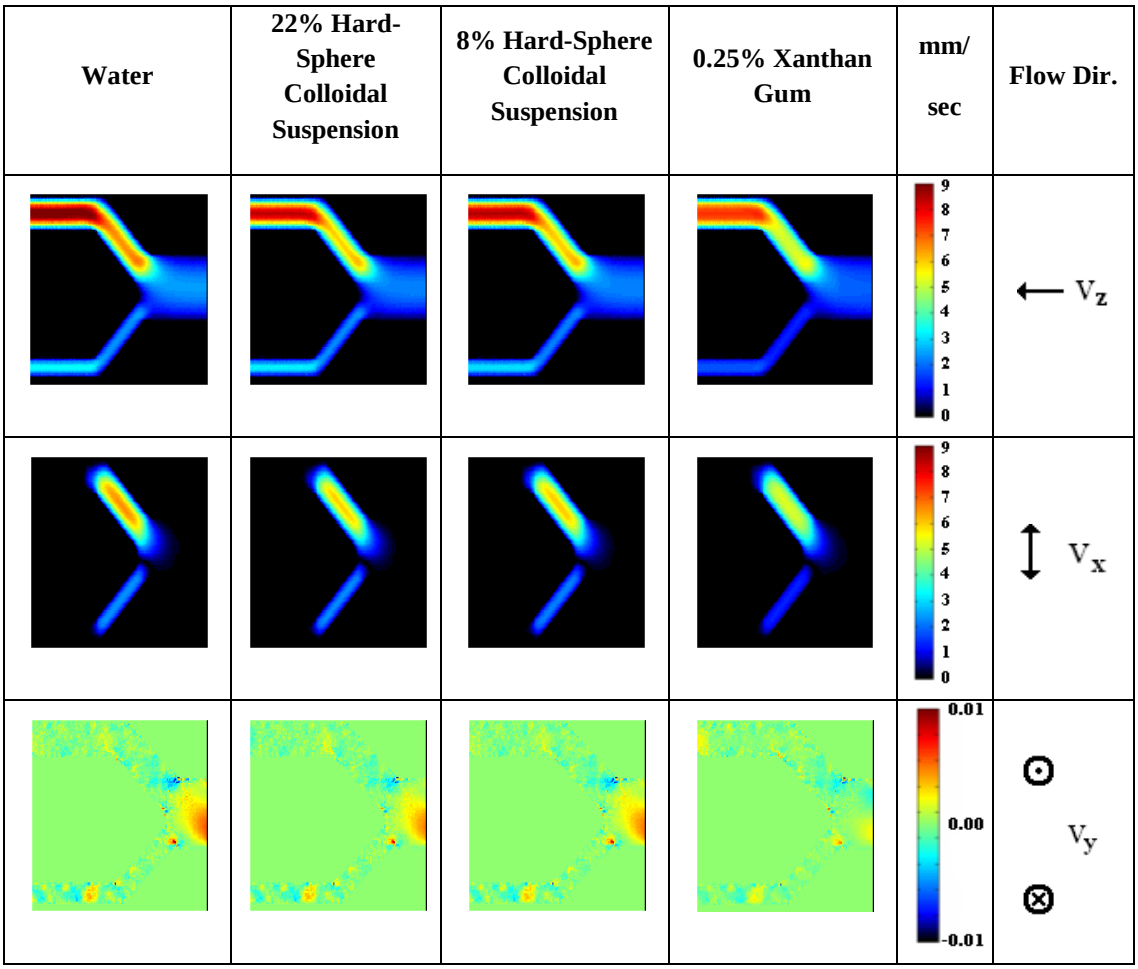

Figure 5.7 Shows the CFD simulation results for comparison to those presented in figure 5.8. The images are averaged and pixilated using Matlab using only points from the midplane of the bifurcation. Three directions of velocity (V_x, V_y and V_z) are presented with fluid flowing from right to left. The scale for the velocity is in mm/sec. The color bar scaling is the same for the V_x and V_z velocity images, but has a different scale for the V_y velocity image.

The non-equilibrium impact of particle jamming due to acceleration and secondary flows is consistent with shear thickening despite the fact that equilibrium rheological measurements characterize the suspension as Newtonian. In the MRM velocity images secondary flows can be seen in the slice direction (V_y) for the four different fluids.

To quantify the difference in secondary flow between the four fluids shown in figure 5.8, the mean velocity magnitude per pixel $\bar{V}_{fluid} = \frac{\Sigma_i^M \Sigma_j^N |V_{i,j,fluid}|}{MN}$ in the bifurcation was calculated and then normalized, $\beta = \frac{\bar{V}_{fluid}}{\bar{V}_{water}}$, so for water β = 1.00, for Xanthan gum β = 0.53, for the 8% hard-sphere colloidal suspension β = 1.10 and for the 22% hard-sphere colloidal suspension β = 3.79.

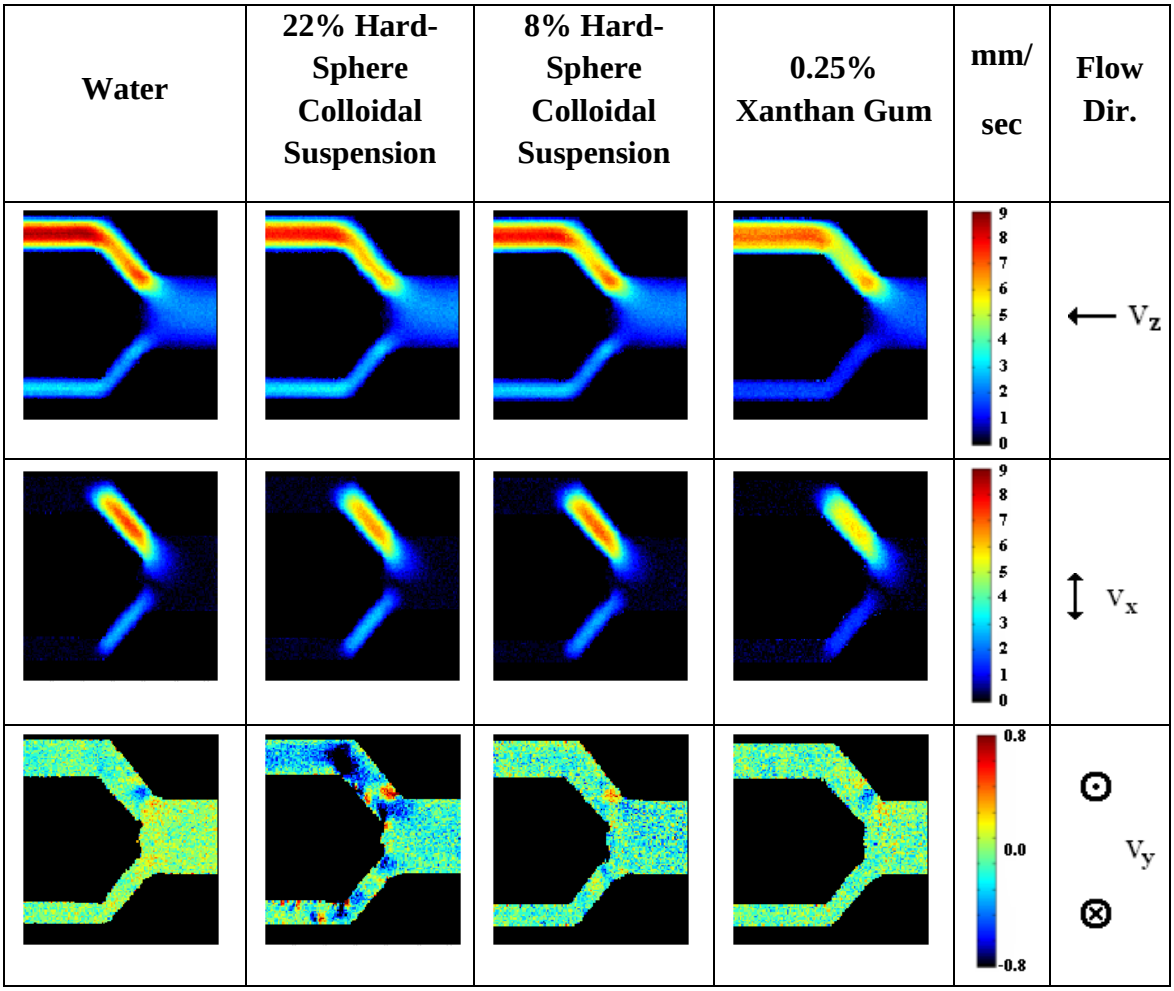

Figure 5.8 Dynamic MRM images of velocity. The images are a 200μm thick slice in the center of the bifurcation encoded for three directions of velocity (V_x, V_y and V_z). The X, Y and Z directions correspond to those presented in figure 5.5. Fluid flows from right to left at 20mL/hr. The scale for the velocity is in mm/sec. The color bar scaling is the same for the V_x and V_z velocity images, but have a different scale for the V_y velocity image.

Looking at figure 5.8, the secondary flow for water can be seen with velocities directed into and out of the slice at the larger outlet channel. When compared with the secondary flow for the Xanthan gum, it can be seen that the intensity of the secondary flow has been decreased in the channel indicated quantitatively by the reduced β value. The 8% hard-sphere colloidal suspension shows little difference with that of water, except for the direction of the secondary flow. However, the increase in secondary flow seen in the 22% hard-sphere colloidal suspension is significant. Although not shown, there is a sudden increase in the secondary flow for the 22% hard-sphere colloidal suspension when the flow is increased from 10mL/hr (β = 1.03, normalized by water at 10mL/hr) to 20mL/hr (β = 3.79) indicating a shear threshold for the onset of microstructural states inducing the observed secondary flow.

The context of the research presented in this study can be found in the detailed studies of particulate flow through arterial and microcapillary bifurcations. Some of these studies model T- and Y- shaped bifurcations and use model spheres to determine the flow characteristics and separation effects [208-210]. In this study a unique cylindrical laser etched bifurcation is used; it is important to emphasize the importance of the geometry, the inflow conditions, and the division of flow into the branches to the details of the local flow field, since individual variability is the rule rather than the exception for parameters such as branch angle, ratio of daughter branch to parent vessel area and flow division [211]. As is to be expected for nonlinear nonequilibrium phenomena the bifurcation studied has significant flow contractions into each outlet branch (3.5:1 for the small branch and 2:1 for the larger branch based on inlet channel

and outlet channel diameters) and stagnation regions due to these contractions. Due to the importance of these flow contractions on secondary flow generation it is important to consider similarities in flow contraction research. [212] have solved the general equations of motion numerically for laminar isothermal flow of Newtonian fluids through a contraction; they observed the formation of a stationary vortex just inside the downstream tube for an axisymmetric contraction for a 1:3 ratio contraction at Re = 150, while signs of a separation were computed at Re as low as 20. Xia *et al.* [213] have seen indications of secondary flow in a Newtonian fluid around the abrupt junction of a 1.61:1 contraction at Re = 12 using dynamic NMR microscopy with a Newtonian fluid. Karino *et al.* [210] studied the secondary flows in a T-bifurcation (without a sudden contraction) with 3mm inlet diameter and branching diameter (d) ratios ranging from d/D = 0.33 to d/D = 1 with the angle between branches of 30^o, 45^o, 60^o and 90^o, over a range of inlet Re = 10 to 350. Vorticities were seen to form in both branches after the bifurcation and were found to depend on the ratio of volumetric flow rates and Reynolds number. The formation of vorticities in both branches was studied as a function of a critical Reynolds number (Re_c). For this geometry the larger vortex in the main outlet branch would not form at the flow split present in our study ($Q_{lg}/Q_{sm} > 5$) but as the angle between the branches is increased the vortex in the smaller channel will form at lower and lower Re_c: for the 90^o branch it occurs for $Re_c \sim 15$.

Given these results on axisymmetric contractions and bifurcation, it is not unexpected to observe the secondary flow at the sharp corner of an asymmetric contraction as can be seen for all four fluids presented in figure 5.8. The main reason for

the secondary flow present at the outer edge at the entrance of the larger inlet branch is because the fluid streamlines cannot abruptly change direction because of the sharp angle in that region of the geometry.

The simple CFD results for V_x and V_z for the four fluids presented in figure 5.7, match the results shown in figure 5.8, with slight discrepancies present because of the finite slice thickness of the MRM results in these two velocity directions, showing that the flow partitioning of fluid into each outlet capillary is preserved using the viscosity models presented in section 5.3.3, particularly that a shear thickening model serves well for the 22% hard-sphere colloidal suspension. For the secondary flow into and out of the slice shown in V_y, there is significant difference with the MRM results because of the factors mentioned previously, *i.e.* finite slice thickness and imperfect matching of flow geometries. Additional errors occur due to the small velocity magnitudes involved, *i.e.* barely larger than those due to noise, and limitation of simulation capacity due to the fine mesh needed to capture the subtle variations at the sharp boundaries. As for the MRM results β values were calculated for the different fluids, for water $\beta = 1.00$, for Xanthan gum $\beta = 0.66$, for the 8% hard-sphere colloidal suspension $\beta = 0.88$ and for the 22% hard-sphere colloidal suspension $\beta = 0.89$. It can be seen that the secondary flow reduction due to Xanthan gum seen in the MRM data is captured in the simulation. For the 8% hard-sphere colloidal suspension the simulation predicts secondary flows of the order of those for water, which is consistent with the MRM results. However, for the 22% hard-sphere colloidal suspension the simulation predicts similar secondary flows as those for the 8% hard-sphere colloidal suspension, but the MRM results show secondary

flows of much higher order. It is to be expected that the simplified shear thickening viscosity mode for the 22% hard-sphere hard sphere colloidal suspension will not capture the secondary flows caused by the changing microstructure states of the colloidal particles in the real system.

Propagators

To get information about the partitioning of particle distribution into each of the outlet channels, propagators were obtained for the 22% hard-sphere colloidal suspension as outlined above in the section 5.2.2. The magnetic field gradient is applied so the propagators measure the displacement perpendicular to the axial flow in the channels. First a combined water and oil propagator was obtained for the three flow rates to get the overall flow of suspension into each of the channels. Then the suspension was doped with Magnevist to cause rapid T_1 relaxation of the water phase leaving the signal from the oil inside the shell detectable during signal acquisition; this allowed for the measurement of only the particle phase propagator for each of the three flow rates as shown in figure 5.9. Slice and displacement measurements were chosen such that negative displacements were due to spins in the larger channel, while positive displacements were due to spins in the smaller channel. Given that we have detected the overall suspending water and particle flow into each of the two channels with the second set of propagator experiments, we are able to find the relative concentration of colloidal particles in each channel, at each flow rate, shown in Table 5.3. This allows the determination of the volume fraction (ϕ) in each of the outlet channels. The data indicate a volume fraction decrease from the mean value of 22% in the larger branch and a corresponding increase in the small branch.

A potential NMR artifact which could impact the data is dephasing of the NMR signal due to motion of the particles generated by the secondary flows which are more predominant in the larger channel. If the particle motions induced by the secondary flows appear random *i.e.* are decorrelated, over the Δ = 25ms displacement observation time dephasing of the signal analogous to diffusion effects may be present [214].

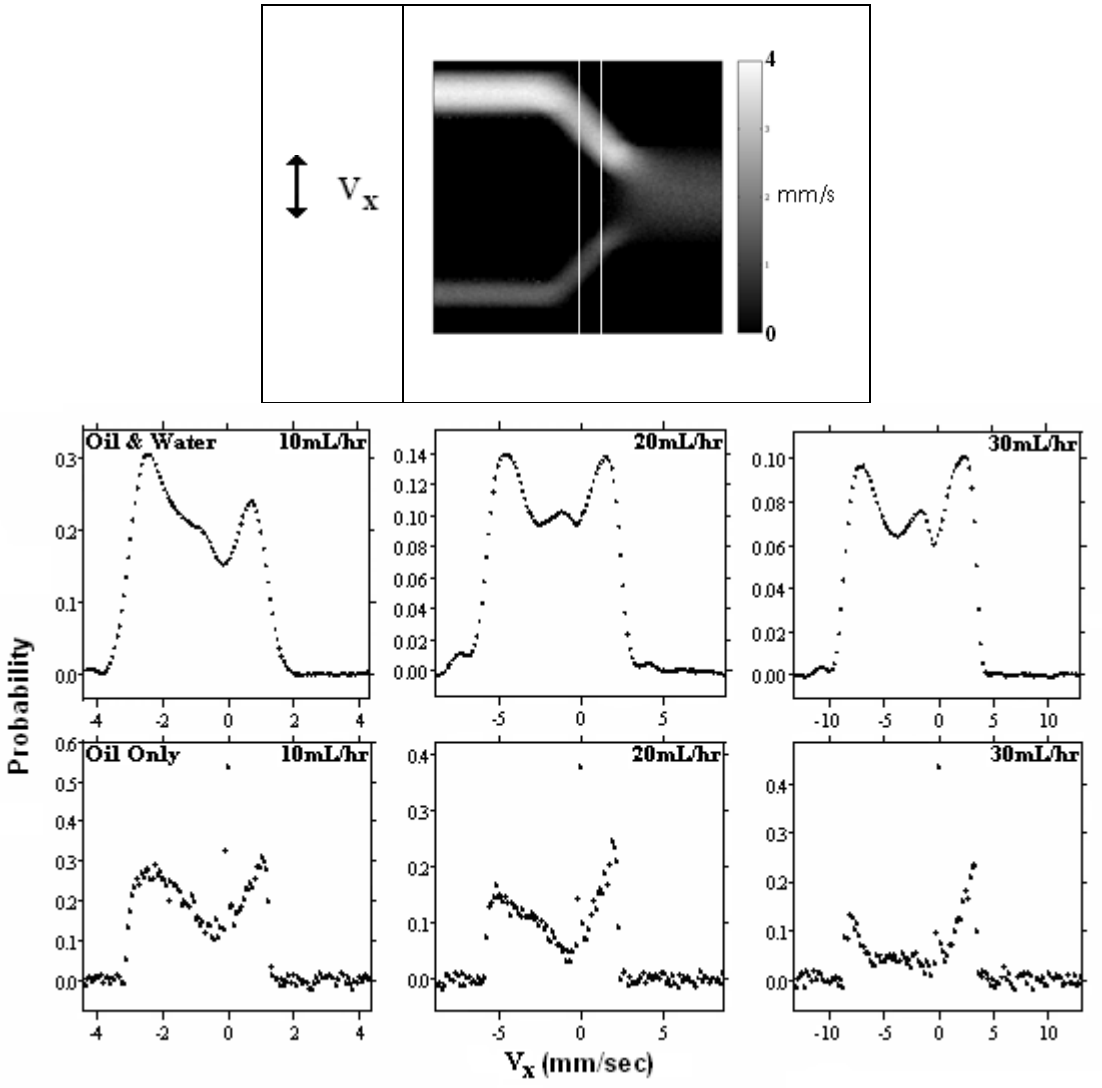

Figure 5.9 The white lines in top image indicate the region excited to obtain the propagators for the combined water & oil signal (middle) and only the oil signal of the particles (bottom) for a 22% hard-sphere suspension at flow rates 10mL/hr (1st column), 20mL/hr (2nd column) and 30mL/hr (3rd column).

Table 5.3.

22%wt Colloidal suspension	Flow Rate:	10mL/hr	20mL/hr	30mL/hr
Water & Oil Propagator	Large Outlet (%)	72.3	68.7	67.9
	Small Outlet (%)	27.7	31.3	32.1
Oil Propagator	Large Outlet (%)	69.0	67.1	65.3
	Small Outlet (%)	31.0	32.9	34.7
Volume Fraction (ϕ)	Large Outlet	0.210	0.215	0.212
	Small Outlet	0.246	0.231	0.238

Mass conservation calculations indicate this effect is small. It is interesting to observe that the volume fraction partitioning appears constant with flow rate given the sudden increase in secondary flows from 10mL/hr to 20mL/hr. This manifests itself as a spike at zero displacement in the oil propagator due to particles at the wall with zero displacement. This spike in probability is not considered when calculating the concentration of oil in each of the outlet channels. The additional bump on the combined water and oil propagator at low negative displacements in the larger outlet channel is due to an increase in secondary flow that causes a higher probability of less displacement over the experimental period Δ = 25ms. The larger outlet channel experiences stronger secondary flow than the smaller outlet over the excited slice region and the particles are entrained in the secondary flow structure.

Conclusions

Velocity maps in all three spatial directions characterize the fluid mechanics inside the flow bifurcation system studied. These include primary and secondary flow information for several fluids of differing constitutive behavior. The velocity profiles of each fluid in the outlet capillary branches of the system provide information about the fluid partitioning at the bifurcation as well as the fluid properties. Power law and Newtonian models gave good fits to the experimental data for 0.25% xanthan gum and water, respectively. An 8% hard-sphere colloidal suspension showed fluid behavior compatible with a Newtonian fluid. An interesting result is the increased flow partitioning for the 22% hard-sphere colloidal suspension toward the smaller channel as the flow rate increases. The ratio Q_{lg}/Q_{sm} decreases as flow rate increases for the 22% hard-sphere colloidal suspension, in contrast to an increasing partition toward the large channel with increasing flow rate for the xanthan gum. This indicates a shear induced effect on the colloidal suspension not predicted by the bulk rheology of the suspensions, causing less fluid to enter the capillary with the higher shear rates. The reverse of this behavior was seen for the shear thinning xanthan gum solution. Nonlinear effects such as particle jamming [107, 108] and microstructural rearrangement [197] may be responsible. The propagator measurements of the signal from the oil inside the particles of the colloidal suspension provide a powerful method for examining separation phenomena inside any NMR suitable flow separation device. This partitioning behavior in bifurcations is important in physiological and microfluidic systems and dynamic MRM provides the portioning behavior directly. Dynamic magnetic resonance microscopy

“particle counting” in a microscale bifurcation has been demonstrated indicating the potential for NMR microfluidic logic gates [195, 196]. The presence of particulates alters the flow partitioning significantly due to particle hydrodynamics and microstructure.

COLLOIDAL PARTICLE DEPOSITION IN POROUS MEDIUM

Introduction

The study of flow through porous media is a rich field encompassing many phenomena of interest in natural and technological settings [215-218]. The non-invasive nature and ability to spectrally resolve different chemical species using Nuclear Magnetic Resonance (NMR) allows for detailed study of the flow characteristics of complex fluids inside a porous medium [219]. Here we study the transport and deposition of hard sphere colloidal particles (radius, $a = 1.25 \pm 0.46\mu m$) in a model porous medium (monodisperse 240μm diameter spheres packed into a 10 mm I.D. liquid chromatography column) and observe the effect deposition has on the flow dynamics through the medium. Pulsed Gradient Spin Echo (PGSE) NMR techniques [1] are used to characterize the flow of water through the medium before and after deposition. The deposition occurs when 20mL of 10wt% hard-sphere colloidal suspensions are pumped through the bead pack, after which the bead pack is flushed with DI water before NMR experiments are conducted. This allows for an observation of the "steady state" dynamics of a Newtonian fluid after various degrees of colloidal deposition have occurred inside the model porous medium. PGSE NMR has found broad application in the study of porous media due to the unique information available by non-invasively probing the internal structures. Many studies have involved single phase Newtonian fluids and non-Newtonian fluids, while those for two or more phases of liquids are scarcer [220-222]. The study of hard-sphere colloidal suspension flow through a porous medium and the observation of both phases

simultaneously is almost non-existent. Prominent exceptions being the recent work of Brosten *et al.* [223] on hard sphere flow in a solid cellular foam. Creber *et al.* [224] have measured the dynamics of an emulsion Much of the previous research on colloidal flow through porous media has involved measuring tracer break through curves [218] which are used to infer the porous media dynamics through an assumed equation modeling the transport. The degree of deposition is determined from these break through curves while the measurement of local concentration has involved invasive techniques.

Theory

In discussing the theory of colloidal transport in a porous medium it is simplest to begin with single phase fluid flow and introduce the relevant dispersion processes. It is the relative importance of these dispersion processes that gives insight into the differences between Newtonian and non-Newtonian fluid flow through the porous medium. After discussing the relevant dispersion processes, models will be introduced which capture both the flow and deposition of colloidal particles inside the porous medium.

Hydrodynamic Dispersion in Porous Media

The non-steady, irreversible spreading of flowing fluid molecules within a porous medium is known as hydrodynamic dispersion. It is the process in which a mass of solute at time $t = 0$, within the flow domain, spreads and occupies an ever-increasing region of the porous media as time increases $t > 0$. It is governed by both mechanical (convective) dispersion and molecular diffusion. A thorough review of the subject matter

can be found elsewhere [31, 225] and only a brief overview will be given here. The dispersion of a fluid in a porous media is impacted by the degree of interconnectivity of the pore space and provides an insight into the morphological characteristics of the porous structure. A large number of dispersion experiments in porous media have been conducted on Newtonian and non-Newtonian fluids [226]. Due to the shear dependence of the viscosity of non-Newtonian fluids as well as their memory effects (*i.e.* visco-elastic fluids), the behavior of non-Newtonian fluids can deviate significantly from those of Newtonian fluids in the same porous media. A useful dimensionless number to characterize dispersion in porous media is the Péclet number (*Pe*) which is the ratio of convective to diffusive transport rates and can be written [219]

$$Pe = \frac{\langle v \rangle l}{D_0} \quad (6.1)$$

where

$$l = \left(\frac{\phi_{liq}}{1-\phi_{liq}}\right) d_p \quad (6.1a)$$

where $\langle v \rangle$ is the fluid's mean interstitial velocity through the system in the axial direction, l is the characteristic length of the system, ϕ_{liq} is the liquid volume fraction or porosity, d_p is the porous media particle diameter and D_0 is the self diffusion coefficient of the fluid. Dispersion can arise from three different processes (see figure 6.1), and quantified by the dispersion tensor $\boldsymbol{D}_{ij}$:

(i) **Mechanical dispersion** occurs due to the bifurcation of streamlines, producing a stochastic velocity field due to the different paths that initially adjacent fluid elements follow as a result of the porous media geometry. This effect promotes mixing in the fluid volume and is purely hydrodynamic, *i.e.*

independent of molecular diffusion [227]. Mechanical dispersion scales with the *Péclet* number, $D^* \sim Pe$, and is the dominant process in dispersion at high *Pe*. It is however never the sole dispersion process as Saffman [227] showed that even at very high *Pe* the other dispersion processes still contribute to the overall dispersion generating a $D^* \sim PeLnPe$ scaling.

(ii) **Taylor dispersion** [59, 228] is the process by which fluid molecules move transversely across streamlines due to Brownian motion causing a spreading of a fluid element over time; this process scales as $D^* \sim Pe^2$ [219] and is the dominant mechanism in ordered porous media [229].

(iii) **Hold-up dispersion** occurs in volume elements inside the porous media where there is effectively no velocity and the only process by which molecules can leave this region and re-enter the flow is due to diffusion processes. It therefore scales as $D^* \sim Pe^2$ [219]. It is probable for many porous media that hold-up dispersion is a negligible contributor when compared to Taylor and mechanical dispersion, dependent on the relative quantity of fluid volume held-up in dead end pores.

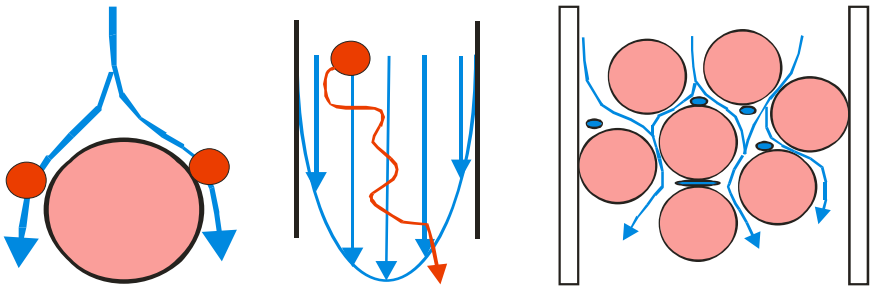

Figure 6.1 Shows the three different dispersion processes [219]: (a) Mechanical dispersion, (b) Taylor dispersion and (c) hold-up dispersion. Each image indicates how each process is a either purely convective (a) a mixture of convective and diffusive (b) or purely diffusive (c). Courtesy S.L.Codd.

In the region of *Pe* number from approximately 100 to 1000 the above processes have been seen to combine with a power law scaling as Pe^{α}, where α describes the degree to which each process dominates the others [219].

In the work presented in this thesis, only two components of the dispersion tensor, $D_{\parallel}$ and $D_{\perp}$, where ∥ and ⊥ refer respectively to the directions parallel and perpendicular to the flow direction, will be considered. This allows us to write the effective dispersion coefficient, *D**, as [31]

$$D^*(t) = \frac{1}{2}\frac{d\sigma^2(t)}{dt} \quad (6.2)$$

where $\sigma^2 = \langle(\xi - \langle\xi\rangle)^2\rangle$ is the variance of the distribution of displacement ξ for a particular time Δ. As $\Delta \to \infty$, *D** asymptotes, *i.e.* all fluid elements experience all possible regions of the sample environment and are therefore all equivalent. Under these circumstances $d\sigma^2/_{dt}$ becomes a constant (*D** = constant), and the dispersion is Fickian in nature, with the probability distribution of displacement (the average propagator) assuming a Gaussian profile [31] described as

$$P(\xi, \Delta) = \frac{1}{\sigma\sqrt{2\pi}} exp\left[-\frac{1}{2}\frac{(\xi - \langle v_z\rangle\Delta)^2}{\sigma^2}\right] \quad (6.3)$$

In his work, Saffman [227] described the axial component of the dispersion tensor through a network of randomly orientated capillaries as

$$D_z = \frac{\langle v_z\rangle d_p}{6}\left(ln\left[\frac{3Pe}{2}\right] - \frac{1}{4}\right) \quad (6.4)$$

This result allows for a direct comparison between the measured results for a porous media and theory.

The hydrodynamic dispersion in porous media allows for a useful framework for the extension to non-Newtonian fluids as the relative importance of dispersion processes can be measured. This can be done by obtaining NMR Stejskal-Tanner plots at different *Pe* numbers and plotting the dispersion coefficient as a function of *Pe*. The slope of this plot indicates which processes are dominant and then a comparison of the Newtonian fluid results with the non-Newtonian fluid results provides insight about the transport. Models based on Continuous Time Random Walk's (CTRW's) have been developed to investigate the effects of local dispersion on particle deposition [230]. The local dispersion can be successfully measured using PGSE NMR techniques [219], which also allows measurements free of entrance effects and requires no assumptions regarding the governing mass transport equation inherent in break through curve methods [231, 232]. The NMR experiments presented here probe the long time limit of colloidal deposition, as the times at which NMR data are obtained are usually much greater than the transient "clean-bed removal" filtration phase [232]. At this "steady" state the rate of colloidal attachment and flow has equilibrated so that the solute and colloid dynamics can be assumed to be steady state.

A simple but very useful first approximation in quantifying flow through porous media is Darcy's law [31]. This is a phenomenologically derived constitutive equation, that describes the flow of a fluid through porous media and can be written as

$$Q = \frac{kA}{\eta}\frac{\Delta P}{L} \quad (6.5)$$

where Q is the volumetric flow rate, k is the conductivity, permeability or hydraulic "ease of transport" of a fluid through the porous medium and is determined by the pore

structure [233, 234], A is the total cross-sectional area, η is the fluid viscosity and ΔP is the pressure drop in the direction of flow across a sample of length L. By using Darcy's law it is possible to relate the superficial velocity v_s, *i.e.* the average velocity of the cross section entering the porous media to the permeability k

$$v_s = \langle v \rangle \phi_{liquid} = \frac{Q}{A} = \frac{k}{\mu}\frac{\Delta P}{L} \quad (6.6).$$

For multiphase fluids, Darcy's law can be augmented by replacing k by k_i in the above expression, where k_i is the permeability for phase i allows the calculation of the superficial velocity of each phase.

Colloidal Deposition in Porous Media

As seen in Chapter 3, there are many simulation methods available to model colloidal transport. However, it is very difficult to combine a complex fluid with a complicated flow boundary structure in a simulation and limited work is available currently for simulations that account for all the intricacies of colloidal transport mentioned in chapter 3 and those to be discussed in this section. The emphasis at the moment is on coarse graining on a scale greater that the pore size of the colloidal transport dynamics to allow for simplified but accurate models. In addition to the mechanisms discussed in chapter 3 that govern the viscosity shear dependence ($\eta_{eff} = \eta(\phi, Pe)$) and shear induced migration of colloidal particles ($\phi(r, Pe(r))$), there is a requirement in porous media to account for the particle deposition inside the porous structure. This can have drastic effects on the flow field within the medium, and change the relative importance of the various dispersion processes on the overall transport

dynamics. Colloidal particle [235-238] deposition is usually modeled by using one of two theoretical approaches to calculate the particle deposition rate onto model collectors (monodisperse spheres in this work) from flowing suspensions. These theoretical approaches are dependent on the reference frame used and are categorized as Lagrangian and Eulerian methods [232, 236, 237]. Lagrangian methods follow the particles as they approach a collector surface, with the frame of reference being relative to the particle. Whereas Eulerian methods follow the particle concentration in time and space and are in a frame of reference relative to the porous media/background structure. The Lagrangian frame of reference is the way PGSE NMR measures a system while the Eulerian frame is most similar to how a system is seen through optical microscopy or by macroscopic observation. Of course with enough information about a system each frame of reference can be recast in the other frame of reference. Inclusion of a thermal random force (Brownian effects) in the equation of motion for the Lagrangian dynamics leads to a Langevin equation governing colloid particle dynamics (see chapter 3). This approach requires multiple simulations of the dynamics of Brownian particles where the motion is eventually averaged, *i.e.* by a Monte Carlo method, or canonical ensemble in molecular dynamics, to acquire a result. This can be compared with the relatively easier Eulerian methods which are concerned with obtaining the concentration distribution (or probability density) of particles in space. Such distributions are described by a set of coupled partial differential equations termed the Fokker-Plank equations [235-238]. For example modeling normal diffusion in an external force field $F(x) = -dV'(x)/dx$

$$\frac{\partial P(x,t)}{\partial t} = \left[\frac{\partial}{\partial x}\frac{V'(x)}{m\eta_1} + D\frac{\partial^2}{\partial x^2}\right]P(x,t) \quad (6.7)$$

where m is the mass of diffusing particle and η_1 denotes the friction constant characterizing the interaction between the test particle and the suspending fluid. The first term on the RHS can represent a drift velocity in terms of a potential $V'(x)$ while the second term is the diffusion. In dilute suspensions of spherical particles where interparticle interactions can be neglected, the Fokker-Plank equation reduces to the common continuity equation or the Advection Diffusion Equation (ADE) [239].

The Advection-Diffusion Equation (ADE)

The ADE arises at the pore scale from mass (probability) conservation on the continuum fluid scale in the porous media. The ADE in its general form can be written as [237, 240]

$$\frac{\partial C}{\partial t} + \boldsymbol{\nabla} \cdot \boldsymbol{J} = Q \quad (6.8)$$

where C is the particle concentration, particle location or probability when normalized, Q is a source term and $\boldsymbol{J}$ is the particle flux vector. The form of the flux depends on the constitutive relation and for normal diffusion (Fickian) can be written as

$$\boldsymbol{J} = -\boldsymbol{D} \cdot \nabla C + \boldsymbol{U}C + \frac{\boldsymbol{D} \cdot \boldsymbol{F}}{k_B T} C \quad (6.9)$$

where $\boldsymbol{D}$ is the particle diffusion tensor, $\boldsymbol{U}$ is the particle velocity, T is the absolute temperature, k_B is the Boltzmann constant and $\boldsymbol{F}$ is the external applied force vector. The 1st, 2nd and 3rd terms in Eqn. 6.9 are respectively the particle transport due to diffusion, advection and external forces. In liquid systems the relevant particle deposition forces are colloidal ($\boldsymbol{F_c}$) and gravitational ($\boldsymbol{F_g}$)

$$\boldsymbol{F} = \boldsymbol{F_c} + \boldsymbol{F_g} \quad (6.10)$$

For the systems in this work the gravitational term is negligible ($\boldsymbol{F_g} \rightarrow 0$) and therefore we will only be interested in the colloidal force ($\boldsymbol{F_c}$) which acts between the suspended colloids and collector surfaces, and can be written in terms of a total interaction potential, $\boldsymbol{F_c} = -\boldsymbol{\nabla V^{total}}$. Using classical Derjaguin-Landau-Verwey-Overbeek (DLVO) theory [241-244] $\boldsymbol{V^{total}}$ is the sum of van der Waals and electrical double layer interactions. Other non-DLVO interactions can be added to this term also. By combining Eqn. 6.8 and 6.9 we obtain an expression for the ADE

$$\frac{\partial C}{\partial t} = -\boldsymbol{\nabla} \cdot (\boldsymbol{U}C) + \boldsymbol{\nabla} \cdot (\boldsymbol{D} \cdot \boldsymbol{\nabla} C) + \boldsymbol{\nabla} \cdot \left(\frac{\boldsymbol{D \cdot V^{total}}}{k_B T} C\right) \quad (6.11).$$

This equation provides the basis for several colloid deposition models, such as the Smoluchowski-Levich and the interaction force boundary layer approximations [245]. The classical ADE assumes that both the velocity vector ($\boldsymbol{U}$) and the diffusion tensor ($\boldsymbol{D}$) can be assumed to be constants (v_0, D) allowing the rewriting of Eqn. 6.11 as

$$\frac{\partial C}{\partial t} = -v_0 \boldsymbol{\nabla} C + D \boldsymbol{\nabla^2} C + \nabla \Phi \quad (6.12)$$

where Φ is the external force, $\Phi = \frac{\boldsymbol{D \cdot V^{total}}}{k_B T} C$. If only advection and diffusion affect the motion of a tracer particle through the porous medium then $\Phi = 0$, and we obtain

$$\frac{\partial C}{\partial t} = -v_0 \boldsymbol{\nabla} C + D \boldsymbol{\nabla^2} C \quad (6.13)$$

Equations analogous to 6.12 and 6.13 have been heavily used in quantifying transport through porous medium, with the Φ term getting particular attention in the next sections. To obtain $C(\mathbf{x})$ from the ADE, proper boundary conditions for the collector surfaces must be specified. Two simplifying models that are commonly used are the perfect sink model [246] and the non-penetration boundary condition [247], and are respectively

$$C = 0 \text{ at } h = 0 \quad (6.14a)$$

$$J_{\perp} = 0 \text{ at } h = 0 \quad (6.14b)$$

where h is the height from the surface of the colloid to the surface of the collector. Eqn. 6.14a is used to obtain the Smoluchowski-Levich approximation [237] and interaction force boundary layer approximation [248] and assumes that all particles that arrive at the collector surface are irreversibly immobilized and disappear from the system. Alternatively Eqn. 6.14b is used to overcome the limitation of not accounting for accumulation of particles by assuming that the particles cannot penetrate the collector surface and is a no flux boundary condition.

Anomalous Transport in Porous Media

Anomalous transport processes can be categorized by a Mean Square Displacement (MSD) which varies non-linearly in time [56]. In porous media transport this definition extends to any transport that does not follow Fickian or normal diffusion transport with constant diffusion and Einstein linear in time variance scaling $\langle z^2 \rangle = 2Dt$, *i.e.* the classical ADE. Decades of research have focused on how to quantify contaminant transport in porous medium and the majority of studies have used the classical ADE [249], which assumes a constant velocity (v_0) and constant diffusion coefficient (D). It has however been seen as far back as 1959 [250] that there is a systematic error in fitting Break Through Curves (BTC), *i.e.* fit to the cumulative distribution of the probability of colloidal particles in the effluent using the classical ADE. It has been demonstrated convincingly by laboratory experiments and modeling that there is generally a scale dependence in the dispersion, or effective diffusion, coefficient [251, 252], contrary to

what is assumed in the classical ADE. The classical ADE also assumes complete homogeneity on the measurement scale of the porous media, while MRI experiments repeatedly show that even with carefully packed monodisperse beads there is significant heterogeneity which causes the existence of preferential flow paths. When tracer experiments resulting in BTC are compared with the classical ADE prediction, the measured BTCs have an anomalous early and late arrival time difference [253]. This behavior has been termed anomalous, or non-Fickian, because the diffusion behavior is scale dependent and does not follow normal diffusion scaling. Even with knowledge about the inaccuracy of the ADE, it has remained the basic equation for describing tracer transport in both fully and partially saturated porous media [249].

Recently, there have been efforts to quantify this non-Fickian behavior, including stochastic perturbative approaches, employing an ensemble-averaged ADE [254] and the more successful continuous time random walk (CTRW) theory [56], a non-perturbative probabilistic modeling framework which has successfully quantified non-Fickian transport in porous media at various scales [231]. The CTRW theory is particularly well suited to capturing the early and late arrivals of tracers measured in BTCs and has been successfully re-applied to classical studies with great success [231].

Additional concerns with the current approaches to modeling colloidal transport involves the use of the DLVO theory [244] of interparticle interactions, which treats colloid stability in terms of a balance between attractive van der Waals forces and repulsive electrical double-layer forces. Although this theory is heavily used to fit experimental data, the agreement is poor because agreement is only achieved by invoking

fitting parameters to accommodate surface potential or charge. Deviations to the theory are usually accounted for by invoking a "zoo" of so called "extra-DLVO" forces [255]. It has been shown that DLVO theory works well for low concentrations of ions of order 0.01M, but it is often wrong for the biological regime or any system where the concentration of ions is of the order of 0.1M or higher [255]. This can be attributed to the separation of the two forces: electrostatic (non-linear Poisson-Boltzmann theory) and the van der Waals (linear Lifschitz theory) because they must be handled at the same level for a correct description to emerge [255].

Colloid Filtration Theories

Filtration theories describe the deposition of particles during the "clean bed removal" stage, where the filtered bed is modeled as groupings of unit collectors of a particular geometry. The fluid flow around or through this geometry is described analytically using theories on low *Re* number hydrodynamics [256]. The unit collector removal efficiency η, *i.e.* ratio of number of particles deposited to the number of particles convectively transported towards the collector; for the single collector is

$$\eta_0 = \frac{I}{UC_0\pi a_c^2} \quad (6.15)$$

where C_0 is the bulk concentration, U is the fluid approach velocity and I is the actual deposition rate on a collector with radius a_c. For a granular filter composed of uniform spheres a mass balance can be used to obtain [257]

$$ln(C/C_0) = -\frac{3}{4}\frac{(1-\phi)\eta L}{a_c} \quad (6.16)$$

where ϕ is the porosity and L is the depth of the granular medium.

In practice an empirical collision/attachment efficiency (α) is introduced as a weighting from 0 to 1 of the calculated single collector removal efficiency (η_0) to obtain the overall collector removal efficiency

$$\eta = \alpha\eta_0 \quad (6.17).$$

Since the flow field around an individual spherical collector is influenced by neighboring collectors, various flow models have been produced to describe the flow field in a packed bed of spherical collectors. Of these models Happel's sphere-in-cell model [258] is the most commonly used. We will now discuss two useful models to describe η: the Interaction force boundary layer (IFBL) approximation and Rajagopalan and Tien's correlation equation.

Interaction Force Boundary Layer (IFBL)

IFBL assumes a boundary layer, characterized by the Debye length, so that the colloidal interactions can be characterized as dominant close to the collector surface in a region where convective forces are negligible, and an outer layer where colloidal interactions vanish while convective forces are important. Using this approach Spielman and Frielander [259] obtained the following expression for the collector removal efficiency η

$$\eta = 4A_S^{1/3}\left(\frac{D_\infty}{2a_cU}\right)^{2/3}\left(\frac{\beta}{1+\beta}\right)S(\beta) \quad (6.18a)$$

$$\beta = \frac{\sqrt[3]{2}}{3}\Gamma\left(\frac{1}{3}\right)A_S^{-1/3}\left(\frac{D_\infty}{Ua_c}\right)^{-1/3}\left(\frac{k_Fa_c}{D_\infty}\right) \quad (6.18b).$$

Here A_S is a porosity dependent parameter of Happel's sphere-in-cell model, D_∞ is the colloid bulk diffusion coefficient, k_F is a pseudo-first-order rate constant accounting for

the retardation effect of double layer repulsion on deposition rate and $S(\beta)$ is a function tabulated by Spielman and Friedlander [259]. In the limit of no colloidal or hydrodynamic interactions, $\beta \to 0$, $S(\beta) = 1$, we obtain the Smoluchowski-Levich approximation for capture of small, Brownian colloids in a porous medium [237, 257]

$$\eta_{SL} = 4A_S^{1/3}\left(\frac{D_\infty}{2a_c U}\right)^{2/3} \qquad (6.19)$$

where (η_{SL}) is the single collector efficiency (based on physical considerations) and therefore the theoretical collision/attachment efficiency α in this theory is

$$\alpha = \left(\frac{\beta}{1+\beta}\right)S(\beta) \qquad (6.20).$$

Rajagopalan and Tien's Correlation Equation

Based on numerical results Rajagopalan and Tien [260] have suggested a correlation equation to obtain η_0 based on a Lagrangian type equation of motion. This equation accounts for the effect of hydrodynamic interactions and van der Waals attraction on colloid deposition rate

$$\eta_0 = 4A_S^{1/3}\left(\frac{D_\infty}{d_c U}\right)^{2/3} + A_S N_{LO}^{1/8} N_R^{15/8} + 3.38\times 10^{-3} A_S N_G^{1.2} N_R^{-0.4} \qquad (6.21)$$

where N_{LO} characterizes the van der Waals attraction, N_R is an aspect ratio and N_G is a gravitational force number. These are defined as [258]

$$N_{LO} = \frac{4A_{123}}{9\pi\mu d_p^2 U} \qquad (6.22a)$$

$$N_R = \frac{d_p}{d_c} \qquad (6.22b)$$

$$N_G = \frac{(\rho_p-\rho)g d_p^2}{18\mu U} \qquad (6.22c)$$

where A_{123} is the Hamaker constant of the interacting media, d_p is the particle diameter, d_c is the diameter of the collector, g is the gravitational acceleration, μ is the fluid viscosity and ρ_p and ρ are the density of particles and fluid respectively. An additional formulation of Eqn. 6.21 is when $a_c \to b$, *i.e.* where removal rate of particles by a unit collector is normalized by the convective flux of particles toward the projected area of the sphere-in-cell envelope

$$\eta_0 = (1-\epsilon)^{2/3}\left[4A_S^{1/3}\left(\frac{D_\infty}{d_c U}\right)^{2/3} + A_S N_{LO}^{1/8} N_R^{15/8} + 3.38\times 10^{-3} A_S N_G^{1.2} N_R^{-0.4}\right] \quad (6.23)$$

With these theories and models in place it is now possible to address the experiments presented in this chapter.

Materials and Methods

A 10 mm I.D. and 50 mm length Liquid Chromatography (LC) column (Omnifit®) with mesh grids at the entrance and exit was filled with 240μm monodisperse spheres (Duke Scientific®) with a length from entrance to exit of 30mm or 125 sphere diameters. NMR images of these Clean Bead Packs (CBP) filled with DI water can be seen in figure 6.2 for different slice thicknesses (ΔZ = 0.3, 1.0 and 5.0 mm) through the middle of the column. An important characteristic of this porous media is the ordering that occurs close to the wall, allowing the formation of fluid channels, emphasizing the heterogeneity of the porous medium structure. This bead pack was connected to a high pressure LC pump (Pharmacia® P-500) and a syringe pump (KD Scientific® 270) via a T-connector at the inlet and to an effluent reservoir at the outlet above the NMR system. The experimental procedure involved initially characterizing the flow through the bead

pack by flowing DI water and using PGSE NMR techniques for measuring velocity maps, propagators and diffraction information (see figure 6.3 for NMR timing sequences). Multiple infusion of 20mL of 10%wt colloidal dispersions were added to the flow loop via the syringe pump. While these infusions occurred the flow rates of the HPLC and Syringe pumps were 60mL/hr and 30mL/hr respectively, while at all other times the HPLC and Syringe pump flow rates were 200mL/hr and 0mL/hr. After each infusion into the bead pack, the HPLC pump was used to flow DI water through the system for 1hr at 200mL/hr, so that a steady state of particle deposition could be achieved. The infusion of colloidal dispersion was repeated three times, with the same series of experiments conducted after each infusion. To verify that the system was steady state after each infusion, experiments conducted at the beginning of an experimental series were repeated at the end of each series (24 - 36hrs later); these indicated no change in the dynamics over time. The different states of the porous medium with respect to colloidal deposition are designated: clean bead pack (CBP), after 1^{st} infusion of colloidal dispersion (CS1), after 2^{nd} infusion of colloidal dispersion (CS2) and after 3^{rd} infusion of colloidal dispersion (CS3). To verify that colloids had been deposited the NMR spectra were measured before and after each colloidal dispersion is infused. The growth of the oil peak with increased deposition can be seen clearly in figure 6.4.

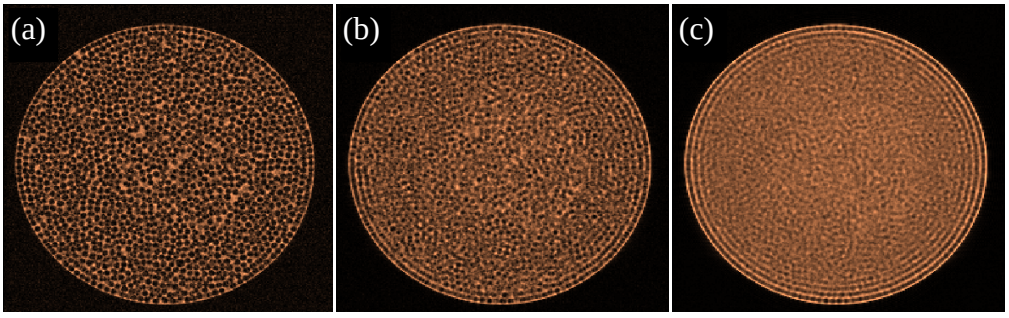

Figure 6.2 NMR images of Clean Bead Pack (CBP) with different slice thickness ΔZ = 0.3mm (a), 1.0mm (b) and 5.0mm (c). Note the long range structuring close to the wall evident as ΔZ increases.

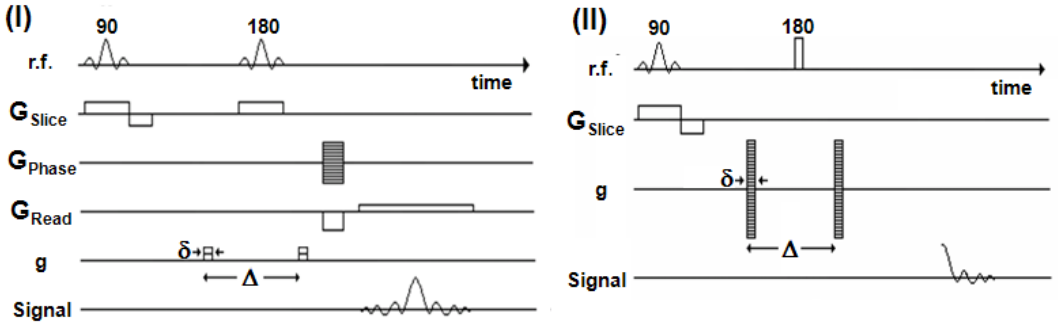

Figure 6.3 NMR timing sequences used to obtain velocity maps (I), propagators and q-space plots (II).

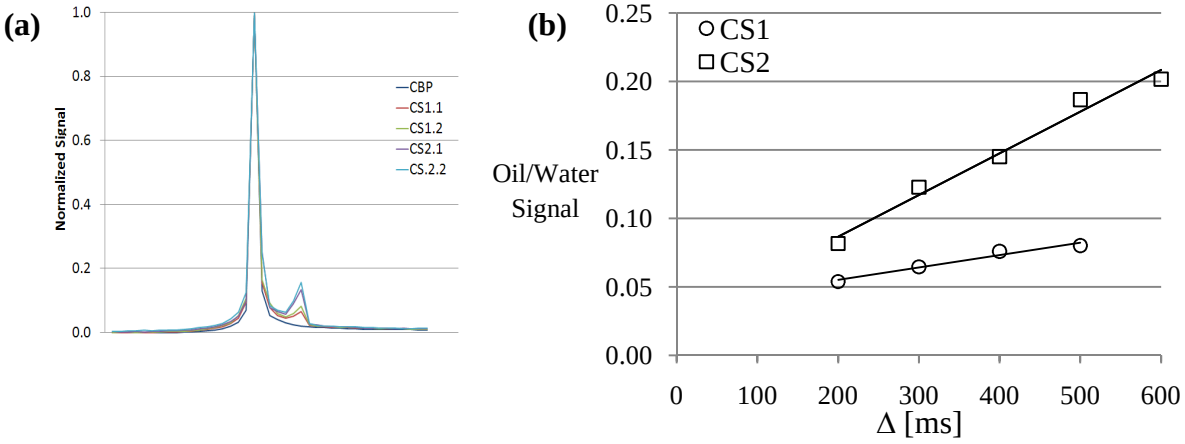

Figure 6.4 (a) Frequency spectra showing growth of oil peak from CS1 to CS2 and (b) ratio of oil peak to water peak at different Δ times; the ratio has been averaged for CS1 & CS2.

Results

The structural ordering of the model porous media can be clearly seen in figure 6.2, demonstrating long range ordered region in the axial z-direction exists at radial positions close to the wall. This ordered region allows for the higher velocities close to the wall (figure 6.5) for the flow of water in the Clean Bead Pack (CBP). After each infusion of the colloidal suspension (CS1 & CS2) there is a marked increase in regions where the velocity has decreased due to particle deposition blocking pores.

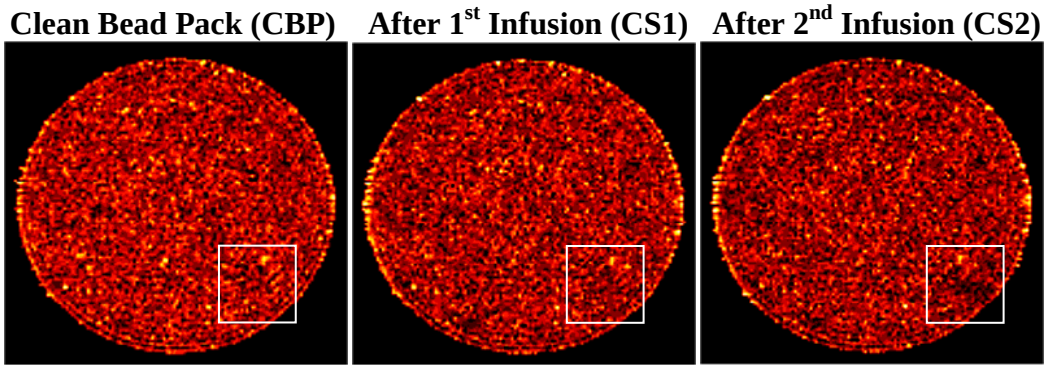

Figure 6.5 Shows the velocity maps for DI water flowing at 200mL/hr through (I) a Clean Bead Pack (CBP), (II) same bead pack after 1st infusion of colloidal particles (CS1) and (III) 2nd infusion (CS2). All scaled the same. ΔZ = 1.0mm.

To study further the effect of the particle deposition on the fluid dynamics inside the model bead pack, water propagators were measured (figure 6.6) at multiple Δ times and compared with the propagators from the Clean Bead Pack (CBP). The higher probability of large displacements and holdup signal, indicative of backbone flow, are visible after the 1st infusion relative to the CBP. For a better comparison, three Δ times (100ms, 200ms and 400ms) are plotted (figure 6.7) for the clean bead pack, after the first infusion (CS1) and second infusion (CS2). These show even more clearly that when

compared with the propagators for the clean bead pack the propagators after infusion (CS1 & CS2) show an increase in both the slow (holdup) and fast (backbone) components. While the spectra in figure 6.4 imply a significant increase in the amount of particles that have been deposited inside the bead pack, the propagators in figure 6.7 indicate that there are minimal changes in the fluid dynamics between the first and second infusion of colloidal particles.

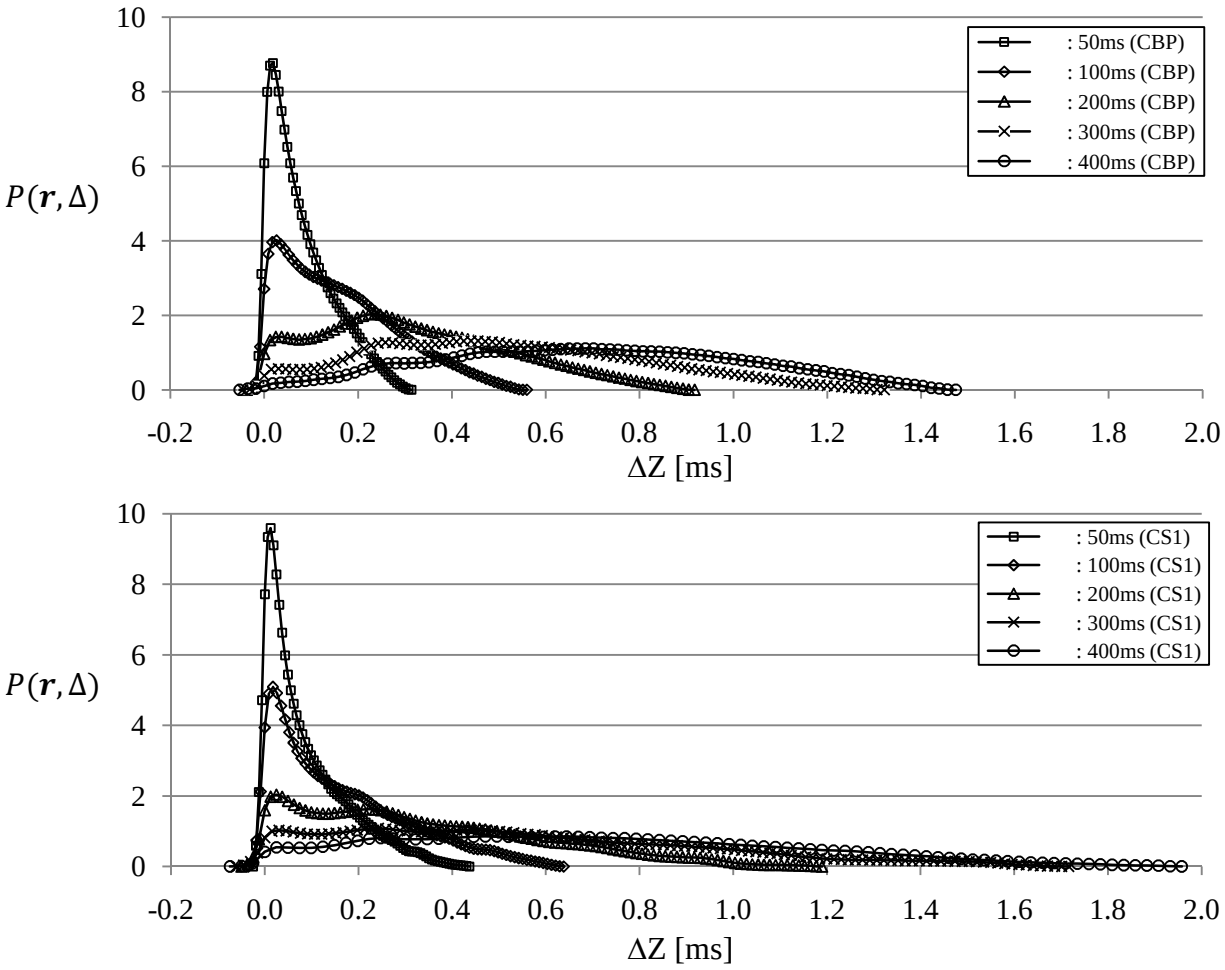

Figure 6.6 Shows (top) propagator experiments for the flow of DI water through a clean bead pack (CBP) and (bottom) through a bead pack after the first infusion of colloidal particles, first experiments (CS1).

This indicates that after the first depostition has occured the heterogeneity of the porous medium has dramatically changes. However during the second infusion the colloidal particles preferentially accumulate in the same regions, resulting in minimal change in the fluid dynamics through the bead pack. To study this effect further the ***q***-space data was analysed (see figure 6.8 & 6.9). For the flow of water through the Clean Bead Pack (CBP) and through the same bead pack after the first infusion of colloidal suspension (CS1) it is clear that the diffraction peak seen has become less sharp after the deposition of colloidal particles which is due to a loss in monodispersity of the pore space which the water molecules are sampling during Δ.

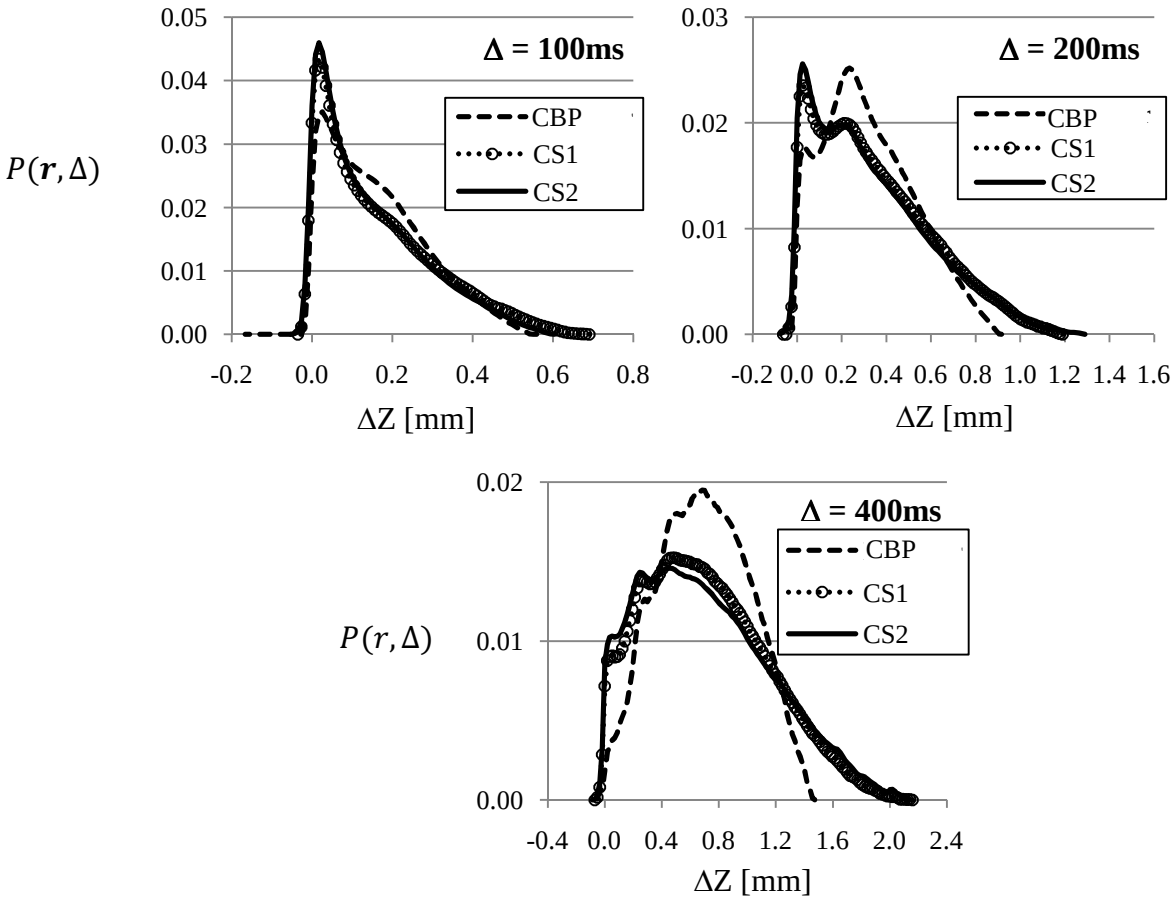

Figure 6.7 Propagator results for DI water flowing through the bead pack at 200mL/hr for (---) clean bead pack (⋯) after the 1st infusion (CS1) and (−) after the 2nd infusion (CS2).

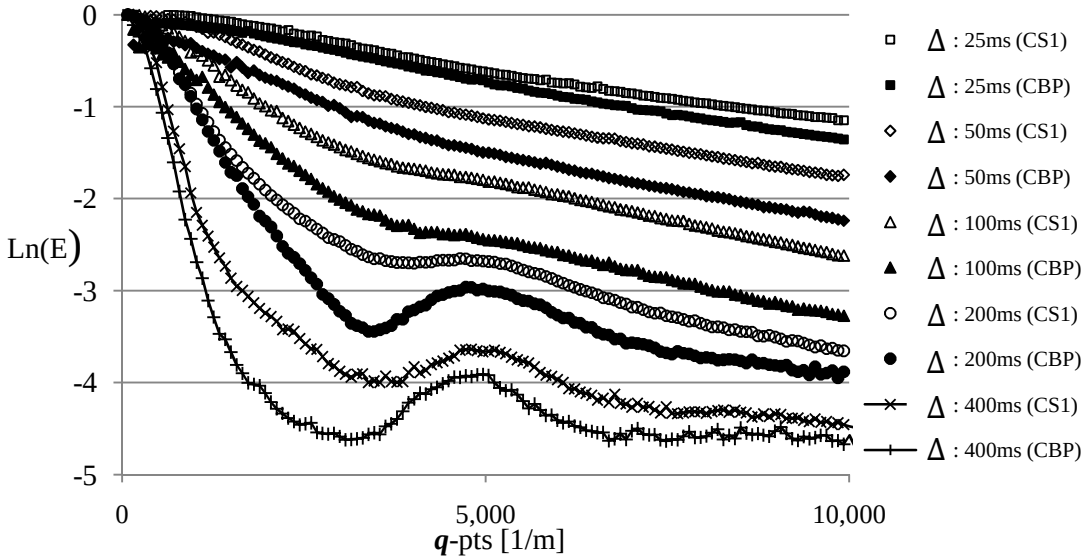

Figure 6.8 Shows the change in diffraction effect as colloidal particles are added to the system. Water flowing at 200mL/hr through a Clean Bead Pack (CBP) and the same bead pack after addition of 1st infusion of colloidal suspension (CS1).

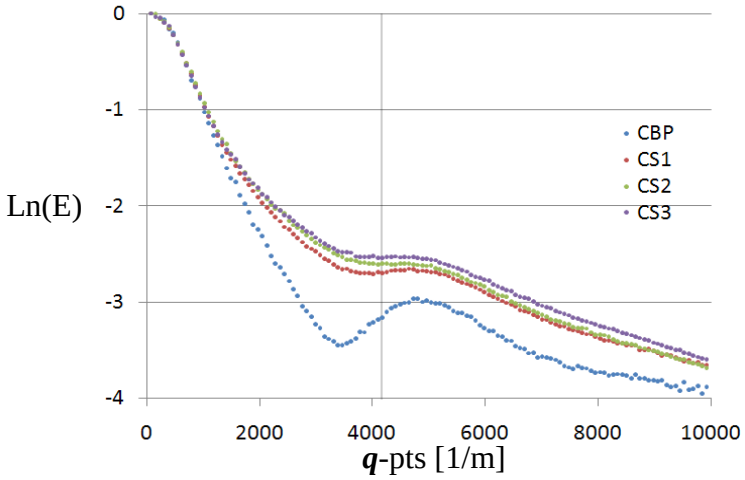

Figure 6.9 Shows the change in diffraction effect as colloidal particles are added to the system. Water flowing at 200mL/hr through a Clean Bead Pack(CBP) and the same bead pack after addition of 1st infusion of colloidal suspension (CS1), addition of 2nd infusion of colloidal suspension (CS2) and addition of 3rd infused colloidal suspension (CS3). The line is $\boldsymbol{q}$ = 1/240µm, *i.e.* the inverse diameter of monodisperse spheres packed in the bead pack.

Since the $\boldsymbol{q}$-points are the reciprocal of distance (m^{-1}), it is analysed to compare the length scales at which the $\boldsymbol{q}$-space data for the CBP deviates from the data after first

(CS1), second (CS2) and third (CS3) infusion of colloidal suspensions for Δ = 200ms (figure 6.9). These indicate that after a significant change in the structure from the CBP to the bead pack after the 1st infusion, there is a much less pronounced change in the structure as more particles accumulate inside the bead pack in subsequent infusion. All four curves overlap for $\boldsymbol{q} < 1000$, indicating that on the coarse length scale of 1mm (~ four bead diameters) there is insignificant difference in the structure, while at shorter length scales there is a significant difference between the structure of the bead packs.

Conclusions

The colloidal deposition measurements presented in this study tell a consistent story as to the fate of colloidal particles after deposition of colloidal particles has occured and the effect this deposition has on the homogeneity of the porous medium. After the inital deposition of colloidal particles, a significant increase in heterogeneity occurs inside the porous medium, while additional depositions, although increasing the quantity of colloid accumulated in the porous media, change the fluid dynamics only minimally. An interesting continuation of this research will use colloidal particles with a flourinated oil allowing for the complete isolation of the particle phase during the continuous flow of colloidal particles thorugh the porous medium. A problem associated with the the flow of colloidal dispersions through a porous medium is the blockage of pores causing an increased pressure drop accross the sample and an eventual catastrophic failure of either the porous medium setup or the pump supplying the driving force. This can be alleviated either by allowing for a larger ratio between the characteristic pore sizes and colloidal

particle sizes or by allowing for a low concentration of colloids to flow through the bead pack; the latter is possible with the use of flourinated oil core particles, which will be distinguishable from the surrounding water signal even at low concentration due to the complete lack of overlap of the spectral frequencies.

POROUS MEDIA REACTIVE TRANSPORT

Introduction

Reactive transport in porous media is an important problem in understanding the spread of contaminants in the Earth's subsurface. Precipitation reaction phenomena are important in transport processes of transuranic environmental contaminant species [261, 262], while dissolution reactions may play a significant role in supercritical fluid transport for carbon sequestration [263]. Precipitation and dissolution reactions during flow of fluids in porous media represent a particular level of complexity for transport modeling, due to the evolution of the pore structure due to reaction, altering flow dynamics [264-267]. Models for these types of systems are often categorized as either continuum or statistical and a broad range of approaches exist [265]. While many methods to model these reactive transport processes in porous media have been developed, data on the alteration of pore scale dynamics due to pore structure altering reactions are limited.

Nuclear Magnetic Resonance (NMR) methods have proven to provide unique data on displacement length and timescale dynamics of hydrodynamic dispersion for flow in three dimensional (3D) porous media [219, 268-271]. Another class of pore structure evolving reactions in porous media [272, 273] to which NMR has been applied is biofouling, *i.e.* biomass generating reactive flows. NMR data have characterized the interaction between pore structure evolution due to biomass growth and the pore dynamics of hydrodynamic dispersion [274-276]. In particular NMR has provided data

indicating the transition from normal diffusive transport to anomalous diffusive transport due to the alteration of the pore structure by biomass growth from homogeneous to heterogeneous [274, 275]. In this paper NMR measurements of the hydrodynamic dispersion in a model porous structure before and after a biofilm mediated precipitation reaction are presented.

Theory

Hydrodynamic Dispersion

Due to the extensive nature of the literature on reactive transport and hydrodynamic dispersion models for porous media, a limited discussion of the applicable theory is provided only to lend context to the discussion of the NMR data. Models are often delineated into categories as statistical or continuum based [265]. This demarcation is somewhat artificial due to the fact that the Advection Diffusion Equation (ADE) can be derived from concepts of both statistical mechanics [277] and continuum mechanics [64]. The ADE

$$\frac{\partial P(Z,t)}{\partial t} = \left[-\langle v_z \rangle \frac{\partial}{\partial z} + D^* \frac{\partial^2}{\partial Z^2}\right] P(Z,t) + R \quad (7.1)$$

gives the time rate of change of probability $P(Z,t)$, which is equivalent to normalized concentration, due to advection by a mean flow $\langle v_z \rangle$ and diffusive spreading due to hydrodynamic dispersion D^*. The appropriate form of the reactive source/sink term R in Eqn. (7.1) for reactive flows is an area of intense research interest [264, 266, 267]. However, as discussed below, the NMR data we acquire compares the hydrodynamic

dispersion dynamics before and after a pore structure altering reaction event, so our primary interest is in the dynamics not the reaction rate behavior of R.

The ADE generates a normal diffusion process in which the dynamics are Gaussian in the long time limit relative to mixing over many pore lengths. Hydrodynamic dispersion processes occurring at a short time-scale, *i.e.* short displacement length-scale, are non-Gaussian due to dynamics on the pore scale. In other words, the preasymptotic dynamics reflect the process of the decay of correlation of dynamics due to fluctuations in velocity by mechanical streamline mixing, diffusion across streamlines and hold up in dead end pores [228]. The pore structure of the porous media determines the impact of the different dispersion mechanisms and controls the approach of the dynamics to the asymptotic Gaussian behavior. Nonequilibrium statistical mechanics models based on memory function equations [54] for the time and length scale dependence of preasymptotic dynamics have been developed [278] and elucidated by PGSE NMR measurements [268]. In heterogeneous pore structure media, where non Gaussian anomalous diffusion scale dependent transport is present for asymptotic times, Continuous Time Random Walk (CTRW) models [230]and non-local continuum approaches [279] result in Fractional Advection Diffusion Equations (FADE) [280]. The applicability of such models to reactive systems with pore evolution has not been demonstrated.

NMR Measurement of Dispersion

NMR provides unique data on transport in porous media due to the ability to noninvasively resolve dynamics within the pore structure. The measurement of

dynamics as a function of varying displacement length and time generates data on a hierarchy of displacement scales. The acquired NMR signal using a standard Pulsed Gradient Spin Echo (PGSE) method shown in figure 7.1 is encoded in the experimental Fourier domain reciprocal to displacement in terms of the wave vector $\boldsymbol{q} = (2\pi)^{-1}\gamma \boldsymbol{g}\delta$ and the displacement observation time Δ [1]. In this way the dynamics are measured as a function of displacement observation time Δ and varying displacement length scale q^{-1}. The measured voltage signal in the NMR experiment is given by

$$E(q,\Delta) = \int P(Z,\Delta) exp[i2\pi qZ] dZ \quad (7.2)$$

where $Z = z'(\Delta) - z(0)$ is the displacement the NMR active nuclei, or spins, and $P(Z,\Delta) = \int (x,y,z) P(z,0,z',\Delta) dxdydz$, ρ is the averaged propagator. There is a Fourier transform relationship between the echo signal $E(q,\Delta)$ acquired by incrementing the gradient amplitude g applied for time δ and the average propagator. The averaged propagator, or van Hove self-correlation function [54], is the conditional probability $P_s(z,0|z',\Delta)$ that a spin residing at z at time 0 moves to z' at time Δ averaged over the initial spin distribution $\rho(x,y,z)$ [1]. Complete details of the dynamics are contained within the propagator for all displacement scales sampled by q. The ability to spatially resolve systems using NMR Imaging (MRI) techniques provides the means to vary spatial averaging scales. MRI has limited spatial resolution since NMR is an inherently low signal to noise technique based on the small differences in energy state populations of the spins. The strength of the method is the ability to probe the impact of coarse graining space on measured translational and rotational molecular dynamics. The important point is that as stated above, the pore scale dynamics induced by the structure

of the porous media is contained within the scale dependent dynamics measured by the propagator without the use of imaging methods [1, 33, 219]. The characterization of the pore scale dynamics without imaging is important due to the limited spatial resolution of MRI to about $(20\ \mu m)^3$ under ideal conditions in a porous column of size of the order of 10 mm. Typical spatial resolutions are of on the order of $(40\ \mu m)^2$ over a slice thickness of approximately 100 μm which generates averaging of dynamics over scales that can obscure pore scale information. Rapid MRI velocity methods capable of acquiring spatial distributions of velocity on times of the order of 50 ms have potential to provide data on variations in flow as reaction are occurring [281, 282]. These methods are limited to spatial resolutions greater than $(100\ \mu m)^3$ due to signal to noise considerations, rendering them ineffective at measuring pore scale dynamics.

Experimental Details

Model Bead Pack and Microbiology

A 10 mm I.D. and 30 mm length liquid chromatography column (Omnifit®) with a frit at the entrance and 220 μm mesh at the exit was packed with $d_p = 241\ \mu m$ diameter monodisperse polystyrene beads (Duke Scientific 4324A). After assembly the porosity was measured to be $\phi = 0.41$ by analyzing NMR images of the bead pack and confirmed by the measurements of the mean velocity inside the bead pack and total volumetric flow rate through the bead pack. Experiments utilized a dual syringe HPLC pump (Pharmacia P-500) which allows controlled volumetric flow rates. DI water, media without and with calcium was pumped through the bead pack against gravity to a reservoir above the

column. The DI water was doped with Magnevist to allow for a shortened NMR experimental repetition time T_R this was unnecessary for the medium with and without calcium as the salts and sugars reduce the spin-lattice T_1 magnetic relaxation time. NMR measurements were conducted for the flow of these three fluids through the Clean Bead Pack (CBP) to acquire baseline results for later comparison with the Inoculated and precipitated Bead Pack (IBP).

For the experiments, the column was inoculated with a culture of the ureolytically active bacterium *Sporosarcina pasteurii* (formerly classified as *Bacillus pasteurii*) in a growth medium described by Ferris and Stehmeier [283]. The medium includes 3 g/L nutrient broth (Becton, Dickinson and Company), 20 g/L urea (Fisher Scientific), 10 g/L ammonium chloride (Fisher Scientific), and 2.1 g/L sodium bicarbonate (Fisher Scientific). Calcium chloride dehydrate (Acros Organics) is added to the medium at a concentration of 3.7 g/L when media was desired with sufficiently high calcium concentration for precipitation to occur. In the process of bacterially facilitated urea hydrolysis (ureolysis), the production of ammonium and dissolved inorganic carbon during decomposition of urea by the bacteria increases the solution pH and carbonate concentration, which increases saturation and favors calcium carbonate precipitation. The reaction mechanism is illustrated in the following equations [284]

$$CO(NH_2)_2 + H_2O \rightarrow \quad NH_2COOH + NH_3 \rightarrow \quad 2\,NH_3 + CO_2 \text{ (Urea hydrolysis)}$$

$$2NH_3 + 2H_2O \leftrightarrow \quad 2NH_4^+ + 2OH^- \text{ (pH increase)}$$

$$CO_2 + 2\,OH^- \leftrightarrow \quad CO_3^{2-} + H_2O \text{ (Carbonate formation)}$$

$$CO_3^{2-} + Ca^{2+} \leftrightarrow \quad CaCO_{3\,(solid)} \text{ (Precipitation)}$$

While the hydrodynamic alterations resulting from calcium carbonate precipitation in the porous media were of primary interest in this experiment work is ongoing to further correlate the reaction kinetics to the changes in hydrodynamics.

MR Experiments

The bead pack was secured in a 20mm ID radiofrequency (rf) coil and placed inside a 300 MHz vertical standard bore superconducting magnet. A Bruker Avance III spectrometer was networked to the superconducting magnet. A Bruker Micro2.5 microimaging probe and gradient amplifiers were used which allowed imaging using gradients up to 1.48 T/m in all three directions. PGSE experiments were conducted to acquire propagator data on the probability of spin displacement and q-space data to measure any diffraction effects. Additionally, standard imaging sequences were used to acquire images through the whole bead pack and T_2 maps of slices through the bead pack. The experimental parameters for these different experiments are listed below:

PGSE experiments: acq-pts = 512, $\boldsymbol{q}$-pts = 130, slice thickness: 1mm, T_R = 2sec, δ = 2 ms, Δ = [25, 50, …, 600]ms, $\boldsymbol{g}_{\max}$ = 0.19-1.04 T/m, SW = 50kHz, N_A = 8. Experimental time = 35min.

T_2 imaging experiments: pixels = 256x256, FOV = 11x11mm2, Voxel resolution: 43x43x2000 μm^3, T_E = [10, 20, …160]ms, T_R = 1sec, SW = 50kHz, N_A = 8, Experimental time = 34min.

NMR imaging experiments (5 slices): pixels = 256x256, FOV = 30x11mm^2, voxel resolution: 117x43x2000 μm^3, T_E = 14ms, T_R = 1sec, SW = 50kHz, N_A = 1, Experimental time = 4min.

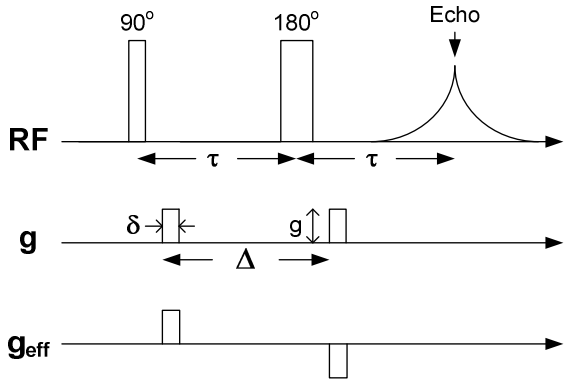

Figure 7.1 Pulsed Gradient Spin Echo (PGSE) NMR pulse sequence used to generate propagators of motion over a range of displacement lengths reciprocal to the experimentally incremented wave vector $\boldsymbol{q} = (\boldsymbol{2\pi})^{-1}\boldsymbol{\gamma g \delta}$ and displacement observation time Δ.

After NMR experiments had been conducted on the Clean Bead Pack (CBP), the column was inoculated by adding 6.5 mL of a *Sporosarcina pasteurii* culture to the top of the column and reversing flow through the column at 10mL/hr. The bacteria were allowed to attach at no-flow condition for 60 minutes, during which three MRI images were obtained. Then calcium-free medium was flowed for 60 minutes before any further NMR experiments were conducted. Approximately 4 hours after inoculation calcium-containing medium was pumped through the beadpack at 400mL/hr for 10minutes. PGSE NMR and MRI measurements were performed. Additional injection of media with calcium was done after 5 hours of NMR experiments. Between NMR experiments a flow calcium-free medium was pumped through the column at 10mL/hr to maintain nutrient supply for bacterial growth. All PGSE NMR experiments were conducted at a flow rate of 400 mL/hr. The ureolytic activity of the bacteria was assessed by acquiring fluid samples at the exit of the magnet and measuring the pH value as a function of flow rate.

Results

Optical Images and MRI

Stereo microscope (Nikon SMZ1500) optical images of the beads extracted from various locations in the packed column after the experimental run are shown in figure 7.2. The images indicate an axial variation in the amount of precipitate and biomass. The entrance fitting shows significant deposition. The bottom of the column, the flow inlet region, and the top flow outlet of the column appear similar while the middle region where the PGSE NMR measurements are localized has slightly less precipitate and biomass. Figure 7.3 shows a stereo microscope image of a single sphere in which a deposition layer is apparent on the sphere surface. A fluorescent microscope image indicates the deposition material in the images of figure 7.3 is composed of attached biomass, stained green and $CaCO_3$ precipitate crystals, visible in orange/red. The microscope images in figures 7.2 and 7.3 indicate the deposition of precipitate and biomass in pores between spheres as well as fairly uniform coating around the spheres. Interestingly T_2 spin-spin magnetic relaxation maps [1, 285] in figure 7.4 show little or no impact from the precipitate and biomass. This is in contrast to NMR studies of thick biofilm forming bacteria which give significant T_2 relaxation variations in porous media due to the impact of the extracellular polymeric substance (EPS) on the rotational mobility of water molecules constrained within the EPS hydrogel [274, 286]. This is attributable to the fact that most of the pore blockage evident in figure 7.2 is $CaCO_3$ with thin layers of biomass as shown in figure 7.3. The $CaCO_3$ reduces the amount but in

contrast to the presence of biofilm does not significantly impact T_2 relaxation of the remaining pore water.

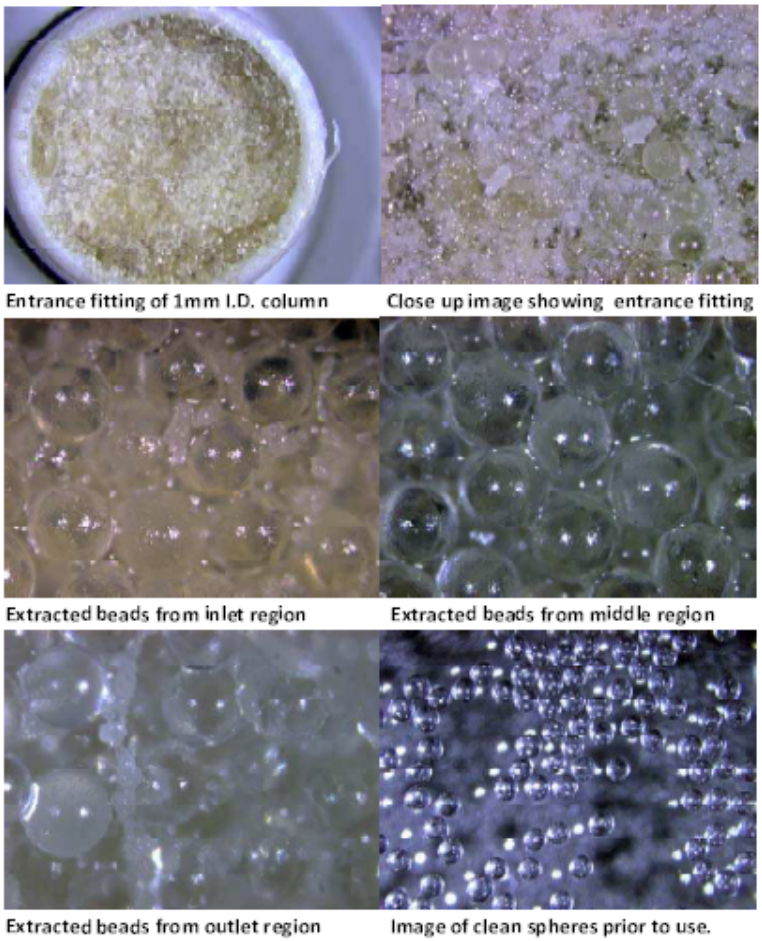

Figure 7.2 Selected stereo microscope (Nikon SMZ1500) images of beads from different regions of the porous media column showing the deposition of biomass and precipitate. The diameter of each bead is 241μm, providing a scale for each image.

MRI images of the signal intensity in the packed column as a function of the reaction process are shown in figure 7.5. As mentioned above the spatial resolution averages signal intensity over multiple pores. In the data shown the volume elements over which the averaging occurs *i.e.* the spatial resolution of the images are 117μm by 43 μm in plane over 2 mm slices.

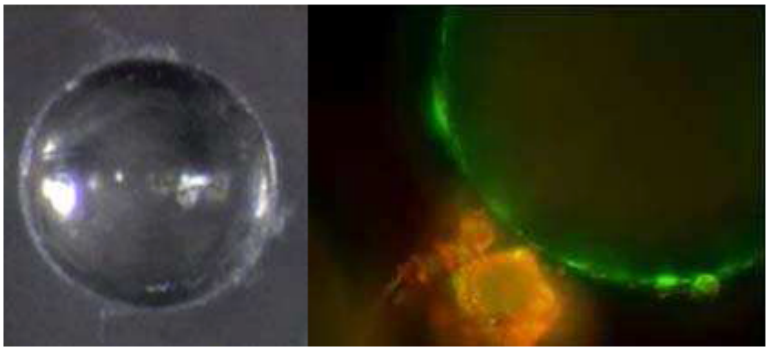

Figure 7.3 A stereo microscope image (left) of biomass attached to a 241µm diameter sphere that was extracted from the column. This bead was gently treated with 10% nitric acid (HNO3) to dissolve the precipitates and visualize only attached biomass. A fluorescent microscope image (Nikon Eclipse E800, 40x objective) (right) of an extracted sample that was stained with Syto 9 and Propidium iodide (Invitrogen LIVE/DEAD®). Syto 9 (green) highlights the bacteria with intact cellular membranes, which appear to be at a higher density surrounding the bead. Propidium iodide (red) highlights cells with compromised membranes. A precipitate crystal is highlighted by the propidium iodide. This is due to either a higher density of cells with compromised membranes surrounding the precipitate and/or staining of the organic matrix associated with the calcium carbonate by the propidium iodide.

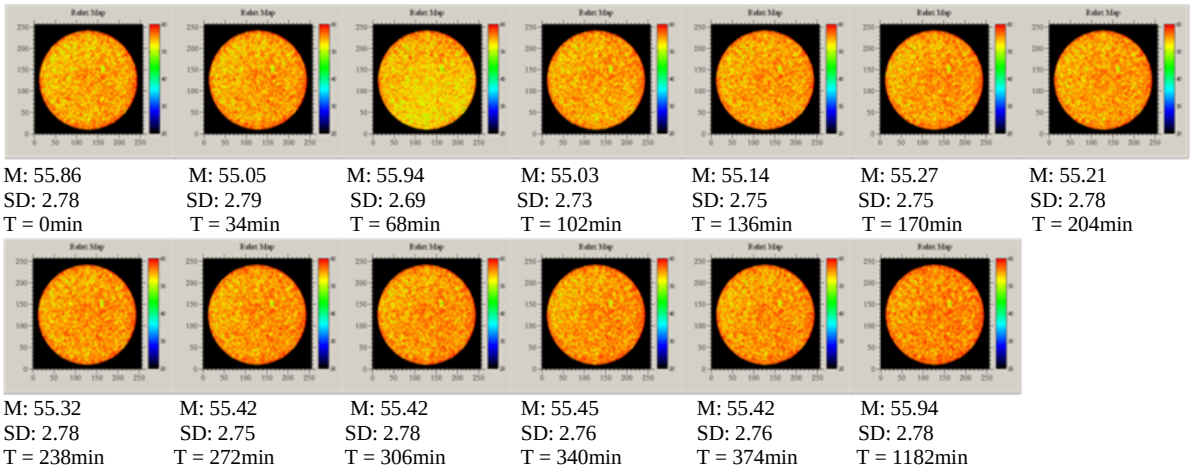

Figure 7.4 T_2 magnetic relaxation maps of a slice through the column taken at varying times T in minutes, after bacterial inoculation and challenge with Ca. The mean T_2 relaxation time calculated from the image pixels in ms are given, *e.g.* M: 54.8618 ms, as are the standard deviations among pixels, *e.g.* SD: 2.7770 ms. Spatial variations occur with reaction progression but the mean values are indistinguishable.

Two features are apparent. First a region of increased signal intensity near the flow entrance on one side of the column after the introduction of Ca which persists throughout the experiment. Second the appearance of low signal intensity potentially due

to the generation of gas through bacterial growth. No significant details regarding the reaction process on the pore structure is evident, again showing the limitation of direct NMR imaging to provide significant information on pore evolution.

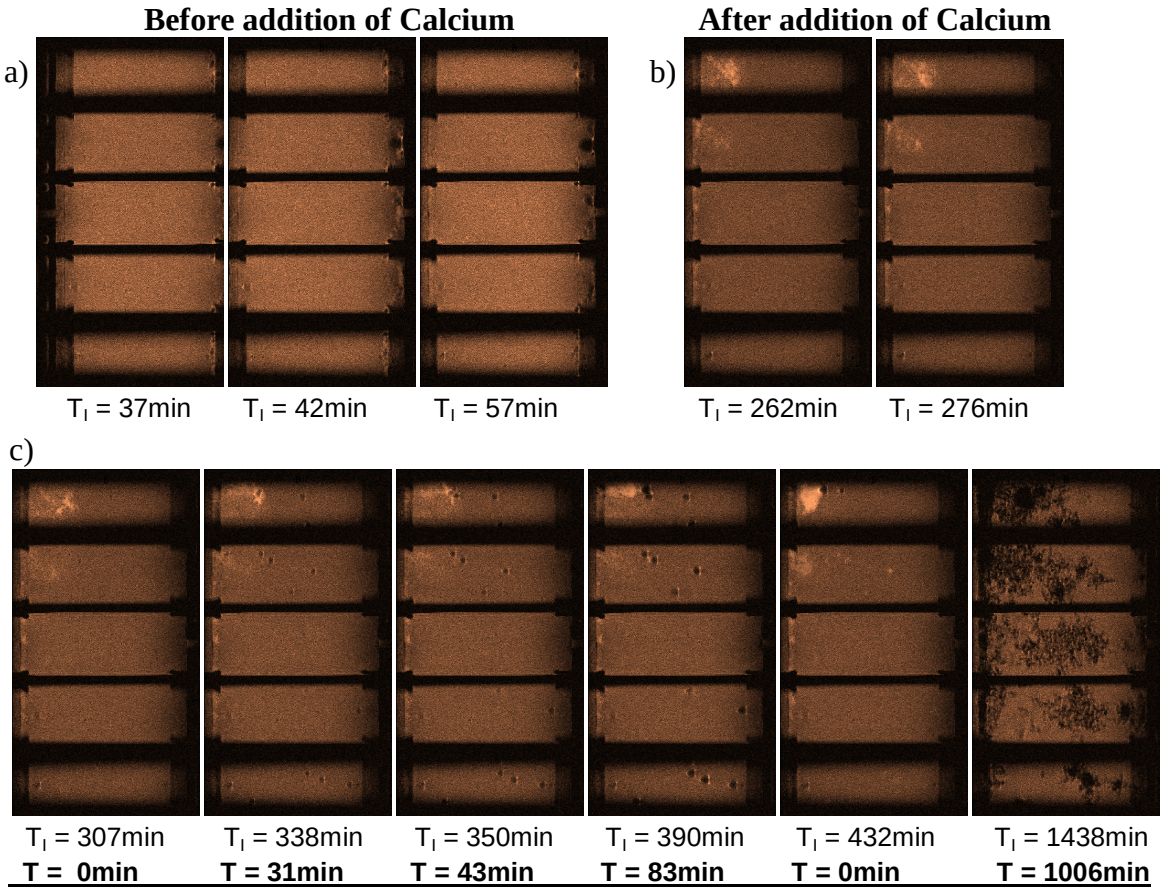

Figure 7.5 A series of MR Images of five 2mm thickness slices across column. T_I is the time after inoculation and T is the elapsed time for a particular experimental series a) Images obtained after inoculation, before any flow experiments. b) Images obtained after flow of calcium-containing medium for 10 minutes at 400mL/hr. These show lower signal intensity due to presence of calcium in column and a bright region close to the wall (top two images). c) Images obtained after flow of calcium-containing medium for 24 minutes at 400mL/hr, showing growth of dark spots over time. After T_I = 390min the column was flushed with calcium-free medium at 400mL/hr resulting in removal of dark spots (T_I = 432min). Then the column was left to rest for ~20hrs, resulting in the re-growth of dark spots over time (T_I = 1438m). Between MR Images calcium-free medium was pumped through the column at 10mL/hr to maintain nutrient supply for bacterial growth. The column was flushed again with calcium-free medium at 400mL/hr before further experiments were conducted. MRI parameters (5slices): 256x256 points, Voxel resolution: 117x43x2000µm, FOV = 30x11 mm, T_E = 14ms, T_R = 1s, SW: 50kHz.

PGSE NMR Measurements

In contrast to the limited information provided by spatially resolved NMR the measurement of dynamics is highly sensitive to the reaction induced pore structure change [274, 275]. Figure 7.6 shows the displacement time Δ dependence of the dynamics as given by the propagator for a 400 ml/hr flow rate before (figure 7.6a) and after (figure 7.6b) reaction. The clean bead pack (figure 7.6a) indicates the well known progression of the dynamics from the preasymptotic regime with a Poisson like distribution of displacements within single pores at short displacement time Δ = 25ms to near Gaussian behavior at the longest observation time Δ = 600 ms. Interestingly the post reaction dynamics (figure 7.6b) show a similar general progression with displacement time. However, closer inspection of the propagators at each time Δ, shown in figure 7.7, indicates significant differences in the dynamics on the pore scale. At displacement observation time Δ = 25 ms the water molecules are within a pore and the propagator reflects the distribution of velocity within the pores. Over this time little or no Taylor dispersion due to diffusion across streamlines occurs since the diffusion length $l_D = (2D_o\Delta)^{1/2} \sim 10$ μm is a small fraction of the pore size $l_p = d_p \phi/(1-\phi) \sim 167$ μm based on the Clean Bead Pack (CBP).

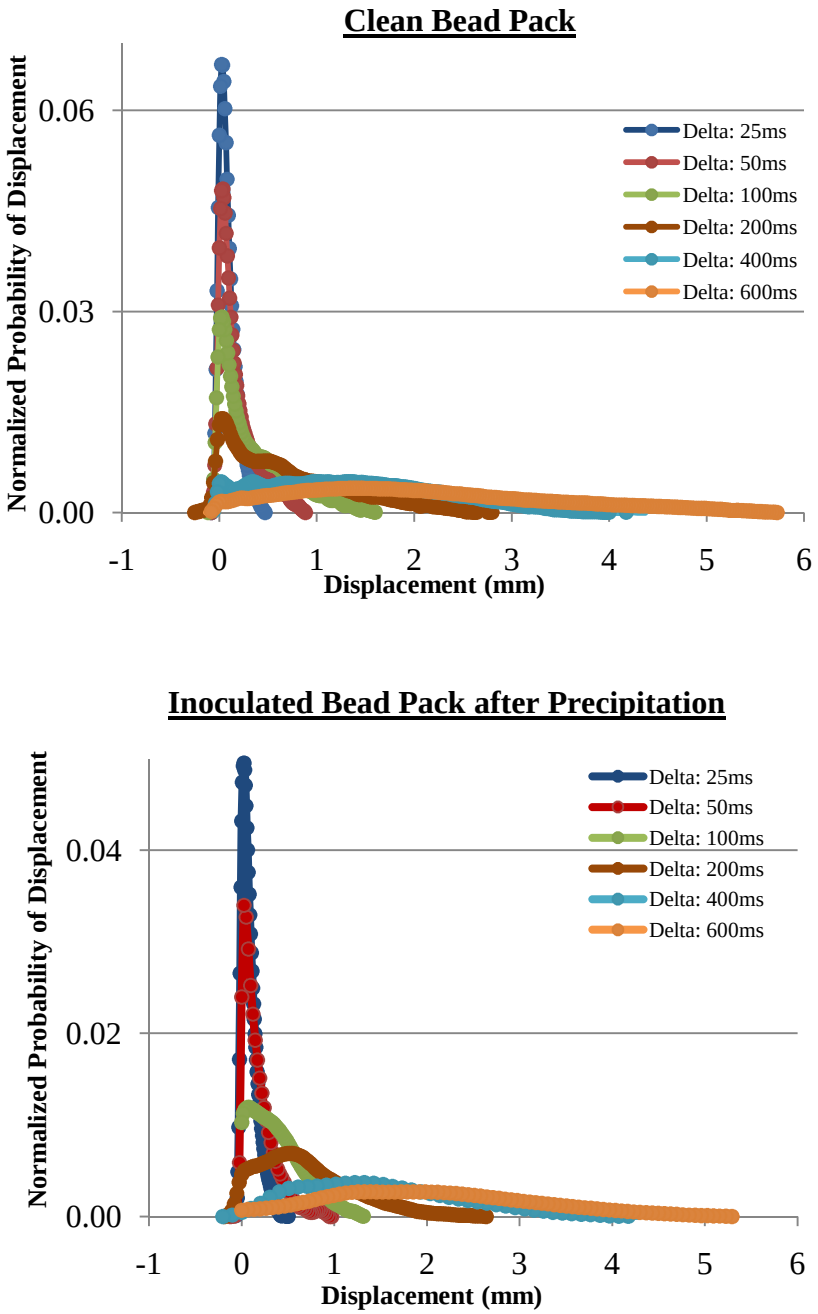

Figure 7.6 (color online) Comparison of clean bead back (CBP/blue or black) and inoculated bead pack (IBP/red or grey) for displacement observations times Δ shown on each figure.

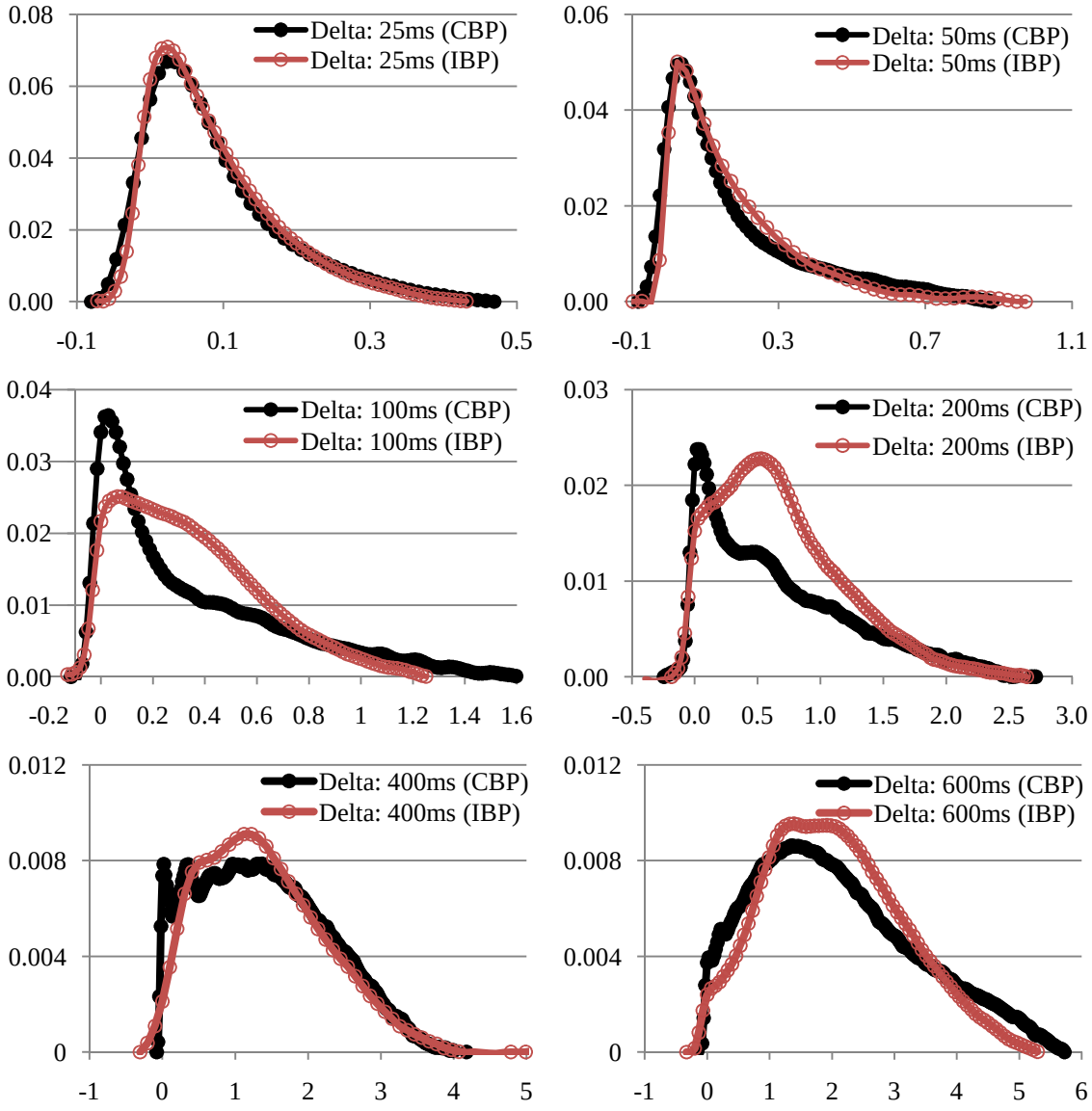

Figure 7.7 Propagators as a function of displacement observation time for 400 ml/hr flow of media without calcium in a) the clean bead pack and b) the inoculated bead pack after precipitation.

Mechanical mixing due to streamline crossing induced by the tortuous flow path was not observed either, since the time to transit a pore based on the superficial velocity $\langle v \rangle$ = 3.45 mm/s is $\tau_v = l_p/\langle v \rangle \sim 48$ ms. Despite the precipitate and biomass evident in figures 7.2 and 7.3 the pore scale distribution of displacements due to velocity within a

pore are nearly the same. At displacement time $\Delta = 50$ ms the molecules have just transited a single pore on average and the distribution of displacements is still quite similar however some variation at displacements on the order of one or two pore lengths l_p is beginning to be evident. Once the displacement observation time is such that significant dispersion due to sampling of multiple pores begins to occur, $\Delta = 100$ ms a significant change in the dynamics between the CBP and the Inoculated and precipitated Bead Pack (IBP) occur. The CBP still exhibits a strong peak at small displacements on the order of the pore length while the displacement distribution for the IBP has a sizeable number of molecules with intermediate displacements. Of interest are the absence of a large displacement tail in the IBP indicating that significant channeling is not occurring and the onset of oscillations on the CBP displacement probability due to correlations in motion from the ordering of the monodisperse packing of the CBP generating a diffraction like effect in the $\boldsymbol{q}$-space data [219, 270, 274, 275]. Analogous differences are present at $\Delta = 200$ ms. By displacement time $\Delta = 400$ ms the oscillations due to the homogeneous structure of the CBP are clearly evident and the CBP maintains a larger distribution of molecules at small displacements. The dispersion in the IBP is actually smaller than the CBP as evidenced by the narrower distribution of displacements. The distributions at displacements greater than about 1.7 mm are the same indicating a similarity in the dispersion dynamics after molecular sampling of 10 pore lengths. These observations re-emphasize the strength of PGSE NMR measurements since potentially important changes in pore structure can be directly revealed, which cannot be detected by traditional (dye) tracer measurements, MRI, or other methods, which require averaging

over larger time or length scales. At the longest displacement observation time Δ = 600 ms the IBP dynamics are more narrowly distributed around the mean displacement and again more molecules have small displacements in the CBP. This persistence of a larger distribution of molecules with small displacements indicates that rather than the precipitation reaction generating significant dead end pores or greater surface area for no slip condition stagnant molecules the precipitate is decreasing the hold up of molecules. Coupled to the narrower distribution of dynamics in the IBP this indicates that the precipitate alters the pore structure such that microscale mixing is enhanced allowing the displacements to be more homogeneous. The precipitate is generating a rough and irregular surface at the micro scale smaller than a pore length, or bead diameter, which alters the dynamics at intermediate displacement scales by mechanical mixing of streamlines near pore walls in contrast to the smooth and ordered CBP. At this longest observation time the distribution of displacements for the reacted IBP is approaching a Gaussian distribution more rapidly than the CBP, including fewer molecules undergoing displacements greater than 4 mm.

Despite the fact that all the information on the dynamics is present in the propagator, in considering the impact of the precipitation altered pore structure on the dynamics it is useful to look at the propagator data in the reciprocal $\boldsymbol{q}$-space. Figure 7.8 shows data for Δ = 400 ms for the CBP with deionized (DI) water and media flowing through it, as well as data for flow of media without Ca as the reaction proceeded in the IBP after inoculation and injection of Ca enriched media. Data shown for the IBP is taken every 5 minutes as the reaction proceeds.

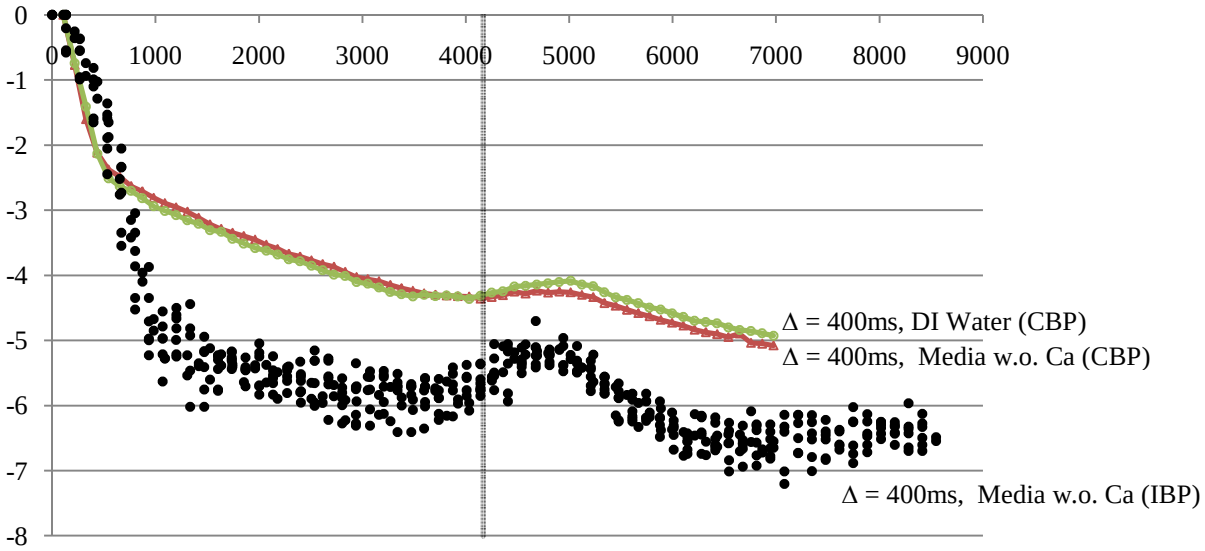

Figure 7.8 PGSE data plotted in *q*-space showing the diffraction effect due to the ordered structure of the porous media for the Clean Bead Pack (CBP) and Inoculated and precipitated Bead Pack (IBP) at displacement observation time of Δ = 400 ms. The data for the IBP taken over several hours after precipitation has occurred indicates that while there is increased noise due to the pore structure evolving the dynamics are consistent over a long time period.

Note the increase in the rate of signal decay for the IBP relative to the CBP at low ***q***, corresponding to large displacements. This indicates the more rapid approach to Gaussian behavior and more rapid loss of correlation in displacement dynamics in the reactive transport IBP system. At this observation time the coherent diffraction peak at the characteristic pore structure size [32] is evident for both the CBP and the IBP. In the IBP the maxima and minima of the diffraction peak are broadened and shifted to slightly lower values of ***q*** indicating a broader distribution of pore sizes in the IBP due to the reactive change in the pore structure. The IBP data is noisy but consistent over many hours of observation of the flow. The precipitate is not fully blocking the pores and increasing hold up dispersion in dead end pores which would generate large displacements due to channeling. Rather the precipitate alters the pore structure more subtly by coarsening the surfaces and broadening the pore size distribution so that mixing

and dispersion within pores is enhanced but longer range structure is not lost as evidenced by the coherent diffraction effects in the $\boldsymbol{q}$-space data.

Conclusions

NMR measurements of a homogeneous model porous medium of 241 μm polymer beads were carried out before and after a biologically mediated precipitation reaction in order to explore the impact of reactive pore structure alteration on transport dynamics. MRI data is shown to be of limited use in analyzing these systems based on limitations in spatial resolution. In contrast, PGSE NMR measurements allowed for the acquisition of propagator data as a function of displacement time (and length), which clearly indicated alteration of the pore structure. The precipitation reaction alters the pore structure relative to a clean bead pack such that fewer molecules undergo small displacements within individual pores over a range of displacement times and generates a narrower distribution of dynamics which approaches a Gaussian distribution more rapidly. The pore surfaces of the reactive IBP were roughened and enhanced mixing and mechanical dispersion on the pore scale resulting in the observed dynamics. Integration of such information into conceptual and mathematical models has the potential to improve quantitative predictions of the impact of reactive processes on flow and transport in porous media.

FLOW THROUGH BETA-LACTOGLOBULIN GEL

Introduction

Gels are found in a wide variety of biological, chemical and food systems and have therefore received much attention [287-293]. Gels can generally be categorized into particulate or polymer gels [294], where the former consists of particulates (mono- or polydisperse, soft or hard) forming an extended structure, while the latter consists of a flexible polymer network formed by either covalent crosslinks or by physical aggregation and is of interest in this study. Polymer gels can be further categorized as transparent or opaque, hard or soft, brittle or rubbery, homogeneous or heterogeneous, *etc*. All these different categories are a symptom of the diversity of gel architecture which not only depends on the polymer but also the gelation process, where variables such as pH, ionic strength, temperature, solvent and copolymers can cause drastically different morphologies. Previous dynamics studies [295-302] have focused on understanding the fundamental interrelation between the structure of the polymer and the dynamic properties of the constituent macromolecules and solvent. Polymer gels consist of cross-linked polymer networks and a large amount of solvent causing a large average mesh size [303] (ξ) of polymer network compared with the size (R) of solvent molecules (or tracers), allowing for a relatively un-restricted diffusive motion of these molecules [295, 296, 304]. The ratio R/ξ is an important characteristic length for the gel structure, characterizing the subdivision of flow into two regimes, *i.e.* $R/\xi > 1$, where self-diffusion is believed to proceed by the reptation mechanism [305], and $R/\xi < 1$, where macroscopic

flow is realized. A recent interest in the fluid dynamics through gels is the use of stimuli-responsive hydro-gels as active functional components in fluidic and micro-fluidic flow devices [306-308] where the amount of solvent uptake and flow resistance depend on the chemistry of the polymers, solvent, temperature and pH. This study focuses on gels prepared from bovine β-lactoglobulin, a member of the lipocalin family. β-lactoglobulin is one of the most highly studied gel polymers, having been characterized with a wide range of techniques, both biochemical and physical [309]. The interest in studying this protein originates from its importance for the milk industry, where milk proteins play a range of roles which make dairy products and products containing dairy components valuable. These roles include nutrition, physical functionality, and breakdown under controlled conditions to produce nutritional or functional products. It is also because of the fouling of heated surfaces, gelling in processing equipment, and even non-gelling during the manufacture of certain products [310].

β-lactoglobulin is a globular protein which is the main component of whey. When heat-denatured it forms self-similar aggregates characterized by a fractal dimension and whose degree of branching determines the eventual morphology of the gel [311]. It has several genetic variants of which A and B are the most abundant and have been shown to aggregate at the same rate [312]. Generally, heat denaturation of globular proteins causes interactions between proteins such as the formation of covalent disulfide bridges [313]. In the absence of salts, globular proteins often form transparent gels of cross linked strands (diameter < 10nm) at a pH higher or lower than pI, the isoelectric point, while forming opaque gels consisting of agglomerated spherical protein particles

close to pI [314, 315]. β-lactoglobulin (pI = 5.2) adheres to this general picture, forming white particulate gels at pH 4-6, while forming transparent fine-stranded gels above and below this pH range [316]. It has been shown that close to pI, β-lactoglobulin precipitates out of solution even at room temperature and cannot form stable aggregates reproducibly, while for pH > 5.8 the aggregation process does not depend strongly on pH [314]. In this study the two gels used are at pH = 5.2 and pH = 7.0, and respectively have heterogeneous and homogeneous structural morphologies at the macroscopic scale (> $100\mu m$). Therefore theoretical interest for this study is in the aggregation process consistent with pH ≥ pI. A different process has been shown to govern aggregation at pH < pI. Two types of aggregation may occur for β-lactoglobulin. Spontaneous aggregation of native proteins and aggregation due to heat-induced denaturation, with different types of bonds formed in each case. For heat-induced denaturation the important concentrations are the critical association concentration (CAC) below which aggregation does not occur, gelation concentration (C_g) above which gel formation occurs and salt concentration (C_s). C_s can dramatically change the structure of a gel, causing densification of aggregates due to increased branching, cause a decrease in CAC and decreased flexibility [311, 317]. The gels used here have concentration C = 90g/L which is well above the expected CAC and C_g for pH = 5.2 and 7.0 [311, 314], while C_s = 0.3M NaCl falls into a high ionic strength regime. The aggregation of β-lactoglobulin seems to follow two steps [314]. First a pre-aggregation occurs during which monomers aggregate into 50-100 monomer units forming strong bonds which are irreversible. If $C < C_g$ these pre-aggregates will not aggregate further [318]. However if $C > C_g$ these pre-aggregates

form larger aggregates, creating a gel of linear or branched units depending on the pH and salt concentration. The rate at which aggregates form is strongly dependent on temperature. The gels used in this study are formed at pH 5.2 and 7.0 at high salt concentrations (0.3M NaCl) and are therefore both categorized as white particulate gels [316] due to the branching induced.

The focus of this work is to quantify the hydrodynamic dispersion of solvent water during pressure driven flow through β-lactoglobulin gels of homogeneous and heterogeneous structure. The application of pulsed gradient spin echo (PGSE) nuclear magnetic resonance (NMR) to measure the displacement length and time scale dependent dynamics demonstrates the applicability of the theory of hydrodynamic dispersion in porous media to analyze flow in gels. This represents a significant extension over current analysis of advective transport in gels which have focused on measurements of hydrodynamic permeability assuming classic D'Arcy law velocity scaling with pressure drop [299, 302, 319].

Theory

Transport in Polymer Gels

Polymer networks have been extensively studied, where NMR has been used to study the restricted solvent or tracer transport [320, 321] and directly measure the network structure [298, 320, 321]. From these studies it is clear that the proton containing polymer networks have associated water molecules, which allow for the use of cross-relaxation spectroscopy to detect water-protein interactions and the immobilized

component of the gel [298]. This study will not be concerned with the direct detection of the polymer network motion. Rather the diffusive and advective motion of the solvent molecules is directly measured and interaction with the polymer structure indicates the polymer network structure.

In polymer gels the diffusion of solvent or probe particles is obstructed/restricted by the mesh network, *i.e.* molecules freely diffuse at short time scales ($t << \tau$) but are restricted at long time scales ($t >> \tau$) by the network, the time scales being defined relative to the solvent-structure interaction time (τ). The ratio of probe size and polymer mesh size plays an important role in determining the diffusion of the solvent molecules inside the network as pointed out in the introduction. Measurements and theory indicate that the diffusion coefficient can be described by simple scaling laws which generally show the diffusion coefficient decreasing (become more restricted) as polymer concentration increases [300]. Due to the variability inherent in modeling diffusion in polymer systems multiple models have emerged based on free volume theory, hydrodynamic theory and obstruction effects [300]. For example, Altenberger and Tirrell [295] have considered two mechanisms restricting the mobility of diffusible particles, *i.e.* scattering by the obstacle and the "self-interaction" due to the reflection of hydrodynamic disturbances from the obstacle, when either mechanism is dominant the expected self-diffusion coefficient is respectively

$$D^* \sim (1-\phi)D_0 \text{ and } D^* \sim (1-\phi^{1/2})D_0 \qquad (8.1)$$

While Cukier [296] used a renormalized Navier-Stokes equation to account for screening effects in the interaction between tracers and gel monomers, to obtain

$$\frac{D_0}{D^*} = e^{kR} \quad (8.2)$$

where R is the radius of the tracers, k is the screening parameter, which characterizes the resistance of the polymer network to the motion of the tracers. $k \sim \phi^{\kappa}$ where $\kappa = 0.5$ (mobility is restricted by strong hydrodynamic effects) and $\kappa = 1.0$ (scattering effects are dominant). As indicated by Eqn. (8.2) if the tracer is a small molecule $D^* \sim D_0$, while Eqn. (8.1) indicates that respectively for $\phi = 0.09$, $D^* = 0.91D_0$ and $0.70D_0$.

Experimental results for diffusion in gels are usually obtained while varying ϕ or the degree of swelling. The study that is performed here keeps ϕ constant while varying the experimental displacement observation time (Δ). A similar relationship between D^* and ϕ exists between D^* and Δ, *i.e.* D^* decreases with increasing Δ, with the difference being that as $\Delta \rightarrow \infty$, D^* should asymptote once the probe molecules have all experienced similar environments. This type of $D^*(\Delta)$ study using NMR is displacement scale dependent and requires significant accounting of surface effects between the polymer network and the probe molecules, as well as any potential relaxation weighting effects (T_1, T_2) as Δ increases [322, 323].

Advective transport of solvent through polymer networks has been studied [299, 302, 319], these studies show that the gel network infers hydrodynamic friction as well as deforming from its initial configuration by the drag force, with the flow process being determined by the balance between the viscoelastic response of the polymer network and the solvent flow. In investigating convective transport through gels this viscoelastic network response adds complexity relative to the study of rigid or purely elastic porous media.

Despite the significance, the solvent flow process inside polymer gels has yet to be measured in detail [302], this is where the ability of NMR to study the system non-destructively and acquire varied transport information inside the gel using a Lagrangian reference frame will be utilize to obtain new information for furthering understanding of solvent transport inside gels.

D'Arcy's law is a phenomenological description of flow through a porous media which has been shown theoretically to apply for $Re_{pore} < 1$ and can be written as

$$Q = \frac{kA}{\eta}\frac{\Delta P}{L} \quad (8.3)$$

where Q is the volumetric flow rate, k is the permeability, A is the total cross-sectional area, η is the fluid viscosity and ΔP is the pressure drop in the direction of flow across a sample of length L. For gels under conditions of high porosity ($1 - \phi \sim 1$) the permeability k is related to ξ and η by equation [297]

$$k = \frac{\xi^2}{\eta} \quad (8.4)$$

If the tracers are liquid molecules it is possible to use the effective permeability $k^* = k\eta$, by using $\frac{k^*}{\eta} = \frac{1}{f}$, where $f = \frac{\zeta_c N_A C}{M_0}$ is the friction coefficient where N_A is the Avagadro number, C is the polymer concentration, M_0 is the molecular weight of a monomer and ζ_c is the monomer friction coefficient. It is possible to obtain

$$\xi^2 = \frac{\eta}{f} \quad (8.5)$$

allowing the determination of structural pore sizes. This can then be compared with the results from the hydrodynamic length scales measured in this study.

Hydrodynamic Dispersion in Porous Media

The non-steady, irreversible spreading of flowing fluid molecules within a porous medium is known as hydrodynamic dispersion. It is the process in which a mass of solute at time t = 0, within the flow domain, spreads and occupies an ever-increasing volume of the porous medium as time increases t > 0. It is governed by both mechanical dispersion due to mechanical mixing of advective flow streamlines, the slow motion of molecules near solid surfaces [324] and molecular diffusion across streamlines [59]. A thorough review of the subject matter can be found elsewhere [31, 225] and only ideas related to interpretation of our data will be given here. The dispersion of a fluid in a porous media indicates the degree of interconnectivity of the pore space and provides an insight into the morphological characteristics of the porous medium. A large number of dispersion experiments in porous media have been conducted on Newtonian and non-Newtonian fluids [226]. The Péclet number (*Pe*) is the ratio of advective to diffusive forces that characterizes dispersion in porous media and can be written [219]

$$Pe = \frac{\langle v \rangle l}{D_0} \quad (8.6)$$

where $\langle v \rangle$ is the fluid's mean velocity through the system, l is the characteristic length of the system and D_0 is the self diffusion coefficient of the fluid. The dispersion tensor components, $D_{\parallel}^{*}$ and $D_{\perp}^{*}$, where $\parallel$ and $\perp$ refer respectively to the longitudinal direction parallel-to- and transverse direction perpendicular-to-flow directions of the dispersion tensor, are of interest. The effective dispersion coefficient, *D**, can be defined as [31]

$$D^{*}(\Delta) = \frac{1}{2}\frac{d\sigma^2(\Delta)}{d\Delta} \quad (8.7)$$

where $\sigma^2 = \langle(\boldsymbol{r} - \langle \boldsymbol{r} \rangle)^2\rangle$ is the variance of the distribution of the displacement, $\boldsymbol{r}$, for a particular time Δ. As $\Delta \to \infty$, D^* asymptotes to a constant value in systems with homogeneous structure exhibiting normal diffusion characterized by the Einstein relation $\sigma = 2D^*\Delta$ [56]. Under these circumstances $d\sigma^2/d\Delta$ becomes a constant ($D^* \neq f(\xi, \Delta)$), and the dispersion is Fickian in nature. The probability distribution of displacement, *i.e.* the average propagator, is Gaussian [31] and is written as

$$P(\boldsymbol{r}, \Delta) = \frac{1}{\sigma\sqrt{2\pi}} exp\left[-\frac{1}{2}\frac{(\boldsymbol{r}-\langle v\rangle\Delta)^2}{\sigma^2}\right] \quad (8.8)$$

The longitudinal transport in the system is modeled by the advection diffusion equation

$$\frac{\partial P}{\partial t} + \langle v\rangle \frac{\partial P}{\partial z} = \boldsymbol{D}^* \frac{\partial^2 P}{\partial z^2} \quad (8.9)$$

When the dynamics exhibit asymptotic normal diffusion. In systems in which heterogeneous structure generates correlated dynamics of the flowing fluid non-local (non-Fickian) dispersion dynamics occur [280]. Power law correlations in permeability variations [279] and other long range structural correlations can generate anomalous diffusion dynamics resulting in $\sigma^2(\Delta) = 2D^*(\Delta)\Delta \propto \Delta^\alpha$ with $\alpha < 1$ subdiffusive and $\alpha > 1$ super diffusive. The longitudinal transport in such systems is modeled by Continuous Time Random Walks (CTRW) and fractional advection diffusion equations [325].

Materials and Methods

A 10 mm I.D., 30 mm length Liquid Chromatography (LC) column (Omnifit®) with a frit at the entrance is filled with 9%wt β-lactoglobulin (Sigma-Aldrich®) and 0.3M NaCl dissolved in water overnight. The pH of the mixture is adjusted to pH 5.2 and 7.0 to respectively produce a heterogeneous and homogeneous gel. The mixture is then heated from room temperature to 90^{o}C using a RTE-111 water bath (NesLab®) to allow for the aggregation of the proteins into a gel structure inside the LC column. These gel filled LC columns are then connected to a dual syringe High Pressure LC (HPLC) pump (Pharmacia P-500®) and NMR experiments are performed. A Bruker 250MHz superconducting magnet with a Mirco2.5 (Bruker Biospin, Karlsruhe Germany) microimaging probe ($\mathbf{g}_{max}$: 0.86T/m (40A) in three orthogonal (X,Y,Z) gradient directions) and 20mm rf coil is used. Experiments at no flow conditions and at constant volume flow conditions are done with volumetric flow rates of 10, 20 and 30 mL/hr. In the homogeneous gel pure water and 0.3M NaCl fluids are used to check the impact of the flowing fluid on the gel elastic response. To characterize the gel structure NMR images (MRI's), velocity maps, stereo and compound microscopy images were obtained (Fig. 8.1). The homogeneous gel was found to compact with increasing flow rate and tear in the middle at a flow rate of 30mL/hr (see Fig. 8.2), while the heterogeneous gel maintained its structure at all flow rates tested (up to 100mL/hr). This morphological difference is associated with the higher pressures required to maintain the volumetric flow rates through the homogeneous gels, while the heterogeneous gel requires much lower pressure drops due to its open structure. The strain ($\Delta L/L$) on the gels was

quantified from the MRI's by the change in the height (ΔL) of the gel relative to their original heights (L).

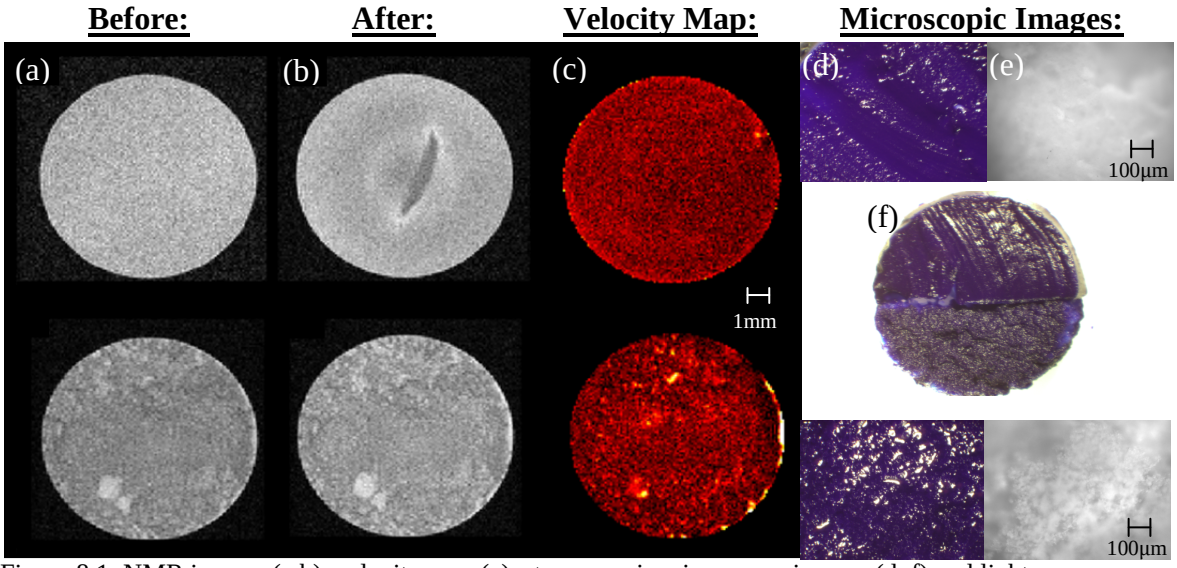

Figure 8.1 NMR images (a,b), velocity map (c), stereoscopic microscopy images (d, f) and light microscopy images (e) of the homogeneous (top) and heterogeneous (bottom) gels. NMR experimental parameters: 256x256pixels, 1 Average, SW: 50kHz, T_R: 1sec or 5sec, 2min, T_E: 12ms, 1mm slice, FOV: 12mmx12mm or 11mmx11mm, Voxel Resolution: 47x47x1000 μm^3 or 43x43x1000 μm^3. Gradients for velocity maps: 60 and 460mT/m, δ: 1ms, Δ: 20ms.

The gel structure and flowing solvent transport molecular dynamics were investigated using PGSE NMR techniques to obtain the probability distribution of displacement, reciprocal ***q***-space data and dispersion coefficients in directions parallel and perpendicular to the flow direction. The PGSE pulse sequence (figure 4a) and velocity imaging sequence, which combines PGSE and MRI sequences (figure 4b) show the timing of the application of radiofrequency (rf) and magnetic field gradients. These experiments were conducted at no-flow as well as during the application of the different volumetric flow rates (10, 20 and 30mL/hr).

NMR Experiments

The NMR theory presented here serves as a brief overview for the NMR pulse sequences used to measure the transport phenomena in this study, more details can be found elsewhere [1]. If the translational motion of a nucleus in fluid molecule has a time dependent displacement of $\boldsymbol{r(\Delta)}$ then the self-motion of the molecule is described by the conditional probability $P(\boldsymbol{r}|\boldsymbol{r'},\Delta)$ that a nuclear spin originally at $\boldsymbol{r}$ will move to $\boldsymbol{r'}$ over time Δ. The PGSE sequence (figure 4a) applies a magnetic field gradient pulse **g** of duration δ, which initially imparts a spatially dependent phase shift $\phi(\boldsymbol{r})$ on the spins $\phi(\boldsymbol{r}) = \gamma\delta\boldsymbol{g}\cdot\boldsymbol{r}$. After delay time Δ, the NMR active molecules, spins, will have migrated to $\boldsymbol{r'}$, and a second equivalent but oppositely orientated due to the 180° rf pulse, gradient pulse is applied to the system. The net phase shift imposed on the spins by the pair of gradient pulses is $\phi(\boldsymbol{r}) = \gamma\delta\boldsymbol{g}\cdot(\boldsymbol{r'}-\boldsymbol{r})$. For the case of stationary spins, a perfectly refocused echo occurs. In the case of motion, there is a net phase shift in the echo, which is a product of the dynamic displacement $(\boldsymbol{r'}-\boldsymbol{r})$ and the wave vector $\gamma\delta\boldsymbol{g}$. The normalized echo signal that is acquired following this second gradient pulse has the form

$$E(\boldsymbol{g},\delta,\Delta) = \int \rho(\boldsymbol{r}) \int P_i(\boldsymbol{r}|\boldsymbol{r'},\Delta)\, exp[i\gamma\delta\boldsymbol{g}\cdot(\boldsymbol{r'}-\boldsymbol{r})]d\boldsymbol{r'}d\boldsymbol{r} \quad (8.10)$$

where $E = \frac{S(g)}{S(0)}$ which eliminates relaxation effects and $\rho(\boldsymbol{r})$ is the initial spin density of the sample. As negligible motion is assumed to occur during gradient during δ and $\delta \ll \Delta$ the so-called "narrow pulse approximation" is applied [1].

The total signal is a superposition of transverse magnetization, in which each phase term $exp[i\gamma\delta\boldsymbol{g}\cdot(\boldsymbol{r'}-\boldsymbol{r})]$ is weighted by the probability of a spin, originally

located at $\boldsymbol{r}$, moving to $\boldsymbol{r'}$ in the time Δ, *i.e.* $\rho(\boldsymbol{r})P_i(\boldsymbol{r}|\boldsymbol{r'},\Delta)$. Introducing a dynamic displacement $\boldsymbol{R} = \boldsymbol{r'} - \boldsymbol{r}$ and taking the ensemble average over all spins, $\int \rho(\boldsymbol{r})\, P_i(\boldsymbol{r}|\boldsymbol{r'},\Delta)d\boldsymbol{r}$ yields the average propagator or van Hove self correlation function, $P(\boldsymbol{R},\Delta)$ [1].

It is useful to introduce the concept of $\boldsymbol{q}$-space, the dynamic analogue of the static reciprocal space, $\boldsymbol{k}$-space, where $\boldsymbol{q} = \frac{\gamma\delta\boldsymbol{g}}{2\pi}$. Now we can write

$$E(\boldsymbol{q},\Delta) = \int P(\boldsymbol{R},\Delta)\, exp[i\gamma\delta\boldsymbol{q}\cdot\boldsymbol{R}]d\boldsymbol{R} \quad (8.11).$$

This equation shows that $P(\boldsymbol{R},\Delta)$ is obtained from a Fourier transform of $E(\boldsymbol{q},\Delta)$ with respect to $\boldsymbol{q}$.

For random diffusive displacements and considering motion in only one direction, the average displacement propagator takes the form of a Gaussian distribution of displacements

$$P(\boldsymbol{R},\Delta) = \frac{1}{2\sqrt{\pi D\Delta}}\, exp\left[-\frac{\boldsymbol{R}^2}{4D\Delta}\right] \quad (8.12).$$

The Fourier transform of this gives us the expected signal amplitude; an exponential decay, characterized by a purely diffusive coefficient *D*

$$E(\boldsymbol{q}) = exp(-D(2\pi\boldsymbol{q})^2\Delta)\cdot exp(i2\pi\boldsymbol{q}\cdot\langle\boldsymbol{v}\rangle\Delta) \quad (8.13).$$

The well-known Stejskal-Tanner equation [30] includes a correction of the diffusion time to account for the finite duration of the gradient pulse. Therefore a plot of Ln($E(\boldsymbol{q})$) versus $(2\pi\boldsymbol{q})^2(\Delta - \delta/3)$ results in a linear relationship whose slope is the effective diffusion coefficient of the sample.

The ***q***-space pulse sequences presented above to measure spin displacement can be combined with NMR imaging (***k***-space) methods to obtain an image where each pixel has ***q***-space information, allowing for the imaging of coherent motion from the phase shift of the signal known as a velocity map [1, 285].

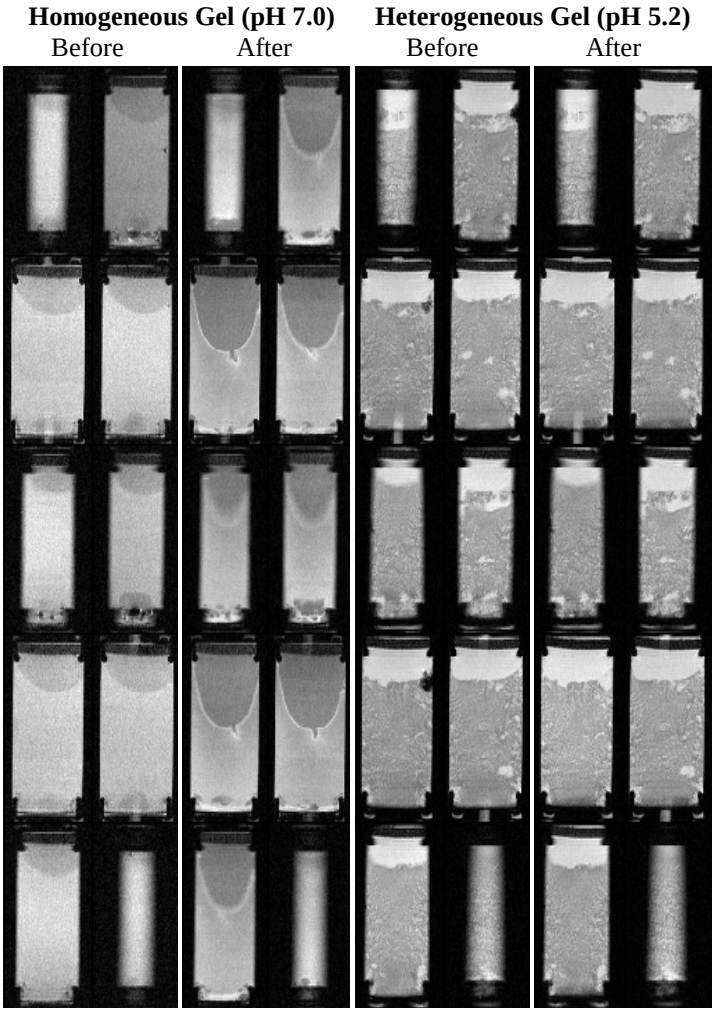

Figure 8.2 NMR Images show a series of 1mm slices through the LC column showing the pH 7.0 (left) and pH 5.2 (right) gels before and after a full experimental run. For the pH 7.0 gel the lighter colored regions indicate the location of the gel, while for the pH 5.2 gel this is the water region and the gel regions are darker. This difference is due to different relaxation times for the experiments (1sec vs. 5sec). NMR experimental parameters: 256x256pixels, 1 Average, SW: 50kHz, T_R: 1sec or 5sec, T_E: 40ms, 1mm slice, FOV: 30mmx12mm, Voxel Resolution: 117x47x1000 μm^3.

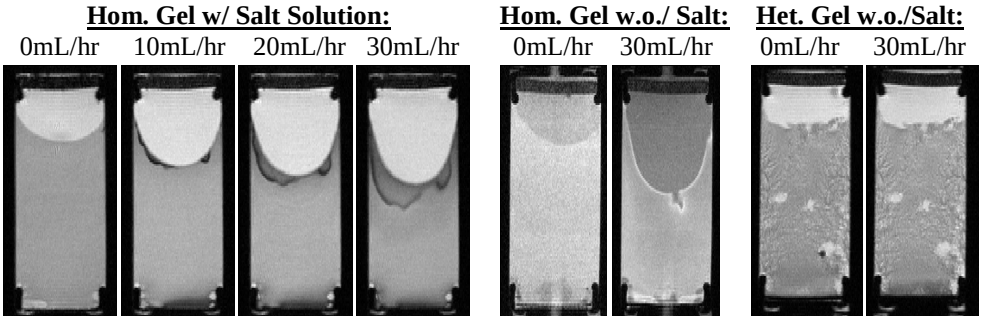

Figure 8.3 NMR images of gels after flow ceases for the indicated volumetric flow rates through the homogeneous and heterogeneous gels. NMR experimental parameters: 256x256pixels, 1 Average, SW: 50kHz, T_R: 1sec or 5sec, T_E: 40ms, 1mm slice, FOV: 30mmx12mm, Voxel Resolution: 117x47x1000 μm^3.

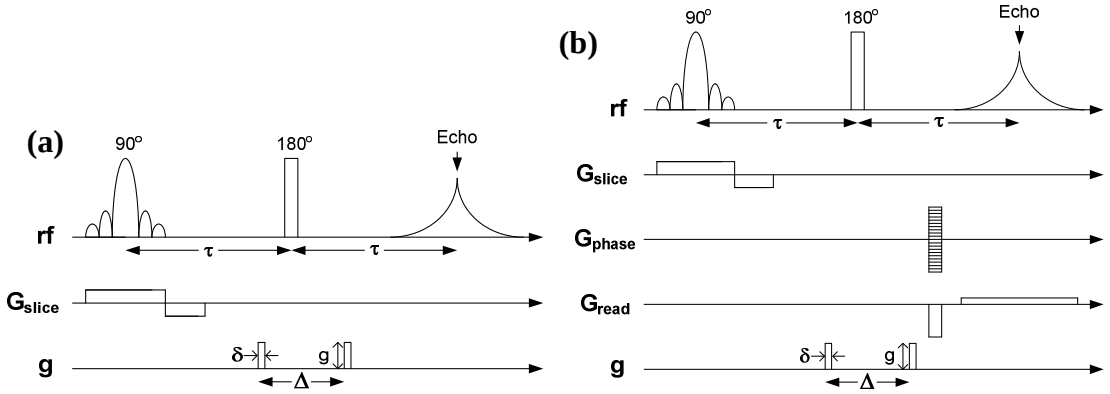

Figure 8.4 (a) Slice selective pulsed gradient spin echo (PGSE) sequence to measure spin displacement. $\boldsymbol{\tau}$ is the echo time, $\boldsymbol{\Delta}$ is the measurement time, $\boldsymbol{\delta}$ and $\boldsymbol{g}$ are the duration and magnitude of the pulsed field gradients. (b) Slice selective velocity map pulse sequence.

Results and Discussion

Imaging Structure and Velocity

Figure 8.1 shows NMR images of the gels used in this study before and after flow experiments as well as velocity maps during flow. For comparison, stereo microscope and compound microscope images of the same gels sliced in the middle are also shown, the gels have been stained with a crystal violet dye. These show that the pH = 7.0 gel is homogeneous on the macroscopic scale ($\geq 100\mu m$) while the pH = 5.2 gel is

heterogeneous on the macroscopic scale. These differences are due to the microscopic structure of the proteins as they denature and aggregate during the preparation of the gels. On the (μm) scale both gels have some heterogeneity, with the homogeneous gel having much smaller gaps between aggregates (figure 8.1e). The velocity maps are particularly illuminating, they are averaged over a 1mm slice with an in-plane resolution of $47\times47\mu m^2$ and show clear signs of flow heterogeneity for the β-lactoglobulin gel formed at pH 5.2, while only minimal flow heterogeneity exists for the β-lactoglobulin gel formed at pH 7.0. It is evident, figure 1 bottom row, that the heterogeneous gel has many openings in the gel structure on the order of 100 - 1000μm. This heterogeneity is expected to allow significant backbone flow, similar to percolation structures [326], across the gel during flow experiments. This explains the ability of the heterogeneous gel to resist structural deformation, even at high flow rates (100mL/hr), due to the lower pressure gradient required to push the solvent molecules through the gel at fixed volumetric flow rate. This is contrasted by the homogeneous gel which on the scales > O(10μm) is homogeneous, figure 8.1. This is important because at the shortest experimental time of this study (Δ = 25ms) the standard deviation (σ) for the displacement of water molecules due to free diffusion, *i.e.* the diffusive length $l_D \sim \sqrt{2D_0\Delta}$, is 10$\mu m$, indicating that on this displacement scale there should be homogeneity in flow dynamics of solvent molecules across the gel, characterized by a Gaussian distribution of displacement during flow experiments.

Since there are no macro-scale openings for backbone flow development in the homogeneous gel, pressure gradients across this gel are much higher than those for the

heterogeneous gel. This explains why this gel gets compressed, see figure 8.2 and 8.3, and finally fractures for the flow of DI water once the gel structure has compressed/deformed sufficiently. To determine the impact of the presence of NaCl in the flowing solvent on the homogeneous gel elastic response and fracture 0.3M NaCl is also used. As can be seen in figure 8.3, a darkened region forms when a salt solution (0.3M NaCl) is pumped through the homogeneous gel, which is not present when DI water without salt is the flowing solvent. This region propagates further into the gel with increasing flow rate. The elastic strain $\Delta L/L$ for the DI water and 0.3M NaCl solution are similar but the NaCl flow does not fracture the gel.

To investigate the origins of this phenomena, a T_2 relaxation experiment (figure 8.5) was performed on the gel after flow experiments had been conducted. Spin-Spin or T_2 magnetic relaxation provides information on the rotational mobility of the water molecules.

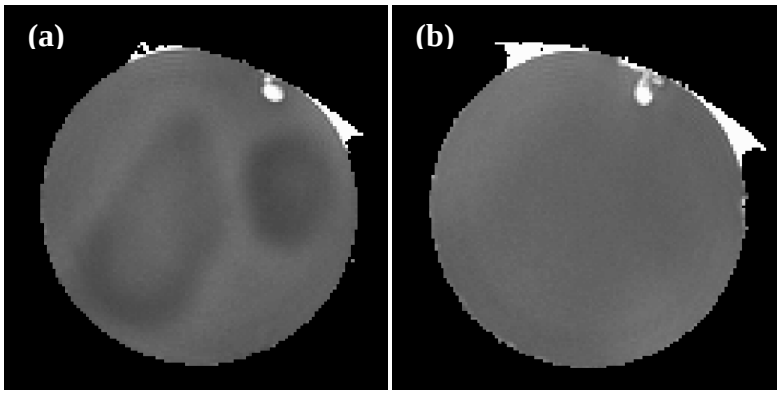

Figure 8.5 $\boldsymbol{T_2}$ relaxation map for the homogeneous gel after flow experiments, done to investigate the darkened region visible in the NMR images (figure 8.3) when 0.3M NaCl is flowed through the gel. 1 mm slices of the excitation region (a) and 2mm down steam (b) from this region. $\boldsymbol{T_{2,gel} \sim 0.2 T_{2,water}}$, $\boldsymbol{T_{2,dark\ regions\ of\ gel} \sim 0.81 T_{2,light\ region\ of\ gel}}$. NMR experiment parameters: 256x256pixels, 16 average, SW: 50kHz, T_R: 5sec, T_E: 12ms, 16 echos, 10x1mm slices, FOV: 12mmx12mm, Voxel Resolution: 47x47x1000 μm^3 .

In regions of greater gel polymer density the restricted slower rotational molecular motion decreases T_2 relative to more mobile water molecules in lower polymer density regions. The gel was removed from the LC column and placed inside a 20mm O.D. glass vial. T_2 relaxation images are presented which show 1mm slices of a region corresponding to the excitation region used for the flow experiments (figure 8.5a) and a region two millimeters downstream (figure 8.5b), where no darkening of the gel had occurred. A bright region of free water trapped by capillary between the inner wall of the glass vial and the gel was used to obtain the T_2 relaxation time of free water ($T_{2,water}$). The non-darkened gel regions have $T_{2,light\ region\ of\ gel} \sim 0.2T_{2,water}$, while the darkened gel regions have $T_{2,dark\ regions\ of\ gel} \sim 0.81T_{2,light\ region\ of gel}$ a 20% lower T_2 indicates greater restriction of rotational mobility of the water molecules in the dark region of the images. A potential NMR artifact related to the addition of salts requires more rf power to cause the same angular spin magnetization flip. This rf pulse intensity variation would alter the relative image intensity of the bright and dark regions if salt were concentrating in the low signal intensity region. NMR imaging experiments were conducted determine if this signal intensity variation was due to salt concentration. The 180^o rf pulse strength was varied by 1db over a range of 10db above and below the correct 180^o rf pulse. These experiments showed negligible signal intensity impact within experimental error, indicating that this lowering of pixel intensity in the NMR images is not due to higher local salt concentrations.

An explanation of this effect may be found in the gel literature, where it has been shown that the effect of high salt concentrations on β-lactoglobulin during the

aggregation process is to increase aggregate branching and cause an increase in local protein density. At salt concentrations higher than 0.1M the critical association concentration (CAC) drops to less than or equal to 0.1g/L while the gelation concentration (C_g) equals 1g/L at 0.4M NaCl [311]. For the current experiments C = 90g/L and therefore C >> CAC and C_g so the activation energy for aggregation is low, indicating that the pressure driven flow introduces sufficient energy and contact between aggregates at high pressure regions to cause local densification of gel aggregates in the presence of salt. These denser regions are distinguishable by NMR (figure 8.3) as the flow rate and hence strain increases. These regions of local gel density increase correlate to the local stress and serve as indicators for sub-micron gel structural changes and as location predictors for macroscopic fracture.

Flow Dynamics by NMR

NMR flow dynamics experiments were conducted for both the homogeneous and heterogeneous gels at flow rates of 0, 10, 20 and 30mL/hr. Before examining the data, it is important to clarify the relative scales of displacement due to advection and diffusion in the two gels. The flow rates 10, 20 and 30mL/hr correspond the mean solvent velocities of 35.4 μm/sec, 70.7 μm/sec and 106.1 μm/sec based on the volumetric flow divided by the cross sectional area of the LC column the superficial velocity. For the range of experimental displacement observation times used in this study, Δ = 0.025 - 0.600s, the advective mean displacements based on the superficial velocity range from 0.9 – 63.7μm, increasing linearly with increasing Δ. The standard deviation (σ) for the displacement due to the free diffusion of water at 20^{o}C on the same time scale, Δ = 0.025

- 0.600sec, is 10 - 49 μm, where the width of the Gaussian distribution goes as $\sqrt{\Delta}$. Since the variance of displacement is affected by both these processes, it is expected that unless significant advective driven hydrodynamic dispersion occurs due to mechanical, Saffman and Taylor dispersion processes, the overwhelming contribution will be due to the diffusion of the solvent molecules within the gel structure.

Propagator experiments showing the probability of displacement for the homogeneous and heterogeneous gels at Δ = 200ms, for the flow rates of 0, 10, 20 and 30mL/hr are shown in figure 8.6. For the homogeneous gel (figure 8.6a), the probability distribution is Gaussian and changes minimally with increasing flow rate, by broadening mean and a displacement shift to a larger displacement. As will be seen below the width of the Gaussians change with increasing flow rate due to the impact of advective motion. The Gaussian dynamics for the homogeneous gel (figure 8.6b) is contrasted by the flow through the heterogeneous gel which shows a significant change in the probability distribution of displacement with increasing flow rate. The data show a transition towards a probability distribution with a significant long displacement, backbone flow, contribution.

To compare the propagator data the variance of the propagator for both gels and all flow rates and experimental times investigated are presented in figure 8.7. To calculate this variance the standard statistical definitions are used of mean (1^{st} raw moment) $\mu = \sum_i x_i P(x_i)$ and variance (2^{nd} central moment) $\sigma^2 = \sum_i (x_i - \mu)^2 P(x_i)$ of the normalized propagator are used.

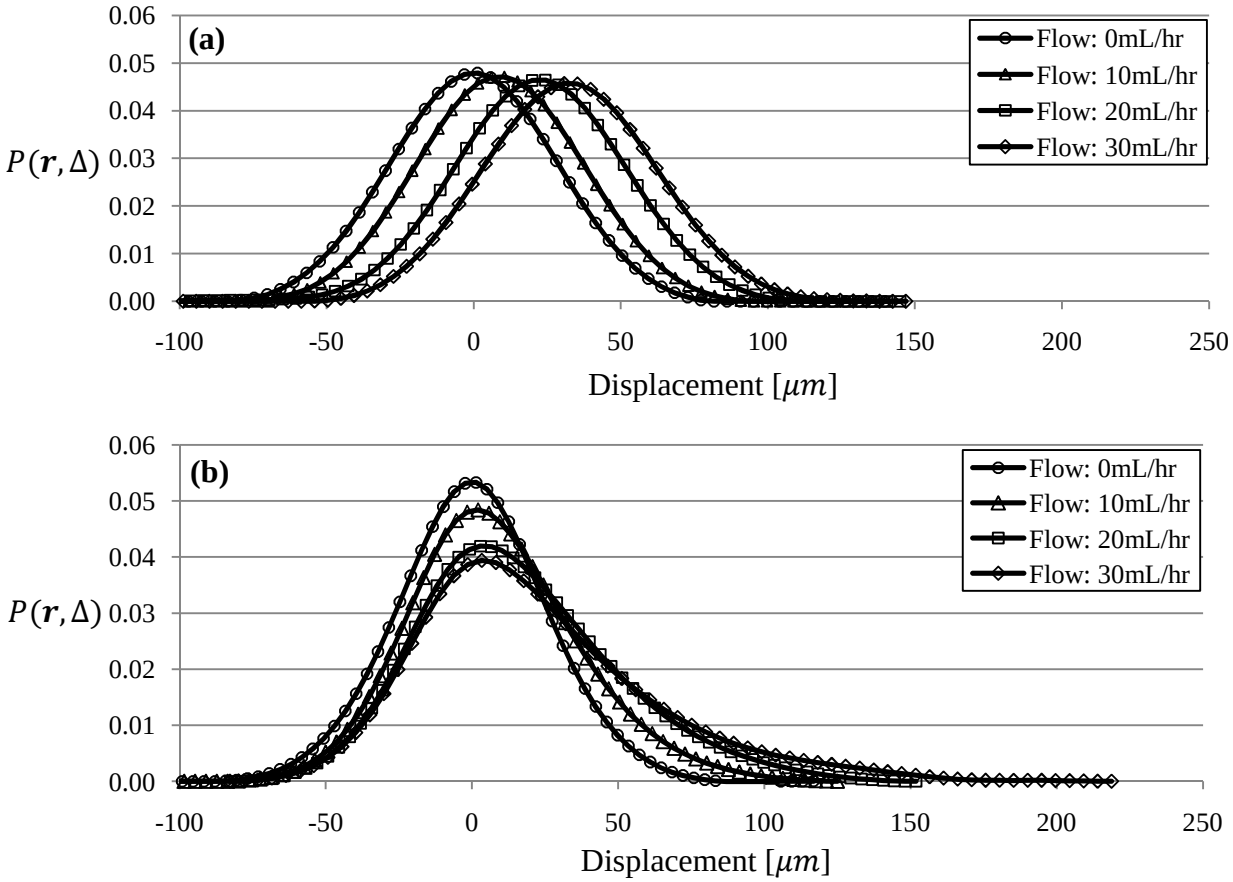

Figure 8.6 Propagators for the flow of DI water through the homogeneous (a) and heterogeneous (b) gels in the direction parallel to the flow direction at increasing flow rate for Δ = 200ms.

A useful method to further analyze the propagator data is to look at the stretched exponential wavelength scaling: $E(q,\Delta)\sim\exp(-cq^{\beta})$ which corresponds to a space fractional ADE. This approach has been previously used in a phenomenological fashion to characterize the non-Gaussian nature of PGSE data [327, 328]. The low ***q***-space data is fit with this scaling, where $\beta \sim 1$ corresponds to an exponential, while $\beta \sim 2$ corresponds to a Gaussian probability distribution. The results of fitting the low q-space data for flow rates 0 – 30mL/hr in the parallel-to-flow direction is shown in Table 8.1.

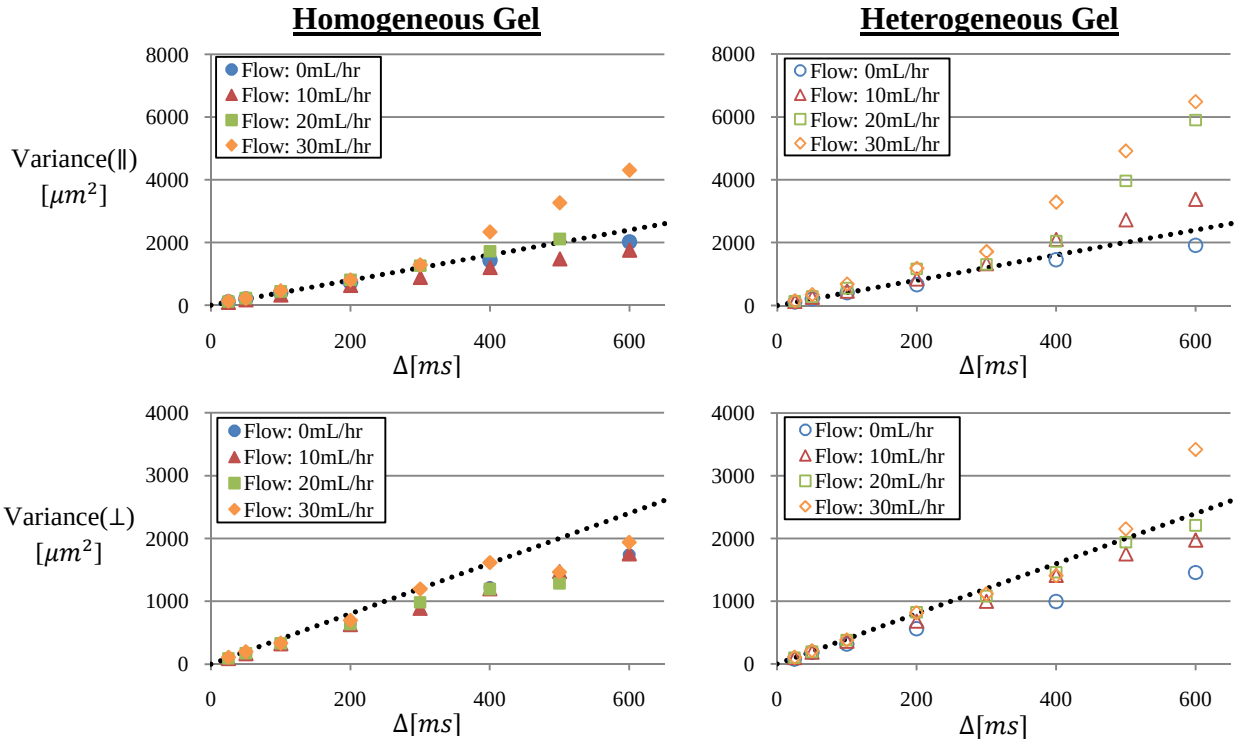

Figure 8.7 Variance obtained from the probability distributions obtained using propagator experiments for the homogeneous (filled symbols) and heterogeneous (open symbols) gels at 0, 10, 20 and 30mL/hr, in directions parallel (∥) and perpendicular (⊥) to the axial flow direction. The dotted line shows the mean square displacement for free diffusing water at 20°C.

Table 8.1

			Homogeneous Gel	Heterogeneous Gel
Δ [ms]	**Flow Rate [mL/hr]**	**Dir**	**β**	**β**
25	0	Z	1.85	1.67
100	0	Z	1.80	1.67
400	0	Z	1.83	1.69
25	10	Z	1.89	1.82
100	10	Z	1.80	1.69
400	10	Z	1.63	1.72
25	20	Z	1.82	1.75
100	20	Z	1.80	1.49
400	20	Z	1.65	1.41
25	30	Z	1.86	***
100	30	Z	1.87	***
400	30	Z	1.89	***

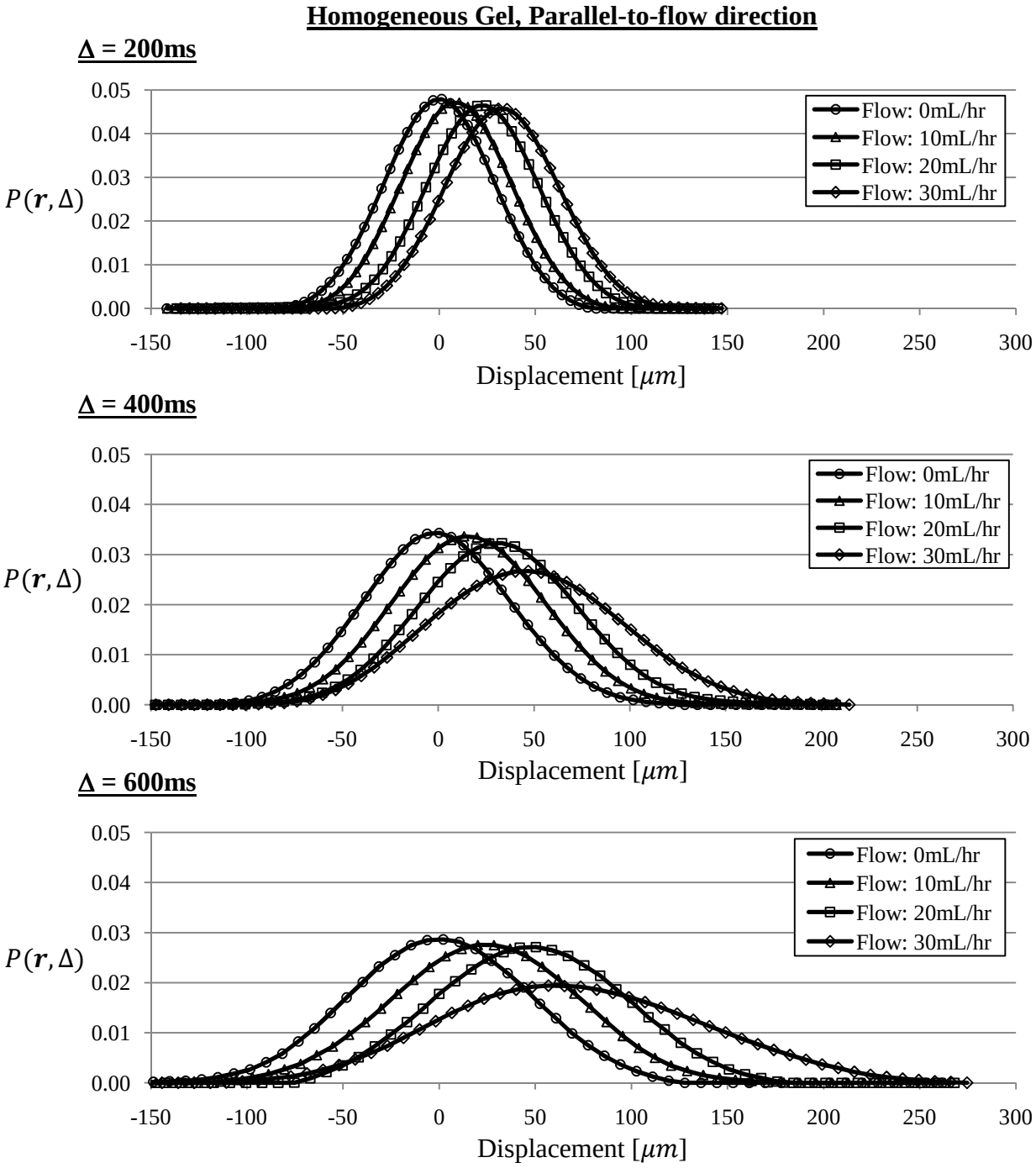

Figure 8.8 Shows the evolution of the propagators with flow rate at different experimental times (Δ = 200, 400 and 600ms) for the homogeneous gel.

These indicate that there is some restriction to the free diffusion of the homogeneous and heterogeneous gels ($\beta < 2$) and that the heterogeneous gel has a more exponential probability distribution than the homogeneous distribution as water flows through the systems, confirming the results from the propagator data.

In the flow direction for the homogeneous gel, for the first three flow rates (0mL/hr, 10mL/hr and 20mL/hr) the variance is linear with time. The dispersion at 10mL/hr is systematically lower than the pure molecular diffusion at 0mL/hr, while the 20mL/hr flow is higher than both. At a flow rate of 30mL/hr, the variance follows the variance for 20mL/hr up till Δ = 300ms, and then deviates significantly with much higher dispersion at $\Delta \geq$ 400ms. This can be clearly seen by comparison of the propagators for each flow rate at fixed displacement observation times shown in figure 8.8. In the perpendicular-to-flow direction for the homogeneous gel, the variance for the first three flow rates (0mL/hr, 10mL/hr and 20mL/hr) is approximately the same over the whole range of Δ, while for 30mL/hr it varies but trends with the lower flow rate data.

An important aspect of the transport in the homogeneous gel is that the gel is compressing as the flow rate increases (figure 8.3) and at the 30mL/hr flow rate, the darkened region (discussed above) has reached the slice being excited for the propagator experiments. Therefore the highest flow rate data (30mL/hr) deviation from the lower flow rate data trends is due to the gel structural changes directly affecting the measured dynamics. This compression also explains the hydrodynamic dispersion at 10mL/hr being lower than the dispersion at 0 mL/hr, since the diffusion contribution to the dispersion has decreased due to increased restriction, which is not offset by the

hydrodynamic dispersion due to the advective dynamics since this flow rate the diffusive length scale is larger than the advective length scale. Since there is minimal contribution due to advection induced hydrodynamic dispersion in the perpendicular-to-flow direction the only data which deviates significantly is for 30mL/hr, while the 10mL/hr data is only slightly lower on average than the 0mL/hr data.

In the parallel-to-flow and perpendicular-to-flow directions for the heterogeneous gel, the variance follows the general trend of increasing variance with increasing flow rate at the same experimental time (Δ). An important result is the large change in the slope of the variance as a function of Δ seen at $\Delta > 300$ms for both the flows at 20mL/hr and 30mL/hr. This is associated with a significant growth in a long displacement (backbone flow) tail in the probability distribution of displacement, evident in figure 8.9. Figure 8.9 shows another interesting trend in the heterogeneous gel propagators, which is the initial shift in the peak of the probability distribution towards higher mean displacements as the flow increases, which then ceases at long experimental times (Δ = 400 & 600ms) and high flow rates (20mL/hr and 30mL/hr). This behavior is indicative of a hold-up like effect whereby solvent molecules are stuck in non advective regions [329].

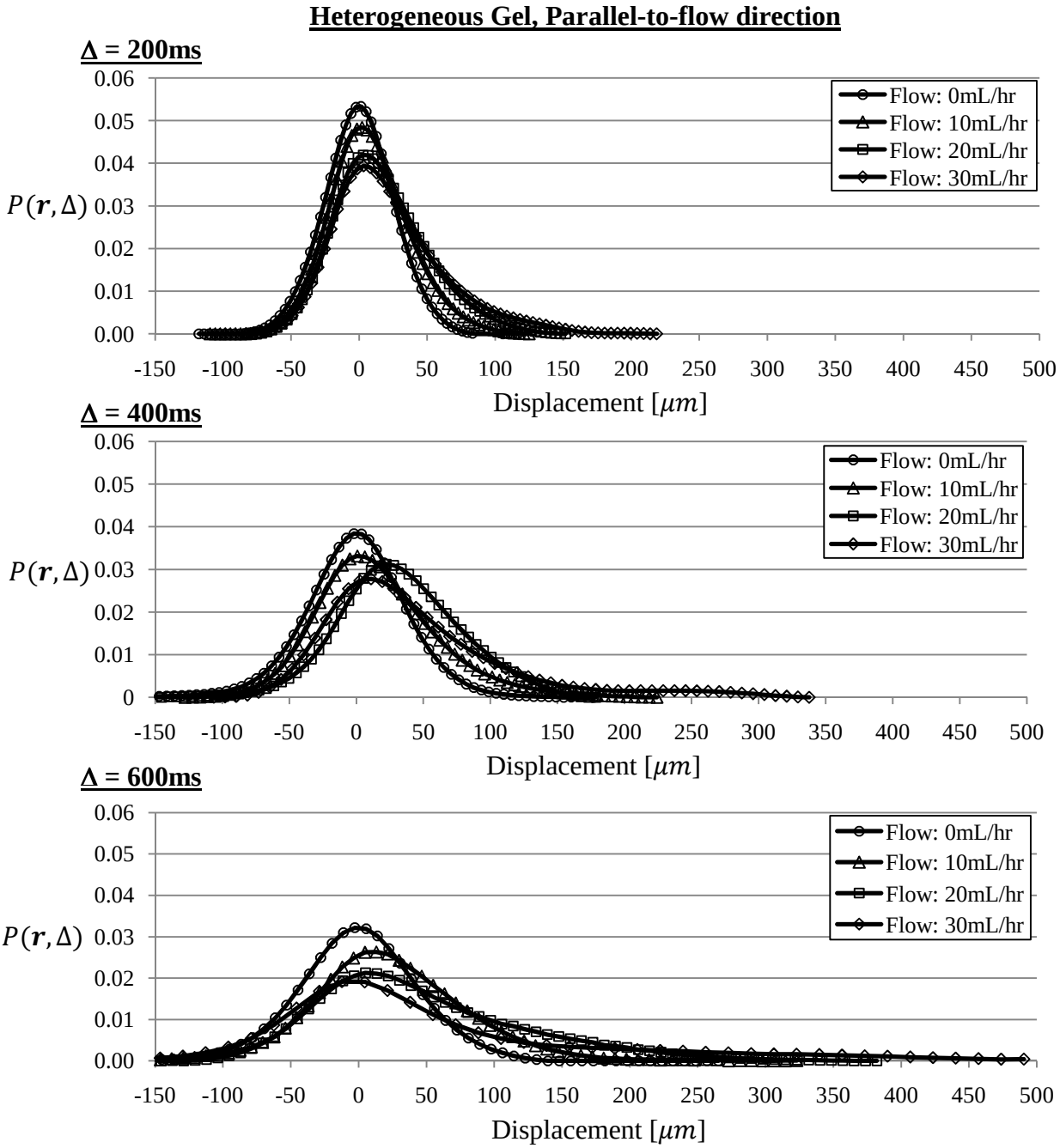

Figure 8.9 Shows the evolution of the propagators with flow rate at different experimental times (Δ = 200, 400 and 600ms) for the heterogeneous gel.

This behavior can be explained by consideration of a two population model. One population of solvent molecules behaves as in the homogeneous gel, *i.e.* has a Gaussian-like distribution of displacement shifting to higher mean displacements with increasing

flow rates. The solvent molecules of the second population occupy the fast flow regions, seen clearly in the velocity map shown in figure 8.1. The solvent molecules can move between these populations by molecular diffusion, with an increased probability of having occupied both populations as Δ increases. However as the mean displacement of the first population increases, more and more molecules will experience the second population, with a displacement of $\sim 25\mu m$ indicating an approximate limit as to how far the molecules can displace without experiencing the second population. The $\sim 25\mu m$ length is obtained from the cross-over point of the probability distribution functions at Δ = 200ms.

This two population model shows what effect the tearing in the middle of the homogeneous gel has on the propagator. Figure 8.10 shows the propagators in the parallel-to-flow direction at a flow rate of 20mL/hr at Δ = 100ms for the heterogeneous gel, the homogeneous gel and the homogeneous gel after a fracture has formed (see figure 8.1 for NMR image of the fracture).

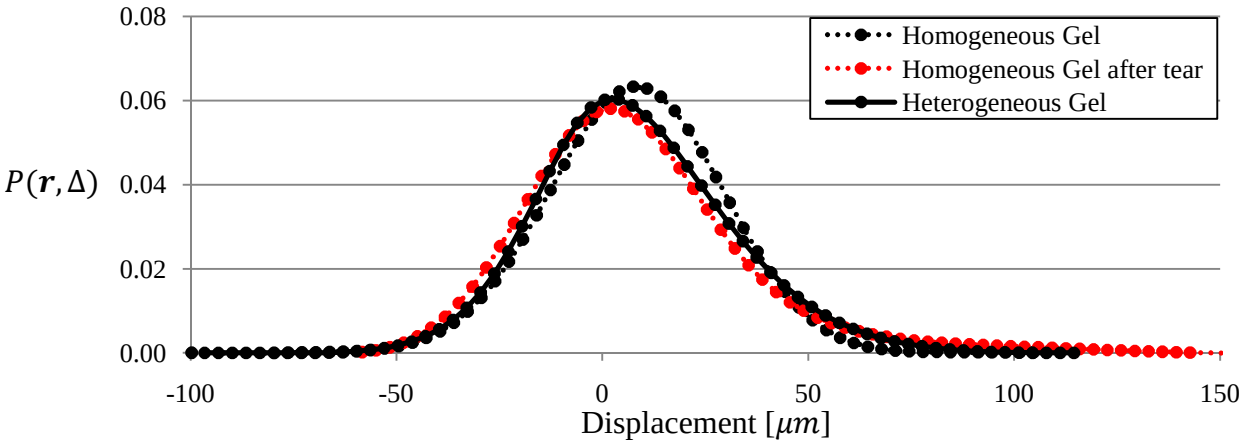

Figure 8.10 Propagators for the homogeneous gel before and after tearing and the heterogeneous gel at a flow rate of 20mL/hr for Δ = 100ms, parallel-to-flow direction.

The similarities in the propagators for the heterogeneous gel and the homogeneous gel after tearing are striking considering how dissimilar in structure and dynamics the two gels are. After fracture a preferential flow path has been created where the two population model is clearly applicable.

To further examine the transport behavior inside the different gels, the dispersion coefficient (D^*) was measured using low-q experiments and Stejskal-Tanner plots [1]. Experiments were done while varying the measurement time (Δ) and the flow rate both in the parallel-to-flow and perpendicular-to-flow directions, see figure 8.11. The dispersion coefficients in the parallel- and perpendicular-to-flow direction were normalized using the free diffusion of water at 20^{o}C, $D_w = 2 \times 10^{-9}$ m^2/s, to allow for a clear presentation of the dispersion relative to free-diffusion and an easier comparison with the variance data. When comparing the normalized dispersion coefficient and the variance data it is important to emphasize that the former is obtained from the low-$\boldsymbol{q}$ data, $E(\boldsymbol{q}, \Delta) = 1.0 – 0.7$, which correspond to large displacements, *i.e.* signal effects due to structures of lengths O($50\mu m$) and larger affect the experiment, while the propagator is acquired from the entire $\boldsymbol{q}$-space data and therefore measures all displacements. The dispersion coefficient is related to the variance through a gel structure dependent relationship, *i.e.* the relationship of how the solvent molecules traverse through the gel structure on the time scales being investigated.

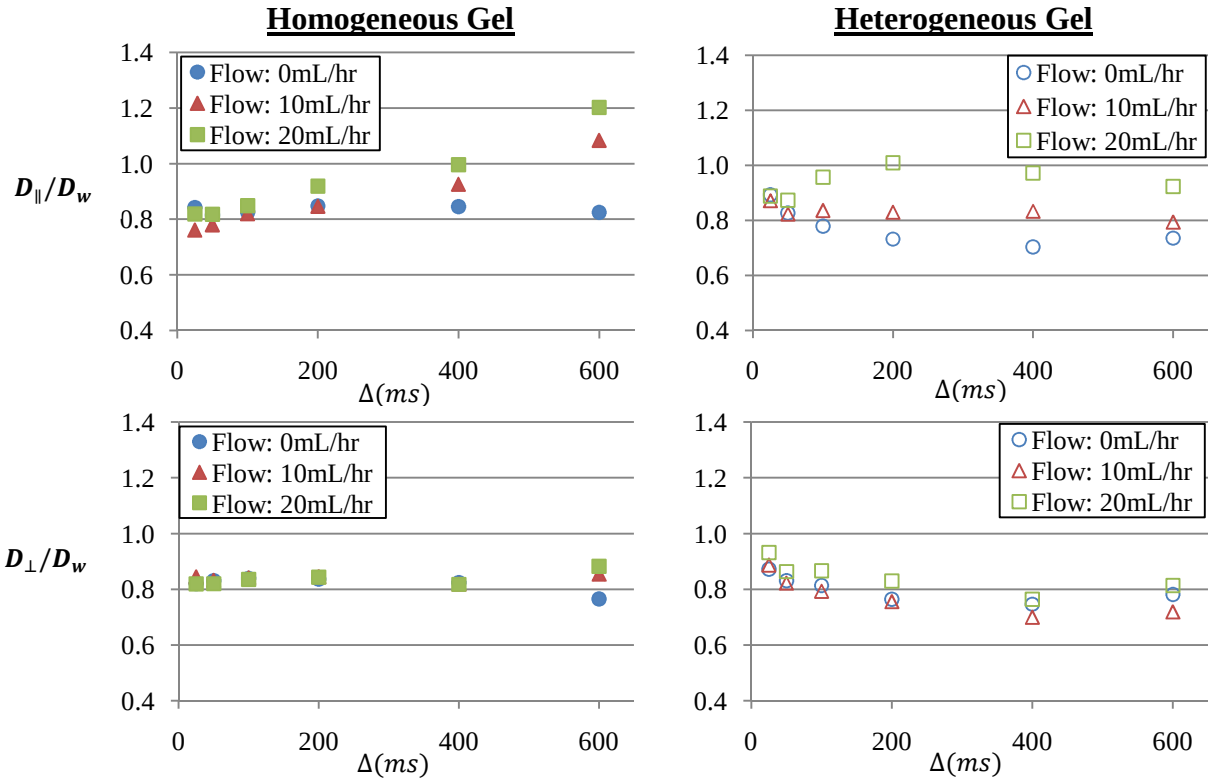

Figure 8.11 Shows the normalized effective diffusion coefficients as a function of time (Δ) for the homogeneous (closed circles) and heterogenous gels (open circles) at different flow rates (0mL/hr, 10mL/hr and 20mL/hr). NMR experimental parameters: Acq_size: 256, 32$\boldsymbol{q}$-pts, G_{max}: 0.344 – 0.129T/m for Δ = 25-600ms, δ = 4ms, SW: 5kHz, N_{avg}: 8, ΔZ: 1mm.

To address these relationships, first a simple restricted dynamics relationship is assumed, where the solvent molecules have all experienced a similar motional restriction due to the gel phase length scale a such that $\Delta \gg \tau$, where $\tau \sim \frac{a^2}{D_0}$ is the correlation time of the solvent-structure interaction. The variance

$$\langle \boldsymbol{r}^2(\Delta) \rangle = 2D_R\Delta \quad (8.14)$$

where $D_w > D_R$ and D_R is the restricted solvent molecule diffusion coefficient . It can be seen that this relationship models the correct linear relationship of variance with time for the no flow data for the homogeneous gel, where $D_{\parallel}/D_w$ and $D_{\perp}/D_w$ are approximately constant while the variance (figure 8.7) has a linear dependence with Δ. This relationship

also agrees with the perpendicular-to-flow direction data for the homogeneous gel. For the heterogeneous gel, the data is affected by the restriction length scale, since a larger diffusive length scale is present ($\tau \sim \frac{a^2\text{het}}{D_0} >> \frac{a^2\text{hom}}{D_0}$) $\Delta \sim O(\tau)$, and therefore has a time dependent relationship associated with increased restriction with time. Using the propagator displacements due to diffusion, O(10 μm), it is evident from figure 8.11 that on this length scale there are multiple populations within the excitation slice and therefore a decreasing effective diffusion with time as is well known for porous media [322] is expected.

In the presence of flow a two component model which accounts for the addition of a convective dispersion component:

$$\langle \boldsymbol{r}^2(\Delta) \rangle = 2D_R\Delta + K_\alpha \Delta^\alpha \quad (8.15)$$

with a linear addition of a diffusive and ballistic motion ($\alpha = 2$) terms, where $K_2 = \langle U^2 \rangle$ [54] assumes an independence and separation of scales. Figure 8.12 shows Eqn. (8.15) and Eqn. (8.12) compared with the parallel-to-flow direction variance data for the homogeneous and heterogeneous gels at flow rates of 0mL/hr and 30mL/hr, where D_R is obtained from the average of the stationary flow dispersion data, $D_\parallel/D_w$ = 0.86, for the homogeneous gel and $\langle U^2 \rangle$ = (106.1 μm/sec)^2. To fit Eqn. (8.12) to the heterogeneous gel α = 2 fits well, while for the homogeneous gel α = 1.86 fits the data well. Both models use $K_2 = \langle U^2 \rangle$. These equations form an envelope for the data and it is therefore reasonable to assume that the normalized dispersion coefficients (figure 8.11) fall within a description which accounts for a ballistic motion and restricted diffusion.

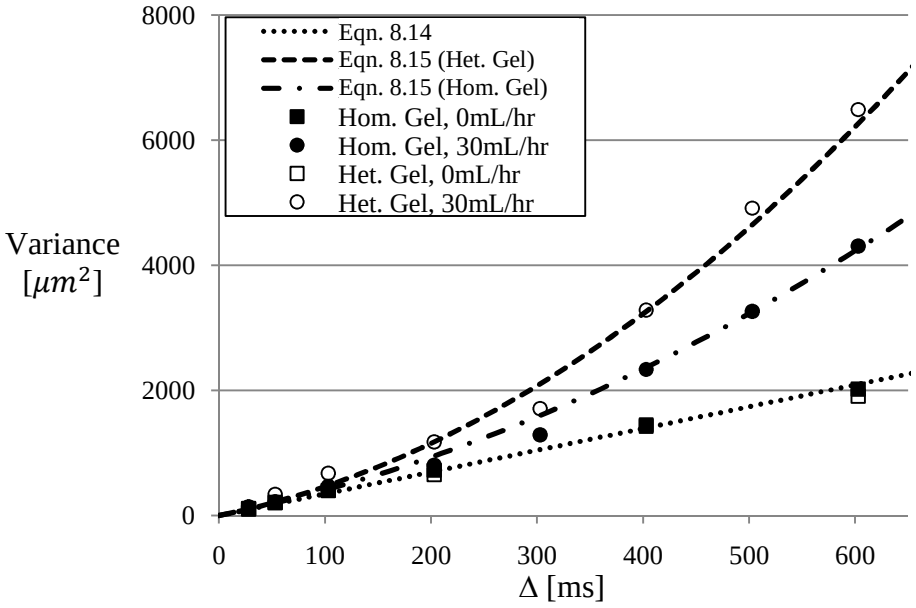

Figure 8.12. Eqn. 8.14 & 8.15 fit to the variance obtained from propagator experiments for flow parallel-to-flow direction at 0mL/hr and 30mL/hr for the homogeneous and heterogeneous gels. The power for Δ^{α} in Eqn. 11 is $\alpha = 2$ for the heterogeneous gel and $\alpha = 1.86$ for the homogeneous gel, while $K_{\alpha} = \langle U^2 \rangle$.

The former causing an increasing dispersion coefficient with time while the latter causes a constant dispersion coefficient with time. This relationship accounts for the trending for the homogeneous data and to some extent explains the heterogeneous gel data, which after encountering the effects of an initial restriction, tends up due to the convective component. However at a long enough time ($\Delta > 200ms$) a second restriction affects the data, which corresponds to the effect seen for the propagators in figure 8.9 and was discussed above using the two population model. It is these restrictions on the time/length scale of solvent displacement which cause the non-trivial relationship between the dispersion and variance data.

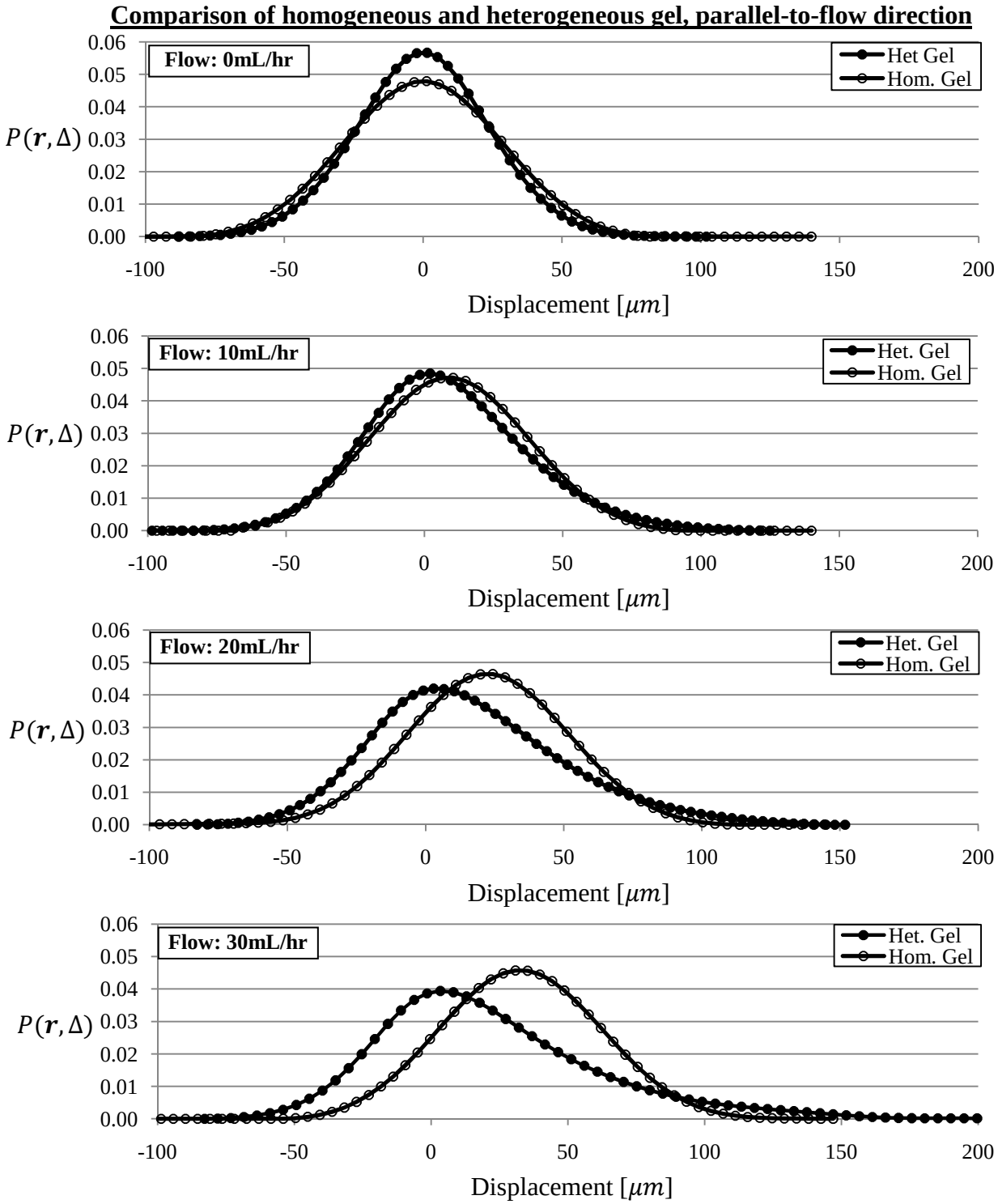

Figure 8.13 Shows propagators for heterogeneous and homogeneous gels at different flow rates 0, 10, 20 and 30mL/hr, for Δ = 200ms in the direction parallel (∥) to the flow direction.

To illustrate the difference between the homogeneous and heterogeneous gel further, the propagators for both gels are presented together at Δ = 200ms for increasing flowrate 0, 10, 20 and 30mL/hr, see figure 8.13. The stationary data shows that the solvent displacement in the heterogeneous gel is more restricted than in the homogeneous gel at Δ = 200ms. This difference increases with time for Δ < 200ms, and is approximately constant at longer times. This corresponds with the behavior for the dispersion coefficients seen in figure 8.11. As the flow rate increases the heterogeneous gel experiences a significant change in it probability distribution, with a tail forming at higher displacement, while at displacement less than the mean it still has a Gaussian-like shape. This explains much of the remaining difference between the two gels from the dispersion coefficients, with the restriction phenomena seen in figure 8.9 explaining the difference at long times ($\Delta > 200ms$) and high flow rates (20 and 30mL/hr).

Conclusions

This study of β-lactoglobulin gels has used Dynamic NMR experiments to probe the solvent dynamics through two different gel structures, heterogeneous (pH 5.2) and homogeneous (pH 7.0). These have shown the wealth of information that can be gleaned about the internal gel structure and solvent dynamics, but also demonstrate the difficulties in analyzing a non-rigid porous medium which for the homogeneous gel experiences significant deformation and at high enough hydrodynamic stresses. The solvent dynamics through the homogeneous gel showed a Gaussian-like probability distributions of displacement on the length and time scales investigated, while the heterogeneous gel

experienced significant back-bone flow and has at least two displacement/time dependent solvent-structure restrictions allowing measurement of important gel structure length scales.

IMAGING THE EFFECTS OF PEPTIDE SURFACTANT

Introduction

Controlling the properties of fluid-fluid interfaces is important in many fields including oil recovery, waste water treatment, food processing and pharmaceutical formulation. When a liquid droplet is suspended in an immiscible fluid and subsequently sheared, the droplet will deform. This deformation is dependent on the fluid-fluid interfacial properties which can be altered by the addition of surfactants [330]. A fascinating new group of peptide bio-surfactants have recently received attention because of their ability to tune such interfacial systems between a mobile 'detergent state' and a mechanically strong 'film state' via various external stimuli [331-333]. The peptide surfactants that are of interest in this study are AM1 (Ac-MKQLADS LHQLARQ VSRLEHA-$CONH_2$) and AFD4 (Ac-MKQLADS LHQLAHK VSHLEHA-$CONH_2$) which are based on the amphipathic peptide Lac21 [334]. These peptides have been shown to form a α-helical conformation at fluid-fluid interfaces [331] with metal-ion-binding histidine side chains resulting in the formation of an interfacial film. While AM1 permits intermolecular bridging by metal cations, AFD4 additionally allows for intramolecular bridging. It has been observed that AFD4-Zn(II) films formed at an air-water interface have much greater mechanical strength than equivalent films formed with AM1 [332], consistent with the doubled metal-ion bridging capacity. Reversible switching between this mechanically strong 'film state' and a mobile 'detergent state' can be induced *in situ* by the addition of a chelating agent or changing the pH of the bulk

solution, in both cases altering the binding potential between the histidine imidazole group and the metal cation. This controlled switching between states has been demonstrated for peptide surfactants and can be used to selectively stabilize and destabilize foams and emulsions [331-333, 335-337].

In this study a rapid Nuclear Magnetic Resonance (NMR) imaging technique based on the RARE [338] rapid imaging pulse sequence is used to investigate the deformation of droplets sheared in a Taylor-Couette device. The systems investigated are neutrally buoyant droplets (36 wt% Toluene/ 64 wt% Chloroform) suspended in Glycerol and stabilised by various surfactants. The NMR imaging technique used is a modified RARE sequence (ROTACOR [339]) which compensates for the rotation of the sample during the image acquisition time, this allows for the minimization of blurring due to droplet motion compared with a standard RARE sequence. ROTACOR has previously been demonstrated to accurately determine the deformation of a water droplet in viscous silicone oil in a Taylor-Couette system [339]. Here we use it to explore the effect of the bio-surfactants on droplet deformation.

Taylor-Couette System

The droplet deformation of a Newtonian droplet in a Newtonian suspending fluid has been extensively studied starting with the work of G.I. Taylor [340, 341] with many comprehensive reviews available [330, 342]. Useful experimental comparisons for the Taylor-Couette system used in this study are those of H.P. Grace [343] which showed a single droplet being deformed over a wide range of shear rate (from a spherical droplet to

burst of the droplet). Droplet deformation in the unbounded case is characterized by the flow type (*i.e.* vorticity), the capillary number (*Ca*) and the viscosity ratio (λ) which is the ratio of the discrete phase viscosity (η_d) and the continuous phase viscosity (η_c). The capillary number (*Ca*) = $(\eta_c \dot{\gamma} a)/\sigma$ measures the ratio of viscous forces versus surface tension, where η_c is the continuous phase viscosity, $\dot{\gamma}$ is the shear rate, a is the un-deformed droplet radius and σ is the interfacial tension. Droplet deformation is generally treated analytically by small deformation models [340, 341, 344, 345], ellipsoidal shape models [346-348] and slender body models [349, 350], depending on the relative shape and deformation of the droplets. Additionally, models to account for the effects of droplet confinement have recently been reviewed [351].

For the current study the droplet deformation *D* is defined as [341]

$$D = \frac{L-B}{L+B} \qquad (9.1)$$

where *L* and *B* are respectively the length and breadth of the droplet. Since the ratio of the un-deformed droplet radius (a) to gap width (H) for the system being studied is $\left(\frac{a}{H}\right)$ = 0.38 deviations from the unbounded flow models are expected [351]. Shapira and Haber [352] studying the effects of confinement derived an analytical expression for the droplet deformation based on Lorentz's reflection methods for the small to moderate deformation regime and found that although the drop shape calculated by Taylor [340, 341] is not altered the magnitude of deformation increases

$$D_{SH} = D_{Taylor}\left[1 + C_s \frac{1+2.5\lambda}{1+\lambda}\left(\frac{a}{H}\right)^3\right] \qquad (9.2)$$

where

$$D_{Taylor} = Ca\frac{16+19\lambda}{8(1+\lambda)}sin\theta cos\theta \qquad (9.3)$$

C_s is the shape factor [352] which is a function of the droplet to gap ratio $\left(\frac{a}{H}\right)$ where $C_s = 5.699$ for $\left(\frac{a}{H}\right)$ = 0.5. θ is the droplet orientation angle, which is $\theta = {}^{\pi}/_{4}$ for Taylor's small deformation theory [341]. Taylor's predictions for D are in good agreement with experimental data up to drop deformations well beyond the range of validity of the small deformation theory, even through the observed drop shape is quite different from the predicted one [353, 354]. Further extension to large droplet deformation requires numerical simulations [351]. Janssen and Anderson have used Boundary-Integral-Method (BIM) to simulate the 3D droplet deformation and breakup of Newtonian fluids in a Newtonian matrix for λ = 1 [355] with recent extension to non-unit λ case [356].

Additional complexity emerges when surfactants are added to the droplet system. Surfactants cause the deformation to depend on the evolving distance of surfactant on the interface, producing temporal and spatial gradients in the interfacial tension. Surfactant dilution and surfactant convection compete and dominate depending on the magnitude of Marangoni stresses, surface saturation and interactions, capillary number, viscosity ratio and initial interfacial tension (σ_0) [357]. Surfactant dilution tends to increase interfacial tension while surfactant convection decreases the interfacial tension [330]. If the surfactant is soluble in the continuous phase the effects of surfactant dilution and convection are both reduced [357].

Imaging Pulse Sequence

When a normal RARE NMR imaging pulse sequence is used on a rotating system significant distortion in the image will occur at high-rotational rates due to motion during the acquisition time of the image (typically 384 ms for a 128 x 128 images). ROTACOR works by re-orientating the direction of the imaging gradients between each echo acquisition, as shown in figure 9.1. This means that the directions of the perpendicular read and phase gradients, defining the image orientation, rotate after each echo acquisition at the frequency of the object of interest, ω. For higher rotational rates, (ω > 2rev/s), motional blurring due to rotation between echoes occurs, this can be partially alleviated by appropriately adjusting gradient directions for each individual gradient application in figure 9.1.

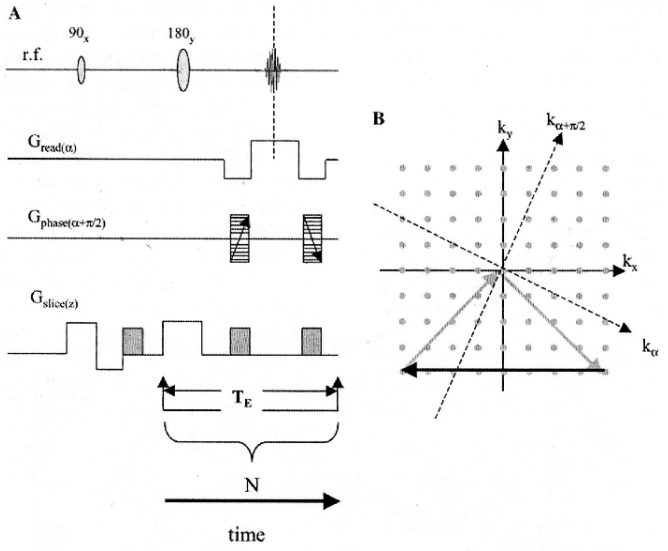

Figure 9.1 The ROTACOR pulse sequence (A) and the associated k-space raster (B). The read and phase directions are rotated with respect to the laboratory-frame after each echo acquisition such that the orientation of k-space is constant relative to the rotating object. After each echo acquisition the system is returned to the center of k-space. Homospoil gradients are applied in the slice direction on either side of the refocusing 180° pulse. The direction of the read and phase gradients (α, $\alpha+\pi/2$) are rotated by ω (the rotation frequency).

For the successful implementation of ROTACOR, the following conditions must be met [339]

(i) The centre of rotation of the object being imaged and the effective centre of the imaging gradients must coincide.

(ii) The angular velocity (ω) of the object to be imaged and of the ***k***-space raster (acquired NMR data) must be matched.

Condition (i) requires careful placement of the sample inside the magnet, the two cylinders of the Taylor-Couette cell also need to be accurately axially aligned. Condition (ii) can be met by tuning ω as applied to the imposed gradients and hence eliminating image blurring. This is possible as the sheared droplet in the Taylor-Couette cell migrates to an equilibrium radial position [346]. This equilibrium radial position also allows calculation of the velocity (v_ϕ) and the shear rate ($\dot{\gamma}$) at this equilibrium position [340]

$$v_\phi = \Omega r_i \frac{R\left(1-R^{-2}\right)}{K\left(1-K^{-2}\right)} \qquad (9.4)$$

and

$$\dot{\gamma} = \frac{2\Omega R^{-2}}{1-K^{-2}} \qquad (9.5)$$

where $R = {r_{eq}}/{r_o}$, $K = {r_i}/{r_o}$, r_i is the outer radius of the inner tube and r_o is the inner radius of the outer tube, r_{eq} is the equilibrium position of the droplet, and Ω is the angular velocity of the inner cylinder. Therefore the angular velocity of the deformed droplet can be calculated,

$$\omega = \frac{v_\phi}{r_{eq}} \qquad (9.6).$$

Materials and Methodology

For the droplet system in this study the continuous phase consists of glycerol (Fischer Scientific) while the disperse phase is a mixture of 36 wt% toluene (Sigma Aldrich) and 64 wt% chloroform (Sigma Aldrich). The choice of the chemical system is directed by the compatibility of glycerol and toluene with the peptide bio-surfactants and the desirability, in terms of the NMR acquisition time window, of density matching the discrete and continuous phases by adding chloroform to the discrete phase. The surfactants used in this study are non-ionic Tween 60 (Sigma Life Science) and the peptide bio-surfactants AM1 and AFD4.

The NMR images are obtained using a Bruker DMX 300 spectrometer with a magnetic field strength of 7.07 Tesla using a 25mm inner-diameter rf coil, the field of view (FOV) is 20mm by 20mm, with 128 x 128 image pixels and a slice thickness of 5mm giving a voxel resolution of 156x156x5000 μm^3. The rotating gradient wave forms needed for the rotational compensation used in ROTACOR are generated with in-house software (IDA) using a sine/cosine modulation in the x and y gradient directions for both the read and phase gradients. The wide-gap Taylor-Couette system used in this study consists of an 18mm I.D. thick walled glass cylinder and a 10mm O.D. hollow inner cylinder filled with a 90% wt glycerol solution. The device is sealed at the top and bottom and the inner cylinder is rotated by a motor at the top of the magnet using a rheoNMR setup [358]. 10mL of Glycerol were placed in the space between the inner and outer cylinders and the discrete droplet to be imaged is added to this continuous phase using an Eppendrof Multipipette Plus to produce a 15 µL droplet at an appropriate height

for imaging. The Taylor-Couette system is then placed inside the Bruker DMX 300 spectrometer. The inner cylinder of the Taylor-Couette system is rotated at 0.0, 0.2, 0.4, 0.6, 0.8, 1.0, 1.5 and 2.0 revolutions per second (rev/s) giving eight different data acquisitions for each fluid setup. 16 images are obtained running ROTACOR at each of the rotation rates for reproducibility, with a 10 second interval between each image to allow for spin lattice (T_1) relaxation of the sample. Contrast between the continuous phase (Glycerol) and the discrete phase (Chloroform/Toluene) is achieved by inversion recovery [1]. Inversion recovery is the use of an 180^o rf pulse prior to the ROTACOR pulse sequence. If the time period between the 180^o rf pulse and the first 90^o rf pulse of the ROTATCOR sequence is $0.6931 \times T_{1,Glycerol}$ the signal from the glycerol is nulled while the discrete phase will retain signal due to having a different T_1. For this study the fluid inside the Taylor-Couette system is replaced when each new droplet is added to eliminate any dilution or contamination of the continuous phase.

The nonionic surfactant (2 wt% Tween 60) is added to the discrete phase before the discrete phase is added to the continuous phase, while 4 µL of peptide bio-surfactants (2µL of 17.7µM surfactant (AM1 and AFD4) in HEPES buffer and 2µL of 10mM $ZnSO_4$) are added to the continuous phase close to the droplet and allowed to migrate to the fluid-fluid interface. An example of images obtained in this study are presented in figure 9.2a, which shows three images of a stationary and rotating (0.2rev/s and 1.0rev/s) 15 µL droplet with 2 wt% Tween 60. Faint signal is seen from the 90 wt % glycerol solution in the centre of the cell. Elongation of the droplet with increasing shear rate is obvious. To allow for an easier comparison of this elongation over the full range of

rotational rates considered (0.0 – 2.0 rev/s), the images are rotated such that they are in phase, and the vicinity of the droplet is then selected. Such a series of images over the full shear range is shown in figure 9.2b. It is evident from figure 9.2b that as the droplet is elongated, it aligns with the curvature of the streamlines in the Taylor-Couette system. To allow for the most concise presentation of the data, the deformation of each droplet is made quantitative by calculating the deformation $D = \left(\frac{L-B}{L+B}\right)$. Multiple repeats enabled the calculation of standard deviations.

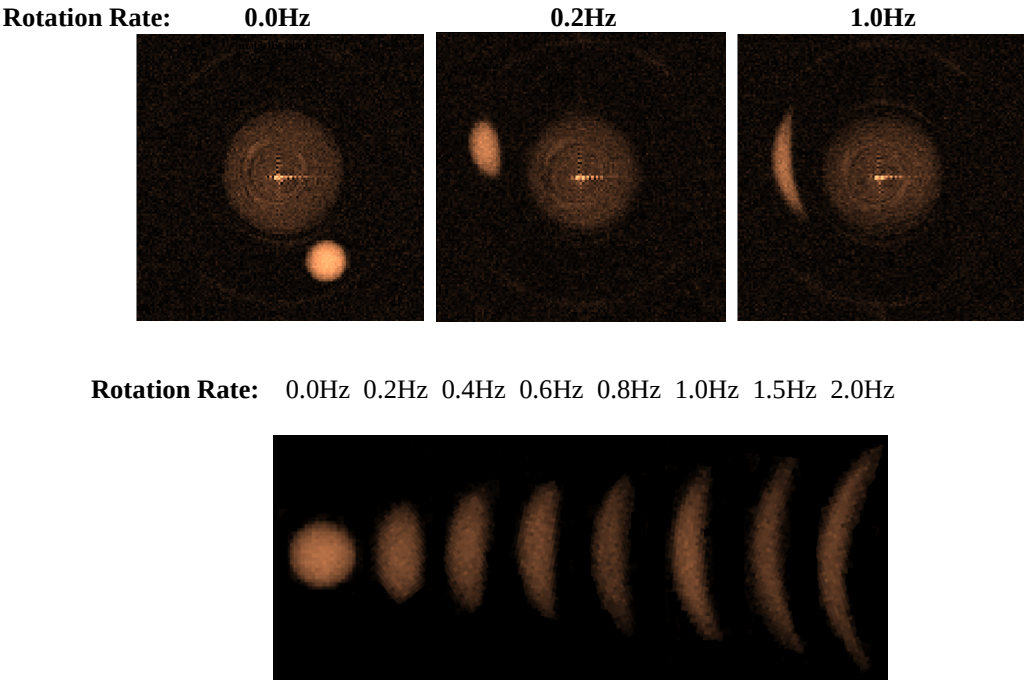

Figure 9.2 (A) Shows NMR images of a stationary droplet (0 rps) and a rotating droplet (0.2 rps and 1.0rps). (B) Shows the progression of droplet deformation at increasing rotational rates (0 – 2.0 rps), for this image the noise has been gated out and the drops have been cropped out of a larger image and rotated so as to allow for the easiest comparison. The droplet used in these images is 15μL (34%wt toluene/66%wt chloroform) with 2%wt Tween60 in glycerol. The inner cylinder is filled with a 90% Glycerol solution.

Interfacial Tension Measurements

Static Interfacial Tension (IT) measurements were conducted using drop shape analysis. A square vile was filled with the continuous phase and 150 μl droplets added with a pipette, these then resided on a glass cover slip. The apparatus was inverted depending on the relative densities of the droplet and continuous phases. A Canon EOS 20D digital camera with a Canon EF-S 17–85mm *f*/4-5.6 IS USM lense was used to obtain all side view images of the droplets. When acquiring each picture the camera is mounted in such a way that it always focuses on the interface between the droplet and solid surface. For the droplets with 2%wt Tween60, the Tween60 is added to the discrete phase, while for the peptide surfactants 4μL droplets are added of each solution to the continuous phase (glycerol) by adding them close to the base of the droplet and then mixing the glycerol around the droplet. This procedure and concentrations were identical to those used in the Taylor-Couette system.

The acquired images were analysed using the Axisymmetric Drop Shape Analysis-Profile (ADSA-P) method [359, 360] enabling extraction of the interfacial tension. This drop shape analysis method however requires density differences between the droplet and the continuous phases. This of course was not the case for the neutrally buoyant systems (64/36 wt% chloroform/toluene in glycerol) considered in this work. Hence the chloroform/toluene concentration was varied and the relationship between interfacial tension and concentration determined; hence the required interfacial tension could be determined by interpolation. Sample images are shown for this concentration

range with water as the continuous phase in figure 9.3a. The resultant variation of interfacial tension with droplet concentration is plotted in figure 9.3b.

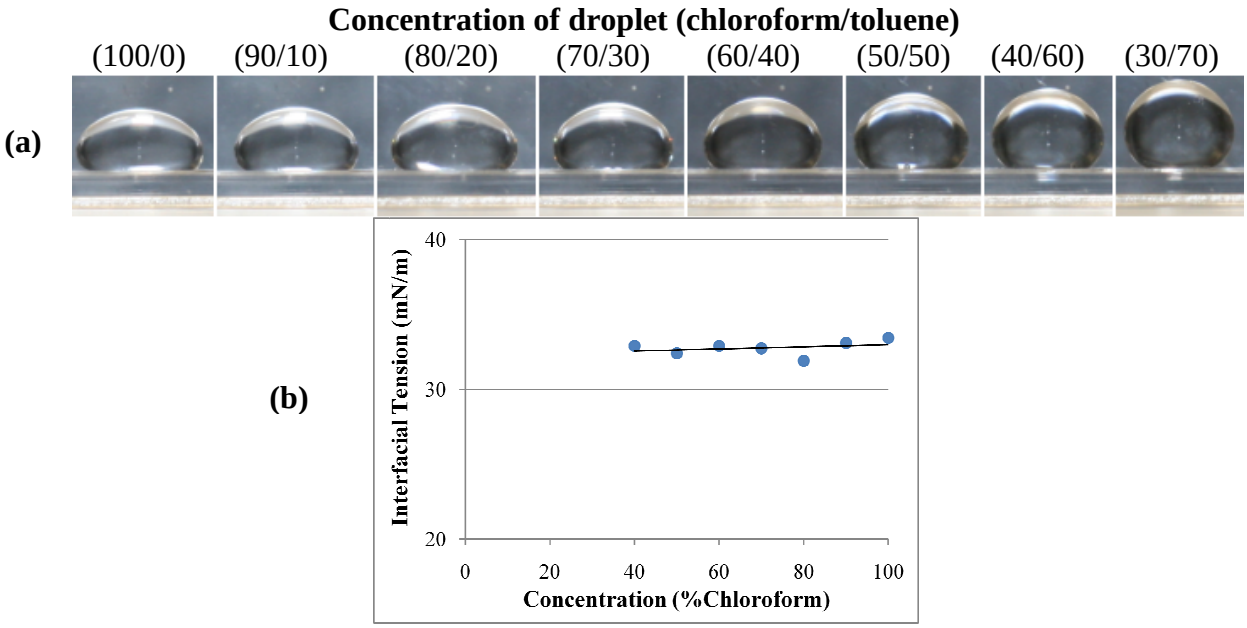

Figure 9.3 (a) images of droplet as concentration increases and (b) a plot of resulting interfacial tension measurement as a function of concentration with a linear fit used to estimate the value at 64% chloroform.

Table 9.1

Continuous Phase	**Interfacial Tension (mN/m)**	**Literature & Estimate Values 100% Chloroform/100% Toluene**
Water	32.6 ± 2.0*	(32.8,31.6)/(36.1, 32.7) [361] 33.0/32.6 (Estimates)
Water + 2 wt% Tween 60	6.2 ± 0.6*	(4.1 to 2.8)/(7.0 to 2.4)*** 5.1 ± 2.0 (Estimate)
Glycerol	19.4 ± 1.2*	18.91** [362]
Glycerol + 2 wt% Tween60	7.5 ± 0.7*	Not Available
Glycerol + AM1	11.9 ± 1.7*	Not Available
Glycerol + AFD4	12.4 ± 3.1*	Not Available
Glycerol + AM1 + EDTA	11.9 ± 1.7*	Not Available

Estimates are determined using Eqn. 9.7.

*± 3 Standard Deviations (99% Confidence Interval) obtained from 3 replicated experimental runs for each continuous phase investigated.

** Benzene as discrete phase.

*** Measured start and end interfacial tensions using NP-OE_{20} surfactant with toluene-in-water and carbon tetrachloride-in-water systems [363].

Validation of this methodology was conducted using both literature values where available or using the following semi-empirical expression [17]

$$\sigma_{ij} = \frac{\sigma_i + \sigma_j - 2\beta(\sigma_i\sigma_j)^{\frac{1}{2}}}{1 - 2\alpha(\sigma_i\sigma_j)^{\frac{1}{2}}} \quad (9.7)$$

with α = 0.075, β = 1, where $\sigma_i$and σ_j are the surface tension of species i and j and σ_{ij} is the interfacial tension. The required surface tension values are obtained from the literature [361].

Results and Discussion

The focus of this study is to investigate the effect peptide surfactants have on the deformation (D), as defined in Eqn. 9.1, of a droplet being sheared in a Taylor-Couette system. To this end 15 µL droplets are sheared at a series of rotation rates and the average deformation of each droplet is calculated. Figure 9.4a shows the deformation at different rotational rates for four systems: (i) no surfactant, (ii) 2 wt% Tween 60, (iii) 4 µL bio-surfactant AM1 and (iv) 4 µL AFD4. Figure 9.4b shows the effects of confinement on the droplet deformation (D) where the Shapira and Haber (D_{SH}) model accounts for the deformation at low shear rates better than the Taylor (D_{Taylor}) model. Table 9.1 presents a summary of the values of interfacial tension measured for the various systems considered. Note the good agreement with literature and estimated values.

Figure 9.4a shows that the deformation (D) is greatest for the 2 wt% Tween60 surfactant system, showing an increase in the deformation of the droplet relative to a

droplet with no surfactant, this is an expected result [364] and corresponds favorably with the interfacial tension results, see Table 9.1.

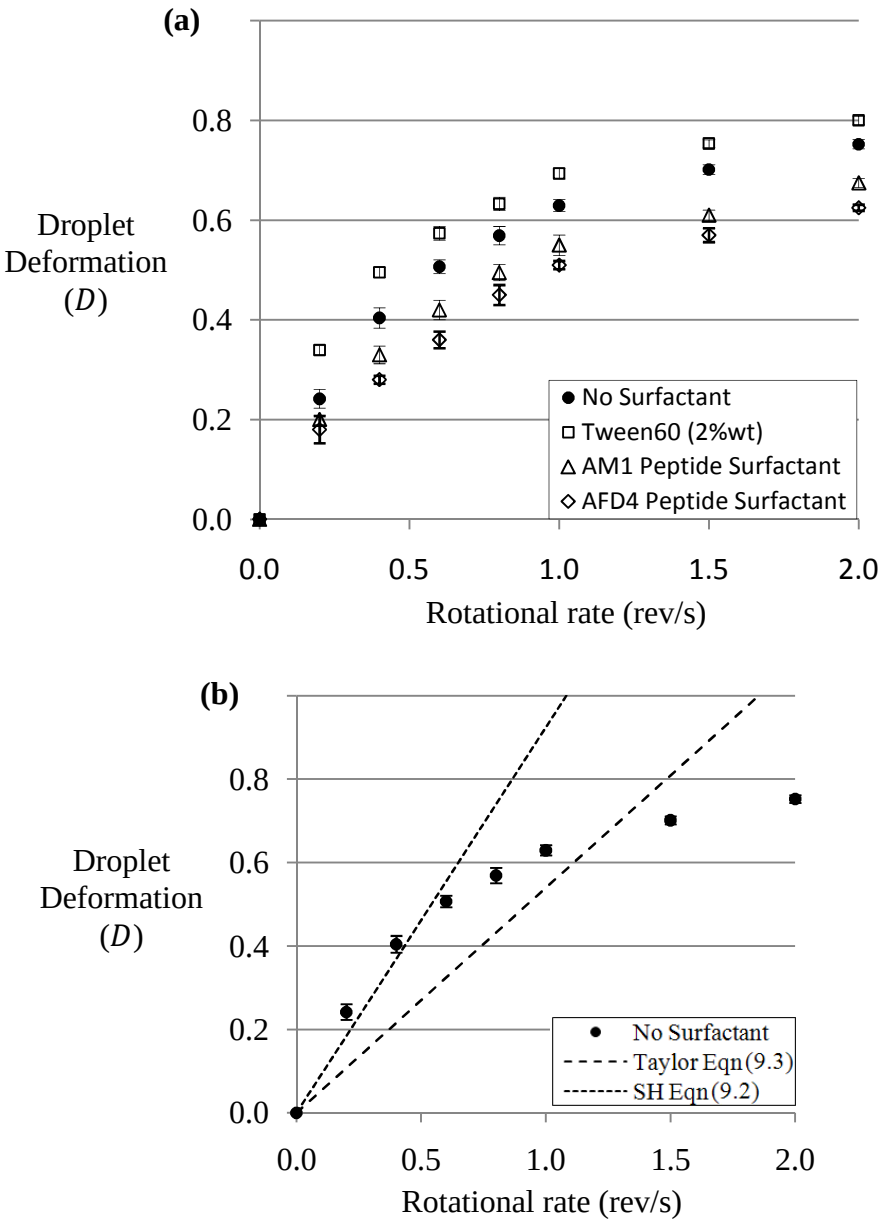

Figure 9.4 (a) Shows the droplet deformation (D) for the different droplet systems investigated as a function of the rotational rate. (b) shows the droplet deformation (D) of the droplet without surfactant fit with the Shapira and Haber (D_{SH}) model and the Taylor (D_{Taylor}) model.

These results were reproducible when employing 2 wt % Triton X-100 instead of 2 wt % Tween 60 as the surfactant. For both the bio-surfactants systems, the droplet deformation is however decreased relative to the system containing no surfactant. Note that the error bars result from multiple repetition of each measurement. This decrease in deformation for the bio-surfactant systems is contrary to the measured reduction in static interfacial tension (as presented in Table 9.1), we attribute this to the increase in mechanical strength of the interface due to Zn/bio- surfactant film formation. It is interesting that the effect of this mechanically strong layer is evident in the sheared droplet system but not in the static system as used for IT measurement.

To investigate this further, a pair of experiments were performed where initially the peptide bio-surfactant was added to the droplet system with Zn(II) present in solution allowing the formation of the 'film state' at the fluid-fluid interface, the deformation of the droplet is measured over a range of rotation rates which show results consistent to those presented in figure 9.5 for the AM1 peptide surfactant. Then EDTA is added (10µL of 100mM) in excess to the continuous phase close to the droplet and allowed to mix with the continuous phase by gentle stirring. Given time to mix with the continuous phase and to allow for any removal of Zn(II) from the peptide surfactant structure the deformation of the droplet is then re-measured over a range of rotation rates. The results of these experiments are presented in figure 9.5. These show that the deformation of the droplet is increased due to the removal of Zn(II) by EDTA; the resultant extent of deformation is similar to that for the system without any surfactant added (as presented in figure 9.4a,b).

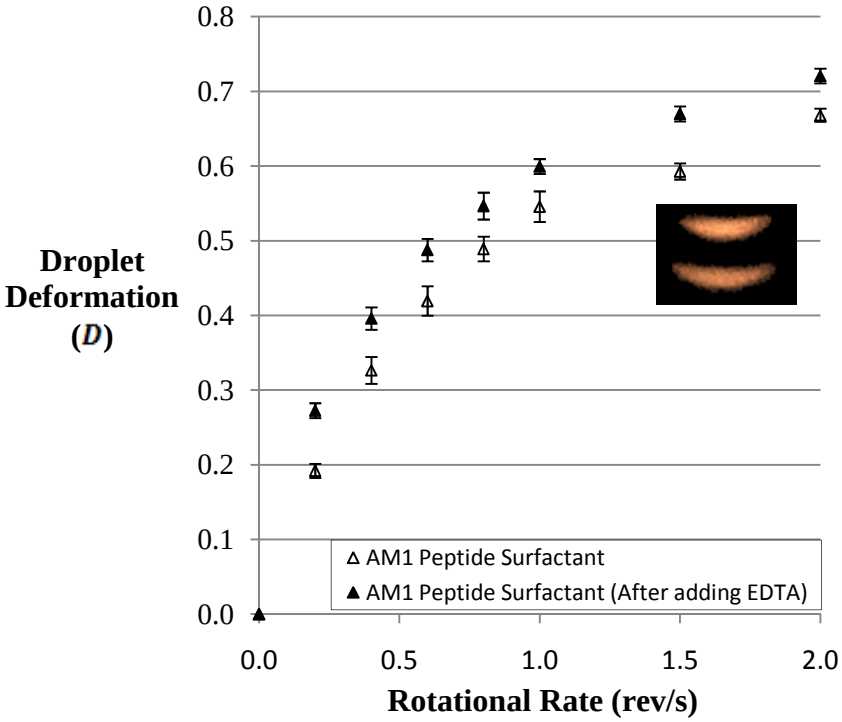

Figure 9.5 Shows how the deformation of the AM1 peptide surfactant system increases after the addition of an excess amount of EDTA to the system. The insert picture shows a droplet with AM1 surfactant that is being deformed at a rotational rate of 1.5rps, the upper image is for a AM1/$ZnSO_4$ system and the lower image is after the addition of an excess of EDTA.

Conclusions

In this study ROTACOR was used to image the deformation of a (toluene/chloroform) droplet in glycerol at different rotational rates adding both nonionic surfactant (Tween 60) and peptide bio-surfactants (AM1 and AFD4) to the system to see how that would change the deformation. The droplet at any rotational rate was deformed more by the addition of the nonionic surfactant (2 wt% Tween60) than with no surfactant present, while the addition of the peptide bio-surfactant caused less deformation of the droplet. Given previous results for the peptide surfactants [331-333], it is evident that the mechanically strong interfacial film formed by the peptide surfactants and Zn results in a

decrease in droplet deformation at a particular shear rate, despite reducing the interfacial tension as measured using droplet shape analysis.

Future work will focus on relaxing the requirement for neutrally buoyant droplets by tracking their movement vertically through the NMR rf coil and modifying the acquisition sequence appropriately. Lower continuous phase or higher droplet phase viscosities require higher rotational velocities in order to effect significant droplet deformation. ROTACOR will be adjusted such that gradient direction is effectively continuously updated during application, thus allowing higher rotational velocities to be used.

Acknowledgements

The work presented in this chapter was conducted during a five month NSF funded visit to the Magnetic Resonance Research Centre (MRRC) at the University of Cambridge, UK. It was conducted under the supervision of Prof. Michael L. Johns from the Department of Chemical Engineering and in collaboration with Prof. Anton P.J. Middelberg from the Department of Chemical and Bimolecular Engineering at the University of Queensland, Australia.

FUTURE DIRECTIONS OF STUDY

Given the scope of the research presented in this dissertation only a limited number of suggestions for future work will be presented here.

For the microcapillary work (chapter 4) some obvious extensions of the research presented would be examining different concentrations of colloidal suspensions as well as colloidal suspensions of different sizes. This would greatly extend the applicability of the research. Additionally work on examining the effect of entrance lengths would receive considerable attention. Finally similar examinations of non-spherical, non-hard sphere systems or biological systems would be of interest.

For the bifurcation work (chapter 5) an extension towards examining different concentrations, flow rates and even different rheological systems would be useful. Further examination of the separation phenomena seen is also warranted in collaboration with more sophisticated CFD simulations, for example examining Stokesian dynamics simulations at a contracting bifurcation would potentially corroborate the jamming effects seen in the bifurcation system as well as the separation effects.

For the colloidal suspension flow through a porous medium (chapter 6), future research could use fluorinate oil-core particles to clearly differentiate the colloid signal from the suspending fluid and observe the colloids as they are deposited. Another direction would be to examine systems with a lower rate of deposition or even systems where no deposition is expected to occur, for example porous media with larger pore sizes, less dead end pores or repulsive surfaces.

For the reactive transport through porous media (chapter 7) future work could focus on monitoring the replicability of inoculation protocols, to study for example the effect of initial conditions (*i.e.* high or low shear for short or long times) on initial bacterial placement and in return how this affects the transport dynamics. An important experiment for the current system is to create a bead pack where the highest shear region is in the middle of the rf coil allowing for a direct observation of the fluid dynamics at the region of highest calcium carbonate deposition.

For the fluid transport through Beta-lactoblobulin gels (chapter 8) it would be interesting to examine a gel at low pH (*i.e.* pH < 4.0) and see if those gels have the same transport dynamics as the homogeneous gel at pH 7.0 as these are expected to be morphologically similar on the macroscopic scale but have a different microscopic morphology. The examination of different gels with the same experimental procedures is also of interest to see which groups of gels show similar flow dynamics. Direct testing of gels as fluid gates might also be interesting. Further examination of the effect of NaCl on the different compression effects in Beta-lactoglobulin gels is also warranted.

For the investigation of peptide surfactants (chapter 9) it would be interesting to apply other rheological geometries (cone-and-plate, parallel-plate) inside the NMR and observe the rheological properties of these surfactants in detail. Additionally, investigating systems which do not require a small viscosity ratio (λ) would be of interest for better comparison with literature, since there is a large quantity of theoretical and experimental results for viscosity ratios closer to unity. Extending the available

rotational rates by improving the ROTACOR pulse sequence would be important for its future applicability.

REFERENCES CITED

[1] P. T. Callaghan, *Principles of Nuclear Magnetic Resonance Microscopy* (Clarendon, Oxford, 1991).

[2] A. Abragam, *Principles of Nuclear Magnetism* (Clarendon Press, Oxford, 1961).

[3] T. C. Farrar, *Introduction to pulse NMR spectroscopy* (The Farragut Press, Madison, 1997).

[4] E. Fukushima, and S. B. W. Roeder, *Experimental Pulse NMR: A nuts and bolts approach* (Addison-Wesley, Reading, MA, 1981).

[5] M. H. Levitt, *Spin Dynamics: Basics of Nuclear Magnetic Resonance* (Wiley & Sons, Chichester, 2008).

[6] C. P. Slicher, *Principles of Magnetic Resonance* (Harper and Row, New York, 1963).

[7] R. Feynman, R. Leighton, and M. Sands, *The Feynman Lectures on Physics* (Addison-Wesley, New York, 1966), Vol. 2.

[8] F. Bloch, W. W. Hansen, and M. Packard, Physical Review **70**, 474 (1946).

[9] E. M. Purcell, H. C. Torrey, and R. V. Pound, Physical Review **69**, 37 (1946).

[10] M. Castillo, L. Kwock, and S. K. Mukherji, American Journal of Neuroradiology **17**, 1 (1996).

[11] A. Mittermaier, and L. E. Kay, Science **312**, 224 (2006).

[12] L. F. Gladden, Chemical Engineering Science **49**, 3339 (1994).

[13] L. F. Gladden, Chemical Engineering Journal and the Biochemical Engineering Journal **56**, 149 (1995).

[14] D. A. McQuarrie, *Quantum Chemistry* (University Science Book, Sausalito, CA, 1983).

[15] J. Gribbin, *In Search of Schrodinger's Cat* (Bantam Books, New York, 1984).

[16] J. D. Jackson, *Classical Electrodynamics* (Wiley, New York, 1999), p. 808.

[17] C. J. Terblanche, E. C. Reynhardt, and J. A. v. Wyk, Solid State Nuclear Magnetic Resonance **20**, 1 (2001).

[18] H. Y. Carr, and E. M. Purcell, Physical Review **94**, 630 (1954).

[19] S. Meiboom, and D. Gill, Review of Scientific Instruments **29**, 688 (1958).

[20] E. L. Hahn, Physical Review **80**, 580 (1950).

[21] H. C. Torrey, Physical Review **104**, 563 (1956).

[22] J. W. Cooley, and J. W. Tukey, Mathematics of Computation **19**, 297 (1965).

[23] H. Nyquist, Trans. AIEE **47**, 617 (1928).

[24] A. D. Bain, Journal of Magnetic Resonance **56**, 418 (1984).

[25] W. A. Edelstein *et al.*, Physics in Medicine and Biology **25**, 751 (1980).

[26] J. Frahm, W. Hanicke, and K. D. Merboldt, J. Magn. Reson. **72** (1987).

[27] M. Doyle *et al.*, Lancet **2** (1986).

[28] A. M. Houseman *et al.*, Br. J. Radiol. **61** (1988).

[29] J. Henning, A. Nauerth, and H. Frieburg, Magn. Reson. Med. **3** (1986).

[30] E. O. Stejskal, and J. E. Tanner, Journal of Chemical Physics **42**, 288 (1965).

[31] J. Bear, *Dynamics of Fluids in Porous Media* (Dover, New York, 1972), p. 764.

[32] P. T. Callaghan, S. L. Codd, and J. D. Seymour, Concepts in Magnetic Resonance **11**, 181 (1999).

[33] P. T. Callaghan *et al.*, Nature **351**, 467 (1991).

[34] L. L. Latour *et al.*, Journal of Magnetic Resonance Series A **101**, 342 (1993).

[35] P. N. Sen, L. M. Schwartz, and P. P. Mitra, Magnetic Resonance Imaging **12**, 227 (1994).

[36] D. S. Grebenkov, Rev Mod Phys **79** (2007).

[37] J. S. Murday, and J. M. Cotts, J. Chem. Phys. **48** (1968).

[38] M. L. Johns, Curr. Opin. Colloid Interface Sci. **14** (2009).

[39] K. R. Brownstein, and C. E. Tarr, Phys Rev A **19** (1979).

[40] R. Brown, Phil Mag **4**, 161 (1828).

[41] A. Einstein, Annalen Der Physik **19**, 371 (1906).

[42] M. Smoluchowski, Annalen Der Physik **21**, 765 (1906).

[43] J. F. Brady, Journal of Chemical Physics **99**, 567 (1993).

[44] W. B. Russel, D. A. Saville, and W. R. Schowalter, *Colloidal Dispersions* (Cambridge University Press, Cambridge, UK, 1989).

[45] J. F. Brady, Current Opinion in Colloid & Interface Science **1**, 472 (1996).

[46] Y. Yurkovetsky, and J. F. Morris, Journal of Rheology **52**, 141 (2008).

[47] L. Antl *et al.*, Colloids and Surfaces **17**, 67 (1986).

[48] H. Wassenius, M. Nyden, and B. Vincent, Journal of Colloid and Interface Science **264**, 538 (2003).

[49] J. J. Stickel, and R. L. Powell, Annual Review of Fluid Mechanics **37**, 129 (2005).

[50] J. Vermant, and M. J. Solomon, Journal of Physics-Condensed Matter **17**, R187 (2005).

[51] N. H. March, and M. P. Tosi, *Atomic Dynamics in Liquids* (Dover, New York, 1976).

[52] J. F. Brady, and G. Bossis, Annual Review of Fluid Mechanics **20**, 111 (1988).

[53] E. Alos, O. Mazet, and D. Nualart, Annals of Probability **29**, 766 (2001).

[54] J. P. Boon, and S. Yip, *Molecular Hydrodynamics* (Dover, New York, 1980).

[55] S. Abe, and A. K. Rajagopal, Journal of Physics a-Mathematical and General **34**, 8727 (2001).

[56] R. Metzler, and J. Klafter, Physics Reports-Review Section of Physics Letters **339**, 1 (2000).

[57] P. N. Pusey, Journal of Physics a-Mathematical and General **11**, 119 (1978).

[58] S. L. Codd *et al.*, Physical Review E **60**, R3491 (1999).

[59] G. Taylor, Proceedings of the Royal Society of London Series a-Mathematical and Physical Sciences **219**, 186 (1953).

[60] C. Vandenbroeck, Physica A **168**, 677 (1990).

[61] B. J. Berne, J. P. Boon, and S. A. Rice, Journal of Chemical Physics **45**, 1086 (1966).

[62] J. J. Stickel, R. J. Phillips, and R. L. Powell, Journal of Rheology **50**, 379 (2006).

[63] J. R. Dorfman, *An Introduction to Chaos in Nonequilibrium Statistical Mechanics* (Cambridge University Press, Cambridge, UK, 1999), p. 287.

[64] R. B. Bird, W. E. Stewart, and E. N. Lightfoot, *Transport Phenomena* (Wiley & Sons, New York, 2002), p. 905.

[65] D. A. Drew, Annual Review of Fluid Mechanics **15**, 261 (1983).

[66] R. W. Nash, R. Adhikari, and M. E. Cates, Physical Review E **77** (2008).

[67] P. G. Saffman, Studies in Applied Mathematics **52**, 115 (1973).

[68] I. M. Janosi *et al.*, Physical Review E **56**, 2858 (1997).

[69] P. Gaspard, and T. Gilbert, New J. Phys. **10**, 30 (2008).

[70] P. Gaspard, *Chaos, Scattering and Statistical Mechanics* (Cambridge University Press, Cambridge, 2005).

[71] A. J. Lichtenberg, and M. A. Lieberman, *Regular and Chaotic Dynamics* (Springer-Verlag, New York, 1992), Vol. 38, p. 692.

[72] D. J. Pine *et al.*, Nature **438**, 997 (2005).

[73] F. R. daCunha, and E. J. Hinch, Journal of Fluid Mechanics **309**, 211 (1996).

[74] I. Rampall, J. R. Smart, and D. T. Leighton, Journal of Fluid Mechanics **339**, 1 (1997).

[75] D. R. Foss, and J. F. Brady, Journal of Fluid Mechanics **407**, 167 (2000).

[76] G. Drazer *et al.*, Journal of Fluid Mechanics **460**, 307 (2002).

[77] G. Drazer *et al.*, Journal of Fluid Mechanics **511**, 237 (2004).

[78] Y. Wang, R. Mauri, and A. Acrivos, Journal of Fluid Mechanics **327**, 255 (1996).

[79] T. N. Phung, J. F. Brady, and G. Bossis, Journal of Fluid Mechanics **313**, 181 (1996).

[80] J. F. Brady, J. Chem Phys **98** (1993).

[81] D. L. Ermak, and J. A. McCammon, Journal of Chemical Physics **69**, 1352 (1978).

[82] S. R. Rastogi, N. J. Wagner, and S. R. Lustig, Journal of Chemical Physics **104**, 9234 (1996).

[83] R. C. Ball, and J. R. Melrose, Physica a-Statistical Mechanics and Its Applications **247**, 444 (1997).

[84] A. A. Catherall, J. R. Melrose, and R. C. Ball, Journal of Rheology **44**, 1 (2000).

[85] H. Binous, and R. J. Phillips, Journal of Non-Newtonian Fluid Mechanics **85**, 63 (1999).

[86] I. L. Claeys, and J. F. Brady, Journal of Fluid Mechanics **251**, 411 (1993).

[87] M. Loewenberg, and E. J. Hinch, Journal of Fluid Mechanics **321**, 395 (1996).

[88] G. P. Muldowney, and J. J. L. Higdon, Journal of Fluid Mechanics **298**, 167 (1995).

[89] C. Pozrikidis, Journal of Fluid Mechanics **246**, 301 (1993).

[90] A. Z. Zinchenko, and R. H. Davis, Journal of Computational Physics **157**, 539 (2000).

[91] S. Chen, and G. D. Doolen, Annual Review of Fluid Mechanics **30**, 329 (1998).

[92] A. J. C. Ladd, and R. Verberg, Journal of Statistical Physics **104**, 1191 (2001).

[93] G. R. McNamara, and G. Zanetti, Phys Rev Lett **61** (1998).

[94] D. A. Edwards *et al.*, Physics of Fluids a-Fluid Dynamics **2**, 45 (1990).

[95] J. Feng, H. H. Hu, and D. D. Joseph, Journal of Fluid Mechanics **277**, 271 (1994).

[96] J. Feng, H. H. Hu, and D. D. Joseph, Journal of Fluid Mechanics **261**, 95 (1994).

[97] B. Fornberg, Journal of Fluid Mechanics **225**, 655 (1991).

[98] C. K. Ghadder, Phys Fluids **7** (1995).

[99] P. J. Hoogerbrugge, and J. Koelman, Europhysics Letters **19**, 155 (1992).

[100] G. A. Bird, *Molecular Gas Dynamics* (University Press, London, 1976).

[101] W. G. Hoover *et al.*, Computers & Mathematics with Applications **28**, 155 (1994).

[102] J. J. Monaghan, Annual Review of Astronomy and Astrophysics **30**, 543 (1992).

[103] D. H. Rothman, Geophysics **53**, 509 (1988).

[104] A. J. C. Ladd, M. E. Colvin, and D. Frenkel, Physical Review Letters **60**, 975 (1988).

[105] M. Frank *et al.*, Journal of Fluid Mechanics **493**, 363 (2003).

[106] J. F. Morris, and J. F. Brady, International Journal of Multiphase Flow **24**, 105 (1998).

[107] P. Hebraud, and D. Lootens, Mod Phys Lett B **19**, 613 (2005).

[108] M. E. Cates *et al.*, Phys Rev Lett **81**, 1841 (1998).

[109] G. K. Batchelor, Journal of Fluid Mechanics **83**, 97 (1977).

[110] I. M. Krieger, and T. J. Dougherty, Transactions of the Society of Rheology **3**, 137 (1959).

[111] G. K. Batchelor, J. Fluid Mech **83** (1970).

[112] D. R. Foss, and J. F. Brady, Journal of Fluid Mechanics **401**, 243 (1999).

[113] L. V. Woodcock, Faraday Discuss. **106**, 325 (1997).

[114] P. N. Pusey, and W. Vanmegen, Nature **320**, 340 (1986).

[115] P. N. Pusey *et al.*, Physical Review Letters **63**, 2753 (1989).

[116] J. X. Zhu *et al.*, Nature **387**, 883 (1997).

[117] J. L. Harland, and W. vanMegen, Physical Review E **55**, 3054 (1997).

[118] U. Gasser *et al.*, Science **292**, 258 (2001).

[119] V. J. Anderson, and H. N. W. Lekkerkerker, Nature **416**, 811 (2002).

[120] S. Auer, and D. Frenkel, Physical Review Letters **91** (2003).

[121] P. N. Pusey *et al.*, Philosophical Transactions of the Royal Society a-Mathematical Physical and Engineering Sciences **367**, 4993 (2009).

[122] K. Kremer, M. O. Robbins, and G. S. Grest, Physical Review Letters **57**, 2694 (1986).

[123] E. B. Sirota *et al.*, Physical Review Letters **62**, 1524 (1989).

[124] A. K. Arora, and B. V. R. Tata, Advances in Colloid and Interface Science **78**, 49 (1998).

[125] S. Auer, and D. Frenkel, Nature **413**, 711 (2001).

[126] B. J. Ackerson, Journal of Rheology **34**, 553 (1990).

[127] S. D. Kulkarni, and J. F. Morris, Journal of Rheology **53**, 417 (2009).

[128] S. R. Rastogi, N. J. Wagner, and S. R. Lustig, Journal of Chemical Physics **104**, 9249 (1996).

[129] H. Wassenius, and P. T. Callaghan, European Physical Journal E **18**, 69 (2005).

[130] V. Viasnoff, and F. Lequeux, Phys Rev Lett **89**, 065701 (2002).

[131] P. Sollich, S. Fielding, and P. Mayer, Journal of Physics-Condensed Matter **14**, 1683 (2002).

[132] M. Cloitre, R. Borrega, and L. Leibler, Phys Rev Lett **85** (2000).

[133] J. P. Bouchaud, Journal De Physique I **2**, 1705 (1992).

[134] M. Fuchs, and M. E. Cates, Journal of Rheology **53**, 957 (2009).

[135] M. Kruger, and M. Fuchs, Physical Review E **81**.

[136] J. R. Brown *et al.*, Physics of Fluids **21** (2009).

[137] J. Bergenholtz, J. F. Brady, and M. Vicic, Journal of Fluid Mechanics **456**, 239 (2002).

[138] A. P. Gast, and W. B. Russel, Physics Today **51**, 24 (1998).

[139] H. Lowen, Journal of Physics-Condensed Matter **16**, V7 (2004).

[140] M. Carpineti, and M. Giglio, Physical Review Letters **68**, 3327 (1992).

[141] P. Varadan, and M. J. Solomon, Langmuir **19**, 509 (2003).

[142] P. Varadan, and M. J. Solomon, Journal of Rheology **47**, 943 (2003).

[143] K. A. Dawson, Current Opinion in Colloid & Interface Science **7**, 218 (2002).

[144] K. N. Pham *et al.*, Science **296**, 104 (2002).

[145] J. F. Morris, Rheologica Acta **48**, 909 (2009).

[146] P. Dhaene, J. Mewis, and G. G. Fuller, Journal of Colloid and Interface Science **156**, 350 (1993).

[147] J. Bender, and N. J. Wagner, Journal of Rheology **40**, 899 (1996).

[148] B. J. Maranzano, and N. J. Wagner, Journal of Chemical Physics **117**, 10291 (2002).

[149] J. F. Brady, Chemical Engineering Science **56**, 2921 (2001).

[150] H. J. Wilson, and R. H. Davis, Journal of Fluid Mechanics **421**, 339 (2000).

[151] J. Mewis, and G. Biebaut, Journal of Rheology **45**, 799 (2001).

[152] J. R. Melrose, and R. C. Ball, Journal of Rheology **48**, 937 (2004).

[153] G. Bossis, and J. F. Brady, Journal of Chemical Physics **80**, 5141 (1984).

[154] A. Singh, and P. R. Nott, Journal of Fluid Mechanics **412**, 279 (2000).

[155] A. Sierou, and J. F. Brady, Journal of Rheology **46**, 1031 (2002).

[156] F. Gadalamaria, and A. Acrivos, Journal of Rheology **24**, 799 (1980).

[157] N. J. Wagner, and W. B. Russel, Physics of Fluids a-Fluid Dynamics **2**, 491 (1990).

[158] R. C. Ball, and J. R. Melrose, Advances in Colloid and Interface Science **59**, 19 (1995).

[159] A. J. Banchio, and J. F. Brady, Journal of Chemical Physics **118**, 10323 (2003).

[160] J. Bergenholtz, J. F. Brady, and M. Vicic, J Fluid Mech **456**, 239 (2002).

[161] P. A. Arp, and S. G. Mason, Journal of Colloid and Interface Science **61**, 21 (1977).

[162] J. R. Smart, and D. T. Leighton, Physics of Fluids a-Fluid Dynamics **1**, 52 (1989).

[163] S. L. Zeng, E. T. Kerns, and R. H. Davis, Physics of Fluids **8**, 1389 (1996).

[164] Y. Zhao, and R. H. Davis, Journal of Fluid Mechanics **492**, 101 (2003).

[165] H. J. Wilson, and R. H. Davis, Journal of Fluid Mechanics **452**, 425 (2002).

[166] I. E. Zarraga, D. A. Hill, and D. T. Leighton, Journal of Rheology **44**, 185 (2000).

[167] V. G. Kolli, E. J. Pollauf, and F. Gadala-Maria, Journal of Rheology **46**, 321 (2002).

[168] A. Singh, and P. R. Nott, Journal of Fluid Mechanics **490**, 293 (2003).

[169] P. R. Nott, and J. F. Brady, Journal of Fluid Mechanics **275**, 157 (1994).

[170] R. A. Bagnold, Proceedings of the Royal Society of London Series a-Mathematical and Physical Sciences **225**, 49 (1954).

[171] J. F. Morris, and F. Boulay, Journal of Rheology **43**, 1213 (1999).

[172] I. Cohen, T. G. Mason, and D. A. Weitz, Physical Review Letters **93** (2004).

[173] D. Semwogerere, J. F. Morri, and E. R. Weeks, Journal of Fluid Mechanics **581**, 437 (2007).

[174] J. F. Brady, and J. F. Morris, Journal of Fluid Mechanics **348**, 103 (1997).

[175] J. M. Bricker, and J. E. Butler, Journal of Rheology **51**, 735 (2007).

[176] D. J. Jeffrey, J. F. Morris, and J. F. Brady, Physics of Fluids a-Fluid Dynamics **5**, 2317 (1993).

[177] D. Leighton, and A. Acrivos, Journal of Fluid Mechanics **181**, 415 (1987).

[178] R. M. Miller, and J. F. Morris, Journal of Non-Newtonian Fluid Mechanics **135**, 149 (2006).

[179] C. E. Pearson, *Numerical Methods in Engineering and Science* (Van Nostrand Reinhold, New York, 1986).

[180] A. Loxley, and B. Vincent, Journal of Colloid and Interface Science **208**, 49 (1998).

[181] C. W. Macosko, *Rheology Principles, Measurement and Applications* (Wiley-VCH, New York, 1994).

[182] R. B. Bird, R. C. Armstrong, and O. Hassager, *Dynamics of Polymeric Liquids, Volume 1 Fluid Dynamics* (Wiley Interscience, New York, 1987).

[183] V. N. Michailidou *et al.*, Physical Review Letters **102**, 4 (2009).

[184] J. F. Brady, and M. Vicic, Journal of Rheology **39**, 545 (1995).

[185] X. Z. Tang, and A. H. Boozer, Physica D **95**, 283 (1996).

[186] J. R. Dorfman, *An Introduction to Chaos in Nonequilibrium Statistical Mechanics* (Cambridge University Press, Cambridge, UK, 1999).

[187] G. I. Taylor, Proceedings of the London Mathematical Society **20**, 196 (1922).

[188] G. I. Taylor, Proceedings of the Royal Society of London Series a-Mathematical and Physical Sciences **151**, 0421 (1935).

[189] H. Tennekes, and J. L. Lumley, *A First Course in Turbulence* (MIT Press, Cambridge, Massachusetts, 1990), p. 300.

[190] S. Chien *et al.*, Am J Physiol **248**, H568 (1985).

[191] A. R. Pries *et al.*, Microvasc Res **38**, 81 (1989).

[192] B. W. Roberts, and W. L. Olbricht, AICHE J **52**, 199 (2006).

[193] R. D. Jaggi, R. Sandoz, and C. S. Effenhauser, Microfluid Nanofluid **3**, 47 (2007).

[194] S. Yang, A. Undar, and J. D. Zahn, Lab Chip **6**, 871 (2006).

[195] M. J. Fuerstman, P. Garstecki, and G. M. Whitesides, Science **315**, 828 (2007).

[196] M. Prakash, and N. Gershenfeld, Science **315**, 832 (2007).

[197] J. Vermant, and M. J. Solomon, J Phys-Cond Mat **17**, R187 (2005).

[198] A. Loxley, and B. Vincent, J Colloid Interf Sci **208**, 49 (1998).

[199] H. Wassenius, M. Nyden, and B. Vincent, J Colloid Interf Sci **264**, 538 (2003).

[200] H. Wassenius, and P. T. Callaghan, J Magn Reson **169**, 250 (2004).

[201] H. Wassenius, and P. T. Callaghan, Euro Phys J E **18**, 69 (2005).

[202] J. R. Brown *et al.*, Phys Rev Lett **99**, 240602 (2007).

[203] R. Kubo, M. Toda, and N. Hashitsume, *Statistical Physics II: Nonequilibrium Statistical Mechanics* (Springer-Verlag, Berlin, 1991).

[204] M. P. Escudier *et al.*, J Non-Newton Fluid **97**, 99 (2001).

[205] D. R. Foss, and J. F. Brady, J Fluid Mech **407**, 167 (2000).

[206] G. K. Batchelor, J Fluid Mech **83**, 97 (1977).

[207] M. A. Alves, P. J. Oliveira, and F. T. Pinho, J Non-Newton Fluid **110**, 45 (2003).

[208] G. Bugliarello, and G. C. C. Hsiao, Science **143**, 469 (1964).

[209] R. Ditchfield, and W. L. Olbricht, J Biomech Eng-T ASME **118**, 287 (1996).

[210] T. Karino, M. Motomiya, and H. L. Goldsmith, in *Biologic and Synthetic Vascular Prostheses*, edited by J. C. Stanley (Grunne & Stratton, New York, 1982).

[211] D. P. Giddens, T. D. Tang, and F. Loth, in *Biological Flows*, edited by M. Y. Jaffrin, and C. G. Caro (Plenum Press, New York, 1995).

[212] E. B. Christiansen, T. R. Carter, and S. J. Kelsey, AICHE J **18**, 372 (1972).

[213] Y. Xia, P. T. Callaghan, and K. R. Jeffrey, AICHE J **38**, 1408 (1992).

[214] J. D. Seymour *et al.*, Phys Fluids A-Fluid **5**, 3010 (1993).

[215] M. Sahimi, Rev. Mod. Phys. **65**, 1393 (1993).

[216] M. Prat, Chem. Eng. J. **86**, 153 (2002).

[217] B. Berkowitz, and R. P. Ewing, Surv. Geophys. **19**, 23 (1998).

[218] P. R. Johnson, N. Sun, and M. Elimelech, Environmental Science & Technology **30**, 3284 (1996).

[219] J. D. Seymour, and P. T. Callaghan, Aiche Journal **43**, 2096 (1997).

[220] J. J. Tessier, and K. J. Packer, Physics of Fluids **10**, 75 (1998).

[221] A. J. Sederman, and L. F. Gladden, Magnetic Resonance Imaging **19**, 339 (2001).

[222] W. M. Holmes, and K. J. Packer, Magnetic Resonance Imaging **21**, 389 (2003).

[223] T. Brosten *et al.*, Journal of Colloid and Interface Science (2010).

[224] S. A. Creber, T. R. R. Pintelon, and M. L. Johns, Journal of Colloid and Interface Science **339**, 168 (2009).

[225] P. G. Saffman, Journal of Fluid Mechanics Digital Archive **6**, 321 (1959).

[226] R. P. Chhabra, J. Comiti, and I. Machac, Chemical Engineering Science **56**, 1 (2001).

[227] P. G. Saffman, Journal of Fluid Mechanics **6**, 321 (1959).

[228] J. Salles *et al.*, Physics of Fluids a-Fluid Dynamics **5**, 2348 (1993).

[229] D. L. Koch *et al.*, Journal of Fluid Mechanics **200**, 173 (1989).

[230] B. Berkowitz *et al.*, Reviews of Geophysics **44** (2006).

[231] M. Levy, and B. Berkowitz, Journal of Contaminant Hydrology **64**, 203 (2003).

[232] J. N. Ryan, and M. Elimelech, Colloid Surf. A-Physicochem. Eng. Asp. **107**, 1 (1996).

[233] F. A. L. Dullien, Aiche Journal **18**, 62 (1972).

[234] F. A. L. Dullien, and P. N. Mehta, Powder Technology **5**, 179 (1972).

[235] M. H. Peters, and R. X. Ying, Chemical Engineering Communications **108**, 165 (1991).

[236] X. Jia, and R. A. Williams, Chemical Engineering Communications **91**, 127 (1990).

[237] Z. Adamczyk *et al.*, Advances in Colloid and Interface Science **19**, 183 (1983).

[238] T. J. Murphy, and J. L. Aguirre, Journal of Chemical Physics **57**, 2098 (1972).

[239] V. G. Levich, *Physiochemical Hydrodynamics* (Prentice-Hall, Englewood Cliffs, NJ, 1962).

[240] M. Elimelech, Separations Technology **4**, 186 (1994).

[241] N. Tufenkji, and M. Elimelech, Langmuir **20**, 10818 (2004).

[242] M. Bostrom, D. R. M. Williams, and B. W. Ninham, Physical Review Letters **87** (2001).

[243] S. H. Behrens *et al.*, Langmuir **16**, 2566 (2000).

[244] Z. Adamczyk, and P. Weronski, Advances in Colloid and Interface Science **83**, 137 (1999).

[245] K. E. Nelson, and T. R. Ginn, Langmuir **21**, 2173 (2005).

[246] L. Song, and M. Elimelech, Colloid Surf. A-Physicochem. Eng. Asp. **73**, 49 (1993).

[247] Z. Adamczyk, and T. G. M. Vandeven, Journal of Colloid and Interface Science **80**, 340 (1981).

[248] E. Ruckenstein, and D. C. Prieve, Journal of the Chemical Society-Faraday Transactions Ii **69**, 1522 (1973).

[249] A. Cortis, and B. Berkowitz, Soil Sci. Soc. Am. J. **68**, 1539 (2004).

[250] A. E. Scheidegger, In: Proceedings of theory of fluid flow in porous media conference, Univ. Oklahoma, 101 (1959).

[251] B. Berkowitz, and H. Scher, Advances in Water Resources **32**, 750 (2009).

[252] B. Berkowitz, H. Scher, and S. E. Silliman, Water Resources Research **36**, 149 (2000).

[253] A. Cortis *et al.*, Physical Review E **70**, 8 (2004).

[254] S. P. Neuman, and D. M. Tartakovsky, Advances in Water Resources **32**, 670 (2009).

[255] M. Bostrom, D. R. M. Williams, and B. W. Ninham, Physical Review Letters **87**, 4 (2001).

[256] J. Happel, and H. Brenner, *Low Reynolds Number Hydrodynamics* (Prentice Hall, NJ, 1963).

[257] K. M. Yao, M. M. Habibian, and C. R. Omelia, Environmental Science & Technology **5**, 1105 (1971).

[258] J. Happel, Aiche Journal **4**, 197 (1958).

[259] L. A. Spielman, and Friedlan.Sk, Journal of Colloid and Interface Science **46**, 22 (1974).

[260] R. Rajagopalan, and C. Tien, Aiche Journal **22**, 523 (1976).

[261] A. B. Kersting *et al.*, Nature **397**, 56 (1999).

[262] B. Nagy *et al.*, Nature **354**, 472 (1991).

[263] J. P. Kaszuba, D. R. Janecky, and M. G. Snow, Chemical Geology **217**, 277 (2005).

[264] S. Emmanuel, and B. Berkowitz, Advances in Water Resources **28**, 337 (2005).

[265] M. Sahimi, G. R. Gavalas, and T. T. Tsotsis, Chemical Engineering Science **45**, 1443 (1990).

[266] A. M. Tartakovsky *et al.*, Water Resources Research **43** (2007).

[267] S. Emmanuel, and B. Berkowitz, Geophysical Research Letters **34** (2007).

[268] T. R. Brosten *et al.*, Phys. Rev. Lett. **103** (2009).

[269] L. Lebon *et al.*, Magnetic Resonance Imaging **14**, 989 (1996).

[270] B. Manz, P. Alexander, and L. F. Gladden, Physics of Fluids **11**, 259 (1999).

[271] U. M. Scheven, R. Harris, and M. L. Johns, Phys. Rev. Lett. **99** (2007).

[272] T. P. Clement, B. S. Hooker, and R. S. Skeen, Ground Water **34**, 934 (1996).

[273] M. Thullner, and P. Baveye, Biotechnology and Bioengineering **99**, 1337 (2008).

[274] J. D. Seymour *et al.*, Phys. Rev. Lett. **93** (2004).

[275] J. D. Seymour *et al.*, Advances in Water Resources **30**, 1408 (2007).

[276] D. A. G. von der Schulenburg *et al.*, Biotechnology and Bioengineering **101**, 602 (2008).

[277] R. M. Mazo, *Statistical Mechanical Theories of Transport Processes* (Pergamon Press, Oxford, 1967), p. 166.

[278] J. H. Cushman, X. L. Hu, and T. R. Ginn, Journal of Statistical Physics **75**, 859 (1994).

[279] D. L. Koch, and J. F. Brady, Physics of Fluids **31**, 965 (1988).

[280] J. H. Cushman, and T. R. Ginn, Water Resources Research **36**, 3763 (2000).

[281] K. Kose, Phys. Rev. Lett. **72**, 1467 (1994).

[282] A. J. Sederman *et al.*, Journal of Magnetic Resonance **166**, 182 (2004).

[283] F. G. Ferris *et al.*, Journal of Canadian Petroleum Technology **35**, 56 (1996).

[284] F. G. Ferris *et al.*, Geochimica Et Cosmochimica Acta **68**, 1701 (2004).

[285] B. Blumich, *NMR Imaging of Materials* (Clarendon Press, Oxford, 2000).

[286] B. C. Hoskins *et al.*, Journal of Magnetic Resonance **139**, 67 (1999).

[287] M. Annaka, and T. Tanaka, Nature **355**, 430 (1992).

[288] F. Ilmain, T. Tanaka, and E. Kokufuta, Nature **349**, 400 (1991).

[289] K. Y. Lee, and D. J. Mooney, Chemical Reviews **101**, 1869 (2001).

[290] O. Okay, Progress in Polymer Science **25**, 711 (2000).

[291] Y. Qiu, and K. Park, Advanced Drug Delivery Reviews **53**, 321 (2001).

[292] N. M. Sangeetha, and U. Maitra, Chemical Society Reviews **34**, 821 (2005).

[293] A. M. Stephan, European Polymer Journal **42**, 21 (2006).

[294] P. J. Flory, Faraday Discuss Chem Soc **57** (1974).

[295] A. R. Altenberger, and M. Tirrell, J. Chem. Phys. **80**, 2208 (1984).

[296] R. I. Cukier, Macromolecules **17**, 252 (1984).

[297] P. G. Degennes, Macromolecules **19**, 1245 (1986).

[298] R. G. Bryant, Annu. Rev. Biophys. Biomolec. Struct. **25**, 29 (1996).

[299] V. Klepko, Y. Melnichenko, and V. Shilov, Polym. Gels Netw. **4**, 351 (1996).

[300] L. Masaro, and X. X. Zhu, Progress in Polymer Science **24**, 731 (1999).

[301] P. I. Hurtado, L. Berthier, and W. Kob, Phys. Rev. Lett. **98**, 4 (2007).

[302] Y. Y. Suzuki, M. Tokita, and S. Mukai, European Physical Journal E **29**, 415 (2009).

[303] P. G. Degennes, *Scaling Concepts in Polymer Physics* (Cornell University Press, Ithaca, 1979).

[304] M. A. Lauffer, Biophysical Journal **1**, 205 (1961).

[305] P. G. Degennes, J. Chem. Phys. **55**, 572 (1971).

[306] K. F. Arndt, D. Kuckling, and A. Richter, Polymers for Advanced Technologies **11**, 496 (2000).

[307] A. Richter *et al.*, Sensors **8**, 561 (2008).

[308] S. H. Gehrke, Advances in Polymer Science **110**, 81 (1993).

[309] L. Sawyer, and G. Kontopidis, Biochim. Biophys. Acta-Protein Struct. Molec. Enzym. **1482**, 136 (2000).

[310] J. Visser, and T. J. M. Jeurnink, Experimental Thermal and Fluid Science **14**, 407 (1997).

[311] K. Baussay *et al.*, International Journal of Biological Macromolecules **34**, 21 (2004).

[312] C. Le Bon, D. Durand, and T. Nicolai, International Dairy Journal **12**, 671 (2002).

[313] T. Nicolai, and D. Durand, Current Opinion in Colloid & Interface Science **12**, 23 (2007).

[314] S. Mehalebi, T. Nicolai, and D. Durand, International Journal of Biological Macromolecules **43**, 129 (2008).

[315] A. H. Clark, G. M. Kavanagh, and S. B. Ross-Murphy, Food Hydrocolloids **15**, 383 (2001).

[316] M. Langton, and A. M. Hermansson, Food Hydrocolloids **5**, 523 (1992).

[317] P. Aymard *et al.*, Journal De Chimie Physique Et De Physico-Chimie Biologique **93**, 987 (1996).

[318] C. Le Bon, T. Nicolai, and D. Durand, Macromolecules **32**, 6120 (1999).

[319] A. Suzuki, and M. Yoshikawa, J. Chem. Phys. **125** (2006).

[320] N. Loren, M. Nyden, and A.-M. Hermansson, Adv Colloid Interface Sci **150**, 5 (2009).

[321] N. Loren *et al.*, Biomacromolecules **10**, 275 (2009).

[322] P. N. Sen, Concepts Magn. Reson. Part A **23A**, 1 (2004).

[323] P. P. Mitra, P. N. Sen, and L. M. Schwartz, Physical Review B **47**, 8565 (1993).

[324] P. G. Saffman, Studies in Applied Mathematics **50**, 93 (1971).

[325] B. Berkowitz, Advances in Water Resources **25**, 861 (2002).

[326] M. Sahimi, *Applications of Percolation Theory* (Taylor & Francis, Bristol, 1994).

[327] J. D. Seymour *et al.*, Phys. Rev. Lett. **93**, 4 (2004).

[328] M. Kopf *et al.*, Biophysical Journal **70**, 2950 (1996).

[329] D. Kandhai *et al.*, Phys. Rev. Lett. **88**, 4 (2002).

[330] H. A. Stone, Annual Review of Fluid Mechanics **26**, 65 (1994).

[331] A. F. Dexter, A. S. Malcolm, and A. P. J. Middelberg, Nature Materials **5**, 502 (2006).

[332] A. F. Dexter, and A. P. J. Middelberg, Journal of Physical Chemistry C **111**, 10484 (2007).

[333] A. P. J. Middelberg *et al.*, Journal of the Royal Society Interface **5**, 47 (2008).

[334] R. Fairman *et al.*, Protein Science **4**, 1457 (1995).

[335] A. F. Dexter, and A. P. J. Middelberg, Industrial & Engineering Chemistry Research **47**, 6391 (2008).

[336] L. Z. He *et al.*, Langmuir **25**, 4021 (2009).

[337] A. S. Malcolm *et al.*, ChemPhysChem **10**, 778 (2009).

[338] J. Hennig, A. Nauerth, and H. Friedburg, Magnetic Resonance in Medicine **3**, 823 (1986).

[339] A. J. Sederman *et al.*, Journal of Magnetic Resonance **171**, 118 (2004).

[340] G. I. Taylor, Proceedings of the Royal Society of London Series a-Containing Papers of a Mathematical and Physical Character **138**, 41 (1932).

[341] G. I. Taylor, Proceedings of the Royal Society of London Series a-Mathematical and Physical Sciences **146**, 0501 (1934).

[342] J. M. Rallison, Annual Review of Fluid Mechanics **16**, 45 (1984).

[343] H. P. Grace, Chem Eng Commun **14**, 225 (1981).

[344] J. M. Rallison, Journal of Fluid Mechanics **98**, 625 (1980).

[345] Barthesb.D, and A. Acrivos, Journal of Fluid Mechanics **61**, 1 (1973).

[346] E. D. Wetzel, and C. L. Tucker, Journal of Fluid Mechanics **426**, 199 (2001).

[347] N. E. Jackson, and C. L. Tucker, Journal of Rheology **47**, 659 (2003).

[348] P. L. Maffettone, and M. Minale, Journal of Non-Newtonian Fluid Mechanics **78**, 227 (1998).

[349] G. I. Taylor, Proc Intl Congr Appl Mech, 11th, Munich, 790 (1964).

[350] A. Acrivos, and T. S. Lo, Journal of Fluid Mechanics **86**, 641 (1978).

[351] P. Van Puyvelde *et al.*, Polymer **49**, 5363 (2008).

[352] M. Shapira, and S. Haber, International Journal of Multiphase Flow **16**, 305 (1990).

[353] V. Sibillo *et al.*, Physical Review Letters **97** (2006).

[354] S. Torza, S. G. Mason, and R. G. Cox, Journal of Colloid and Interface Science **38**, 395 (1972).

[355] P. J. A. Janssen, and P. D. Anderson, Phys. Fluids **19**, 11 (2007).

[356] P. J. A. Janssen, and P. D. Anderson, Journal of Computational Physics **227**, 8807 (2008).

[357] K. Feigl *et al.*, Chemical Engineering Science **62**, 3242 (2007).

[358] P. T. Callaghan, Reports on Progress in Physics **62**, 599 (1999).

[359] Y. Rotenberg, L. Boruvka, and A. W. Neumann, Journal of Colloid and Interface Science **93**, 169 (1983).

[360] O. I. del Rio, and A. W. Neumann, Journal of Colloid and Interface Science **196**, 136 (1997).

[361] A. H. Demond, and A. S. Lindner, Environ. Sci. Technol. **27**, 2318 (1993).

[362] B. Janczuk, W. Wojcik, and A. Zdziennicka, Journal of Colloid and Interface Science **157**, 384 (1993).

[363] F. K. Hansen, and H. Fagerheim, Colloids and Surfaces a-Physicochemical and Engineering Aspects **137**, 217 (1998).

[364] W. J. Milliken, H. A. Stone, and L. G. Leal, Physics of Fluids a-Fluid Dynamics **5**, 69 (1993).

APPENDIX A

MATLAB CODE TO PRODUCE PARTICLE CONCENTRATION PROFILES IN A CAPILLARY

Matlab function used to fit concentration profiles and example of input parameters to obtain ϕ = 0.22 and the correct Pe_B:

Bisection_Method_Circular (0.4,1.8,0.75,0.2965,11.769)
Pe_B = 10
Bisection_Method_Circular (0.4,1.8,0.75,0.4895,115.2)
Pe_B = 100
Bisection_Method_Circular (0.4,1.8,0.75,0.5619,309.818)
Pe_B = 270
Bisection_Method_Circular (0.4,1.8,0.75,0.6204,1146)
Pe_B = 1000

****

```
function [T] = Bisection_Method_Circular(A,Lambda_B,Lambda_H,C_0,dPdx)
global dUdx Pe rho P S h
%close all
eps = 0.000000001;
%Data for Delta = 250ms
X_1 =
[0.992,0.975,0.957,0.940,0.922,0.904,0.885,0.866,0.847,0.827,0.806,0.78
5,0.764,0.742,0.719,0.695,0.671,0.645,0.619,0.591,0.563,0.532,0.500,0.4
65,0.428,0.387,0.341,0.287,0.220,0.091];
X_1 = X_1/2;
DATA_1
=[0.124,0.120,0.119,0.128,0.139,0.149,0.154,0.168,0.165,0.183,0.180,0.1
92,0.192,0.207,0.208,0.196,0.195,0.235,0.217,0.222,0.236,0.238,0.250,0.
238,0.266,0.267,0.249,0.311,0.391,0.399];
X_1PTS(1:30) = -X_1(1:30);
X_1PTS(31:60) = X_1(30:-1:1);
DATA_1PTS(1:30) = DATA_1(1:30);
DATA_1PTS(31:60) = DATA_1(30:-1:1);

%Bisect Method, very slow convergence compared with other root finding
methods
N = 5000
h = 0.0005/N; %m
C_m = 0.68;
rho_h(1) = 1 + 2.5*C_0*((1-(C_0/C_m))^-1) + 0.1*(C_0^2)*((1-
(C_0/C_m))^-2);
    for i = 2:N
        Cb =  C_0;
        Ca =  0;
        y(1) = 0;
        y(i) = y(1) + i*h;
        C_Total(1) = C_0;
        K = abs(Ca - Cb);
        while( K > eps )
            Cmid = (Ca + Cb)/2;
```

```
            FCa = F_C(C_Total(i-1),Ca,y(i-
1),y(i),A,Lambda_B,Lambda_H,dPdx,i);
            FCmid = F_C(C_Total(i-1),Cmid,y(i-
1),y(i),A,Lambda_B,Lambda_H,dPdx,i);
            K = abs(Ca-Cb);
            if FCa*FCmid > 0
                Ca = Cmid;
            else
                Cb = Cmid;
            end
        end
    H(i) = (pi*((y(i)^2)-(y(i-1)^2)))*(1000000); %Area Element(mm2)
    C_T(i) = (Cmid*H(i))/(0.785398163);%Conc at i divided by the area
element
    C_Total(i) = Cmid; %Concentration at i
    rho_h(i) = rho;
    Pe_H(i) = (Pe(i))*((y(i)^2)-(y(i-1)^2))/(0.0005^2);
    K_T(i) = P(i);
    S_T(i) = S(i);
    RT(i) = P(i)-S(i);
    FT(i) = FCmid;
    end
    Area = sum(H); %(mm2)
    dU = h*dUdx;%[m/s]
    y = y*(1/h)*(500/N); %Micrometers
    %plot(y/500,dUdx)
    %xlabel('Radial position (r/R)')
    %ylabel('Shear Rate (1/s)')
U_Const = 0.0015499-((0.0383-0.0881)/1000);
for k = 2:N
    %T(1)= C_Total(1)/C_m;
    %T(k)= C_Total(k)/C_m;
    T(1)= C_Total(1);
    T(k)= C_Total(k);
    U(1) = 0.0015499+(-(0.0383+0.0827))/1000
;%+((0.0379)/1000);%((0.0881-
0.0383)/1000)[0.04];%((0.0379)/1000);%[0.08];%,((0.0383-
0.0881)/1000)[0.04];%[m/s]%(-(0.0383+0.0827))/1000 [0.43s]((-
0.0383)/1000) [0.43]
    U(k) = U(k-1) - dU(k);
end
U_N = U(N)*1000;
%hold on
%plot(y/N,(U/U_Const),'b')
%xlabel('Radial position (r/R)')
%ylabel('V / V_M_a_x')
%AXIS([0 1 0 1])
Conc = sum(C_T)
PeB = sum(Pe_H)

    X_1PTS = X_1PTS*1000; %[micron]
    X_2PTS = X_2PTS*1000;
    X_3PTS = X_3PTS*1000;
    X_4PTS = X_4PTS*1000;
```

```
    TX(N:((2*N)-1)) = T(1:N);
    TX(1:N-1) = T(N:-1:2);
    D(N:(2*N)-1) = Conc;
    D(1:N-1) = Conc;
    yx(N:(2*N)-1) = y(1:N);
    yx(1:(N-1)) = -y(N:-1:2);
    %figure
    %plot(y/500,Pe)
    %xlabel('Radial position (r/R)');
    %ylabel('Peclet Number');
    %figure
    %plot(y/500,rho_h)
    %xlabel('Radial position (r/R)')
    %ylabel('Viscosity (mPa*s)')

    %hold off
    %figure
    %plot(y,K_T)
    %ylabel('N_2')
    %figure
    %plot(y,S_T)
    %ylabel('Differential')
    %figure
    %plot(y,RT)
    %ylabel('N2')
    %figure
    %plot(y,FT)
    %ylabel('Difference')
    %figure
    hold on
    plot(yx/500,D)
    plot(yx/500,TX,'k');
    xlabel('r/R')
    ylabel('C/C_m')
    ylabel('Particle Volume Fraction')
    plot(X_1PTS/500,DATA_1PTS,'r.');
    plot(X_2PTS/500,DATA_2PTS,'g.');
    plot(X_3PTS/500,DATA_3PTS,'b.');
    plot(X_4PTS/500,DATA_4PTS,'m.');
    AXIS([-1 1 0 0.7])

**************************************************************************

function [F] = F_C(C0,C1,y0,y1,A,Lambda_B,Lambda_H,dPdx,i)
global dUdx Pe rho P S h
k = 1.38065*10^-23; %Boltzmann Constant ((m2*kg)/(s2*K))
T = 293; %Temperature (K), T: 20oC
a = 0.00000125; %Radius of spheres (m)
C_m = 0.68; %Maximum concentration packing
E = 1/400; %radius of sphere (a = 2.5micron) / diameter of capillary (D
= 1000micron)
%dPdx = 1; %Pressure gradient, related to the velocity gradient by
rho_0*rho_s*(du/dy)=(dP/dx)*y
rho_0 = 0.001; %Viscosity of water (Pa*sec)
```

```
rho_s = 1 + 2.5*C1*((1-(C1/C_m))^-1) + 0.1*(C1^2)*((1-(C1/C_m))^-2);
%Morris and Boulay [J. Rheol. 43(5)1999 1213-1237]
%rho_s = (1-(C1/C_m))^-2; %Krieger [Adv. Colloid Interf. Sci. 3 (1972)
111-136]
rho = rho_s;
rho_n = 0.75*(((C1/C_m)^2))/((1-(C1/C_m))^2); %Morris and Boulay [J.
Rheol. 43(5)1999 1213-1237]
dUdx(i) = (((dPdx*y1)/(2*rho_0*rho_s)));%+((E)*rho_s));
Pe(i) =(6*pi*rho_0*dUdx(i)*(a^3))/(k*T);
N_2(i) = -0.3*rho_0*rho_n*dUdx(i); % [Pa]
C_1 = -k*T/((4/3)*pi*a^3);
C_2 = ((6*pi*rho_0*a^3)/(k*T))*((dPdx)/(rho_0*rho_s));
C_3 = A*Lambda_B*((6*pi*rho_0*(a^3))/(k*T))*((dPdx)/(rho_0*rho_s));
C_4 = 0.75*Lambda_H;
FA = C_1*(3*C0/(1-(C0/C_m))) + (C_1*(2/9)*C_2)*(y0/((((1-
(C0/C_m))^3)/(C_3*y0*C0))+(((1-(C0/C_m))^2)/((C_4*(C0/C_m)^2)))));
FB = C_1*(3*C1/(1-(C1/C_m))) + (C_1*(2/9)*C_2)*(y1/((((1-
(C1/C_m))^3)/(C_3*y1*C1))+(((1-(C1/C_m))^2)/((C_4*(C1/C_m)^2)))));
P(i) = N_2(i)/y1;
S(i) = (FA-FB)/(y0-y1);
F = FA - FB + P(i)*(y0-y1);

**************************************************************************
```

APPENDIX B

MOMENTS FROM PROPAGATOR EXPERIMENTS FOR MICROCAPILLARY

Calculated Variance from Propagator Experiments, Flow: 0.000mL/hr:

Exp	Delta(ms)	Mean (μm)	Variance (m^2)	Skew ($μm^3$)
1618	25	0.0213	2.61E-13	0.2614
1619	50	-0.0119	3.36E-13	-0.0678
1620	75	-0.0106	3.47E-13	-0.0228
1621	100	-0.0188	2.90E-13	-0.0038
1622	150	-0.0112	2.91E-13	-0.0111
1623	200	0.0390	3.00E-13	0.0812
1624	300	-0.0042	3.69E-13	-0.0737

1st Central Moment	Avg. Mean:	0.006μm

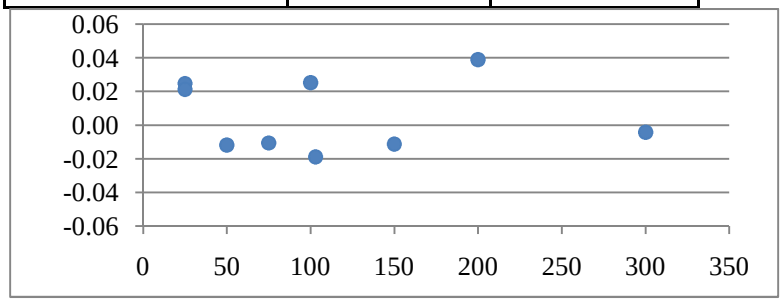

2nd Central Moment	Avg. Variance:	3.00E-13m^2

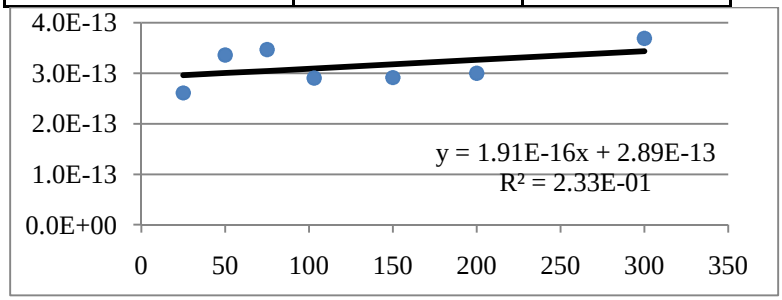

3rd Central Moment	Avg. Skew:	0.01$μm^3$

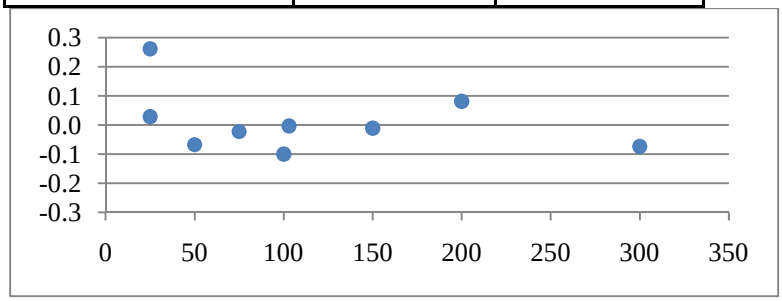

Calculated Variance from Propagator Experiments, Flow: 0.125mL/hr:

Exp	Delta(ms)	Mean (μm)	Variance (m^2/s)	Skew (μm^3)
1588	25	0.0072	1.35E-13	-0.0199
1589	50	0.0252	5.99E-13	-0.0583
1590	75	0.0222	2.26E-13	0.0385
1591	100	0.0340	3.79E-13	-0.1313
1592	125	0.0449	5.05E-13	-0.2177
1593	150	0.1612	4.89E-13	0.0200
1594	175	0.1468	5.99E-13	-0.0583
1595	200	0.2288	1.71E-12	0.2983
1596	250	0.4159	1.36E-12	1.3567
1606	300	0.6747	8.58E-12	-0.5189
1607	400	0.7750	1.07E-11	3.2805
1608	200	0.4462	3.11E-12	0.2283

1st Central Moment	Avg. Mean:	0.249μm

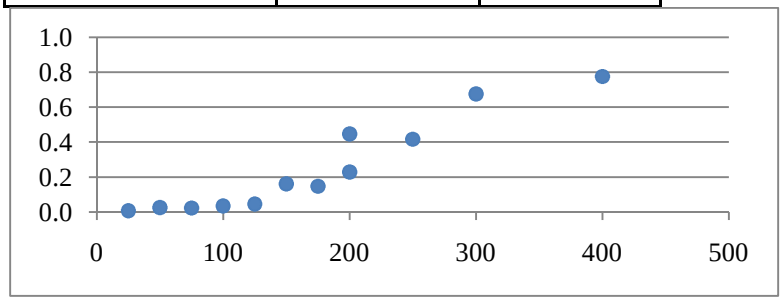

2nd Central Moment	Avg. Variance:	2.37E-12m^2/s

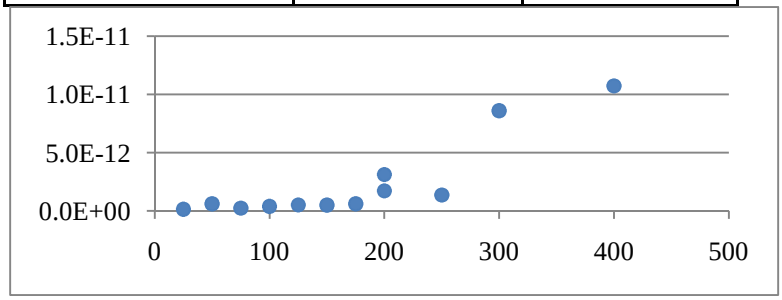

3rd Central Moment	Avg. Skew:	0.35μm^3

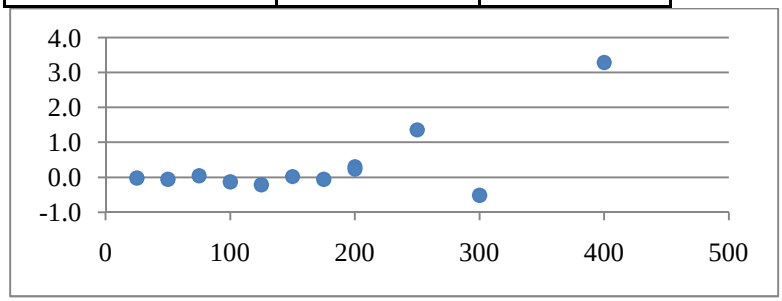

Calculated Variance from Propagator Experiments, Flow: 0.250mL/hr:

Exp	Delta(ms)	Mean (μm)	Variance (m^2)	Skew (μm^3)
1579	25	-0.0160	4.76E-13	-0.01
1580	50	0.0502	7.50E-13	-0.07
1581	75	0.0254	7.00E-13	-0.36
1582	100	0.2568	1.46E-12	0.22
1583	125	0.1533	2.58E-12	-2.15
1584	150	0.2281	4.96E-12	-9.08
1586	175	-0.0936	5.52E-12	-9.38
1587	200	0.4244	6.81E-12	1.95

1st Central Moment	Avg. Mean:	0.129μm

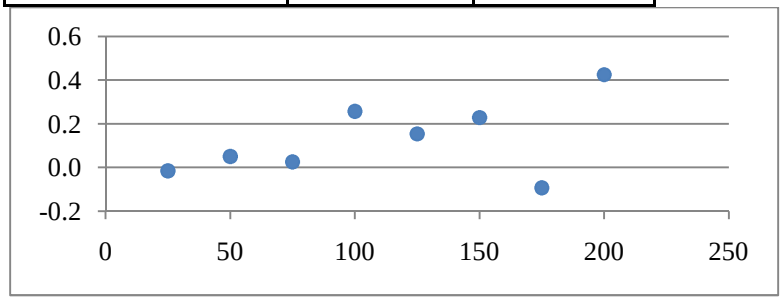

2nd Central Moment	Avg. Variance:	2.91E-12m^2

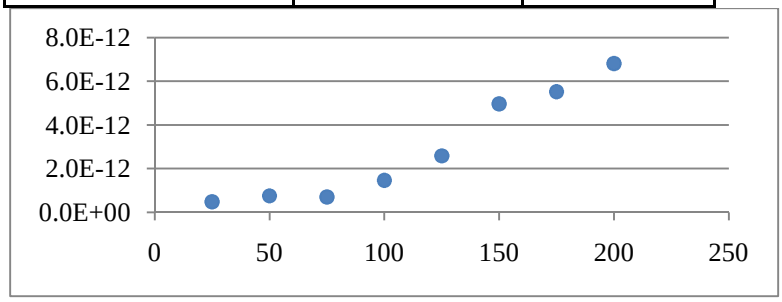

3rd Central Moment	Avg. Skew:	-2.36μm^3

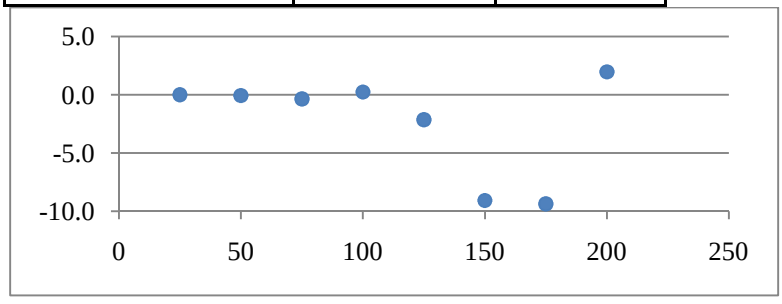

Calculated Variance from Propagator Experiments, Flow: 0.500mL/hr:

Exp	Delta(ms)	Mean (μm)	Variance (m^2/s)	Skew (μm^3)
1598	25	0.1129	9.56E-13	-0.16
1599	50	-0.0105	2.91E-12	-5.81
1600	75	0.2812	4.02E-12	4.85
1601	100	0.2812	4.02E-12	4.85
1602	125	0.3335	5.18E-12	3.94
1603	150	0.7141	8.15E-12	11.77

1st Central Moment	Avg. Mean:	0.285μm

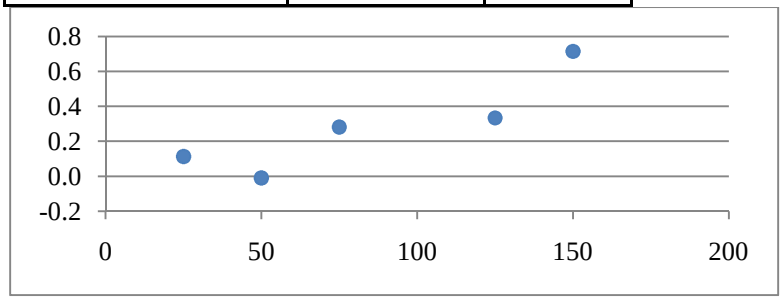

2nd Central Moment	Avg. variance:	4.21E-12m^2/s

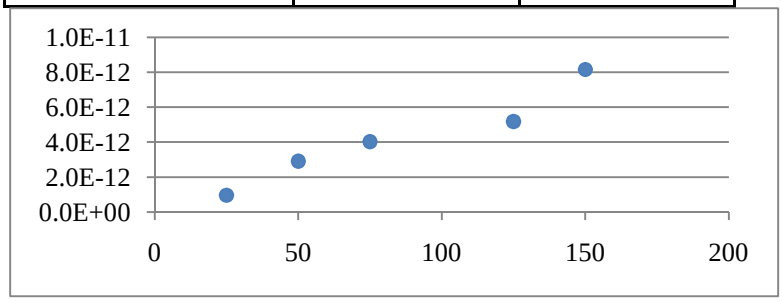

3rd Central Moment	Avg. Skew:	3.24μm^3

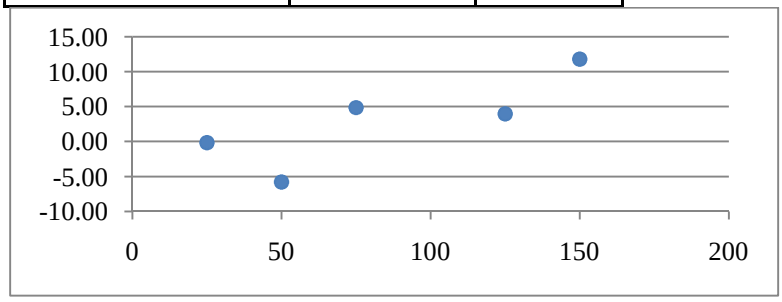

APPENDIX C

MOMENTS FROM PROPAGATOR EXPERIMENTS FOR BETALACTOGLOBULIN GELS

Variances for propagator experiments for the homogeneous gel, with DI water with and without 0.3M NaCl flowing through the gel, showing the similarities between the flow dynamics. This data is from two different homogeneous gels created by the same procedure.

Flow: 10mL/hr	**Variance ∥ to flow (μm^2)**		**Variance ⊥ to flow (μm^2)**	
Δ(ms)	**w.o. salt**	**w. salt**	**w.o. salt**	**w. salt**
25	113.0	115.6	90.2	89.8
100	420.7	454.2	319.2	325.4
200	825.7	840.2	627.8	628.2
300	1204.6	1135.4	905.9	887.6
Flow: 20mL/hr	**Variance ∥ to flow (μm^2)**		**Variance ⊥ to flow (μm^2)**	
Δ(ms)	**w.o. salt**	**w. salt**	**w.o. salt**	**w. salt**
25	118.3	115.6	90.2	89.8
100	449.1	442.5	332.8	330.1
200	955.9	915.0	673.4	636.0

Table C.1 Shows the variance for propagators from two different homogeneous gels with flow of DI water with and without salt (0.3M NaCl) indicating minimal difference between the propagators compared.

APPENDIX D

MATLAB CODE TO MEASURE INTERFACIAL TENSION

Matlab code to measure interfacial tension:

1st obtain point coordinates from a picture.

```
**************************************************************************

global U W
%Glycerol + AFD4 EXPERIMENTS
%*****************************************
A1 = imread('Ch70_GlycerolAFD4.bmp');
%*****************************************

figure
image(A1);
imshow(A1);
%B1 = RGB2GRAY(A1);
%figure
%imshow(B1)
for h = 1:40
    H(h) = impoint;
    pos = getPosition(H(h));
    U(h) = pos(1,1);
    W(h) = pos(1,2);
end

**************************************************************************
```

2nd fit the points using the ASDA-P method.

```
**************************************************************************
close all
global U W
tic
%A1 = imread('Droplet_8020CT.bmp');
%figure
%image(A1);
%B1 = RGB2GRAY(A1);
%figure
%imshow(B1)
%BW1 = EDGE(B1,'roberts',0.024);
%BW2 = EDGE(B1,'sobel',0.024);
%BW3 = EDGE(B1,'prewitt',0.024);
%BW4 = EDGE(B1,'log',0.002);
%BW = BW1 + BW2 + BW3; %+ BW4;
%figure
%imshow(BW1)
%figure
%imshow(BW2)
%figure
%imshow(BW3)
%figure
%imshow(BW4)
%figure
```

```
%imshow(BW)
    LENGD = 5.85;
    U_1 = U-max(U);
    W_1 = -(W-max(W));
    a = max(W_1);
    b = min(W_1);
    c = a-b;
    wa = abs(max(U_1));
    wb = abs(min(U_1));
    d = wa-wb;
    U_1 = ((U_1-(d/2))/c)*LENGD;
    W_1 = (W_1/c)*LENGD-(LENGD);
    plot(U_1,W_1,'.')
    answer = 1;
            %All length units is mm
            rho = 0.0291*10^-6; %density difference between fluids
           (kg/mm3)
            g = 9800;    %mm/s2
while answer == 1;
    clear xi yi SUML
    A_1 = input('Sigma_Min: ');
    A_2 = input('Sigma_Inc: ');
    A_3 = input('Sigma_Max: ');
    B_1 = input('R0_y_Min: ');
    B_2 = input('R0_y_Inc: ');
    B_3 = input('R0_y_Max: ');

    Sigma_x = [A_1:A_2:A_3];
    h = 0.05;
    R0_y = [B_1:B_2:B_3];
    Length_1 = length(Sigma_x)
    Length_2 = length(R0_y)
    Sigma = Sigma_x;
    R0 = R0_y;
    for o = 1:Length_1
        for d = 1:Length_2
            A = 0;
            i = 2;
            Z(1) = 0;           %Initial Z-location
            X(1) = 0.005;       %Initial X-location
            Theta(1) = 0;       %Initial Angle
            while A~=1
              Theta(i) = Theta(i-1) + h*((2/R0(d))+(((rho*g*Z(i-
1)))/Sigma(o))-(sin(Theta(i-1))/X(i-1)));
              X(i) = X(i-1) + h*(cos(Theta(i-1)));
              Z(i) = Z(i-1) + h*(sin(Theta(i-1)));
                    if Z(i)< Z(i-1)
                        A = 1;
                    elseif i > 1000
                        A = 1;
                    end
                        i = i+1;
            end
                Le = numel(X);
```

```
                for i = (Le+1):2*Le
                    X(i) = -X(i-Le);
                    Z(i) =  Z(i-Le);
                end
                for k = 1:40;
                    for j = 1:2*Le;
                        Dist(j) = sqrt(((X(j)-U_1(k))^2)+((Z(j)-
W_1(k))^2));
                    end
                    L(k) = (min(Dist));
                    clear Dist
                end
                %Ratio_1 = max(abs(X))/max(abs(Z));
                %Ratio_2 = max(abs(U_1))/max(abs(W_1));
                %Ratio = 100*abs(Ratio_1-Ratio_2);
                G(o,d) = sum(L);
                Ratio_3(o,d) = (abs((max(abs(X)))-
(max(abs(U_1)))))*100;
                Ratio_4(o,d) = (abs((max(abs(Z)))-
(max(abs(W_1)))))*100;
                SUML(o,d) = G(o,d) + Ratio_3(o,d) + Ratio_4(o,d);
                clear i A X Z Theta L
        end
    end
    [xi,yi]= find(SUML == min(SUML(:)));
    %[xi,yi] = find(G == min(G(:)));
    %xi = min(xi)
    %yi = min(yi)
    S = Sigma_x(xi)
    R = R0_y(yi)
    SUMLS = SUML(xi,yi)
    G = G(xi,yi)
    Ratio_3 = Ratio_3(xi,yi)
    Ratio_4 = Ratio_4(xi,yi)
g = 9800;    %mm/s2
R0 = R;
Sigma = S; %N/m = kg/s2
B = 0;
q = 2;
toc
    Z_3(1) = 0;           %Initial Z-location
    X_3(1) = 0.005;       %Initial X-location
    Theta(1) = 0;         %Initial Angle
    h = 0.05;
    while B~=1
        Theta(q) = Theta(q-1) + h*((2/R0)+(((rho*g*Z_3(q-1)))/Sigma)-
(sin(Theta(q-1))/X_3(q-1)));
        X_3(q) = X_3(q-1) + h*(cos(Theta(q-1)));
        Z_3(q) = Z_3(q-1) + h*(sin(Theta(q-1)));
        if Z_3(q)< Z_3(q-1)
        B = 1;
        elseif q > 1000
        B = 1;
        end
```

```
        q = q+1;
    end
        Le1 = numel(X_3);
        for l = (Le1+1):2*Le1
            X_3(l) = -X_3(l-Le1);
            Z_3(l) =  Z_3(l-Le1);
        end
figure
hold on
plot(U_1,W_1,'.')
plot(X_3,-Z_3,'. r')
xlabel('X(mm)')
ylabel('Z(mm)')
%AXIS([-1 1 -1 0])
hold off
figure
surf(SUML)
clear X Z X_3 Z_3
answer = input('Is it close (Yes = 0, No = 1)')
%close all
end
```